An Evaluation of the Influence of Residual Stress on the Fatigue Crack Growth Behavior of Additively Manufactured Metals

By

CHRISTINE MARIE SMUDDE

DISSERTATION

Submitted in partial satisfaction of the requirements for the degree of

DOCTOR OF PHILOSOPHY

in

Materials Science and Engineering

in the

OFFICE OF GRADUATE STUDIES

of the

UNIVERSITY OF CALIFORNIA

DAVIS

Approved:

_____

Jeffery C. Gibeling, Chair

_____

Michael R. Hill

_____

Susan P. Gentry

Committee in Charge

2022

Dedication

This dissertation is dedicated to my family, for providing unwavering support and believing in my ability to complete this degree, and to my 100-year-old grandma, Soledad Chacon, for being a constant inspiration.

Abstract

Additive manufacturing (AM) supports innovative engineering design by enabling the production of complex, high-quality parts on demand, but also introduces significant residual stress and distinctive grain morphologies that influence mechanical behavior. Specifically, AM presents challenges in reliability for fatigue critical applications where residual stress impacts measured crack growth rates for damage tolerant life predictions. Although the importance of these effects has been recognized, they are not well understood. Therefore, the aim of this work is to quantify and compare the influence of process-induced residual stress on measured crack growth rates of AM Type 304L austenitic stainless steel produced by directed energy deposition (DED) and laser powder bed fusion (PBF). Orientation dependence was evaluated by comparing crack growth parallel and perpendicular to the build direction. Alternating stress intensity factor ($\Delta K = K_{max} - K_{min}$) tests, where K characterizes the stress field at the crack tip, were used to assess fatigue crack growth behavior in the near-threshold regime ($<10^{-8}$ m/cycle). To connect process influence and fatigue performance, data were compared to an existing engineering reference material (annealed wrought Type 304/304L austenitic stainless steel).

Fatigue crack growth rates in DED builds manufactured with identical process parameters were investigated. Macroscale residual stress and residual stress intensity factor (K_{res}) profiles of a secondary fatigue specimen were measured using the slitting method. Positive values of K_{res} led to higher fatigue crack growth rates compared to wrought material. While the slitting method provided an estimate of residual stress effects, an accurate means of quantifying K_{res} in individual (primary) specimens offers better insight into the fatigue crack growth behavior of AM material. The on-line crack compliance (OLCC) method was adopted to quantify K_{res} from data collected during a fatigue crack growth rate test. However, the published methodology does not clearly

illustrate the process of determining K_{res}, so a validation study was undertaken using specimens fabricated from aluminum alloy 7050-T74. An improved approach to data analysis based the Schindler influence function was developed and applied to the fatigue test data of DED material. The K_{res} profiles from OLCC showed that DED specimens oriented for crack growth perpendicular to the build direction have larger values of positive K_{res} as compared to those with crack growth parallel. Correcting measured fatigue crack growth rates for the influence of residual stress using K_{res} caused data for both orientations to collapse into a single curve, indicating the primary difference in crack growth rates parallel and perpendicular to the build direction was due to tensile residual stress and that anisotropic grain morphology had a minor influence on the fatigue performance.

PBF builds that were fabricated on different systems using similar process parameters were evaluated using the same fatigue crack growth testing and K_{res} data analysis methods. Initial residual stress measurements revealed higher values in the PBF as compared to DED. The OLCC method indicated similar values of K_{res} for both specimen orientations in the PBF material that were higher than those measured in either orientation of DED, leading to higher measured growth rates in the PBF material compared to DED at the same applied ΔK. Data for both orientations of PBF material demonstrated agreement prior to corrections for residual stress, consistent with the similarity of K_{res}. After corrections, fatigue crack growth rate data were similar in all PBF and DED specimens. Additionally, the corrected data of PBF and DED were consistent with data for wrought material that had been corrected for fatigue crack closure effects, indicating the differing amounts of residual stress was the primary contributor to the different apparent fatigue performance in the materials produced by the AM and conventional methods.

Acknowledgements

I would first like to thank my advisor and mentor, Professor Jeffery C. Gibeling, for his guidance throughout the years of my dissertation research. Thank you for accepting my demand to work with you. I knew UC Davis was where I wanted to be, and I am forever grateful for your mentorship.

I would like to thank my dissertation committee for their constructive feedback and assistance during my graduate career. Professor Michael R. Hill of Mechanical and Aerospace Engineering offered insight to residual stress and provided research conceptualization that significantly impacted my dissertation research. Professor Susan P. Gentry was my mentor in the Materials Science and Engineering department, who provided advice and friendly conversation about engineering education and post graduate opportunities.

I would also like to thank Dr. Christopher San Marchi of Sandia National Laboratories for providing material and advice throughout my graduate research. My internship with you and Dr. Thale Smith at the Hydrogen Effects on Materials Lab was an enlightening experience that inspired the course of my career.

I would like to gratefully acknowledge that this work was primarily funded by a NASA Space Technology Research Fellowship (NSTRF19 – 80NSSC19K1132), and I would like to thank Drs. Edward Glaessgen, Andy Newman, and Wes Tayon at NASA Langley Research Center for their support in a long-distance collaboration during a worldwide pandemic.

I would like to thank my colleagues in the Shake and Break laboratory, primarily Dayane M. Oliveira and Mingwei Zhang. We all started together, and it was a privilege to work with you for the entirety of your graduate careers. As the first to start and the last to finish, it was a privilege of watching you both grow and succeed in all your endeavors. Additionally, I would like to thank

Chris D'Elia of the Materials Performance Laboratory for his support in learning how to perform residual stress measurement.

I would like to thank my pre-pandemic gym friends for their dedication to early mornings and hard work. Boyi Qu and Dayane M. Oliveira motivated our Friday morning workouts before Coffee, Bagel, Donut Day. Matt McNulty, Bradley Harris, and Mike Meloni showed me the importance of including arm day in my workout routine. Additional thanks to Noah Felvey for introducing me to golf and the satisfaction of hitting a small ball as hard as you can after a frustrating week of research.

Thank you to Olivia Schmidt for being the whole reason I visited Davis in the first place. Living with you and Camille Lopez during my first year of graduate school felt like destiny. Thank you to Jose Hernandez, Noah Felvey, and Matt McNulty for welcoming me to the department during my graduate school visit. Your friendship has helped shaped the person I am today, and I am forever grateful.

Thank you to my family, which includes my parents, Paul and Nancy Smudde, and my sister, Dani Smudde Peterson, for all the love, patience, and unwavering support you have provided throughout my lifetime. Thank you to my childhood friends, Sam Hernandez and Megan Geer, for always believing in my intelligence and ability to succeed. Thank you to Sarah D'Amico for inspiring my respect for education and my desire to achieve a graduate degree.

Finally, I would like to thank my partner and my love, Nicholas Bachus, whose support over the last three years has helped me in so many ways, but most importantly it has helped me finish this dissertation. I also would like to thank Runie, my spoiled puppy, whose lifestyle requires more than a graduate school stipend and whose love has motivated me to finish this dissertation and get a real job.

Table of Contents

List of Figures

List of Tables

Chapter 1:
Introduction to Fatigue in Additively Manufactured (AM) Metals

Additive manufacturing (AM) technologies have revolutionized the production of engineering materials by allowing the fabrication of small-volume, high-quality parts directly from computer aided design (CAD) models. AM is an advanced method of materials processing where near net shapes are created through the layer-by-layer deposition of material, providing opportunities in the design of complex components that would otherwise be difficult or impossible to create through conventional manufacturing techniques. While AM offers significant technological advancements supporting innovative engineering design, gaps in understanding mechanical performance of resultant materials and parts have limited its transition to structural applications [1, 2]. Of specific interest is the fatigue damage accumulation that occurs due to cyclic loading. Understanding and accurately predicting damage evolution and component lifetime is still a major challenge [3] and is an important requirement in the design of engineering structures for fatigue critical applications.

Mechanical properties of materials that control service life and capabilities depend on the internal microstructures and stresses formed during manufacturing. Residual stress, internal stress present in the absence of external applied loading, is a side effect of the AM deposition process due to the inherently complex thermal history; in addition to rapid solidification due to high cooling rates, the deposited material experiences continuous remelting and repeated solidification as subsequent layers are added. Since complete residual stress relief is difficult without extensive post-processing of AM materials [4], it is necessary to understand its effects on fatigue performance. Furthermore, nonequilibrium microstructures that contain grains of non-uniform sizes and elongated shapes are formed in AM materials [5]. Both residual stress and microstructure

morphology may influence the mechanical performance of AM materials, specifically under the applied cyclic loading of fatigue conditions.

1.1. Directed Energy Deposition (DED) and Powder Bed Fusion (PBF) of Stainless Steel

Additive manufacturing encompasses all technologies that successfully form three dimensional components by the successive addition of material (layer-by-layer) from engineering CAD models. Individual AM methods can be further defined by processing principles as shown in **Figure 1.1**.

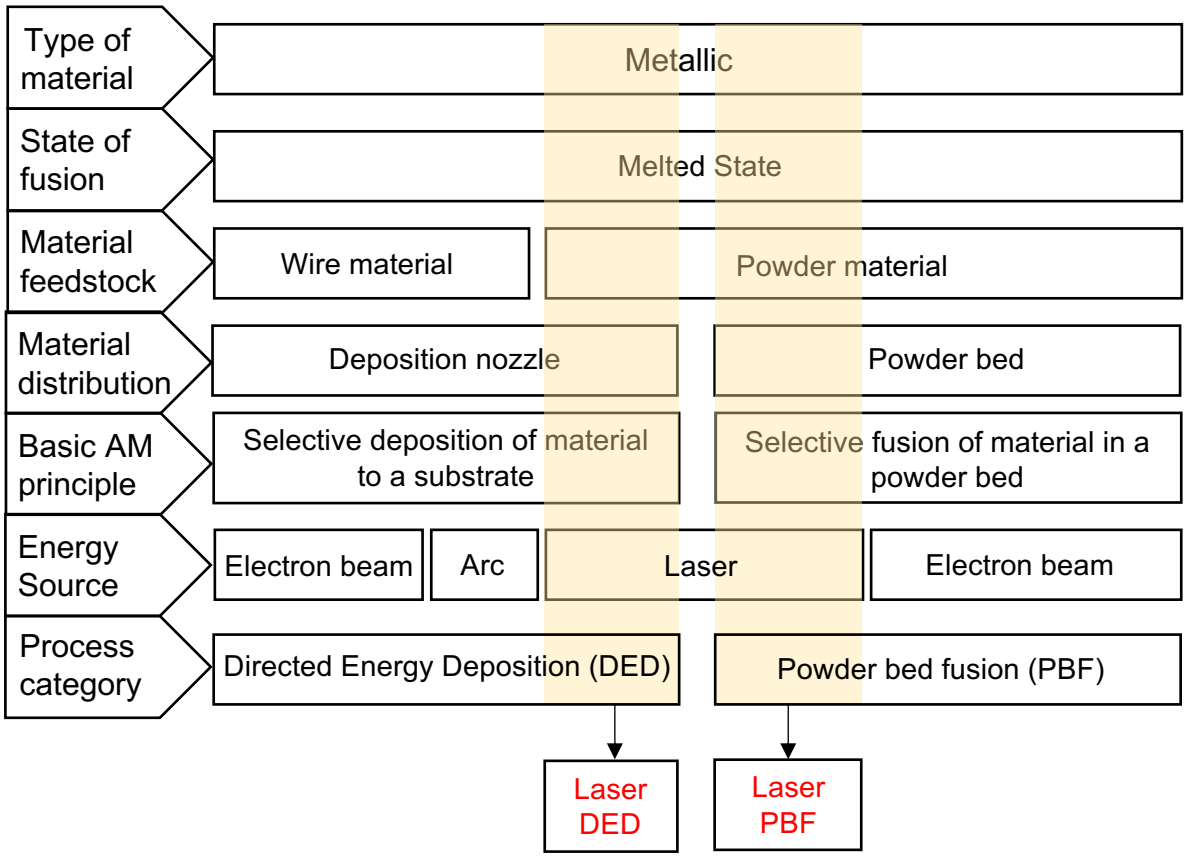

Figure 1.1: *Diagram of AM processing methods. Adapted from [6]. Highlighted methods are of interest in this work.*

A common AM method, laser Directed Energy Deposition (DED), refers to a technique in which a high energy laser is used to create a molten pool into which powder material is blown. Guided by a CAD model, cross sections of the desired geometry are directly deposited layer-by-

layer [6]. Another common AM method, laser Powder Bed Fusion (PBF), refers to an additive manufacturing process in which a laser heat source selectively melts and consolidates regions of a surface of a bed of powder as dictated by a CAD model [6]. In both methods, the molten pool rapidly solidifies in the absence of the energy source (laser) and each subsequent layer reheats part of the already solidified material, resulting in a complex thermal cycle. A schematic of the DED and PBF methods is shown in **Figure 1.2**.

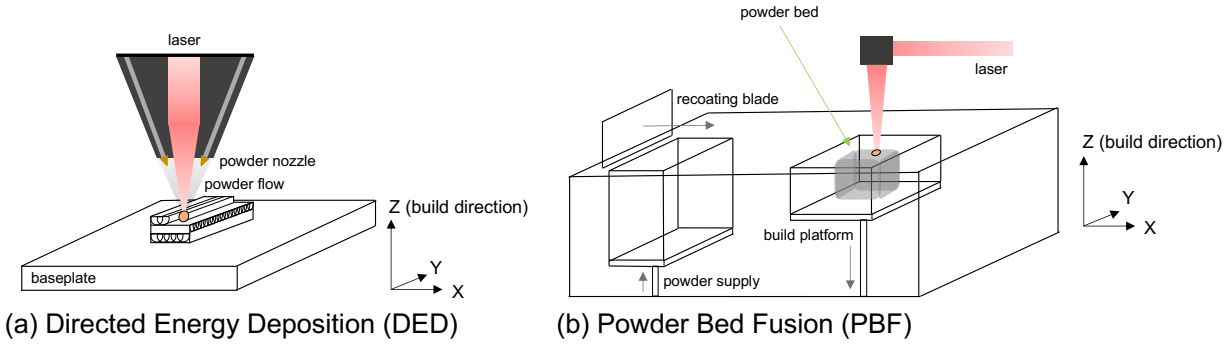

Figure 1.2: *Schematic of (a) DED and (b) PBF manufacturing methods. Adapted from [7].*

DED and PBF each have their own distinct advantages and applications in engineering design. DED occurs with high deposition rates and enables the production of large parts with design flexibility, while PBF offers higher dimensional accuracy and lower surface roughness for the fabrication of small intricate geometries [8-10]. But, in as-built components produced by both DED and PBF, significant temperature gradients lead to the formation of high tensile residual stress at the edges (just below the surface of the build) and compressive residual stress in the center of the resultant builds [11, 12]. While the shape of their residual stress profiles is similar, the cooling rates are orders of magnitude higher in PBF [5, 13, 14], resulting in higher values of tensile and compressive residual stress in PBF as-built material compared to DED. In addition, the higher cooling rates of PBF contribute to finer grain sizes in the inhomogeneous microstructures [15-17] as compared to the average grain sizes present in DED [18, 19].

Austenitic stainless steels are known for their reliable mechanical performance, such as strength, ductility, and resistance to corrosion and oxidation. Their specific chemical composition favors a stable austenitic (face centered cubic - FCC) microstructure and preferred mechanical properties [20, 21], which make them an attractive metal for AM with many engineering applications. DED and PBF are the most common methods for the fabrication of AM austenitic stainless steels [1]. As such, extensive work has been published to further develop the fundamental understanding of the process-structure-properties relationships of these AM processing methods on material properties including strength [16, 19, 22, 23], microstructure and defect formation [13, 16, 18, 19, 24, 25], and fatigue behavior [24, 26-32].

1.2. Residual Stress and Fatigue Crack Growth in DED and PBF Stainless Steel

Before additive manufacturing technologies, such as DED and PBF, can be fully realized for use in fatigue critical applications, the effects of the manufacturing process on fatigue performance must be further elucidated beyond the current state of uncertainty. The evaluation of fatigue crack growth behavior of as-built AM material can aid in the accurate predictions of service life under conditions of cyclic loading since fatigue life after initiation is dominated by the time spent in stable crack growth [33, 34]. Yet, there is little information in the literature on fatigue crack growth behavior of AM austenitic stainless steel [26, 28, 30] and those publications do not investigate or quantify the influence of residual stress on measured fatigue crack growth rates.

The influence of residual stress on fatigue crack growth is amplified near the threshold crack growth rates ($<10^{-8}$ m/cycle), where the contributions from residual stress to crack growth approach the low applied values of the stress intensity factor (K) characteristic of the near-threshold regime [35]. K, which is a function of crack size and applied load, characterizes the stress at the crack tip in a fatigue crack growth test. Residual stress contributes to the applied minimum

(K_{min}) and maximum (K_{max}) values of K, thereby affecting the stress intensity factor ratio (R = K_{min}/K_{max}) and influencing the fatigue crack growth rates in the near-threshold regime [36]. In addition to the process induced residual stress, the unique microstructure formed during layer deposition due to the intense thermal gradients have been reported to contribute to noticeable differences in threshold fatigue crack growth behavior [37, 38]. At the low applied loads, microstructural contributions to crack path behavior may influence fatigue crack growth rates by promoting tortuous crack growth or enabling premature crack face contact in the crack wake (crack closure) that can lead to an artificial retardation of growth rates [39, 40]. Therefore, it is important to understand how each AM process, DED and PBF, affects the mechanical performance and structural reliability by measuring fatigue crack growth rates, recognizing and understanding residual stress effects, and determining the significance of build/orientation specific microstructures.

1.3. Quantification of K_{res} and Correction of FCGR data

Since the presence of residual stress can have an important effect on the as-built AM material's fatigue resistance, quantifying its influence is crucial for an accurate interpretation of fatigue crack growth rate (FCGR) data [41-47]. When a fatigue crack grows through a residual stress field, the total stress intensity factor (K_{tot}) can differ significantly from the applied stress intensity factor (K_{app}) that is associated with the external cyclic loading [44, 46, 48]. Residual stress acting in the crack opening direction causes a residual stress intensity factor (K_{res}) that contributes to the K_{tot} acting at the crack tip. An increase in fatigue crack growth rates due to tensile residual stress (positive K_{res}) is extremely detrimental to fatigue performance, while a decrease in growth rates from compressive residual stress (negative K_{res}) can improve fatigue resistance. Consequently, crack growth rates may be either enhanced or retarded depending on the

nature of the residual stress field [41-43, 47]. Developing a quantitative description of the fatigue performance of additively manufactured materials that accounts for the process induced residual stress and that can be compared to current certification standards for conventionally processed materials is a significant challenge and is of great interest.

An accurate method of quantifying K_{res} values is necessary to account for the influence of residual stress on measured fatigue crack growth rates. Recent developments in FCGR data analysis have led to innovative methods to account for residual stress effects, both tensile and compressive, during fatigue testing. Similar to the imposed cut of the slitting method for measuring residual stress, a fatigue crack growing through a material causes the residual stress to relax and redistribute, resulting in a deformation change that can be measured. As an extension of the slitting method, the on-line crack compliance (OLCC) method quantifies K_{res} as a function of crack size during a fatigue crack growth test through the analysis of compliance data (i.e., load vs. deformation data) while simultaneously collecting FCGR data [49-53]. $K_{res}(a)$ can then be used to assess fatigue behavior and account for the process-induced residual stress using a correction method based on the linear elastic fracture mechanics concepts of superposition [50, 51]. To date, this method to assess and correct fatigue crack growth rates has not been applied to AM materials.

The influence of residual stress on the orientation dependent fatigue crack growth resistance of AM Type 304L stainless steel produced by DED and PBF is evaluated in this work. The stress intensity factor from residual stress (K_{res}) and from applied loading (K_{app}) are considered additive for the same mode of loading. The principle of superposition is used to determine a total stress intensity factor (K_{tot}) and total stress intensity factor ratio (R_{tot}) to represent the net driving force for fatigue crack growth, which can be used to correct fatigue crack growth rate data for residual stress effects.

1.4. Objectives and Scope of Research

This work examines the influence of the AM process on orientation dependent fatigue crack growth behavior of DED and PBF Type 304L austenitic stainless steel. Specifically, the significant contribution of manufacturing-induced residual stress is quantified. Post-test analysis of fatigue compliance data is used to determine the residual stress intensity factor (K_{res}). These values are then used to correct fatigue crack growth rates to determine the intrinsic fatigue resistance of the as-built material. The on-line crack compliance (OLCC) method for determining K_{res} from fatigue crack growth rate test data is validated using quenched aluminum samples before being implemented into the fatigue analysis of the DED and PBF Type 304L stainless steel.

First, the fatigue crack growth behavior of DED Type 304L stainless steel independent of the influence of residual stress is evaluated by quantifying and correcting for K_{res}. The slitting method is used to determine values of K_{res} as a function of crack length in a compact specimen machined from as-built DED material. Decreasing applied alternating stress intensity factor ($\Delta K = K_{max} - K_{min}$) tests are used to explore the near-threshold fatigue crack growth rates below 10^{-8} m/cycle. A corrected stress intensity factor (ΔK_{corr}) is used to account for the effects of K_{res} on fatigue data. In this manner, the intrinsic fatigue crack growth rates of DED Type 304L stainless steel, independent of residual stress, is characterized. A comparison to annealed wrought Type 304/304L stainless steel reveals similar intrinsic fatigue performance in the near-threshold regime.

The well-established slitting method uses strain data to determine the contributions of residual stress to fatigue performance. However, when material available for testing is limited, such as in the case of AM, the sacrifice of fatigue data on the specimens used for slitting is a substantial drawback. Therefore, the recently developed method of on-line crack compliance (OLCC) is evaluated for its applicability in the characterization of the fatigue crack growth

behavior of AM materials. A validation study is performed using an aircraft aluminum alloy with well characterized residual stress. K_{res} determined by OLCC in primary compact (C(T)) fatigue specimens are validated through a comparison to slitting measurements on secondary specimens. Additionally, details of different methods of analyzing the OLCC data are outlined and critical steps for data reduction are recommended.

The OLCC method is then applied to FCGR data from DED and PBF to evaluate residual stress reproducibility in AM components and orientation dependent fatigue behavior due to residual stress. Fatigue crack growth rates of compact fatigue specimens extracted from each build are evaluated and compared to address the repeatability of mechanical performance parallel (vertical) and perpendicular (horizontal) to the build direction at near-threshold values. K_{res} values as a function of crack length are calculated and compared. The intrinsic fatigue crack growth rates of DED and PBF Type 304L stainless steel are found using a corrected stress intensity factor (ΔK_{corr}) method and compared to data for annealed wrought Type 304/304L stainless steel corrected for crack closure using an adjusted compliance ratio (ΔK_{ACR}) method. By characterizing fatigue crack growth rates of AM stainless steel, quantifying residual stress effects (K_{res}), and comparing corrected data to an existing engineering reference material (annealed wrought Type 304/304L stainless steel), this work contributes to a better understanding of the processing-structure-properties relationships essential to the scientific advancement of AM technology.

References

1. DebRoy, T., et al., *Additive manufacturing of metallic components – Process, structure and properties.* Progress in Materials Science, 2018. **92**: 112-224.
2. Lewandowski, J.J. and M. Seifi, *Metal Additive Manufacturing: A Review of Mechanical Properties.* Annual Review of Materials Research, Vol 46, 2016. **46**: 151-186.
3. Yadollahi, A. and N. Shamsaei, *Additive manufacturing of fatigue resistant materials: Challenges and opportunities.* International Journal of Fatigue, 2017. **98**: 14-31.
4. Rangaswamy, P., et al., *Residual stresses in LENS (R) components using neutron diffraction and contour method.* Materials Science and Engineering a-Structural Materials Properties Microstructure and Processing, 2005. **399**(1-2): 72-83.
5. Hofmeister, W., et al., *Solidification in direct metal deposition by LENS processing.* Jom-Journal of the Minerals Metals & Materials Society, 2001. **53**(9): 30-34.
6. ISO/ASTM 52900:2021(E), *Additive manufacturing — General principles — Fundamentals and vocabulary*. 2021. ISO/ASTM International.
7. Zhang, Y., et al., *Additive Manufacturing of Metallic Materials: A Review.* Journal of Materials Engineering and Performance, 2018. **27**(1): 1-13.
8. Li, S.H., et al., *Directed energy deposition of metals: processing, microstructures, and mechanical properties.* International Materials Reviews, 2022.
9. Gorsse, S., et al., *Additive manufacturing of metals: a brief review of the characteristic microstructures and properties of steels, Ti-6Al-4V and high-entropy alloys.* Science and Technology of Advanced Materials, 2017. **18**(1): 584-610.
10. Frazier, W.E., *Metal Additive Manufacturing: A Review.* Journal of Materials Engineering and Performance, 2014. **23**(6): 1917-1928.
11. Mercelis, P. and J.P. Kruth, *Residual stresses in selective laser sintering and selective laser melting.* Rapid Prototyping Journal, 2006. **12**(5): 254-265.
12. Li, C.L., Z.Y.; Fang, X.Y.; Guo,Y.B.;, *Residual Stress in Metal Additive Manufacturing.* 4th CIRP Conference on Surface Integrity (CSI 2018), 2018. **Procedia CIRP 71 (2018)**: 348–353.
13. Griffith, M.L., et al., *Understanding the microstructure and properties of components fabricated by Laser Engineered Net Shaping (LENS).* Solid Freeform and Additive Fabrication-2000, 2000. **625**: 9-20.
14. Hooper, P.A., *Melt pool temperature and cooling rates in laser powder bed fusion.* Additive Manufacturing, 2018. **22**: 548-559.
15. Narasimharaju, S.R., et al., *A comprehensive review on laser powder bed fusion of steels: Processing, microstructure, defects and control methods, mechanical properties, current challenges and future trends.* Journal of Manufacturing Processes, 2022. **75**: 375-414.
16. Qiu, C., et al., *A comprehensive study on microstructure and tensile behaviour of a selectively laser melted stainless steel.* Scientific Reports, 2018. **8**(1): 7785.

17. Tan, C., et al., *Microstructural characterization and properties of selective laser melted maraging steel with different build directions.* Science and Technology of Advanced Materials, 2018. **19**(1): 746-758.

18. Yadollahi, A., et al., *Effects of process time interval and heat treatment on the mechanical and microstructural properties of direct laser deposited 316L stainless steel.* Materials Science and Engineering a-Structural Materials Properties Microstructure and Processing, 2015. **644**: 171-183.

19. Wang, Z.Q., T.A. Palmer, and A.M. Beese, *Effect of processing parameters on microstructure and tensile properties of austenitic stainless steel 304L made by directed energy deposition additive manufacturing.* Acta Materialia, 2016. **110**: 226-235.

20. Lula, R.A., *Stainless steel*. 1986, Metals Park: ASM. 173 pp.

21. Marshall, P., *Austenitic stainless steels : microstructure and mechanical properties*. 1984, London: Elsevier Applied Science. 431 pp.

22. Smith, T.R., et al., *Strengthening mechanisms in directed energy deposited austenitic stainless steel.* Acta Materialia, 2019. **164**: 728-740.

23. Nguyen, Q.B., et al., *High mechanical strengths and ductility of stainless steel 304L fabricated using selective laser melting.* Journal of Materials Science & Technology, 2019. **35**(2): 388-394.

24. Smith, T.R., et al., *Relationship between manufacturing defects and fatigue properties of additive manufactured austenitic stainless steel.* Materials Science and Engineering: A, 2019. **765**: 138268.

25. Brooks, J.A., T.J. Headley, and C.V. Robino, *Microstructures of laser deposited 304L austenitic stainless steel.* Solid Freeform and Additive Fabrication-2000, 2000. **625**: 21-30.

26. Ganesh, P., et al., *Fatigue Crack Propagation and Fracture Toughness of Laser Rapid Manufactured Structures of AISI 316L Stainless Steel.* Metallography, Microstructure, and Analysis, 2014. **3**(1): 36-45.

27. Smith, T.R., et al. *Orientation Effects on Fatigue Behavior of Additively Manufactured Stainless Steel*. in *Proceedings of the ASME 2017 Pressure Vessels & Piping Conference*. 2017. Waikoloa, Hawaii, USA.

28. Riemer, A., et al., *On the fatigue crack growth behavior in 316L stainless steel manufactured by selective laser melting.* Engineering Fracture Mechanics, 2014. **120**: 15-25.

29. Liang, X.Y., et al., *High cycle fatigue behavior of 316L steel fabricated by laser powder bed fusion: Effects of surface defect and loading mode.* International Journal of Fatigue, 2022. **160**: 106843.

30. San Marchi, C.W., et al., *Fatigue and Fracture Behavior of Additively Manufactured Austenitic Stainless Steel*, in *ASTM STP 1620: Structural Integrity of Additive Manufactured Parts*, N. Shamsaei, et al., Editors. 2020, ASTM International: West Conshohocken, PA. 381-398.

31. Pegues, J.W., M.D. Roach, and N. Shamsaei, *Additive manufacturing of fatigue resistant austenitic stainless steels by understanding process-structure-property relationships.* Materials Research Letters, 2020. **8**(1): 8-15.

32. Zhang, M., et al., *Fatigue and fracture behaviour of laser powder bed fusion stainless steel 316L: Influence of processing parameters.* Materials Science and Engineering a-Structural Materials Properties Microstructure and Processing, 2017. **703**: 251-261.

33. Anderson, T.L., *Fracture Mechanics: fundamentals and applications*. 2005: CRC Press. 513-558.

34. Suresh, S., *Fatigue of materials*. 2nd ed. 1998, Cambridge and New York: Cambridge University Press. 679 pp.

35. Vosikovsky, O., L.P. Trudeau, and A. Rivard, *Effect of Residual-Stresses on Fatigue Crack-Growth Threshold.* International Journal of Fracture, 1980. **16**(4): R187-R190.

36. Ritchie, R.O., *Near-threshold fatigue-crack propagation in steels.* International Metals Reviews, 1979. **24**(1): 205-230.

37. Daniewicz, S.R. and N. Shamsaei, *An introduction to the fatigue and fracture behavior of additive manufactured parts.* International Journal of Fatigue, 2017. **94**: 167-167.

38. Shamsaei, N. and J. Simsiriwong, *Fatigue behaviour of additively-manufactured metallic parts.* Procedia Structural Integrity: 3rd International Symposium on Fatigue Design and Material Defects (FDMD 2017), 2017. **7**: 3-10.

39. Vasudeven, A.K., K. Sadananda, and N. Louat, *A Review of Crack Closure, Fatigue-Crack Threshold and Related Phenomena.* Materials Science and Engineering a-Structural Materials Properties Microstructure and Processing, 1994. **188**(1-2): 1-22.

40. Suresh, S. and R.O. Ritchie, *Near-Threshold Fatigue Crack-Propagation - a Perspective on the Role of Crack Closure*, in *Fatigue Crack Growth Threshold Concepts*, D. Davidson and S. Suresh, Editors. 1984, Metallurgical Society of AIME: Warrendale, PA. 227-261.

41. Bucci, R., *Effect of Residual Stress on Fatigue Crack Growth Rate Measurement*, in *Fracture Mechanics: Thirteenth Conference, ASTM STP 743*, R. Roberts, Editor. 1981, American Society for Testing and Materials: West Conshohocken, PA. 28-47.

42. Beghini, M. and L. Bertini, *Fatigue Crack-Propagation through Residual-Stress Fields with Closure Phenomena.* Engineering Fracture Mechanics, 1990. **36**(3): 379-387.

43. Beghini, M., L. Bertini, and E. Vitale, *Fatigue-Crack Growth in Residual-Stress Fields - Experimental Results and Modeling.* Fatigue & Fracture of Engineering Materials & Structures, 1994. **17**(12): 1433-1444.

44. Garcia, C., et al., *Fatigue crack growth in residual stress fields.* International Journal of Fatigue, 2016. **87**: 326-338.

45. Parker, A.P., *Stress Intensity Factors, Crack Profiles, and Fatigue Crack Growth Rates in Residual Stress Fields*, in *Residual Stress Effects in Fatigue, ASTM STP 776*. 1982, American Society for Testing and Materials: West Conshohocken, PA. 13-31.

46. LaRue, J.E. and S.R. Daniewicz, *Predicting the effect of residual stress on fatigue crack growth.* International Journal of Fatigue, 2007. **29**(3): 508-515.

47. McClung, R.C., *A literature survey on the stability and significance of residual stresses during fatigue.* Fatigue & Fracture of Engineering Materials and Structures, 2007. **30**(3): 173-205.

48. Ball, D.L., et al., *A Detailed Evaluation of the Effects of Bulk Residual Stress on Fatigue in Aluminum.* Advanced Materials Research, 2014. **891-892**: 1205-1211.

49. Donald, J.K. and D.A. Lados, *An integrated methodology for separating closure and residual stress effects from fatigue crack growth rate data.* Fatigue & Fracture of Engineering Materials & Structures, 2006. **30**(3): 223-230.

50. Lados, D.A., D. Apelian, and J.K. Donald, *Fracture mechanics analysis for residual stress and crack closure corrections.* International Journal of Fatigue, 2007. **29**(4): 687-694.

51. Lados, D.A. and D. Apelian, *The Effect of Residual Stress on the Fatigue Crack Growth Behavior of Al-Si-Mg Cast Alloys - Mechanisms and Corrective Mathematical Models.* Metallurgical and Materials Transactions A-Physical Metallurgy and Materials Science, 2006. **37A**: 133-145.

52. James, M., et al., *A Methodology for Partitioning Residual Stress Effects From Fatigue Crack Growth Rate Test Data.* Materials Performance and Characterization, 2016. **5**(3): 194-214.

53. Newman, J.A., Smith, S. W., Seshadri, S., James, M. A., Brazill, R., Schultz, R., Donald, J. K., and Blair, A., *Characterization of Residual Stress Effects on Fatigue Crack Growth of a Friction Stir Welded Aluminum Alloy*. 2015: NASA Langley Research Center, Hampton, VA.

Chapter 2:
The Influence of Residual Stress on Fatigue Crack Growth Rates of Additively Manufactured Type 304L Stainless Steel [1]

Abstract

To examine the influence of residual stress on mechanical performance, specifically fatigue crack growth resistance, of additively manufactured (AM) Type 304L stainless steel produced by directed energy deposition (DED) was evaluated and compared to that of conventional wrought Type 304/304L stainless steel. Increasing and decreasing alternating stress intensity factor (ΔK) tests were used to assess fatigue crack growth behavior over a range of crack growth rates in the near-threshold regime ($<10^{-8}$ m/cycle). Bulk residual stress and residual stress intensity factor (K_{res}) profiles of a fatigue specimen were measured using the slitting method. Tensile residual stress at the edges of the DED materials led to positive values of K_{res} and faster fatigue crack growth rates in the DED material as compared to wrought material at the same applied ΔK. Correcting for the effects of K_{res} and crack closure in DED Type 304L and commercially available wrought Type 304/304L stainless steel shows that fatigue crack growth rates are similar at values of ΔK lower than 6 $MPa \cdot m^{0.5}$ when compared to rates in wrought material.

Keywords: Additive manufacturing (AM), directed energy deposition (DED), residual stress, fatigue crack growth, stainless steel

[1] Published: Smudde, C.M., et al., *The influence of residual stress on fatigue crack growth rates of additively manufactured Type 304L stainless steel.* International Journal of Fatigue, 2022. **162.** 106954.

2.1. Introduction

Additive manufacturing (AM) has the potential to revolutionize the production of low volume components for engineering applications. The controlled deposition of material offers the opportunity to produce complex near net shape components on demand that would otherwise be difficult or impossible to create with conventional manufacturing processes. However, before AM materials can expand into structural engineering applications at a large scale, characterization of their mechanical performance, specifically fatigue resistance, is required [1, 2]. Of particular concern to fatigue performance is the fact that even the highest density AM parts exhibit evidence of defects in the as-built condition [3]. Therefore, a damage tolerant design approach, where all materials are assumed to contain defects [4], is essential to the adoption of AM components in structural applications. In damage tolerant design, a thorough understanding of material fatigue crack growth rate behavior is critical to accurately predicting service life under conditions where fatigue resistance is a critical property.

Developing a description of the fatigue performance of additively manufactured materials that is unbiased by the manufacturing process and that can be compared to current certification standards for conventionally processed materials is a significant challenge. The unique microstructure formed during layer deposition and the residual stress induced by the intense thermal gradients of the AM process contribute to noticeable differences in fatigue behavior, especially near the threshold of crack growth rates ($<10^{-8}$ m/cycle) [5, 6]. In this regime, where the applied loads of a traditional fatigue crack growth test are low, microstructural contributions to crack path behavior may influence the crack growth rates by promoting a tortuous crack path or enabling premature crack face contact in the crack wake. In addition, the influence of residual stress on fatigue crack growth is amplified near the threshold regime, where the contributions from

residual stress to the crack growth driving force approach the values of the applied minimum and maximum stress intensity factors (K_{min} and K_{max}).

The influence of microstructure (grain size and morphology) and bulk residual stress on the fatigue crack growth behavior in additively manufactured materials is not well described in the literature. Studies focused on microstructure of AM materials have shown that there is an orientation dependence of the fatigue crack growth behavior due to the anisotropic microstructure of AM materials. Specifically, fatigue crack growth rates differ depending on the orientation of the applied loading relative to the build direction in the Paris and threshold regimes [7-11]. Near surface measurements have revealed that the residual stress at the edges of the AM material is tensile [10], but the influence of residual stress on the fatigue crack growth behavior has not been assessed. Other studies have focused specifically on quantifying manufacturing-induced residual stress in AM materials. For example, in directed energy deposition (DED) material, high uniaxial bulk (macroscale) residual stress directed along the build direction has been determined to have tensile values at the edges and compressive values in the center of the build [12]. However, while the magnitude of residual stress could be minimized by controlling the processing parameters, elimination of residual stress requires post-processing heat treatment, but at the expense of reducing strength. Therefore, it seems essential to understand the influence of process-induced residual stress on the fatigue performance of DED materials.

Quantifying the effects of residual stress in fatigue crack growth data is necessary to reveal the intrinsic fatigue resistance of DED material. By determining the residual stress intensity factor, K_{res}, which characterizes the contribution of residual stress at the crack tip to the total driving force of crack growth, corrections can be made to fatigue crack growth data. In the case of tensile residual stress acting normal to the crack surface, where the crack is considered open, the effective

value of the stress intensity factor is found by the superposition of K_{res} and the stress intensity factor from applied loading (K_{app}). Donald and Lados developed a method for correcting for residual stress by considering the contributions of K_{res} on the minimum (K_{min}) and maximum (K_{max}) stress intensity factors as a mean stress effect, resulting in a corrected alternating stress intensity factor, ΔK_{corr} [13]. Few researchers have utilized the ΔK_{corr} method when evaluating materials with residual stress [14, 15]. To date, the application of this method to AM materials has not been published in the literature.

The objective of this study is to determine the fatigue crack growth behavior of DED Type 304L stainless steel independent of the influence of residual stress by quantifying and correcting for K_{res}. The slitting method was used to determine values of K_{res} as a function of crack size in a compact fatigue crack growth specimen machined from as-built DED material. Decreasing applied alternating stress intensity factor ($\Delta K = K_{max} - K_{min}$) tests were used to explore the near-threshold fatigue crack growth rates less than 10^{-8} m/cycle in the DED material. When the crack growth rates reached a predetermined level of approximately 2-3 x 10^{-10} m/cycle, the tests were continued under constant applied load amplitude conditions to gain insight into the consistency of the fatigue data under ΔK increasing conditions as described in ASTM E647 [16]. Commercially available wrought Type 304/304L material was tested under the same conditions to establish a baseline for fatigue crack growth behavior in typical material. Then, a corrected stress intensity (ΔK_{corr}) method was used to account for the effects of K_{res} on fatigue crack growth rate data. In this manner, the intrinsic fatigue crack growth rates of DED Type 304L stainless steel, independent of residual stress, were characterized.

2.2. Material and methods

2.2.1. Material

The Type 304L stainless steel under evaluation was additively manufactured via directed energy deposition (DED) in a Laser Engineered Net Shaping (LENS®) 750 workstation utilizing the time-invariant processing input parameters listed in **Table 2.1**. A hatch scan pattern that alternated 90 degrees with each layer was utilized during the build process. Gas atomized austenitic stainless steel powder of size 45 μm to 105 μm was used in the deposition process. The chemical composition for the powder as determined by Smith et al. for replicate builds made on the same equipment [17] is given in **Table 2.2**, showing that the powders conformed to standard requirements of 304L grade alloys [18]. Solution annealed commercially available wrought Type 304/304L stainless steel was used for comparison. The chemical composition of the dual certified wrought Type 304/304L is included in **Table 2.2.** The small differences in chemical composition are assumed to have a negligible influence on fatigue crack growth behavior in this study.

Table 2.1: Processing Parameters for DED Type 304L Stainless Steel

Processing Parameter:	**Value:**
Laser power	Yb:fiber 450 W
Laser scan speed	10 mm/s
Hatch increment	0.64 mm
Layer increment	0.20 mm
Oxygen concentration	< 5 ppm
Powder size	45-105 μm

Table 2.2: Composition (wt%) of bulk wrought Type 304/304L gas atomized Type 304L feedstock powder

	Fe	Cr	Ni	Mn	Mo	N	C	Si	O	S	P	Cu
Wrought 304/304L	Bal	18.03	8.14	1.80	0.37	0.072	0.023	0.27	-	0.001	0.036	0.43
DED 304L	Bal	19.1	10.6	1.50	0.07	0.010	0.015	0.60	0.023	0.003	0.005	-

Processing parameters were optimized for greater than 99% density in the DED material. Mechanical tests in similar builds made on the same equipment with the same processing parameters previously exhibited yield strength of 320 MPa for the longitudinal direction, ultimate tensile strength of 620 MPa, and total elongation to failure of 72% [17]. Additionally, large area electron back-scatter diffraction (EBSD) images of the DED Type 304L microstructure demonstrated anisotropic grain shapes that were elongated in the build direction [19]. Replicate vertical wall builds with nominal dimensions of 107 mm x 55.9 mm x 7.62 mm were deposited on individual wrought stainless steel baseplates of dimension 152 mm x 152 mm x 6.35 mm (**Figure 2.1**). Material for fatigue testing and analysis was isolated by first removing the vertical wall builds from the baseplate via wire electrical discharge machining (EDM) (at the solid line in **Figure 2.1**). Then, a thin segment of material from the side of each wall was removed (dashed line) by EDM prior to the machining of fatigue crack growth testing specimens, leaving a plate of material with nominal dimensions of 106 mm (along the build direction) by 38 mm.

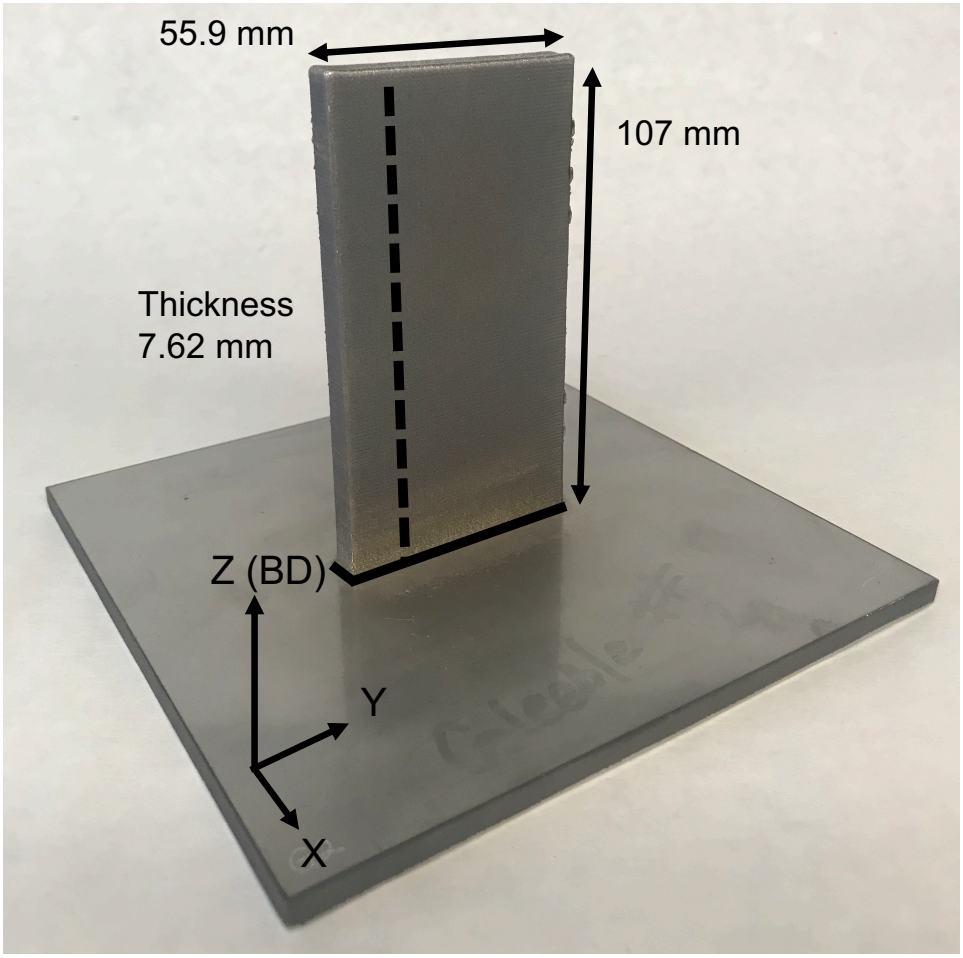

Figure 2.1: *Image of DED vertical wall build with black lines showing the locations of EDM material removal.*

From each plate of the two vertical wall builds (**Figure 2.2**), three compact (C(T)) fatigue crack growth specimens were extracted to evaluate fatigue crack growth behavior in the near-threshold regime. A total of five specimens with the loading axis oriented parallel to the build direction (BD) were used in this study and were differentiated by their build number (DED1 and DED2) and by their extraction location (bottom (B), middle (M), and top (T)) as seen in **Figure 2.2**. C(T) specimens were machined with thickness (B) of 6.35 mm and width (W) of 26.4 mm. Prior to fatigue testing, a notch was introduced to all specimens by wire EDM to a nominal crack size, a_n, of 5.1 mm in compliance with ASTM E647 [16]. The top and bottom specimens from both

DED1 and DED2 were subjected to fatigue crack growth testing, while the middle specimen from DED1 was reserved for residual stress measurement using the slitting method.

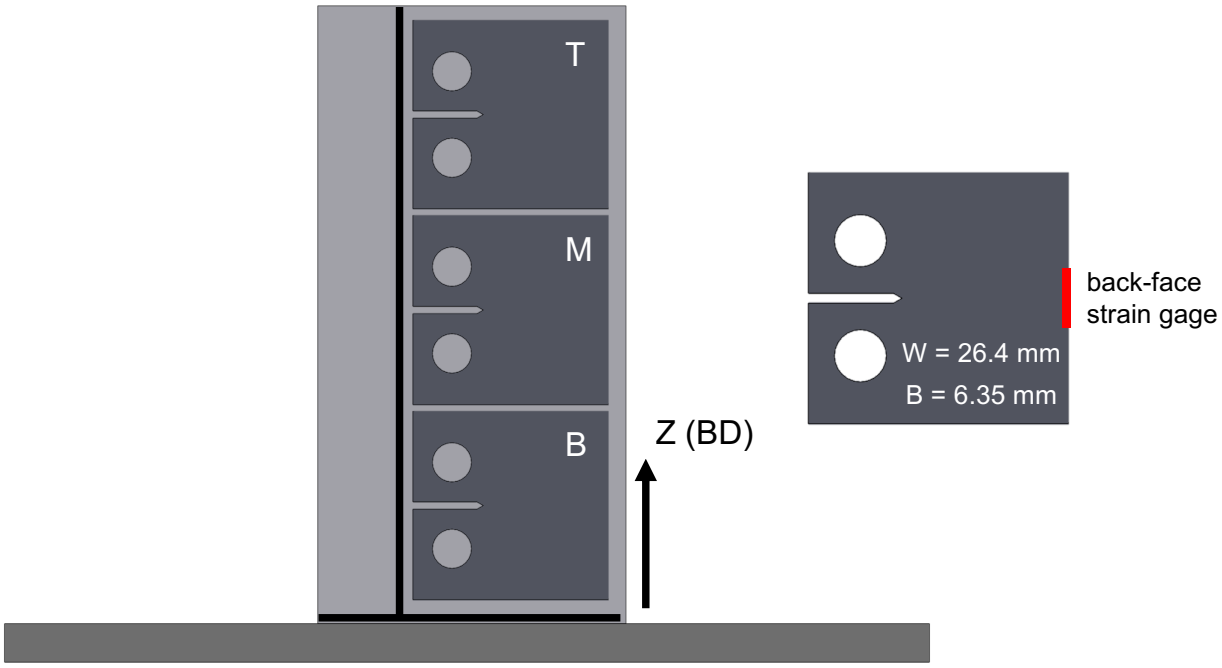

Figure 2.2: *Schematic of C(T) specimen extraction from vertical wall build.*

2.2.2. Residual Stress Evaluation

Residual stress was measured in the DED material using the slitting method. Build-direction residual stress was measured as the C(T) specimens were extracted from the DED plates. After C(T) specimens were completed, the C(T) specimen from the middle of vertical wall build DED1 (DED1-M) was reserved for residual stress analysis of the C(T) geometry. Residual stress was measured prior to the introduction of a fatigue starter notch at the same plane as crack propagation in fatigue tests. The residual stress normal to the crack plane and acting to open the crack was determined as a function of position from the front face of the specimen (x).

The slitting method is a one-dimensional mechanical relaxation technique for determining average through thickness residual stress normal to a plane of interest. Incremental cutting along

the plane results in a redistribution of residual stress and strains which are recorded by a strain gage applied at the back face. An inverse analysis is performed using the strain from each cut increment to determine the average through thickness normal residual stress. In the present work, a strain gage was applied at the back face and slitting was performed by wire EDM using 0.381 mm fixed depth increments to 29.5 mm from the front face or 90% of the total specimen width (90% of 1.25W) [20]. Strain was measured at each cut increment and residual stress was determined using the pulse-regularization inverse analysis technique [21]. The slitting measurement rendered DED1-M unavailable for fatigue testing.

To evaluate the contribution of residual stress to the stress intensity factor, values of K_{res} acting in the crack plane are determined from the strain data collected during the slitting method. The residual stress intensity factor, K_{res}, is determined as a function of crack size as measured from the load line, a* (a* = x - 0.25W). The fitted strain values and a geometry dependent influence function (Z(a*)) as described by Schindler [22] and further developed by Olson for the C(T) geometry [23] were used in Equation (2.1) to determine K_{res}:

$$K_{res}(a^*) = \frac{E}{Z(a^*)}\frac{d\varepsilon(a^*)}{da} \tag{2.1}$$

Here E is the elastic modulus of a fully dense austenitic stainless steel, 200 GPa, and a^* is measured from the load line. The derivative of the strain with respect to the crack size is determined by differentiating a localized curve fit of the strain data. A schematic of the slitting method can be seen in **Figure 2.3**.

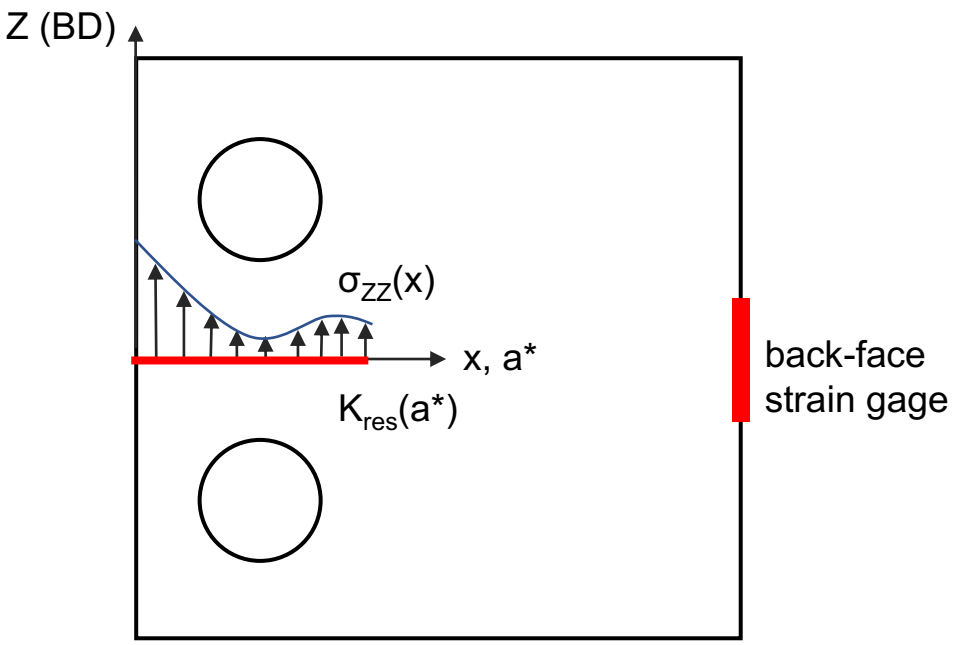

Figure 2.3: *Schematic of slitting method.*

To compare the value of K_{res} at the end of the notch depth, the residual stress intensity factor was determined during the notch cutting using the slitting method as described for DED1-M. This method was applied to the two bottom C(T) specimens (DED1-B and DED2-B) as well as two wrought C(T) specimens, to assess residual stress in the DED and wrought material. The top specimens (DED1-T and DED2-T) were notched without measuring their residual stress intensity factor.

2.2.3. Fatigue Crack Growth Testing

Fatigue crack growth testing of DED and wrought material was performed consistent with the methodology described in ASTM E647 (long cracks) [16] on an Instron 1331 servohydraulic load frame controlled by a MTS TestStar system. MTS 790.40 fatigue crack growth software was used to execute the tests under K-control conditions at an applied stress ratio of 0.1 and frequency of 10 Hz. For crack size monitoring during the fatigue test, the back-face strain compliance method facilitated data collection of compliance data with high accuracy for post-test analysis. A Micro-

Measurements CEA-09-062UWA-350 strain gage was centered on the crack plane on the back face of each C(T) specimens as shown in **Figure 2.2** and strains were measured using a Vishay Instruments P3500 strain indicator. The MTS software was adapted to accept a back-face strain input for the compliance method of determining crack size; the absolute value of the measured strain was multiplied by the specimen width to create a modified back-face strain value that is nominally equivalent to the crack opening displacement at the front face location in ASTM E647 compliance equations. Back-face strain coefficients were entered into the compliance calculation for crack size in the MTS software [16]. During the fatigue crack growth tests, load and COD from BFS data with 500 data points averaged over three cycles represented each crack size and were recorded at 0.051 mm crack increments. A modulus of 200 GPa was consistently employed in the compliance analysis for the materials in this study.

Prior to testing, all specimens were ground to 240 grit and one side was polished to enable visual confirmation that the crack path remained straight. Then, the top and bottom specimens from each build were precracked by an increment in crack size of $\Delta a = 1.3$ mm (to $a/W = 0.25$) using a load shedding methodology incorporated in the MTS TestStar software. The final K_{max} of the precrack was less than the K_{max} at the start of the test in accordance with ASTM E647 [16]. For each specimen, a decreasing applied ΔK procedure was employed to probe the near-threshold crack growth behavior with a starting K_{max} of 11 MPa·m$^{0.5}$ and a load shedding parameter, *C*, of -0.08 mm^{-1}. When the crack growth rates reached values of 2-3 x 10^{-10} m/cycle, the tests were continued at a constant applied load amplitude, resulting in an increasing applied ΔK test. In this manner, the consistency of the fatigue crack growth behavior as a function of loading condition (i.e., ΔK decreasing compared to ΔK increasing) was evaluated for the DED material. To provide data for comparison, similar tests were conducted on solution annealed wrought Type 304/304L

stainless steel (Wrought1,2,3) with mechanical properties reported as yield strength of 320 MPa and ultimate tensile strength of 600 MPa in compliance with ASTM standard A240 [18]. In addition, residual stress was anticipated to be negligible ($K_{res} = 0$) in the wrought material.

2.2.4. K_{corr} Method to Correct Fatigue Data for Residual Stress

The methodology outlined by Donald and Lados to correct for varying residual stress effects in fatigue crack growth data was used to transform the fatigue data of DED material [13]. Since residual stress contributes to both the maximum and minimum stress intensity factors, a fatigue crack growing through a material with a residual stress field experiences a varying total stress ratio (R_{tot}) even when the applied stress intensity factor ratio (R_{app}) is kept constant. Adding the K_{res} values from the slitting of DED1-M to the applied K_{min} and applied K_{max} of the fatigue crack growth tests gives R_{tot} as a function of crack size (Equation (2.2)):

$$R_{tot}(a) = \frac{K_{min,app}(a)+K_{res}(a)}{K_{max,app}(a)+K_{res}(a)} \tag{2.2}$$

Normalized stress intensity factor data, ΔK_{norm}, uses a material specific normalization parameter, *n,* to eliminate the effects of varying total stress ratios due to residual stress as given in Equation (2.3):

$$\Delta K_{norm}(a) = \Delta K_{eff}(a)^{1-n} \cdot \left(K_{max,app}(a) + K_{res}(a)\right)^{n} \tag{2.3}$$

The adjusted compliance ratio (ACR) method outlined in the appendix of ASTM E647 [16] was used to remove the influence of crack closure on measured fatigue crack growth rate data. The ACR method uses the compliance data to determine the deviation from linearity imposed by contact stresses in the crack wake at low applied loads and correct for crack closure while including the influence of crack tip strain [24]. The resulting value of ΔK is the effective stress intensity

factor range ($\Delta K_{ACR} = \Delta K_{eff}$) free of the influence of crack closure needed to compute ΔK_{norm} in Equation (2.3).

Values of ΔK_{norm} were then further modified to reflect growth rates at the applied stress ratio, R_{app}, of 0.1 using the Walker relationship [25], as expressed in Equation (2.4):

$$\Delta K_{corr}(a) = \Delta K_{norm}(a) \cdot \left(1 - R_{app}\right)^{n} \tag{2.4}$$

The value of the normalization parameter, *n*, in Equations (2.3) and (2.4) was determined for the DED material using decreasing ΔK fatigue crack growth test data of wrought Type 304/304L. A single C(T) specimen (Wrought4) was tested at three R_{app} values of 0.1, 0.3, and 0.5 to assess fatigue crack growth rates for a range of applied ΔK values and to provide the necessary data to determine the normalization parameter, *n*. In the absence of residual stress, ΔK_{norm} collapses data tested at different R_{app} values onto a single fatigue crack growth rate curve.

2.3. Results

2.3.1. Residual Stress and K_{res}

Slitting measurements performed during specimen extraction were used to further verify consistency in residual stress throughout the DED material. Measurements performed between bottom (B) and middle (M) specimens (DED-b) and between middle (M) and top (T) specimens (DED-t) are shown in **Figure 2.4**. The expected parabolic residual stress profile across the width of the DED material is slightly shifted due to the asymmetrical removal of material prior to specimen extraction.

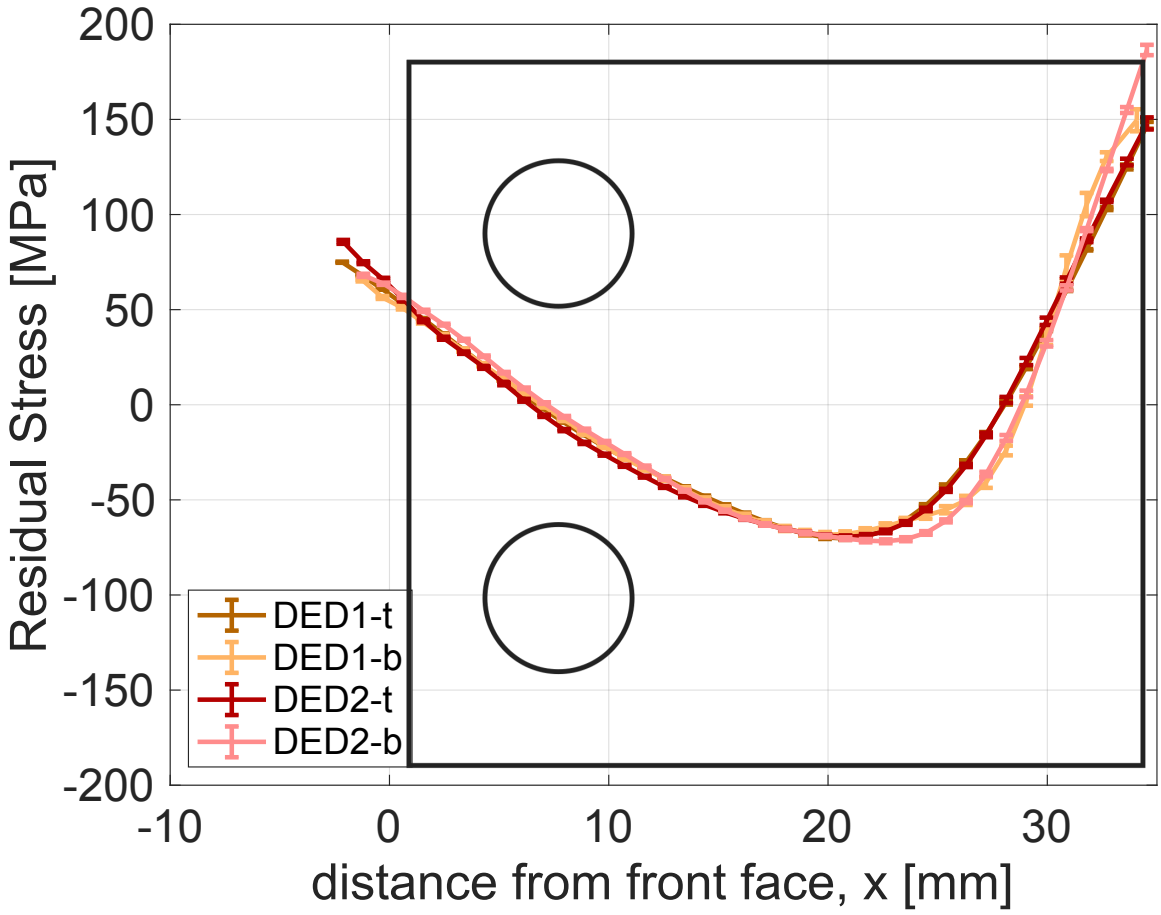

Figure 2.4: *Residual Stress as a function of position from the front face (x) from slitting during specimen extraction with a C(T) specimen geometry superimposed.*

The residual stress acting in the C(T) specimen as a function of position from the front face (x) from the slitting measurement on DED1-M is shown in **Figure 2.5**. The tensile residual stress decreases at relatively constant slope from the front face of the specimen towards compressive residual stress, with an inflection between 5 and 10 mm from the front face. The inflection is attributed to the machined holes in the C(T) specimen geometry, which interrupts the expected parabolic residual stress profile of the DED material. The peak compressive residual stress occurs around 23 mm from the front face, with the residual stress continuously increasing towards tensile values at positions approaching the back face of the specimen ($x > 25$ mm).

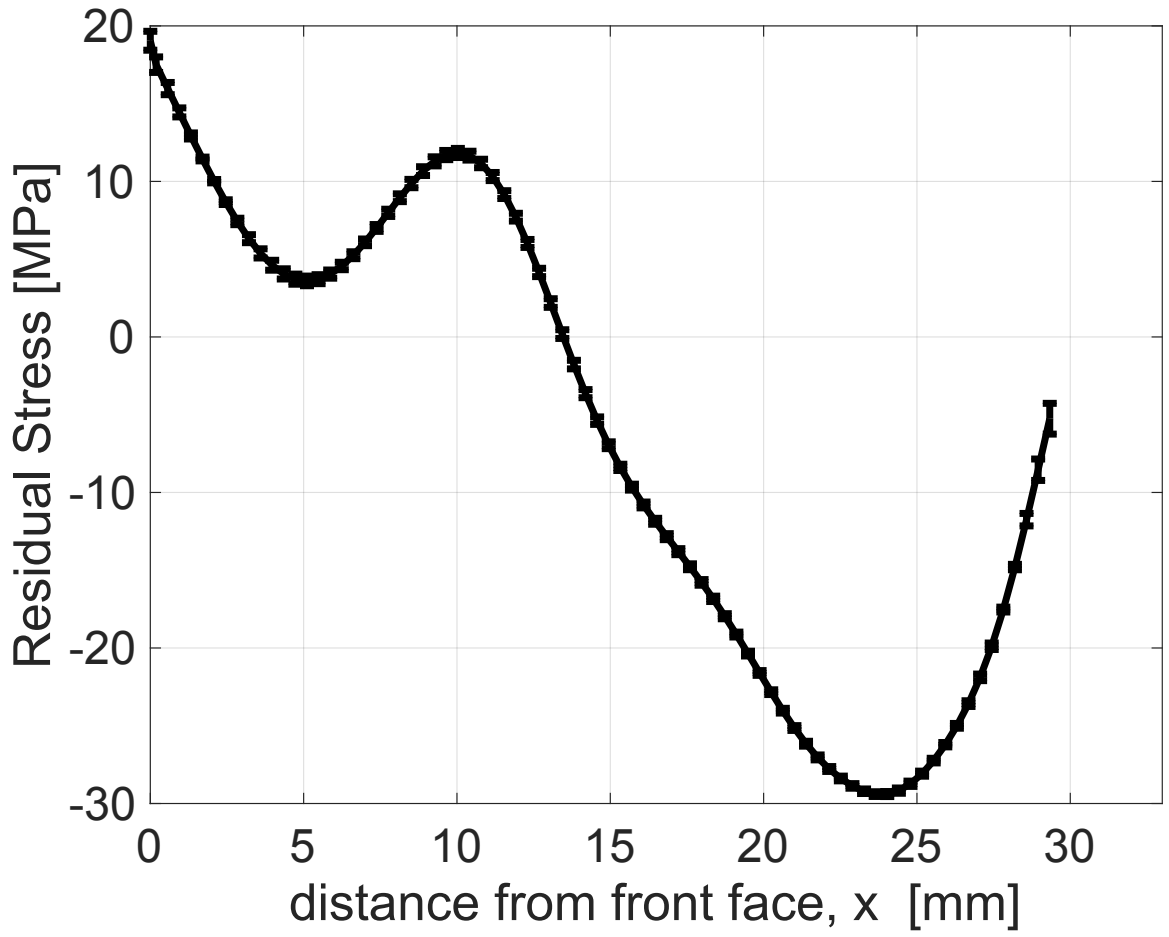

Figure 2.5: *Residual Stress as a function of position from the front face (x) in DED1-M from slitting.*

The corresponding residual stress intensity factor determined from the slitting measurement as a function of crack size as measured from the load line, a*, is plotted in **Figure 2.6**. Tensile residual stress near the front face of the DED specimen (**Figure 2.5**) leads to positive values of K_{res} throughout the entire range of crack size (**Figure 2.6**). The vertical lines in **Figure 2.6** mark the location of the notch tip (solid line) and the crack tip after precracking (dotted line). Results show that crack growth during the fatigue tests would begin with a maximum tensile K_{res} that decreases monotonically as crack size increases. Positive K_{res} should contribute to higher fatigue crack growth rates and lower fatigue thresholds when compared to tests in a residual stress-free material of the same composition and microstructure.

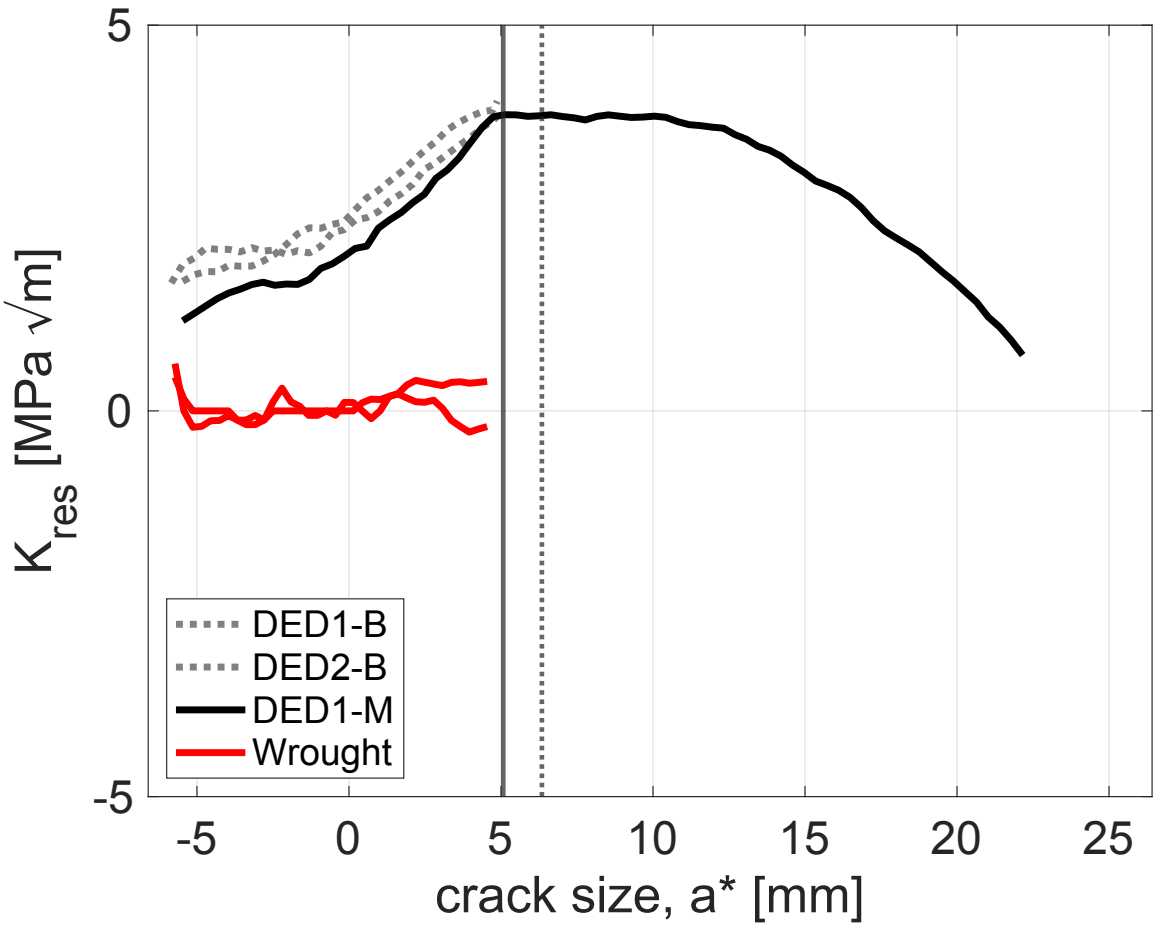

Figure 2.6: *K_{res} as a function crack size for DED Type 304L and wrought Type 304/304L C(T) specimens.*

Figure 2.6 also includes K_{res} values from the notching of the bottom DED C(T) specimens (DED1-B and DED2-B) and two wrought specimens (Wrought1,2). All the DED specimens exhibited a K_{res} value of about 4 MPa·m$^{0.5}$ at the end of the notch, suggesting that the residual stress is relatively similar at each build height sampled in the present work and the slitting results of DED1-M can be used to estimate the K_{res} values of all DED specimens under evaluation. In addition, K_{res} for the wrought specimens verifies the expected negligible residual stress.

2.3.2. Fatigue Crack Growth Results

Before fatigue crack growth data were analyzed, the validity of the COD from BFS compliance method for measuring crack size was verified. The fracture surface of a wrought specimen can be seen in **Figure 2.7**(a) and the fracture surface of DED1-T can be seen in **Figure 2.7**(b). Crack size was measured using ImageJ [26] analysis on the photos in **Figure 2.7** using an average of nine equally spaced positions through the thickness. Measured crack sizes agreed with the values for crack size calculated by the test control software to better than 0.050 mm, which is within the requirements of ASTM E647 [16]. Furthermore, the cracks in both specimens grew straight as defined by the standard.

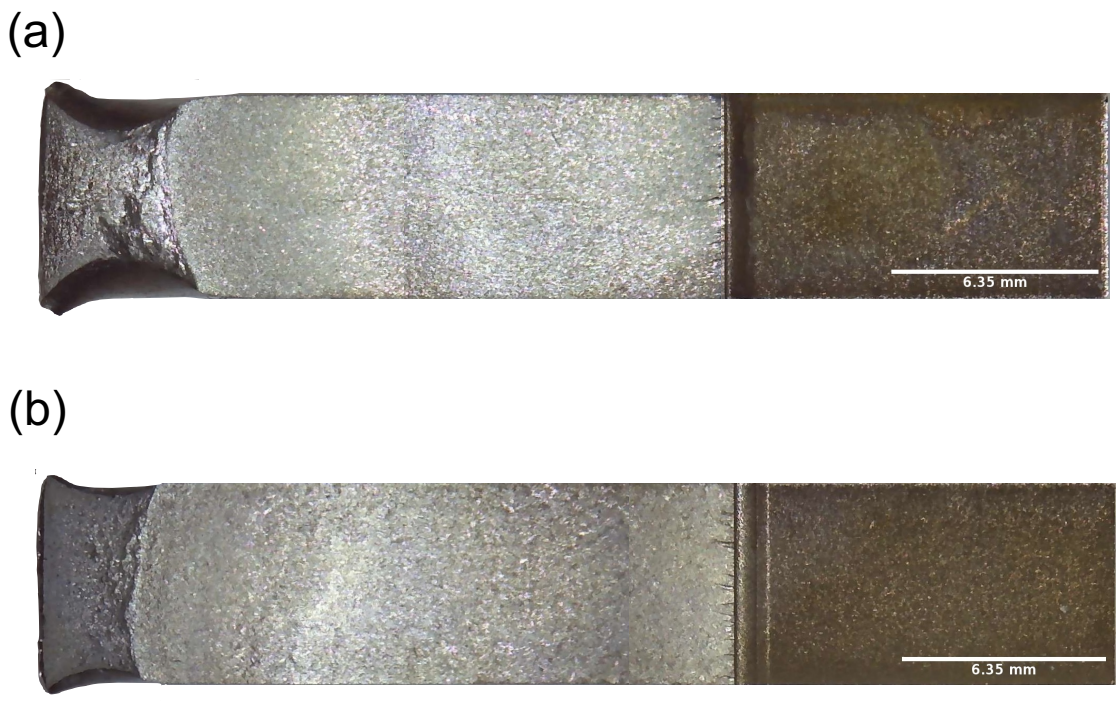

Figure 2.7: *Fracture surfaces of (a) Wrought Type 304/304L (Wrought1) and (b) DED Type 304L (DED1-T).*

The results of the ΔK decreasing and ΔK increasing fatigue crack growth tests for all specimens are plotted in **Figure 2.8** as a function of the applied (non-corrected) ΔK. Fatigue crack growth rates for three wrought specimens with negligible residual stress are plotted for

comparison. Since the first specimen (Wrought1) demonstrated equivalent fatigue crack growth data for ΔK decreasing and ΔK increasing, the remaining two wrought specimens (Wrought2,3) were tested only in ΔK decreasing conditions. The data show fatigue crack growth rates in DED are higher than those in wrought, with the largest differences at lower applied ΔK. The higher fatigue crack growth rates in DED are consistent with the positive values of K_{res} (**Figure 2.6**) determined for the DED material.

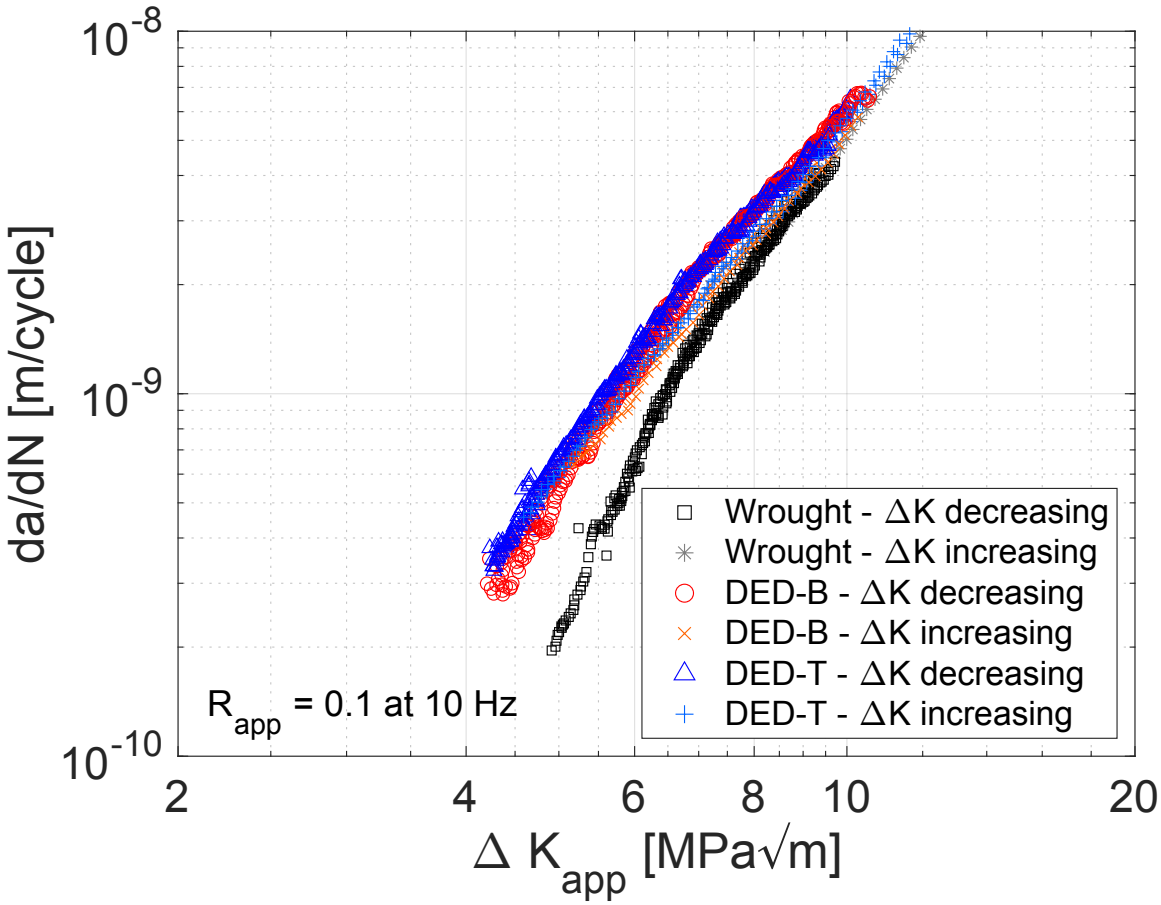

Figure 2.8: *Fatigue crack growth rates (da/dN) vs ΔK_{app} for DED Type 304L and wrought Type 304/304L stainless steel.*

2.3.3. Fatigue Crack Growth Assessment of Wrought Type 304/304L

The wrought Type 304/304L stainless steel with negligible residual stress (K_{res} = 0) was used to provide fatigue crack growth rate data for comparison with the DED Type 304L. The

absence of residual stress in the wrought material also allows the determination of the normalization parameter, *n,* which is assumed to be the same for the wrought and DED stainless steel materials. Fatigue crack growth rates at different R values versus ΔK_{app} are presented in **Figure 2.9**(a) while **Figure 2.9**(b) shows fatigue crack growth rates versus $\Delta K_{ACR.}$ Correcting the data for crack closure was necessary to find the effective values of ΔK, which were needed for the calculation of ΔK_{norm} in Equation (2.3).

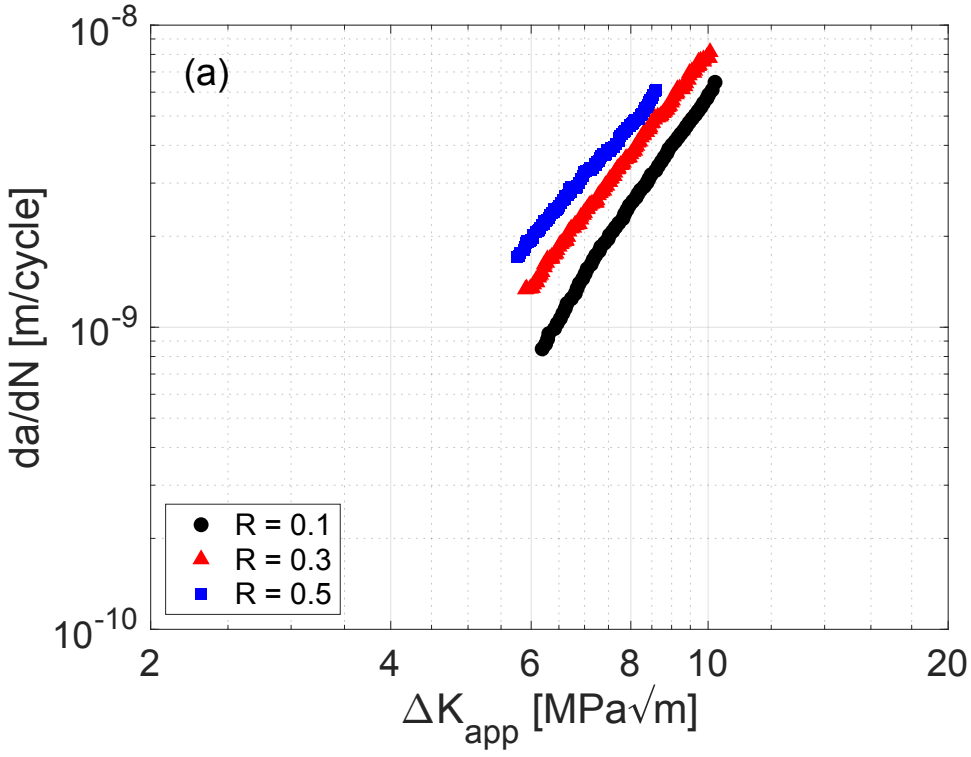

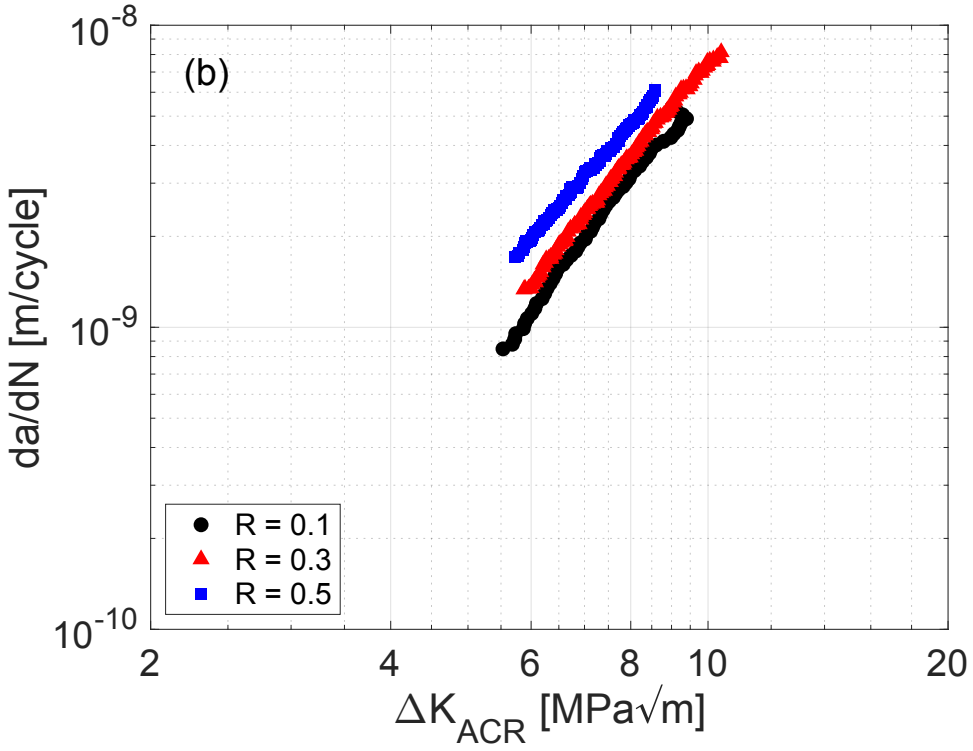

***Figure 2.9**: Fatigue crack growth rates (da/dN) versus ΔK_{app} (a) and ΔK_{ACR} (b) in wrought 304/304L stainless steel for different applied stress ratios.*

The biggest change between the two plots is a shift to the left in the data for R_{app} of 0.1 in **Figure 2.9**(b) as compared to **Figure 2.9**(a). The shift is consistent with a correction for crack closure in the fatigue crack growth data. The negligible difference between ΔK_{app} and ΔK_{ACR} for data at R_{app} of 0.3 and 0.5 is due to the negligible crack closure at these higher stress ratios.

To determine the appropriate value of *n*, ΔK_{norm} was calculated using the effective crack growth data in **Figure 2.9**(b) using a range of values, $n = 0.15$ to 0.35. The normalization parameter value, $n = 0.25$, was visually identified to best collapse the data into a single curve (**Figure 2.10**), and therefore was chosen for ΔK_{corr} analysis of the DED Type 304L material.

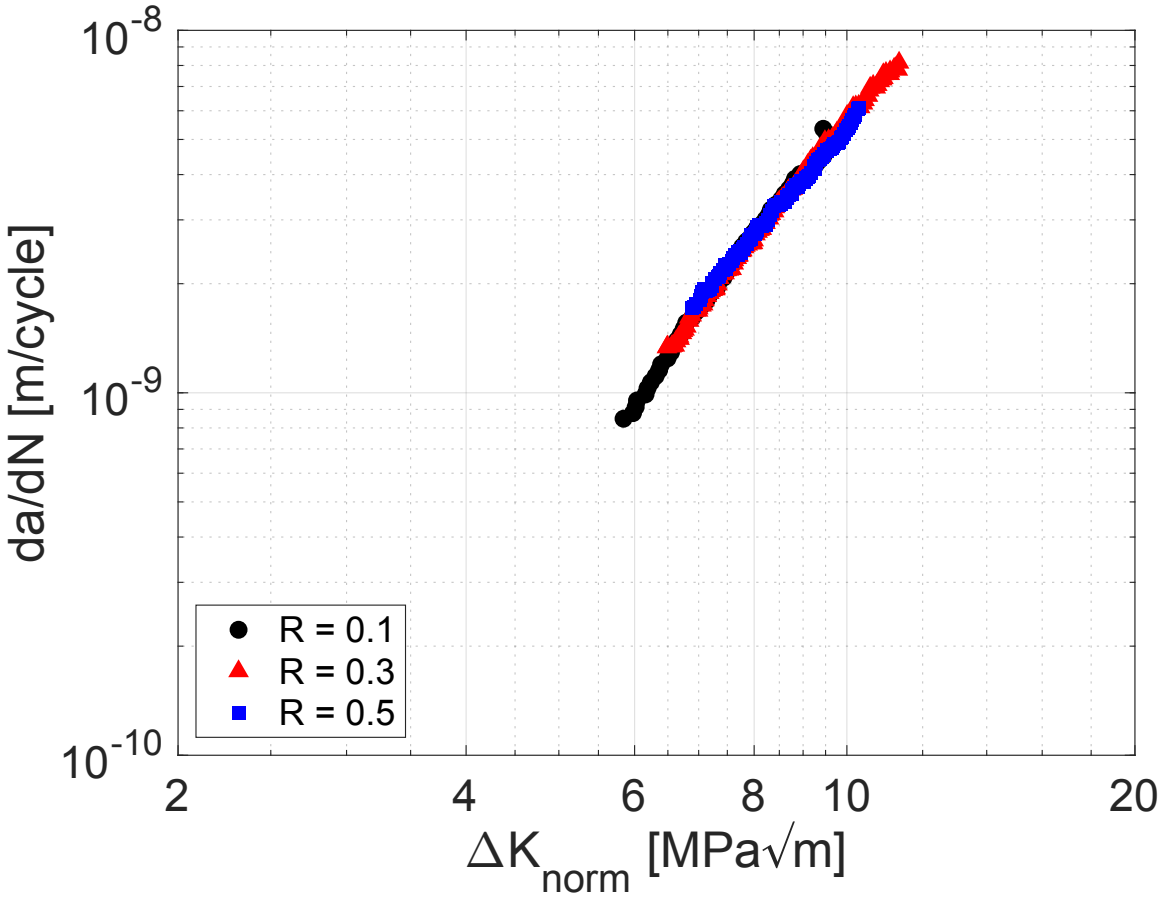

Figure 2.10: *Fatigue crack growth rates (da/dN) vs ΔK_{norm} plots for normalization parameter of 0.25.*

2.3.4. Fatigue Crack Growth Assessment of DED Type 304L

Values of R_{tot} (Equation (2.2)) for the four ΔK decreasing and four ΔK increasing fatigue tests are shown in **Figure 2.11**. Compared to R_{app} of 0.1 (red line), R_{tot} is always greater. During the ΔK decreasing portion of the test, R_{tot} increases as K_{res} becomes a larger contributor relative to $K_{min,app}$ and $K_{max,app}$ (Equation (2.2)). In the ΔK increasing portion of the test, K_{res} becomes a smaller contributor to R_{tot} because K_{res} decreases as the crack extends (**Figure 2.6**) and because the applied K values increase. Thus, R_{tot} trends toward R_{app} during the final stages of the test (a* > 17 mm).

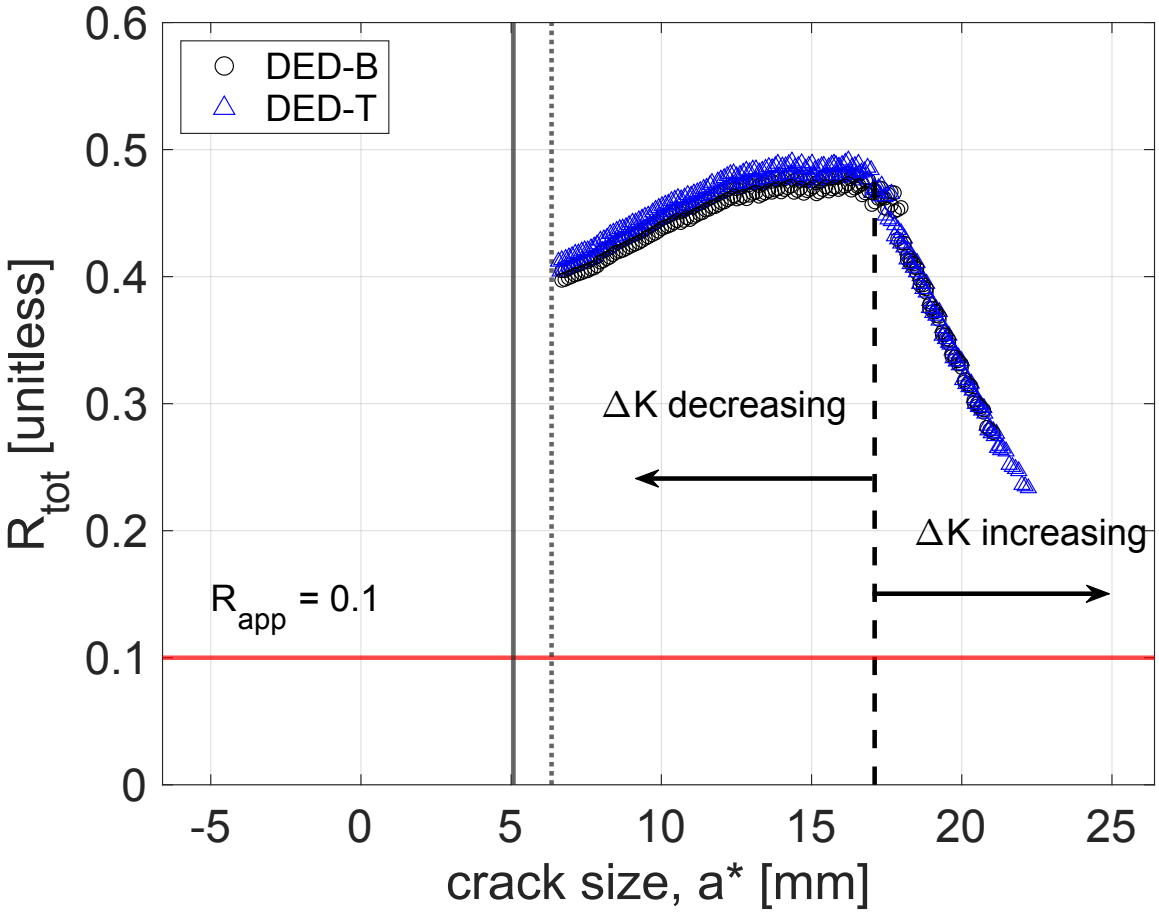

Figure 2.11: *R_{tot} versus crack size for DED Type 304L stainless steel from all four decreasing and increasing ΔK_{app} fatigue tests using K_{res} from slitting. The vertical lines represent the notch tip (solid line) and the end of the precrack region (dotted line) of fatigue crack growth.*

2.3.5. Corrected Fatigue Crack Growth Data

Compliance data for wrought (Wrought1) and DED (DED2-B) specimens are shown in **Figure 2.12**(a) and **Figure 2.12**(b) respectively. In wrought material with nominally zero residual stress, plasticity and roughness lead to crack face contact and a deviation from linearity in the compliance data. In contrast, for the DED material, the positive K_{res} mitigates crack closure by preventing crack face contact, thus ΔK_{ACR} is equal to ΔK_{app}.

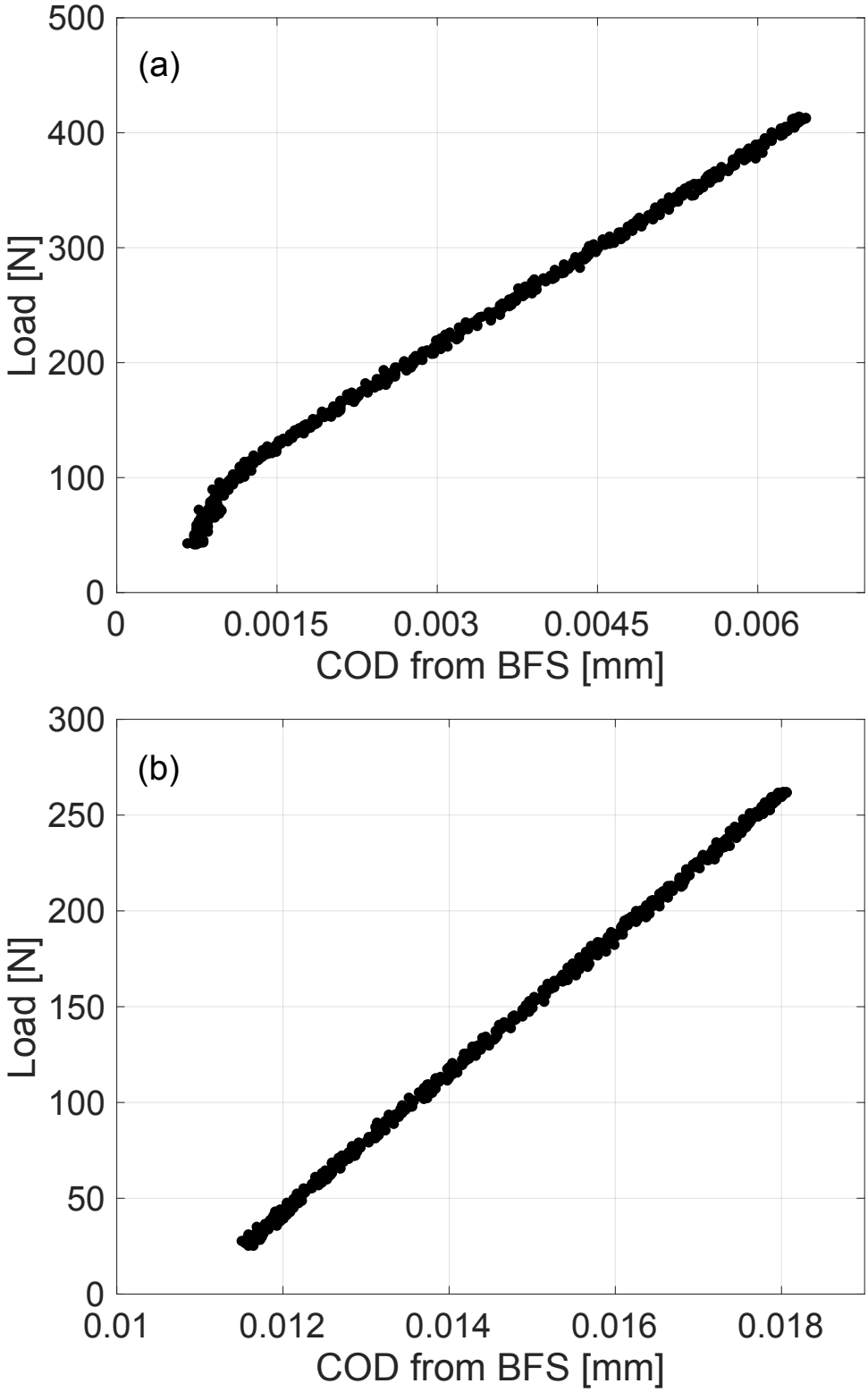

Figure 2.12: *Compliance data for (a) wrought (Wrought1) Type 304/304L stainless steel showing deviation from linearity at ΔK_{app} = 4.9 MPa·m$^{0.5}$ and (b) DED (DED2-B) Type 304L stainless steel showing complete linearity at ΔK_{app} = 4.2 MPa·m$^{0.5}$.*

To compare the intrinsic fatigue resistance of DED material to wrought material, fatigue crack growth data for DED material corrected for residual stress (ΔK_{corr}) are compared to fatigue crack growth data for wrought material corrected for crack closure (ΔK_{ACR}) in **Figure 2.13**. The wrought material has higher fatigue crack growth rates than observed in the DED material after correcting for closure and K_{res}, respectively.

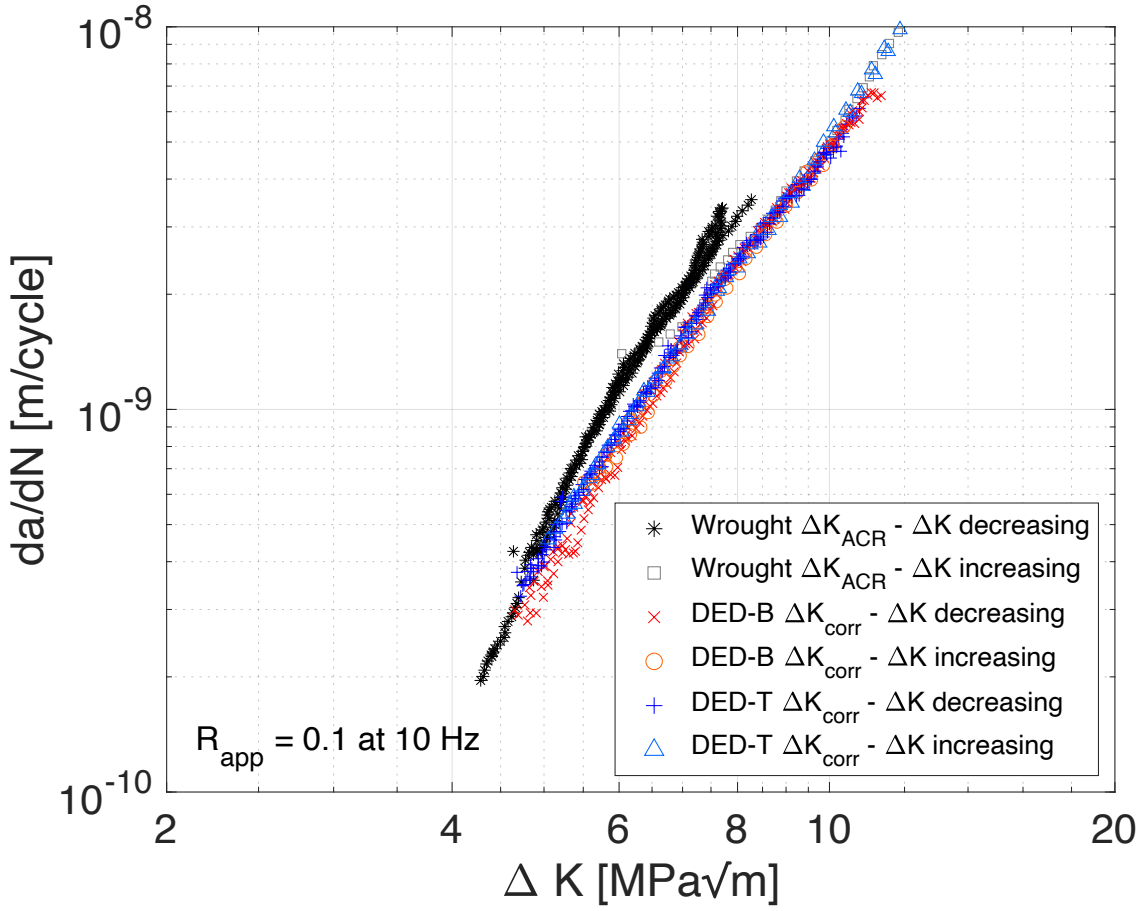

Figure 2.13: *Fatigue crack growth rates (da/dN) vs ΔK_{corr} for DED 304L and ΔK_{ACR} for wrought 304/304L stainless steel.*

2.4. Discussion

Residual stress profiles on multiple planes in the DED vertical wall build are consistent (**Figure 2.4**), suggesting that the residual stress in the build direction is relatively uniform along the height of the build. The lack of variability of residual stress with build height can be attributed

to the refinement and careful control of deposition process parameters. Thus, residual stress in the test specimens is independent of the position of extraction from the build (i.e., bottom (B), middle (M), and top (T)), however, it does vary with position from the front face (x). As shown in **Figure 2.5**, the residual stress near the front face of the C(T) specimen is tensile and becomes compressive towards the middle of the specimen and remains compressive near the back face. The temperature gradients of the deposited material result in rapid solidification of the surfaces and slower cooling rates of the center. As such, tensile residual stress is induced at the surface, which is balanced by compressive residual stress at the center as shown in the slitting results of **Figure 2.4**. This figure highlights the high tensile residual stress at the as-built edges of the DED material, suggesting that if the slitting measurement in **Figure 2.5** had been performed for the entirety of the C(T) specimen length (1.25W), the positions near the back face would return to large values of tensile residual stress.

The slitting method measurements of DED1-M provided an estimate of K_{res}, which acts to drive crack growth in the DED material. The tensile residual stress at the edges of the builds led to positive values of K_{res} close to 4 $MPa \cdot m^{0.5}$ at the front face of the C(T) specimens after sample extraction. This positive value of $K_{res,}$ despite decreasing as the cut progressed through the residual stress field, is sufficient to maintain an open crack wake and accelerate measured fatigue crack growth rates. In the case of positive K_{res}, the net value of the stress intensity factor can be found using the superposition principle without complications of nonlinear crack face contact. That is, if the residual stress field is known, a net driving force for fatigue crack growth can be calculated during post fatigue testing analysis and the ΔK_{corr} method can be used to correct for the influence of residual stress on fatigue crack growth data.

Fatigue crack growth behavior from all four specimens of the two DED vertical wall builds agreed well with each other (**Figure 2.8**) and suggests repeatability in mechanical performance of AM materials manufactured with identical processing parameters. The differences between top and bottom specimens were negligible, especially when compared to the differences between AM and wrought. For all four C(T) specimens, the DED material displayed higher fatigue crack growth rates in the near-threshold regime for equal applied ΔK as compared to the stress-free wrought Type 304/304L (**Figure 2.8**). This difference in fatigue crack growth rate is associated with tensile residual stress and the resulting effects on R_{tot} from the variation of K_{res} and the evolution of ΔK_{app}. The positive K_{res} from the tensile residual stress in DED material led to values of R_{tot} that were higher than the applied stress ratio, $R_{app,}$ of 0.1 for the duration of the fatigue tests. **Figure 2.11** demonstrates that at the low applied ΔK values as the ΔK decreasing test approached the threshold for fatigue crack growth, R_{tot} for the DED tests was close to 0.5, which is significantly different from R_{app} of 0.1. Typically, higher R (for the same ΔK) leads to higher fatigue crack growth rates. This is the principal reason that the crack growth rates are higher in the DED material than in the wrought material at the same values of ΔK_{app}.

Subtle differences between the apparent fatigue crack growth rates are also evident in the ΔK decreasing and ΔK increasing portions of the tests in the DED material. These differences can be attributed to the evolution of K_{res} throughout the specimen. In the initial ΔK decreasing portion of the fatigue crack growth tests, K_{res} is maximum with a shallow slope (**Figure 2.6**), thus the apparent fatigue crack growth rates exhibit the largest effect from residual stress in this region. In the ΔK increasing portion, however, the positive K_{res} values are less than in the initial stages of crack growth and the apparent fatigue crack growth rates are slower than those of the ΔK decreasing (initial) portion of the test. In the absence of residual stress, the wrought material ΔK

decreasing and ΔK increasing portions of the test resulted in consistent fatigue crack growth rates. Therefore, the differences in apparent fatigue crack growth rates of the DED material are associated with the varying K_{res} profile of the DED material. In the absence of crack face contact, the intrinsic fatigue resistance of the DED material can be estimated from the ΔK_{corr} (Equation (2.4)) with ΔK_{eff} equal to ΔK_{app}. For a material with negligible residual stress, R_{app} is equal to R_{tot} for the duration of the fatigue test and ΔK_{corr} is not applicable. Therefore, for the wrought material, post-test analysis is limited to adjusting for crack face contact using ΔK_{ACR}.

The fatigue crack growth rate data are corrected for the influence of process induced bulk residual stress when plotted as a function of ΔK_{corr}. To compare the intrinsic behavior of the DED and wrought materials, the corrected fatigue crack growth data (ΔK_{corr}) of the DED material are plotted with the ΔK_{ACR} of the wrought material in **Figure 2.13**. The fatigue crack growth rate data for the DED material agree, confirming that the differences between the apparent fatigue crack growth rate data were due to the influence of residual stress. Here, the apparent fatigue threshold for DED material, if the current trend is projected to a threshold crack growth rate as defined by the ASTM standard (10^{-10} m/cycle), appears to be similar to that of the wrought material at about 4 MPa·$m^{0.5}$ (**Figure 2.13**). DED and wrought fatigue crack growth rate data converge when both materials have been corrected for residual stress and crack closure respectively, suggesting that the intrinsic fatigue resistance of the two materials are similar near threshold. However, for higher fatigue crack growth rates (>10^{-9} m/cycle) and values of ΔK greater than 6 MPa·$m^{0.5}$, the DED material exhibits slightly lower fatigue crack growth rates as compared to wrought material.

2.5. Conclusions

The residual stresses and unique microstructures formed by high cooling rates and thermal gradients of the manufacturing process are expected to influence apparent fatigue crack growth

rates in AM materials in their as-built state as compared to their wrought counterparts. The present study focused on developing a quantitative understanding of the impact of residual stress on fatigue cracking to evaluate the intrinsic differences between AM and wrought 304/304L materials. The key conclusions are:

1. The results show that near-threshold fatigue crack growth rates in DED Type 304L are influenced significantly by the presence of tensile residual stress. Specifically, for the specimens extracted from the as-built DED Type 304L stainless steel in this study, fatigue crack growth rates were measured to be 3.5 times faster than in commercially available wrought Type 304/304L stainless steel in the near-threshold regime ($<10^{-8}$ m/cycle) at an applied ΔK of 5 $MPa \cdot m^{0.5}$.
2. The residual stress intensity factor, K_{res}, determined from slitting experiment data of both DED and wrought materials revealed positive values ranging from 4 $MPa \cdot m^{0.5}$ at the notch tip to 1 $MPa \cdot m^{0.5}$ at the end of fatigue crack growth for DED Type 304L; in contrast, the wrought material displayed negligible residual stress.
3. The DED Type 304L did not exhibit crack closure, which is consistent with the positive total stress ratio and positive values of K_{res}. In contrast, the effects of crack closure were present in the data for wrought Type 304/304L, consistent with negligible K_{res}.
4. The DED Type 304L stainless steel and the wrought Type 304/304L exhibited similar intrinsic fatigue crack growth rates when the DED Type 304L data were corrected for residual stress using the ΔK_{corr} method and the wrought Type 304/304L data were adjusted for the effects of crack closure using the adjusted compliance ratio (ΔK_{ACR}) method. This comparison demonstrates that the different apparent fatigue crack growth

rates of DED and wrought material can be attributed to the combination of residual stress and crack closure, which are different in these two materials.

5. While similar, corrected crack growth rates in DED Type 304L were slightly lower than those in wrought Type 304/304L. The lower fatigue crack growth rates are hypothesized to be related to the unique microstructure (grain size and morphology) of the DED material, which had a small influence on its intrinsic fatigue crack growth resistance compared to the more significant impact of residual stress.

Acknowledgements

This work was supported by a NASA Space Technology Research Fellowship (CMS) and material was provided by Sandia National Laboratories. Sandia National Laboratories is a multi-mission laboratory managed and operated by National Technology & Engineering Solutions of Sandia, LLC, a wholly owned subsidiary of Honeywell International Inc., for the U.S. Department of Energy's National Nuclear Security Administration under contract DE-NA0003525. This paper describes objective technical results and analysis. Any subjective views or opinions that might be expressed in the paper do not necessarily represent the views of the U.S. Department of Energy or the United States Government.

References

1. Yadollahi, A. and N. Shamsaei, *Additive manufacturing of fatigue resistant materials: Challenges and opportunities.* International Journal of Fatigue, 2017. **98**: 14-31.
2. Fatemi, A., et al., *Fatigue behaviour of additive manufactured materials: An overview of some recent experimental studies on Ti-6Al-4V considering various processing and loading direction effects.* Fatigue & Fracture of Engineering Materials & Structures, 2019. **42**(5): 991-1009.
3. Mishurova, T., et al., *Separation of the impact of residual stress and microstructure on the fatigue performance of LPBF Ti-6Al-4V at elevated temperature.* International Journal of Fatigue, 2021. **148**: 106239.
4. Anderson, T.L., *Fracture Mechanics: fundamentals and applications*. 2005: CRC Press. 513-558.
5. Daniewicz, S.R. and N. Shamsaei, *An introduction to the fatigue and fracture behavior of additive manufactured parts.* International Journal of Fatigue, 2017. **94**: 167-167.
6. Shamsaei, N. and J. Simsiriwong, *Fatigue behaviour of additively-manufactured metallic parts.* Procedia Structural Integrity: 3rd International Symposium on Fatigue Design and Material Defects (FDMD 2017), 2017. **7**: 3-10.
7. Riemer, A., et al., *On the fatigue crack growth behavior in 316L stainless steel manufactured by selective laser melting.* Engineering Fracture Mechanics, 2014. **120**: 15-25.
8. Riemer, A. and H.A. Richard, *Crack Propagation in Additive Manufactured Materials and Structures.* 21st European Conference on Fracture, (Ecf21), 2016. **2**: 1229-1236.
9. Leuders, S., et al., *On the mechanical behaviour of titanium alloy TiAl6V4 manufactured by selective laser melting: Fatigue resistance and crack growth performance.* International Journal of Fatigue, 2013. **48**: 300-307.
10. Gordon, J.V., et al., *Fatigue crack growth anisotropy,texture and residual stress in austenitic steel made by wire and arc additive manufacturing.* Materials Science and Engineering a-Structural Materials Properties Microstructure and Processing, 2018. **724**: 431-438.
11. Ran, X.-z., et al., *Effects of microstructures on the fatigue crack growth behavior of laser additive manufactured ultrahigh-strength AerMet100 steel.* Materials Science and Engineering: A, 2018. **721**: 251-262.
12. Rangaswamy, P., et al., *Residual stresses in LENS (R) components using neutron diffraction and contour method.* Materials Science and Engineering a-Structural Materials Properties Microstructure and Processing, 2005. **399**(1-2): 72-83.
13. Donald, J.K. and D.A. Lados, *An integrated methodology for separating closure and residual stress effects from fatigue crack growth rate data.* Fatigue & Fracture of Engineering Materials & Structures, 2006. **30**(3): 223-230.

14. James, M., et al., *A Methodology for Partitioning Residual Stress Effects From Fatigue Crack Growth Rate Test Data.* Materials Performance and Characterization, 2016. **5**(3): 194-214.

15. Ronevich, J.A., C.R. D'Elia, and M.R. Hill, *Fatigue crack growth rates of X100 steel welds in high pressure hydrogen gas considering residual stress effects.* Engineering Fracture Mechanics, 2018. **194**: 42-51.

16. E647-15, *Standard Test Method for Measurement of Fatigue Crack Growth Rates*. 2015. ASTM International: West Conshohocken, PA.

17. Smith, T.R., et al. *Effects of Extreme Hydrogen Environments on the Fracture and Fatigue Behavior of Additively Manufactured Stainless Steels*. in *Proceedings of the ASME 2019 Pressure Vessels & Piping Conference*. 2019. San Antonio, TX, USA.

18. A240/A240M-19 *Standard Specification for Chromium and Chromium-Nickel Stainless Steel Plate, Sheet, and Strip for Pressure Vessels and for General Applications*. 2019. ASTM International: West Conshohocken, PA.

19. Smith, T.R., et al. *Orientation Effects on Fatigue Behavior of Additively Manufactured Stainless Steel*. in *Proceedings of the ASME 2017 Pressure Vessels & Piping Conference*. 2017. Waikoloa, Hawaii, USA.

20. Hill, M.R., *Chapter 4: The Slitting Method*, in *Practical Residual Stress Measurement Methods*, G.S. Schajer, Editor. 2013, Wiley. 89-108.

21. Schajer, G.S. and M.B. Prime, *Use of inverse solutions for residual stress measurements.* Journal of Engineering Materials and Technology-Transactions of the ASME 2006. **128**(3): 375-382.

22. Schindler, H.J., W. Cheng, and I. Finnie, *Experimental determination of stress intensity factors due to residual stresses.* Experimental Mechanics, 1997. **37**(3): 272-277.

23. Olson, M.D. and M.R. Hill, *Determination of residual stress intensity factor in the compact tension coupon.* Engineering Fracture Mechanics, 2012. **88**: 28-34.

24. Donald, J.K., G.H. Bray, and R.W. Bush, *An evaluation of the adjusted compliance ratio technique for determining the effective stress intensity factor.* Fatigue and Fracture Mechanics: Twenty-Ninth Volume, ASTM STP 1332, American Society for Testing and Materials, West Conshohocken, PA, 1999: 674-695.

25. Dowling, N.E., *Mechanical behavior of materials : engineering methods for deformation, fracture, and fatigue*. 4th ed. 2013, Boston: Pearson. Chapter 9: 416-490.

26. Rasband, W.S., *ImageJ.* U. S. National Institutes of Health.

Chapter 3:
Validation of On-line Crack Compliance Data Analysis Methods for the Residual Stress Intensity Factor [2]

Abstract

Residual stress can significantly impact the fatigue crack growth rate (FCGR) observed in standard tests. In the present study, implementation of the on-line crack compliance (OLCC) method for determining the residual stress intensity factor, K_{res}, in FCGR tests is supported by validation data, details of novel data analysis methods, and strategies for data reduction. Slitting measurements on C(T) specimens of quenched (but not stress relieved) and aged aluminum alloy 7050-T74 provide reference profiles of K_{res} as a function of crack size. The OLCC method quantifies K_{res} profiles from stress intensity factor control and load control FCGR tests over a range of residual stress states. Novel OLCC data reduction techniques are developed, and data analysis attributes and limitations explored, contributing to an improved methodology for standardization. The results demonstrate that the on-line crack compliance method is a valid means of quantifying K_{res} during fatigue crack growth rate testing.

Keywords: Residual stress, residual stress intensity factor, fatigue crack growth rate testing, on-line crack compliance method, aluminum alloys

[2] Submitted: Smudde, C.M., J.C. Gibeling, and M.R. Hill, *Validation of On-line Crack Compliance Data Analysis Methods for the Residual Stress Intensity Factor.* Engineering Fracture Mechanics, 2022.

3.1. Introduction

Fatigue crack growth rate (FCGR) test data play a critical role in the design, operational certification, and maintenance of engineering structural components. However, residual stress, a common side effect of many metal processing and manufacturing techniques, can significantly impact measured fatigue crack growth rates. When a fatigue crack grows through a residual stress field, the stress intensity factor (K) that characterizes stress near the crack tip can differ significantly from the applied stress intensity factor that is associated with the external cyclic loading [1-3]. Specifically, the distribution of residual stress acting in the crack opening direction causes a Mode I residual stress intensity factor (K_{res}) that affects observed specimen behavior. Consequently, crack growth rates may be either enhanced or retarded depending on the nature of the residual stress field [4-7]. An increase in fatigue crack growth rates due to tensile residual stress (positive K_{res}) is extremely detrimental to fatigue performance, while a decrease in growth rates from compressive residual stress (negative K_{res}) can improve fatigue resistance. Even a small magnitude of residual stress can greatly alter the total stress intensity factor under cyclic loading conditions, especially at the low applied K values characteristic of the near-threshold regime [8], or in cases when residual stress causes crack face contact [4, 9, 10]. Therefore, recognizing and understanding the influence of residual stress on observed fatigue behavior is crucial for accurate interpretations of FCGR test data.

A typical approach to account for residual stress in fatigue crack growth analysis uses the principles of Linear Elastic Fracture Mechanics (LEFM) to correlate the observed FCGR behavior of residual stress-bearing specimens to that of residual stress-free specimens (e.g., [7] and [11]). The stress intensity factor from residual stress (K_{res}) and from cyclic applied loads (maximum and minimum values of K_{app}) are considered additive for the same mode of loading at the same crack

size, and the principle of superposition is used to determine a total stress intensity factor (K_{tot}) and total stress intensity factor ratio ($R_{tot} = (K_{min,app}+K_{res})/(K_{max,app}+K_{res})$) to represent the net driving force for fatigue crack growth. The slitting method is a destructive measurement technique that utilizes concepts of LEFM to estimate the values of K_{res} by introducing a cut into a material with residual stress and measuring the deformation response. As such, slitting a secondary (duplicate) specimen over a relevant range of crack size provides values of K_{res} that can be used to determine K_{tot} and R_{tot}, such that fracture mechanics data measured in a primary specimen can be adjusted for the influence of residual stress. Earlier work has applied slitting of secondary specimens to assess effects of residual stress in fracture mechanics tests for FCGR (e.g., [12] and [13]) and monotonic crack growth resistance (R-curve) [10] properties.

Recent developments in FCGR data analysis have led to innovative methods to account for residual stress effects, both tensile and compressive, during fatigue testing. Similar to the imposed cut of the slitting method, a fatigue crack growing through a material causes the residual stress to relax and redistribute, resulting in a deformation change that can be measured. As an extension of slitting, the on-line crack compliance (OLCC) method developed by Lados, Apelian, and Donald quantifies K_{res} by analyzing compliance data (i.e., load vs. deformation data) while simultaneously collecting FCGR data [14-16]. K_{res} as a function of crack size ($K_{res}(a)$) from OLCC can then be used to account for the influence of residual stress on the driving force for crack growth. By utilizing compliance data from FCGR tests, the OLCC method obviates the need for secondary replicate specimens inherent to the slitting approach, removing the uncertainty associated with different residual stress states in the primary and secondary specimens.

While the OLCC method represents a significant advance for the fatigue testing community, there has been limited progress towards its wide-spread adoption. Only a small

number of publications have verified its usefulness and those have not provided a detailed procedure for analysis of the compliance data [9, 17]. Therefore, the goals of this work are to support broader application of the OLCC method by providing K_{res} validation data from primary compact (C(T)) fatigue specimens and comparing it to slitting measurements on secondary specimens, outlining the details of different methods of analyzing the OLCC data, and recommending critical steps for data reduction.

3.2. Methods and Material

3.2.1. Slitting Measurements

Residual stress relaxes and redistributes in a material as a cut or crack progresses, resulting in a dependence of the residual stress intensity factor on cut depth or crack size ($K_{res}(a)$). In this study, the slitting method [18] is employed to determine residual stress profiles and the corresponding $K_{res}(a)$ values in secondary specimens. In a slitting experiment, a cut is made along the plane of interest in an unloaded and unnotched specimen by wire electrical discharge machining (EDM) at fixed increments of cut depth. The deformation response from the release of residual stress acting normal to the cut plane is recorded as a function of cut depth and denoted as $\varepsilon_{res}(a)$. Residual stress normal to the plane of interest (opening stress) as a function of distance from the front face (x) of the specimen is determined from the strain versus cut depth data using a pulse-regularization inverse analysis technique [19]. The computed values of stress represent a profile of residual stress versus position in the uncut part. The details of slitting, including residual stress calculation, are described elsewhere [18, 20, 21].

The slitting method data can also provide the opening-mode (Mode I) K_{res} as a function of crack size, $K_{res}(a)$, for a one-dimensional edge crack in a planar elastic body by relating cut depth to an equivalent value of crack size (a) in a fatigue test specimen. Invoking energy methods and

the LEFM concept of the crack driving force, Schindler [22] approximated the cut from a slitting measurement as a crack and showed that $K_{res}(a)$ can be computed from a geometry dependent (and stress independent) influence function Z(a), the effective elastic modulus E' (for plane stress or plane strain), and the slope of the strain (ε_{res}) versus cut depth data (Equation (3.1)).

$$K_{res}(a) = \frac{E'}{Z(a)} \frac{d\varepsilon_{res}(a)}{da} \tag{3.1}$$

The derivative of strain with respect to crack size (cut depth) is determined by an incremental polynomial fit of the data, as described in [18]. An influence function (Z(a)) developed by Olson for the compact (C(T)) geometry [23] is used in this work.

3.2.2. On-line Crack Compliance Method

Data Analysis Methods

Donald and Lados first introduced the on-line crack compliance (OLCC) method to compute stress intensity factors due to residual stress using readily available data from FCGR tests (load, deformation, and crack size) [14]. They further explored the similarities in LEFM concepts between OLCC and slitting in a subsequent paper with Apelian [15]. Starting from fundamental fracture mechanics definitions and the slitting derivation of Schindler, et al. [12], Lados, Apelian, and Donald [15] present an equation for K_{res} in terms of a ratio of deformation changes measured from crack mouth opening displacement (CMOD) compliance (i.e., load versus CMOD) data at increments of crack size. In the present work, back-face strain (BFS) compliance data is used, thereby expanding on the prior work using CMOD.

Schindler, et al. [12] note that the influence function, Z(a) of Equation (3.1), is derived from a solution for an arbitrary reference load ($P_{ref}(a)$) that provides the stress intensity factor ($K_{ref}(a)$) and a measure of deformation, here taken to be BFS, $\varepsilon_{ref}(a)$, as functions of crack size:

$$Z(a) = \frac{E'}{K_{ref}(a)} \frac{d\varepsilon_{ref}(a)}{da} \tag{3.2}$$

While Equation (3.2) is specific to BFS, an analogous expression [16] enables the determination of an influence function for deformation quantified by CMOD; the two expressions are limited to use with their corresponding deformation measurement. Substituting Equation (3.2) into Equation (3.1) provides:

$$K_{res}(a) = K_{ref}(a) \left[\frac{d\varepsilon_{res}(a)}{da}\right] / \left[\frac{d\varepsilon_{ref}(a)}{da}\right] \tag{3.3a}$$

Although the residual strain is functionally independent of the reference strain, the correlation of the two variables allows Equation (3.3a) to be approximated by:

$$K_{res}(a) \approx K_{ref}(a) \frac{d\varepsilon_{res}(a)}{d\varepsilon_{ref}(a)} \tag{3.3b}$$

which is written as an equality in the prior work [15]. Lados, Apelian and Donald then assume the reference load to be the maximum applied load $P_{max,app}(a)$ in the FCGR test, so that:

$$K_{res}(a) \approx K_{max,app}(a) \frac{d\varepsilon_{res}(a)}{d\varepsilon_{max,app}(a)} \tag{3.3c}$$

where $\varepsilon_{res}(a)$ is determined at zero applied load [14, 15]. They further estimate the derivative in Equation (3.3c) by a finite difference. Noting that compliance data are available at finite increments of crack size, Δa, the derivative notation is replaced by a ratio of finite ranges of deformation (changes in BFS in this study). The resulting equation, as given in the earlier work [14, 15], provides $K_{res}(a_i)$ for the i^{th} crack size increment by what is referred to here as the OLCC difference ratio:

$$K_{res}(a_i) = K_{max,app}(a_i) \frac{\Delta\varepsilon_{res}(a_i)}{\Delta\varepsilon_{max,app}(a_i)} \tag{3.4}$$

To illustrate the data analysis, **Figure 3.1** shows example load versus BFS (i.e., compliance) data for a FCGR test at a constant load amplitude. Throughout the test, data were collected at fixed increments of crack size (Δa). **Figure 3.1** shows data for a selected crack size (a_i, shown in red) and for a crack size *m* increments preceding that crack size (a_{i-m}, in black), where *m* is somewhat large and suitable for illustration. A negative sign is used on the abscissa of **Figure 3.1** because positive applied load on the C(T) results in negative BFS; plotting -BFS makes **Figure 3.1** appear similar to figures of load versus CMOD in the prior work [14, 15]. To account for crack closure, which is common in FCGR test compliance data and especially significant here owing to negative K_{res}, data were only assessed above the opening load (P_{open}) determined using linear regression as described in ASTM E647 [24]. The inverse slope of the data above P_{open} represents the mechanical specimen compliance that is typically used to calculate crack size in FCGR testing. Extrapolation of the linear trend to zero load (dashed lines in **Figure 3.1**) defines the residual strain $\varepsilon_{res}(a_i)$. The data of **Figure 3.1** show significant shifts between $\varepsilon_{res}(a_i)$ and $\varepsilon_{res}(a_{i-m})$, as well as between $\varepsilon_{max}(a_i)$ and $\varepsilon_{max}(a_{i-m})$. In the absence of residual stress, no shift in residual strain would be expected (i.e., ε_{res} would be constant).

To apply the OLCC difference ratio of Equation (3.4), the ratio of the changes in residual strain to the changes in strain at the maximum applied load over the finite increment of crack growth from a_{i-m} to a_i need to be estimated. As such, the difference in residual strain at zero load is defined as:

$$\Delta\varepsilon_{res}(a_i) = \varepsilon_{res}(a_i) - \varepsilon_{res}(a_{i-m}) \tag{3.5}$$

Since the measured deformation at maximum applied load includes strain due to both residual stress and applied load, it is necessary to first apply superposition to subtract the shift in

strain due to residual stress. Therefore, the difference in strain solely from the maximum applied load is:

$$\Delta\varepsilon_{max,app}(a_i) = [\varepsilon_{max}(a_i) - \varepsilon_{res}(a_i)] - [\varepsilon_{max}(a_{i-m}) - \varepsilon_{res}(a_{i-m})] \tag{3.6a}$$

$$\Delta\varepsilon_{max,app}(a_i) = [\varepsilon_{max}(a_i) - \varepsilon_{max}(a_{i-m})] - \Delta\varepsilon_{res}(a_i) \tag{3.6b}$$

where ε_{max} is the measured deformation at maximum applied load. $K_{res}(a_i)$ from the OLCC difference ratio is determined by substituting Equation (3.5) and Equation (3.6b) into Equation (3.4), and noting that $K_{max,app}(a_i)$ is found with $P_{max,app}(a_i)$ using available equations for the C(T) specimen [24].

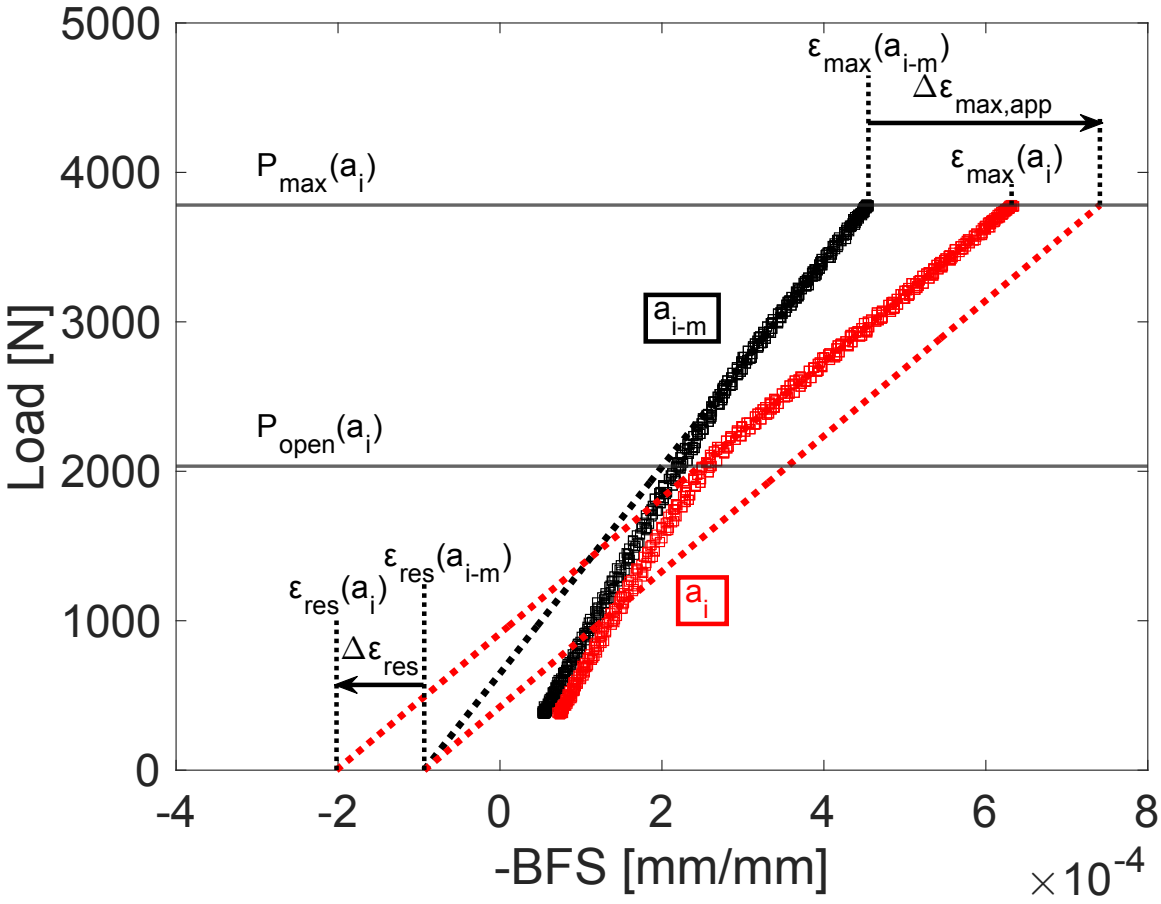

***Figure 3.1**: Schematic of OLCC in the presence of a compressive residual stress field showing data at crack sizes a_i (in red) and a_{i-m} (in black) in a constant load amplitude test (after [14, 15]).*

Equations (3.5) and (3.6) comprise a backward difference approach, which enables $K_{res}(a_i)$ to be determined in real time during an FCGR test. This method is comparable to the forward difference (using crack size increment *i* and *i+1*) as described in the earlier work [14, 15]. A central difference is an alternative that may offer some improvement, as noted below.

Figure 3.2 shows a second plot of example compliance data with two fundamental differences from the data of **Figure 3.1**. First, the specimen was tested under constant ΔK_{app} conditions, so that P_{max} decreases as crack size increases. Second, there are data for three crack sizes: a_i and the crack sizes *m* increments smaller (a_{i-m}) and larger (a_{i+m}). $K_{res}(a_i)$ is then determined from a central difference ratio using:

$$\Delta\varepsilon_{res}(a_i) = \varepsilon_{res}(a_{i+m}) - \varepsilon_{res}(a_{i-m}) \tag{3.8a}$$

$$\Delta\varepsilon_{max,app}(a_i) = [\varepsilon(a_{i+m}) - \varepsilon(a_{i-m})]_{P_{max,app}(a_i)} - \Delta\varepsilon_{res}(a_i) \tag{3.8b}$$

where the measured maximum strain of Equation (3.6b) is replaced in Equation (3.8b) with the strain at each crack size ($\varepsilon(a_{i-m})$ and $\varepsilon(a_{i+m})$) occurring at the same load, $P_{max,app}(a_i)$. These maximum strain values at each crack size are determined from linear fits to the compliance data above P_{open} (dashed lines in **Figure 3.2**), extrapolating as needed. Substituting Equations (3.8a) and (3.8b) into Equation (3.4) allows the determination of $K_{res}(a_i)$ via a central OLCC difference ratio, where the data are assessed over 2*m* increments of crack growth. It is important to note that the same load must be used to determine $\Delta\varepsilon_{max,app}(a_i)$ in Equation (3.8b) and $K_{max,app}(a_i)$ in Equation (3.4) for this data analysis method.

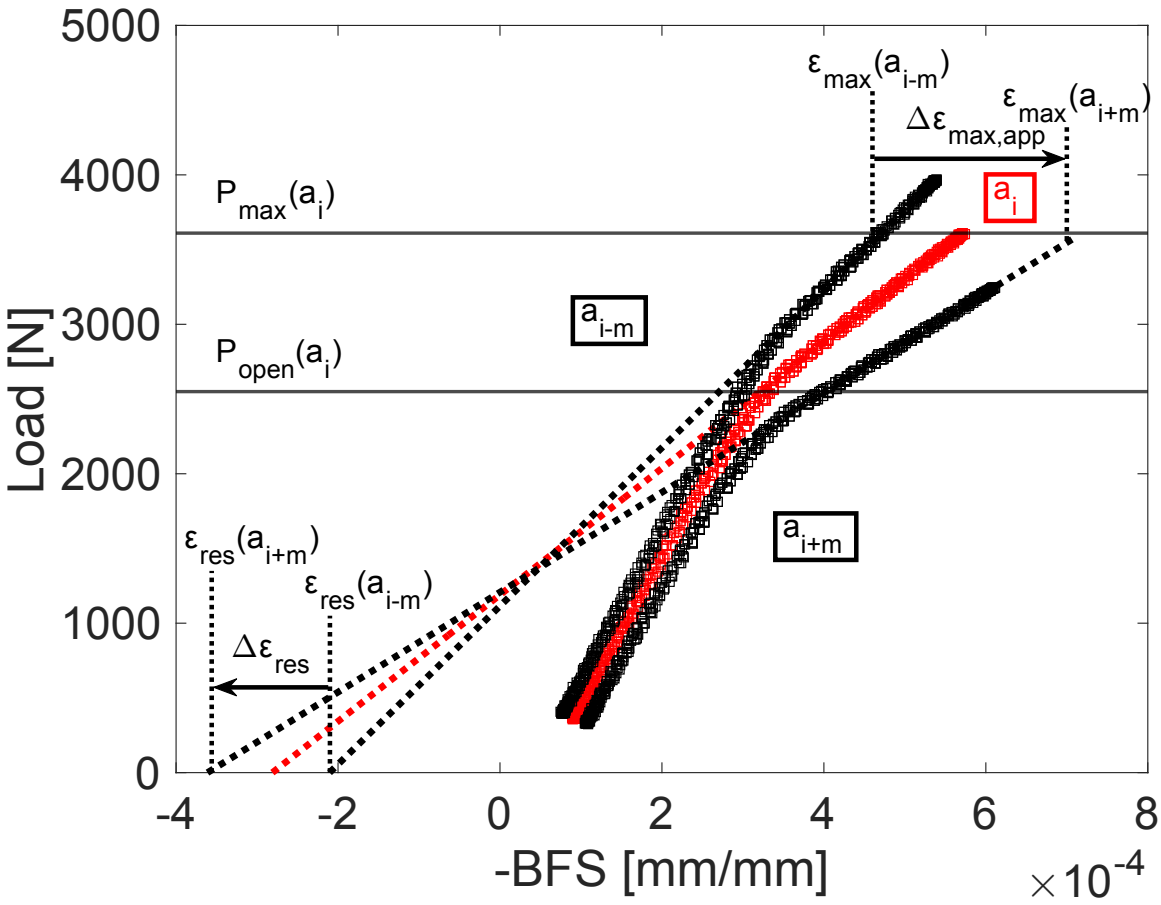

***Figure 3.2**: Schematic of OLCC central difference ratio method for data from a test under constant ΔK (decreasing load) in the presence of a compressive residual stress field.*

While the backward and central difference ratio analyses described are complementary to the forward difference analysis presented previously [14, 15], an improved data analysis that applies a smoothing differential to determine $K_{res}(a_i)$ is proposed in this work. When compliance data are saved during an FCGR test, two sets of strain values can be determined for each crack size: the residual strain, $\varepsilon_{res}(a_i)$, in the manner described above, and a reference strain:

$$\varepsilon_{ref}(a_i) = [\varepsilon(a_i)]_{P_{ref}} - \varepsilon_{res}(a_i) \tag{3.9}$$

where $\varepsilon_{ref}(a_i)$ is found for each crack size from the linear fit to the compliance data above P_{open} evaluated at a specific (but arbitrary) load P_{ref} that must be constant for all crack sizes. Given sequences of strains as functions of crack size, post-test determination of $K_{res}(a_i)$ follows prior

work in slitting [18] by using the incremental polynomial method to determine each of the two derivatives of strain with respect to crack size of Equation (3.3a) ($d\varepsilon_{res}(a_i)/da$ and $d\varepsilon_{ref}(a_i)/da$). The incremental polynomial method appears in ASTM E647 [24], where it is used to determine FCGR from the record of crack size versus cycle count. The analysis recommends a quadratic polynomial fit to a set of 2N+1 consecutive data points, comprising data at a specific crack size, a_i, along with N additional data points at preceding values of crack size and N additional points at succeeding values of crack size (data from crack sizes a_{i-N} to a_{i+N}). The polynomial is used to compute the analytical derivative of the quadratic fit for both strains of interest (ε_{res} and ε_{ref}) at a specified crack size. With the two derivatives determined for each crack size, $K_{res}(a_i)$ is found from Equation (3.3a), with $K_{ref}(a_i)$ computed with P_{ref} and the available equations for the C(T) specimen [24]. In this work, P_{ref} is assumed to be the maximum load at the first recorded crack size (i.e., $P_{ref}(a) = P_{max}(a_1)$) and this method for determining $K_{res}(a)$ using Equation (3.3a) is referred to as the OLCC derivative ratio method.

A final OLCC data analysis approach returns to the theoretical origins of the slitting method and uses Schindler's influence function to determine K_{res} as given by Equation (3.1). This method, referred to as OLCC Z(a), requires a defined influence function for the specimen geometry of interest and the specified deformation measurement (BFS in this study). At the time of the publication of the earlier work by Lados, and Apelian and Donald, an influence function for a C(T) specimen had not been established for BFS deformation data. Since then, Olson and Hill [23] have developed Z(a) for the compact specimen (C(T)) with deformation measured by BFS. Therefore, the OLCC Z(a) method can be used to compute $K_{res}(a)$ from Equation (3.1) with Z(a) from [23] and the derivative of residual strain with respect to crack size ($d\varepsilon_{res}(a)/da$) computed as described for the OLCC derivative ratio method (i.e., using the incremental polynomial method over 2N+1

data points). This approach, like the OLCC derivative ratio method described previously, assumes that the residual stress fields vary smoothly and continuously; if steep gradients of residual stress are present, use of incremental polynomial smoothing may lead to errors.

Estimation of Noise in Data Reduction Methods

Noise about a typically smooth $K_{res}(a)$ profile is expected for OLCC because the data analysis involves derivative estimation, either directly or by ratios of deformation changes, from noisy signals (measured residual strain, $\varepsilon_{res}(a)$, and measured reference strain, $\varepsilon_{ref}(a)$) with respect to crack size. As such, a robust OLCC data analysis method should limit the effects of experimental noise on computed values of K_{res}. For the OLCC central difference ratio, noise can be reduced by increasing *m*, thereby providing larger values of $\Delta\varepsilon_{res}$ and $\Delta\varepsilon_{max,app}$. Similarly, for the OLCC derivative ratio or OLCC Z(a) methods, noise can be reduced by increasing the value of N so that each value of K_{res} is found from a larger set of strain data.

To compare the noise in the calculated values of K_{res} determined by each OLCC data analysis method, compliance data were examined for a representative FCGR test performed under constant ΔK_{app}. The standard error about the trend of $K_{res}(a)$ provides a metric of noise in the data, and was computed for a range of values of *m* and N from 2 to 30 using (from [25]):

$$K_{res(noise)} = \sqrt{\sum_{j=1}^{i-3} \frac{(K_{res(j)} - 3K_{res(j+2)} - K_{res(j+3)})^2}{20(i-3)}} \tag{3.10}$$

where *i* is the total number of crack size increments at which $K_{res}(a)$ is computed. A plot of noise as a function of *m* or N for $K_{res}(a)$ determined by the OLCC central difference ratio, the OLCC derivative ratio, and OLCC Z(a) informs a comparison of these three methods.

3.2.3. Fatigue Crack Growth Rate Testing

A total of four specimens was used for FCGR testing at each residual stress state examined in this study. In addition to the secondary specimens used for slitting tests (described below), two specimens from each stress state were fatigue tested at a constant applied ΔK (ΔK_{app}). Then, the remaining specimens were tested under decreasing ΔK_{app}, increasing ΔK_{app}, or constant load amplitude. The FCGR tests were performed in lab air as described in ASTM E647 [24] at 15 Hz with an applied stress intensity factor ratio ($R_{app} = K_{min,app}/K_{max,app}$) of 0.1 on an Instron 1321 servohydraulic load frame. Prior to testing, specimens were notched via wire EDM and precracked to a/W of approximately 0.25 using a software-controlled load shedding methodology. The final K_{max} of the precrack was less than the K_{max} at the start of the fatigue test in accordance with ASTM E647 [24]. Constant ΔK_{app} tests were programmed for execution at K_{max} of 13.2 MPa·m$^{0.5}$ and decreasing ΔK_{app} tests were programmed to start at K_{max} of 15.4 MPa·m$^{0.5}$ with a load shedding constant (*C*) equal to -0.08 mm^{-1}. Two different increasing ΔK_{app} tests were performed: one at a constant applied load amplitude of 3780 N (starting K_{max} = 12.1 MPa·m$^{0.5}$) and the other with a load increasing constant (*C*) equal to +0.04 mm^{-1} and a starting K_{max} of 11.6 MPa·m$^{0.5}$.

An MTS TestStar II control system was modified to accept back-face strain (BFS) for the compliance method of crack size monitoring. A Micro-Measurements CEA-13-062UWA-350 strain gage (gage length of 1.57 mm) was centered on the crack plane on the back face of each C(T) specimen and strains were monitored using a Vishay Instruments P3500 strain indicator with an analog output fed to the MTS controller as a calibrated input. Load versus BFS data were recorded and indexed. Each compliance data set contains 500 data points from three consecutive cycles and represents an averaged compliance for each crack size. The compliance data sets were saved at crack growth increments of Δa = 0.051 mm for post-test analysis in MATLAB [26]. The

inverse of the slope of the linear region found through least squares linear regression analysis of stored compliance data was used to calculate crack size, a, during post-test analysis. Calculated values of crack size were then compared to those determined by the MTS 790.40 fatigue crack growth software during FCGR testing for control of applied load for tests under K control.

3.2.4. Material and Specimens

Material

For this study, material with a well-controlled residual stress state was required. As such, aircraft aluminum alloy thick plate was chosen, from which quenched bars were made. Quench-induced residual stress in AA 7050-T74 (non-stress relieved) bars is known to be large and repeatable with a nearly symmetric parabolic distribution of stress acting along the bar length, that is tensile in the center and compressive near the edges [1, 27, 28]. In this study, bars were cut from a large section of 102 mm thick AA 7050-T7451 rolled plate, where the -51 suffix indicates stress relief by stretching following heat treatment and quench. Bars were cut with dimensions 310 mm (rolling direction, L) x 76.2 mm (long transverse, LT) x 102 mm (short transverse, ST) as shown in **Figure 3.3**(a). To introduce residual stress, the T7451 bars were reprocessed to T74 temper by solution heat treatment at 750 K, followed by immersion water quenching and artificial aging to the T74 condition, and then used without stress relief. Replicate quenched bars were used in a related study of residual stress and its effects on fatigue crack growth behavior and model-based prediction [29].

Table 3.1 provides mechanical properties for the AA 7050-T7451 starting material, as provided in the certificate of conformance, as well as those of AA 7050-T74, as reported in the ASM Handbook [30].

Table 3.1: Mechanical Properties for AA 7050

	Elastic Modulus	Poisson's Ratio	Yield Strength (σ_y)	UTS (σ_u)
AA 7050-T7451	71,000 MPa	0.33	450 MPa	520 MPa
AA 7050-T74	71,000 MPa	0.33	414 MPa	483 MPa

Fatigue crack growth rate test specimens were extracted from two nominally identical blocks cut from one 7050-T74 bar, referred to as Block 1 (B1) and Block 2 (B2). The blocks had dimension 79.4 mm (L) x 76.2 mm (LT) x 102 mm (ST) and were oriented in the bar as shown in **Figure 3.3**(a). A total of 20 compact (C(T)) specimens, 10 from each block, were extracted symmetrically with respect to the block mid-line to mirror the symmetry of the expected parabolic residual stress field (**Figure 3.3**(b)).

The specimens were machined so that the applied loading direction was along the rolling (L) direction of the parent plate and crack growth occurred along the long transverse (LT) direction, which ASTM E1823 defines as the L-T sample orientation [31]. Specimen dimensions of width (W) 61 mm and thickness (B) 6.35 mm are illustrated in **Figure 3.3**(c). The loading holes of the C(T) specimens accommodated readily available load frame clevises, and as such were slightly smaller than the ASTM recommended diameter of 0.25W. Specimen positions were numbered 1 through 10 from top to bottom of each block. Specimens extracted at increasing distances from the mid-line are expected to have decreasing magnitudes of residual stress. Positions 1 and 10 are referred to as the low (L) residual stress state, positions 3 and 8 are referred to as the medium (M) stress state, positions 2 and 9 as the second medium (M2) stress state, and positions 5 and 6 as the high state (H). Therefore, the specimen from Block 1 at position 1 is expected to have the low stress state and is denoted as B1-1 (L). Specimen positions from each

block for the purpose of this study are shown in **Figure 3.3**(b) (unlabeled positions were not tested).

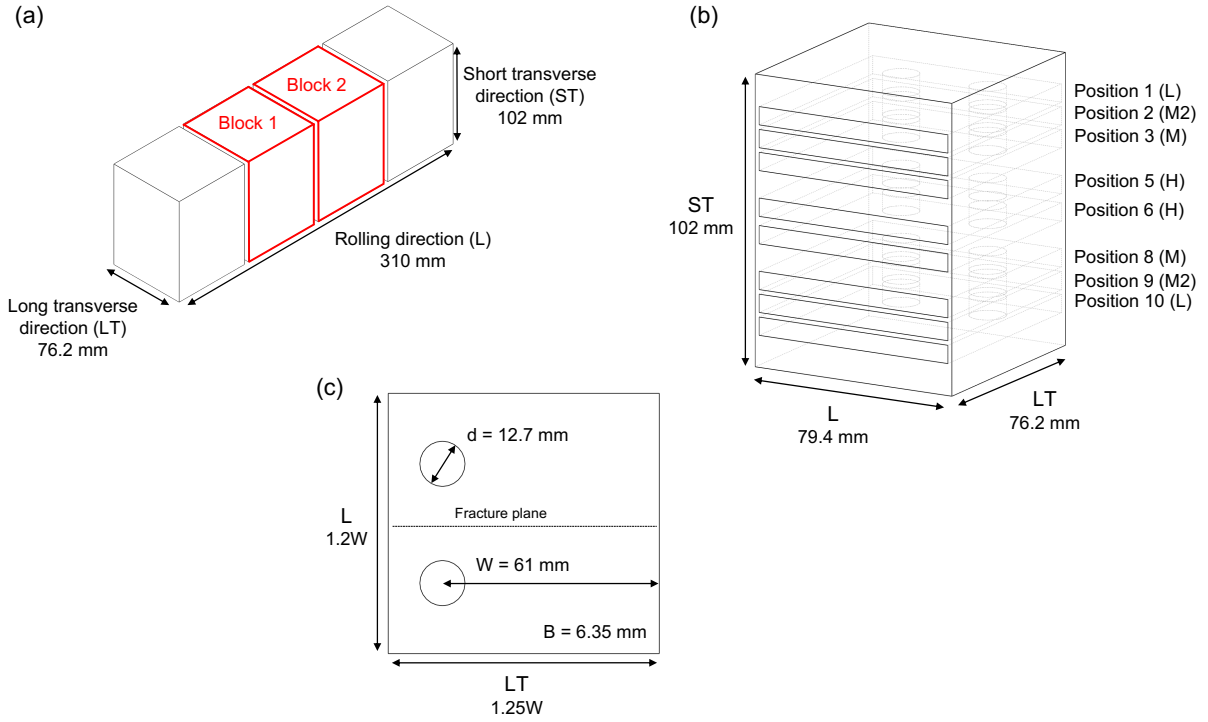

***Figure 3.3**: (a) Bar geometry with extraction of Block 1 (B1) and Block 2 (B2), (b) Block geometry with extraction of specimens and positions labeled, and (c) C(T) specimen geometry.*

Slitting Details for C(T) Geometry

K_{res} was measured in several specimens by the slitting method. The slit was cut in 50 equal cut depth increments, each 1.45 mm, to a final cut depth of about 95% of the total specimen width (95% of 1.25W). BFS data were collected after each cut depth increment using a strain gage applied at the back face (at x = 1.25W) of the crack plane and centered on the specimen thickness. The strain gage was of the same type as those used in the FCGR tests (gage length of 1.57 mm). Strain versus cut depth data were used to determine residual stress as a function of distance from the front face, x, using an inverse analysis described previously [19]. $K_{res}(a)$ was determined using Equation (3.1), where the derivative of strain with respect to cut depth was determined using the

incremental polynomial method, as described earlier for OLCC, with N = 2. Slitting provides values of K_{res} for all crack sizes starting from the front face of the specimen. For the C(T) geometry, it is typically assumed that a = 0 at the loading holes (x = 0.25W). Therefore, slitting provides K_{res} in the C(T) starting at negative values of crack size and may provide a non-zero value when a = 0 (**Figure 3.4**).

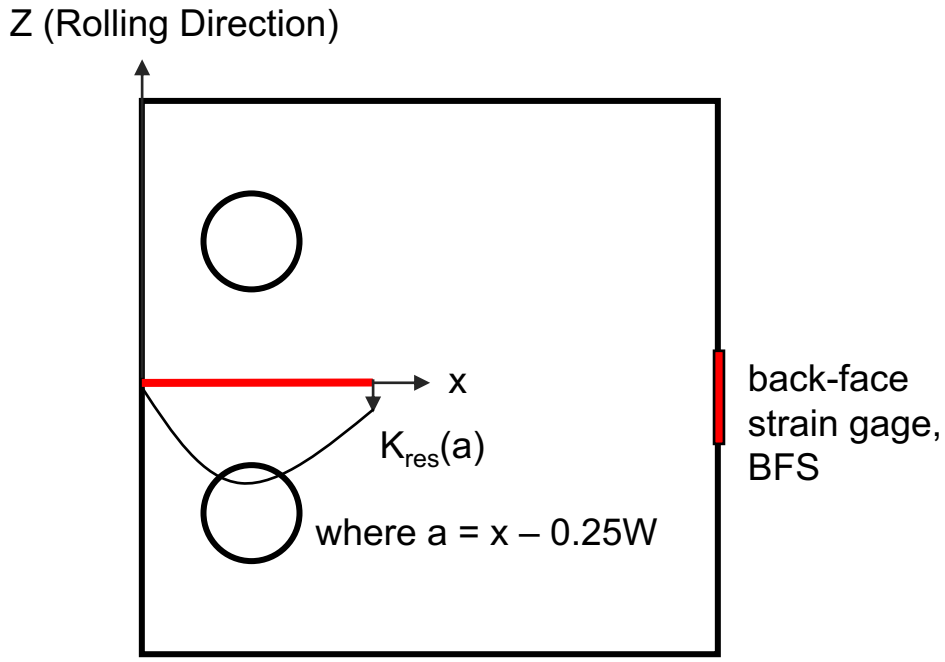

***Figure 3.4**: Schematic of slitting method for the determination of K_{res} as a function of cut depth ($K_{res}(a)$) using back-face strain (BFS).*

Specimen Designations

Results for K_{res} from slitting and OLCC are compared to validate OLCC and to assess the various data analysis methods. The OLCC method was explored in FCGR tests under a range of loading conditions, including constant applied load amplitude, constant ΔK_{app}, and with ΔK_{app} gradients. Specimen designations for slitting and OLCC measurements can be found for reference in **Table 3.2** along with a description of their test type.

Table 3.2: Specimen designations for validation of OLCC

Specimen Name	Test Type	Specimen Name	Test Type
B1-1 (L)	slitting Δa = 1.45 mm (a_{final} = 57.2 mm)	**B2-1 (L)**	ΔK_{app} = 12 MPa·$m^{0.5}$ (a_{final} = 47.9 mm)
B1-2 (M2)	ΔK_{app} = 12 MPa·$m^{0.5}$ (a_{final} = 45.8 mm)	**B2-2 (M2)**	ΔK_{app} = 12 MPa·$m^{0.5}$ (a_{final} = 46.2 mm)
B1-3 (M)	slitting Δa = 1.45 mm (a_{final} = 57.2 mm)	**B2-3 (M)**	ΔK_{app} = 12 MPa·$m^{0.5}$ (a_{final} = 48.1 mm)
B1-5 (H)	slitting Δa = 1.45 mm (a_{final} = 57.2 mm)	**B2-5 (H)**	N/A
B1-6 (H)	ΔK_{app} = 12 MPa·$m^{0.5}$ (a_{final} = 45.2 mm)	**B2-6 (H)**	slitting Δa = 1.45 mm (a_{final} = 57.2 mm)
B1-8 (M)	ΔK_{app} = 12 MPa·$m^{0.5}$ (a_{final} = 48.6 mm)	**B2-8 (M)**	decreasing ΔK_{app} (a_{final} = 32.9 mm)
B1-9 (M2)	increasing ΔK_{app}: P_{max} = 3780 N (a_{final} = 39.8 mm)	**B2-9 (M2)**	increasing ΔK_{app}: C = +0.04 mm^{-1} (a_{final} = 40.8 mm)
B1-10 (L)	ΔK_{app} = 12 MPa·$m^{0.5}$ (a_{final} = 47.6 mm)	**B2-10 (L)**	decreasing ΔK_{app} (a_{final} = 31.1 mm)

3.3. Results and Discussion

3.3.1. Slitting Measurements

The results shown in **Figure 3.5**(a) and **Figure 3.5**(b) confirm the consistency of residual stress and K_{res}, respectively, between the two different AA7050-T74 blocks and relative to the anticipated symmetry about the block mid-line with specimen position. The residual stress fields of specimens B1-5 (H) and B2-6 (H) are nominally the same, so the two blocks are considered identical. The asymmetry of residual stress with respect to x is attributed to the release of residual

stress when the loading holes were machined. Furthermore, specimens extracted from positions adjacent to the mid-line contain the largest magnitudes of residual stress (B1-5 (H) and B2-6 (H)), and the magnitudes decrease as the specimen extraction position moves away from the mid-line, as seen in B1-3 (M) and B1-1 (L) of **Figure 3.5**(a). The large magnitude of compressive residual stress at the front face of B1-5 (H) and B2-6 (H) is consistent with large negative values of K_{res} that become less negative (decrease in magnitude) as crack size increases. Even small changes in the residual stress profiles of (**Figure 3.5**(a)) result in noticeable differences in the K_{res} profiles ((**Figure 3.5**(b)). This is evident in the middle stress state (position 3 and by symmetry, position 8), which has a small difference in residual stress as compared to positions 5 and 6, but a more noticeable difference in K_{res}. The low stress state removed furthest from the center of the block (position 1 and by symmetry, position 10) has a smaller magnitude of residual stress and significantly smaller K_{res} as compared to specimens from the other positions. Overall, the slitting results of secondary specimens verified the expected residual stress trends in the material.

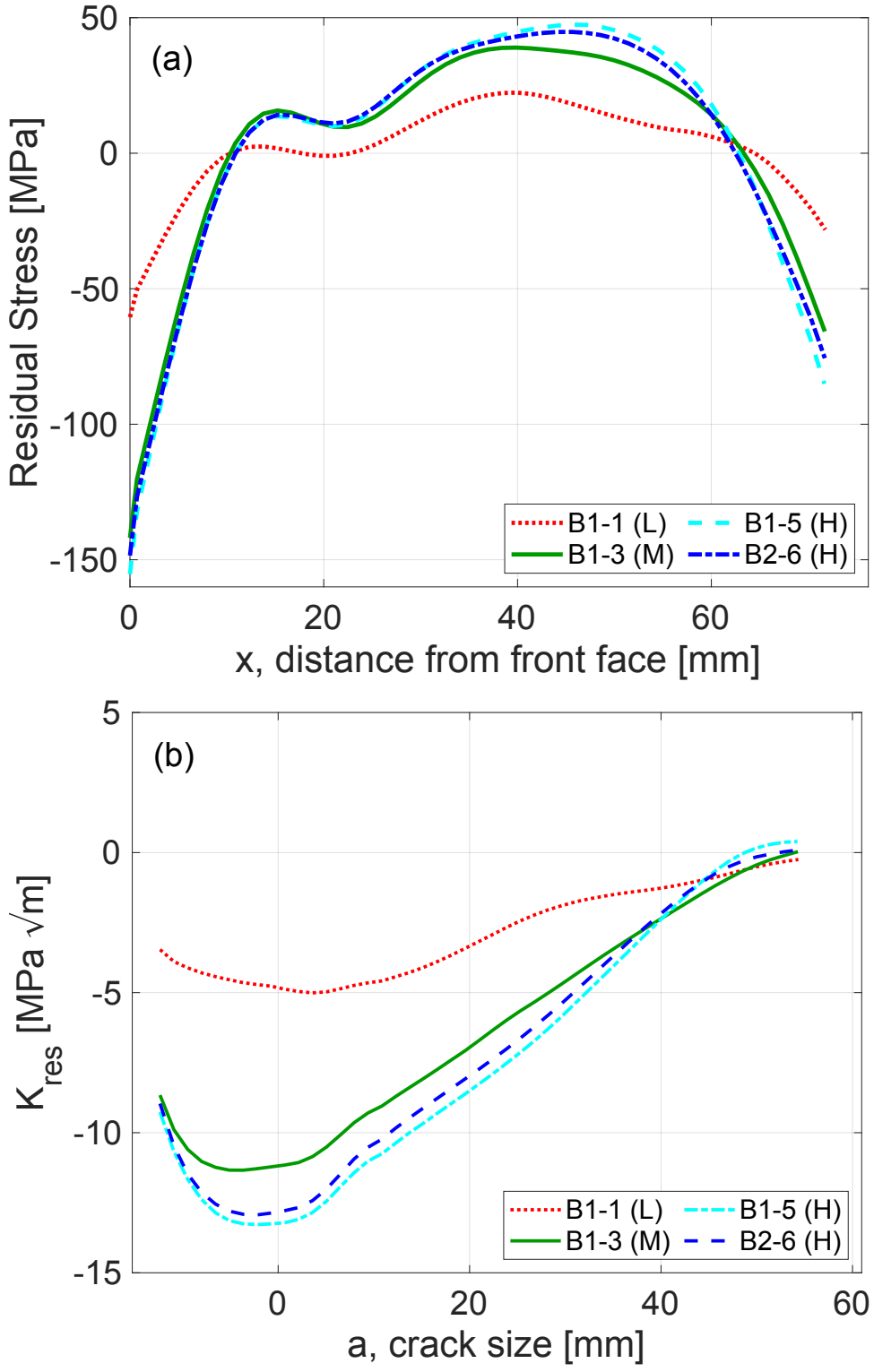

***Figure 3.5**:Comparing (a) Residual stress profiles and (b) K_{res} profiles from slitting of specimens B1-1 (L), B1-3 (M), B1-5 (H), and B2-6 (H).*

3.3.2 On-line Crack Compliance

Comparison of Methods for Data Reduction

Prior to examination of the OLCC data analysis methods, residual strain data (ε_{res}), measured maximum strains (ε_{max}), and the adjusted maximum strain ($\varepsilon_{max,app}$) data from FCGR testing of specimen B1-8 (M) are compared to strain data from slitting of specimen B1-3 (M) from a position equidistant to the block mid-line (**Figure 3.6**). The OLCC strains, ε_{res} and $\varepsilon_{max,app}$, have opposite trends with crack size, resulting in negative values of the derivative ratio, which is consistent with negative K_{res}. Although residual strain (ε_{res}) measured during slitting and OLCC exhibit similar trends, there is an offset between them due to each having a different zero datum (for slitting, an uncut specimen, and for OLCC, a notched and precracked specimen). The difference in zero datum does not affect values of K_{res}, since only derivatives (slopes) are used in their computation.

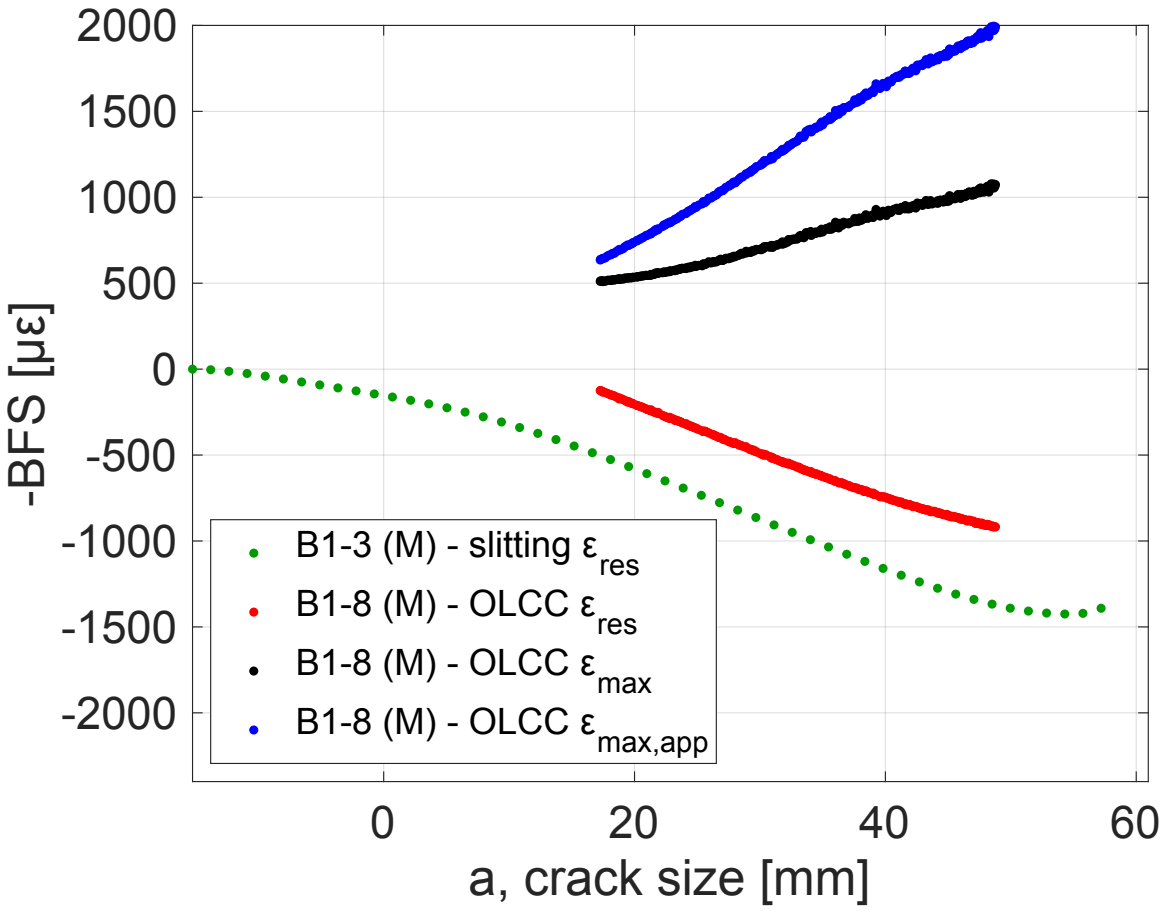

***Figure 3.6**: Comparison of BFS from slitting for B1-3 (M) slitting and OLCC for B1-8 (M).*

Figure 3.7 compares K_{res} determined by slitting in specimen B1-3 (M) to that determined by the OLCC difference ratio method in specimen B1-8 (M), which was tested under constant ΔK_{app} conditions ($P_{max}(a_i)$ decreases as a_i increases). **Figure 3.7**(a) and **Figure 3.7**(b) compare results for the backward difference and central difference over two different increments of crack growth. For the central difference, the difference is taken between crack sizes a_{i+m} and a_{i-m} to find $K_{res}(a_i)$. For the backward difference, the difference is taken between crack sizes a_i and a_{i-2m}. Thus, the two figures reflect deformation changes over crack size increments Δa = 0.56 mm (**Figure 3.7**(a)) and Δa = 1.6 mm (**Figure 3.7**(b)). These results demonstrate that K_{res} from the OLCC difference ratio agrees with the trend from slitting the specimen of the same residual stress state. They further highlight the value of taking the difference over a larger range of crack size, with

OLCC results of **Figure 3.7**(b) exhibiting much smoother trends than those in **Figure 3.7**(a). **Figure 3.7** shows that the backward difference causes a shift in K_{res} to lower (more negative) values at high *m* relative to K_{res} from slitting. The shift increases as *m* increases, indicating a systematic error that is associated with the backward difference data reduction. The central difference does not exhibit a similar error and is therefore preferable.

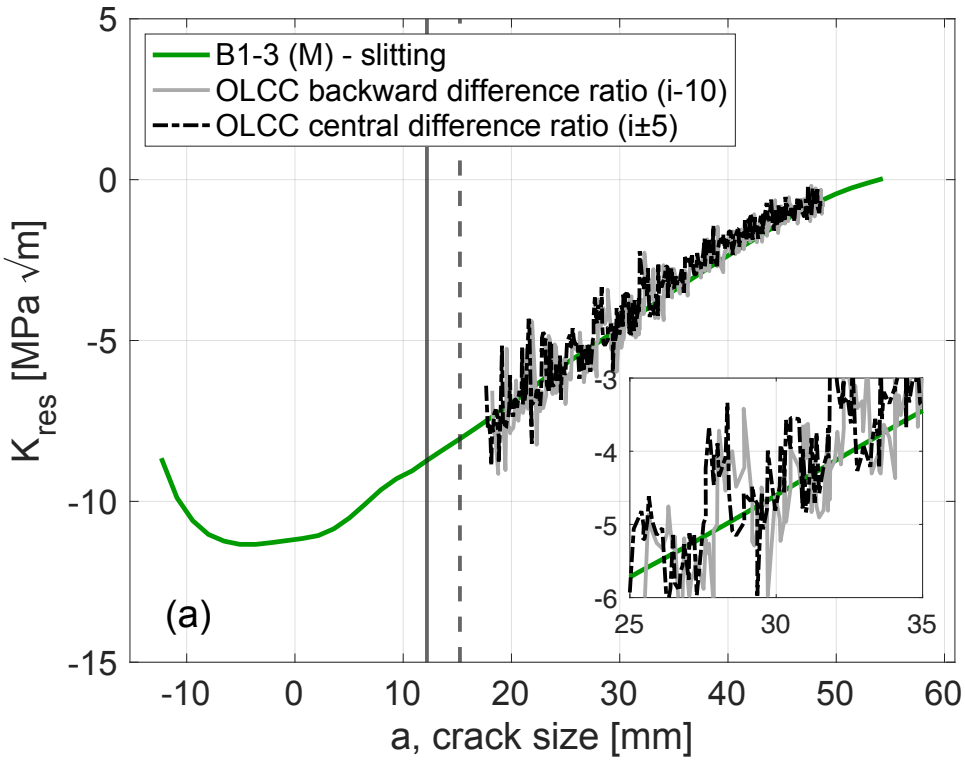

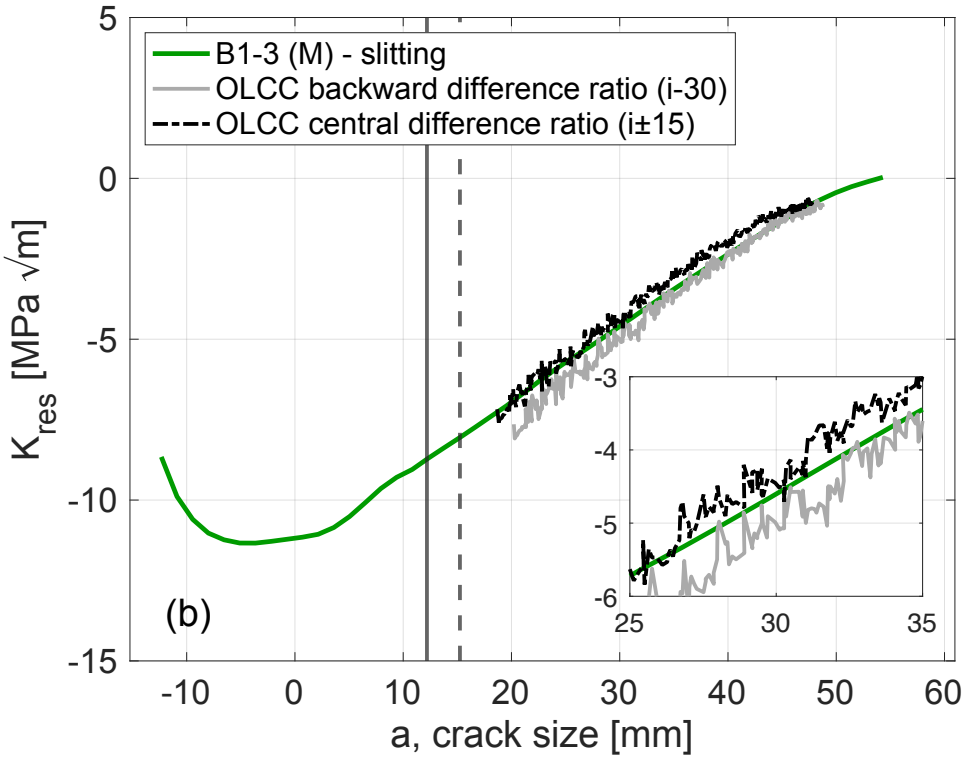

***Figure 3.7**: Comparing backward difference and central difference for the OLCC difference ratio method in specimen B1-8 (M) for values of m representing similar increments of crack size (a) i–10 and i±5 (Δa = 0.56 mm) and (b) i–30 and i±15 (Δa = 1.6 mm).*

Figure 3.8 shows noise in K_{res} (from Equation (3.10)) for the three OLCC data analysis methods over a range of *m* and N, each applied to data from specimen B1-8 (M). Noise decreases monotonically with *m* and N, with small values leading to high levels of noise in the K_{res}(a) profile. **Figure 3.8** further shows that the K_{res}(a) profile from the OLCC difference ratio method has far greater noise than the profiles from the OLCC derivative ratio or OLCC Z(a) methods, the latter two exhibiting nearly identical noise levels. This result indicates that the incremental polynomial method provides derivative estimates (used to compute K_{res}) that are more robust to noise than those obtained by a difference ratio. As seen in **Figure 3.8**, at a value of 10 (where 2N +1 and 2*m* + 1 correspond to Δa of 1.07 mm) noise levels for the OLCC Z(a) and derivative ratio methods are less than 0.04 MPa·$m^{0.5}$, which seems a suitable precision for K_{res} values. Furthermore, minimizing N or *m* allows determination of K_{res} over a larger range of crack size (because estimating $K_{res}(a_i)$

requires truncating data of m or N points at each end of the data set). In this work, a value of m = N = 10 is used to process the data from all tests, taken as an appropriate trade-off between minimizing noise and limiting truncation at both ends of the data sets.

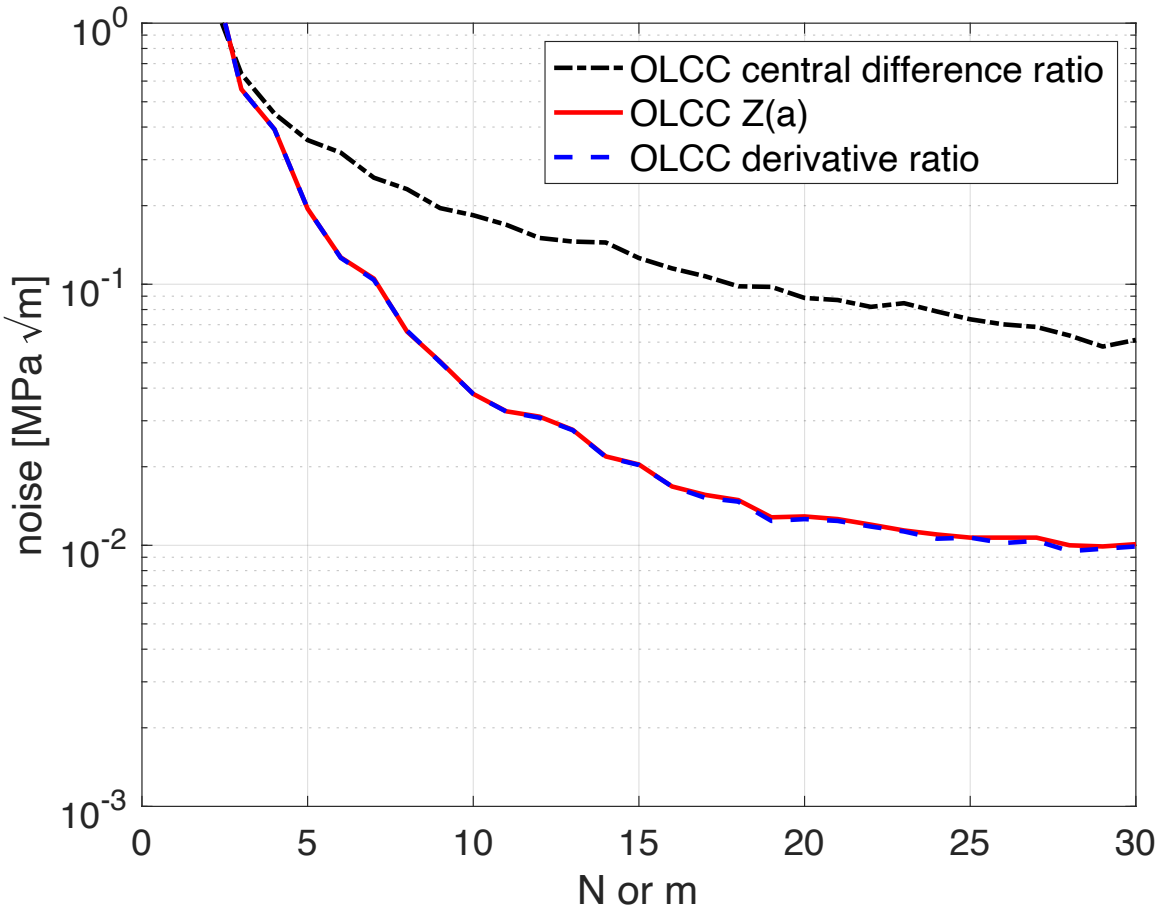

***Figure 3.8**: Noise from K_{res} data analysis using OLCC Z(a) [12], OLCC central difference ratio [14, 15], and OLCC derivative ratio methods for a constant ΔK_{app} test of specimen B1-8 (M).*

A comparison of K_{res} as determined by the three OLCC data analysis methods (with N = *m* = 10) for specimen B1-8 (M) and by slitting for specimen B1-3 (M) is shown in **Figure 3.9**. The K_{res} profiles from the OLCC Z(a) and the OLCC derivative ratio methods are indistinguishable and agree very closely with results from slitting (green line). Since the OLCC method is derived from Schindler's technique for calculating K_{res}, similarity between results of the methods is expected. Furthermore, the inset of **Figure 3.9** shows a higher level of noise from the OLCC

central difference ratio, as expected from **Figure 3.8**, but that the overall trends in K_{res} are similar for the three OLCC data analysis methods. The results of **Figure 3.9** are representative of data analyses for all tests performed in this work; the results that follow employ only the OLCC Z(a) method (with N = 10), which was selected because it relies on only a single set of experimental strain data (ε_{res}).

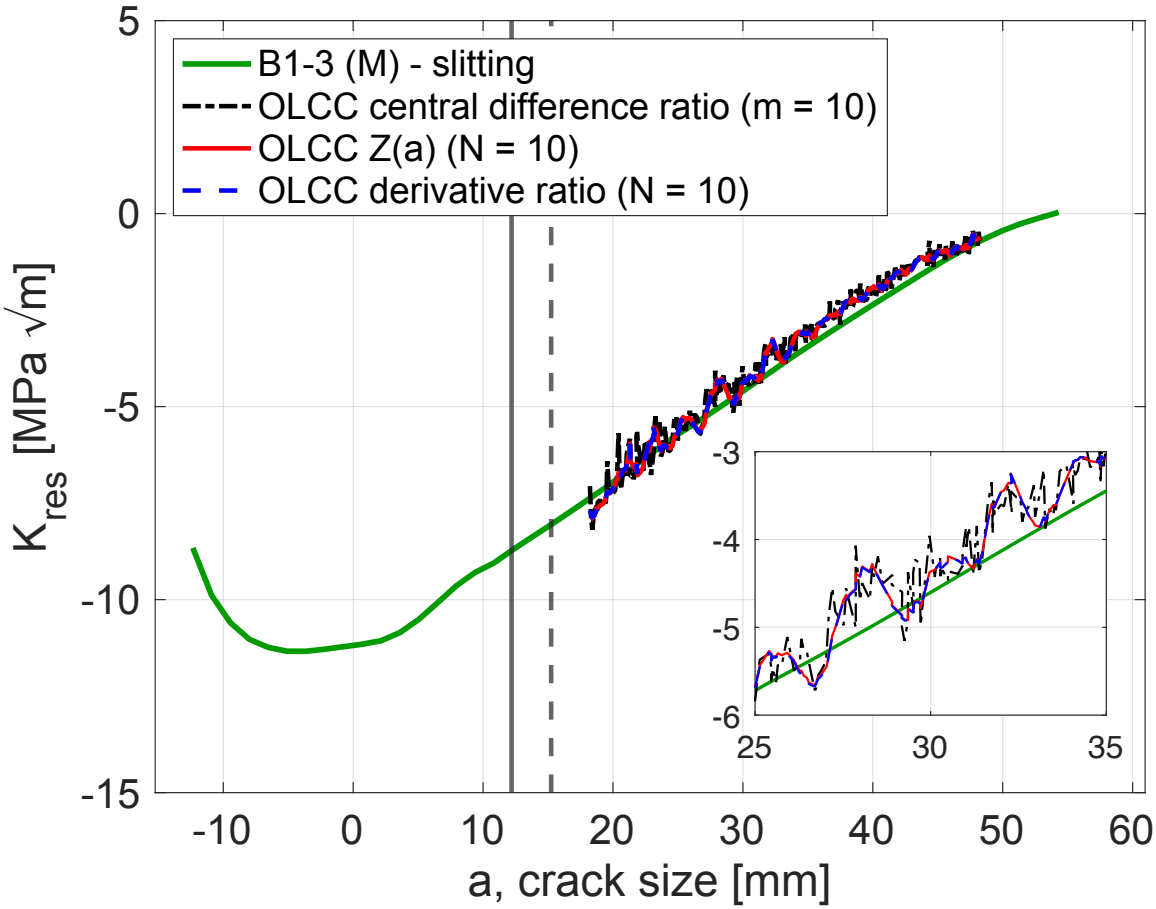

***Figure 3.9**: K_{res} from the three OLCC data analysis methods in specimen B1-8 (M) with data reduction over Δa = 1.07 mm (m = N = 10).*

OLCC K_{res} Results from FCGR Test Data

Figure 3.10 shows K_{res} from constant and decreasing ΔK_{app} fatigue tests of the low (L), middle (M), and high (H) stress state specimens compared to K_{res} from slitting of companion specimens. The location of the notch tip (solid vertical line) and the end of the precrack (dotted

vertical line) are indicated. For these K-control tests, a range of 40% to 90% of P_{max} was used by the FCGR test control software to determine crack size from compliance data, and then determine the appropriate applied load levels. For the low stress state (**Figure 3.10**(a)), the data for B1-1 (L) and B2-1 (L) demonstrate excellent agreement in K_{res} profiles from slitting and OLCC methods. The K_{res} values in sample B1-10 (L) are smaller (less negative) than those in the other two specimens, which is attributed to a slight asymmetry of residual stress in specimens removed farthest from the block mid-line. Results from B2-10 (L), tested under decreasing ΔK_{app}, agree but have fluctuations of about ± 1 MPa·$m^{0.5}$. For the medium stress state, both OLCC K_{res} results from B2-3 (M) and B1-8 (M) show very good agreement with the slitting results from specimen B1-3 (M) (**Figure 3.10**(b)); both samples were tested under constant ΔK_{app}. On the other hand, OLCC K_{res} results from B2-8 (M), tested under decreasing ΔK_{app}, show initial agreement with slitting but then some divergence (of about 1.8 MPa·$m^{0.5}$) at the longest crack size. The OLCC K_{res} profile from the high stress state specimen B1-6 (H) (**Figure 3.10**(c)), tested under constant ΔK_{app}, shows some differences with the slitting results of specimens B1-5 (H) and B2-6 (H), which agree well with each other. In B1-6 (H), the starting K_{res} at the initial crack size (about -10 MPa·$m^{0.5}$) is close to the ΔK_{app} of 12 MPa·$m^{0.5}$. The resulting crack path deviated from the crack plane by 29 degrees, thereby invalidating the FCGR data. When the compliance data were analyzed using the OLCC Z(a) method, a reasonable estimate of K_{res} in B1-6 (H) was obtained, indicating that the OLCC method can provide useful values of K_{res} even for a skewed crack path (no longer a symmetric geometry or solely Mode I crack growth).

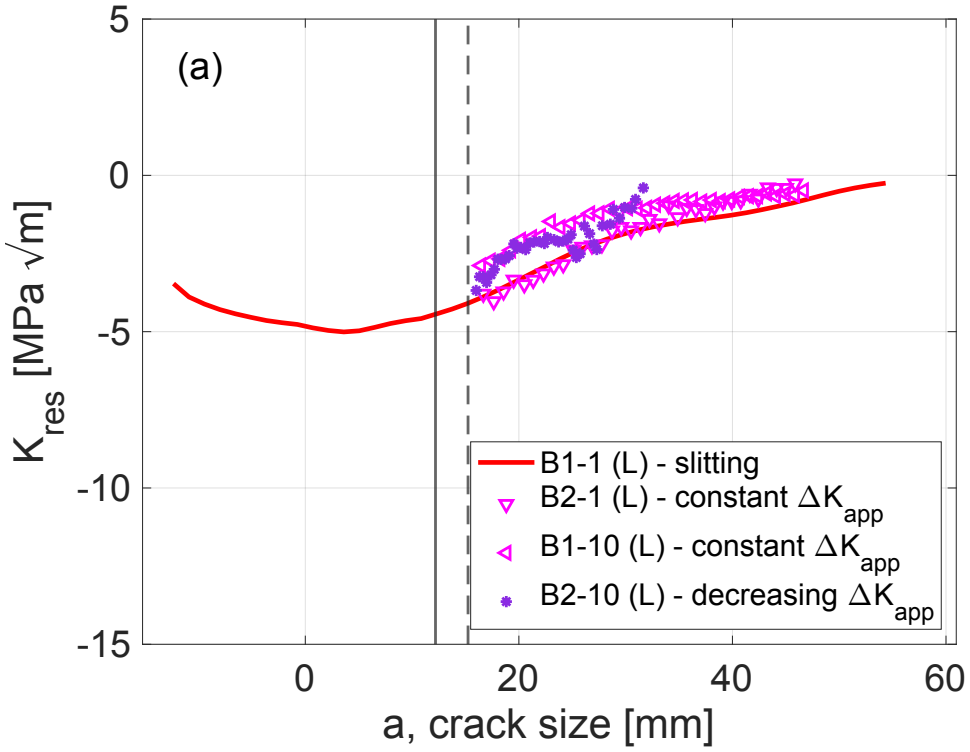
(a)
5
0
-5
-10
-15
0
20
40
60
K_res [MPa √m]
a, crack size [mm]
B1-1 (L) - slitting
B2-1 (L) - constant ΔK_app
B1-10 (L) - constant ΔK_app
B2-10 (L) - decreasing ΔK_app

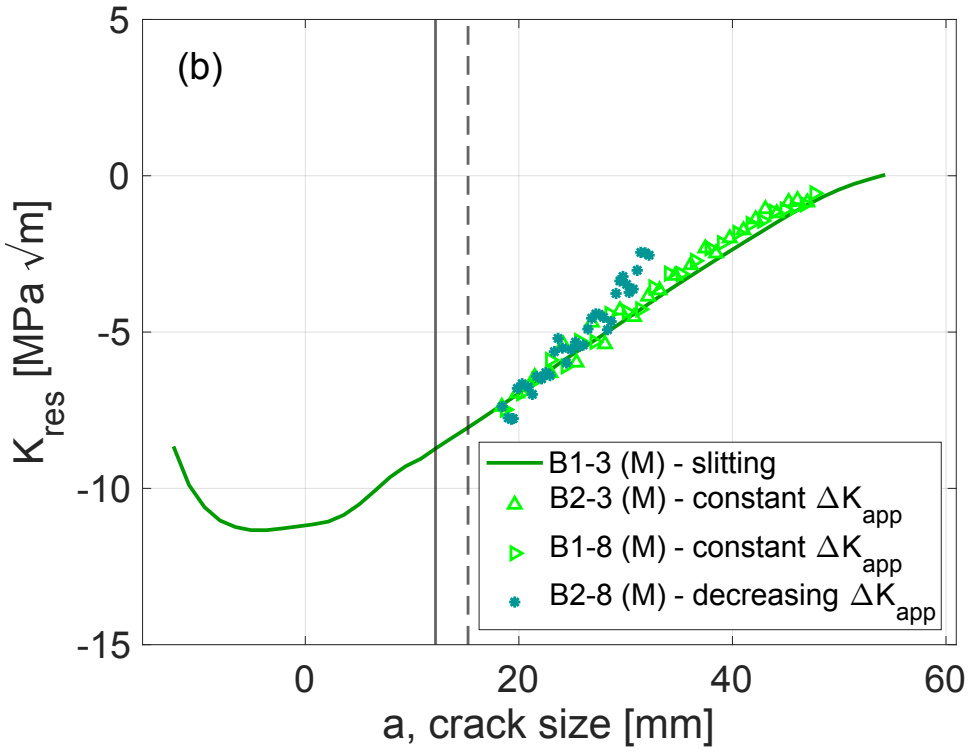
(b)
5
0
-5
-10
-15
0
20
40
60
K_res [MPa √m]
a, crack size [mm]
B1-3 (M) - slitting
B2-3 (M) - constant ΔK_app
B1-8 (M) - constant ΔK_app
B2-8 (M) - decreasing ΔK_app

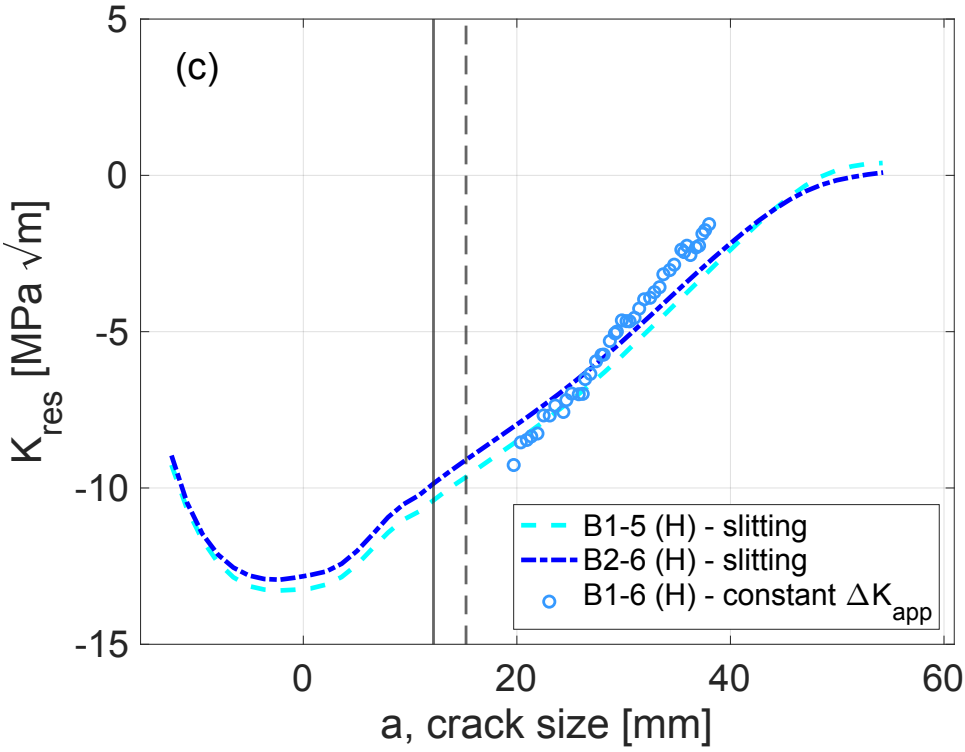

***Figure 3.10**: OLCC K_{res} results for (a) low stress state (b) middle stress state and (c) high stress state.*

Post-test analysis of the compliance data from K control FCGR tests revealed challenges related to test control. **Figure 3.11** shows P_{max} profiles for constant and decreasing ΔK_{app} fatigue tests of the low stress state (L), middle stress state (M), and high stress state (H). The negative K_{res} in the material under evaluation contributed to crack face contact in the crack wake (crack closure) that was far larger than would occur in tests of specimens free of residual stress. As the crack size increased and the loads decreased, P_{open} exceeded the lower limit of 40% of P_{max} used for fitting of the compliance data by the FCGR test control software. This resulted in inaccurate calculated crack size and thus incorrect applied loads during the tests. Post-test analysis of the compliance data made use of a linear fit of the compliance data above P_{open} for crack size determination, which enabled a correct assessment of ΔK_{app} and R_{app} during the test. The dotted lines in **Figure 3.11**(a)

and **Figure 3.11**(b) show the expected load shedding for constant ΔK_{app} at a K_{max} of 13.2 MPa·m$^{0.5}$ and the decreasing ΔK_{app} fatigue tests starting at a K_{max} of 15.4 MPa·m$^{0.5}$ with C = -0.08 mm^{-1}.

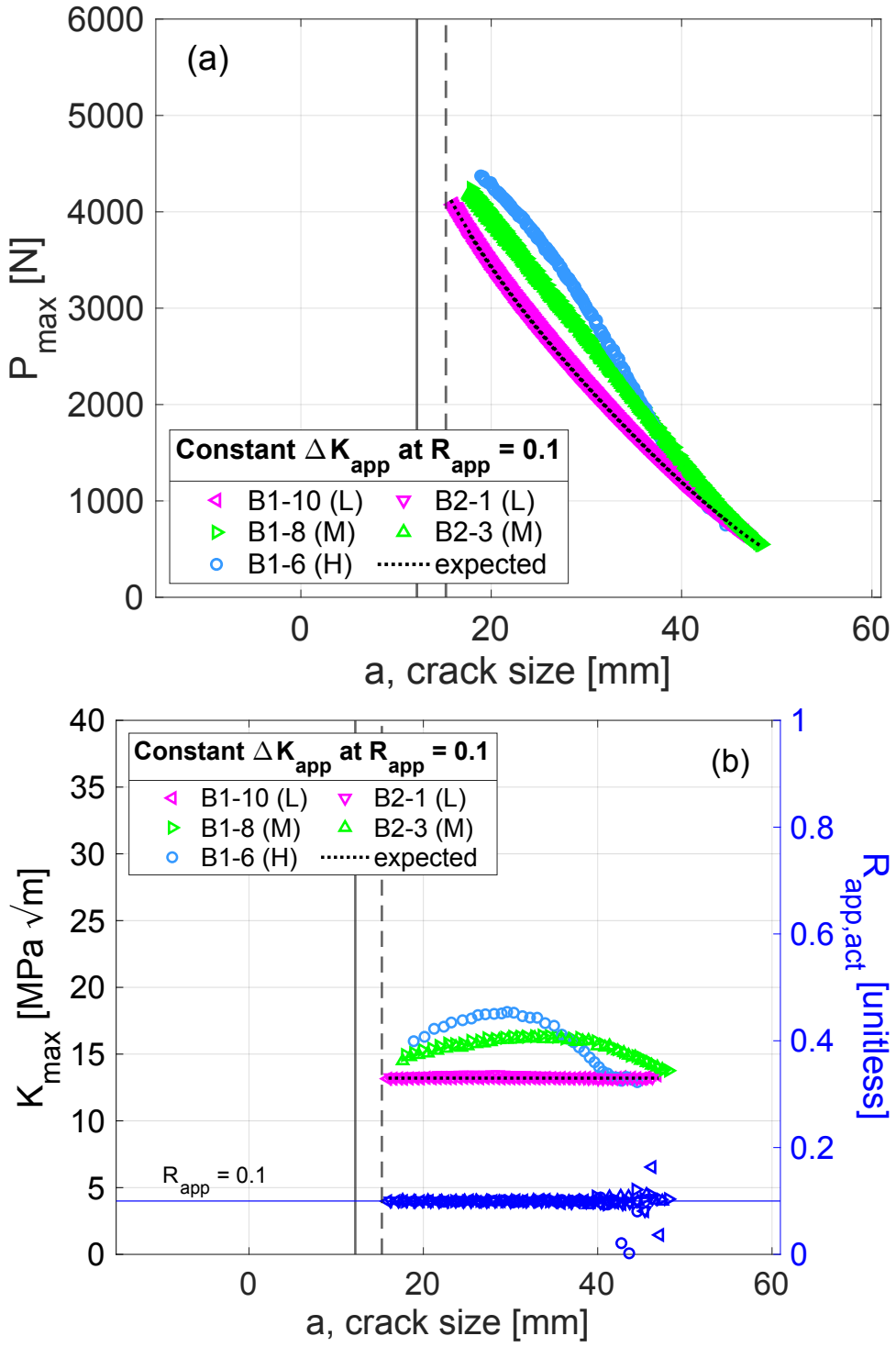

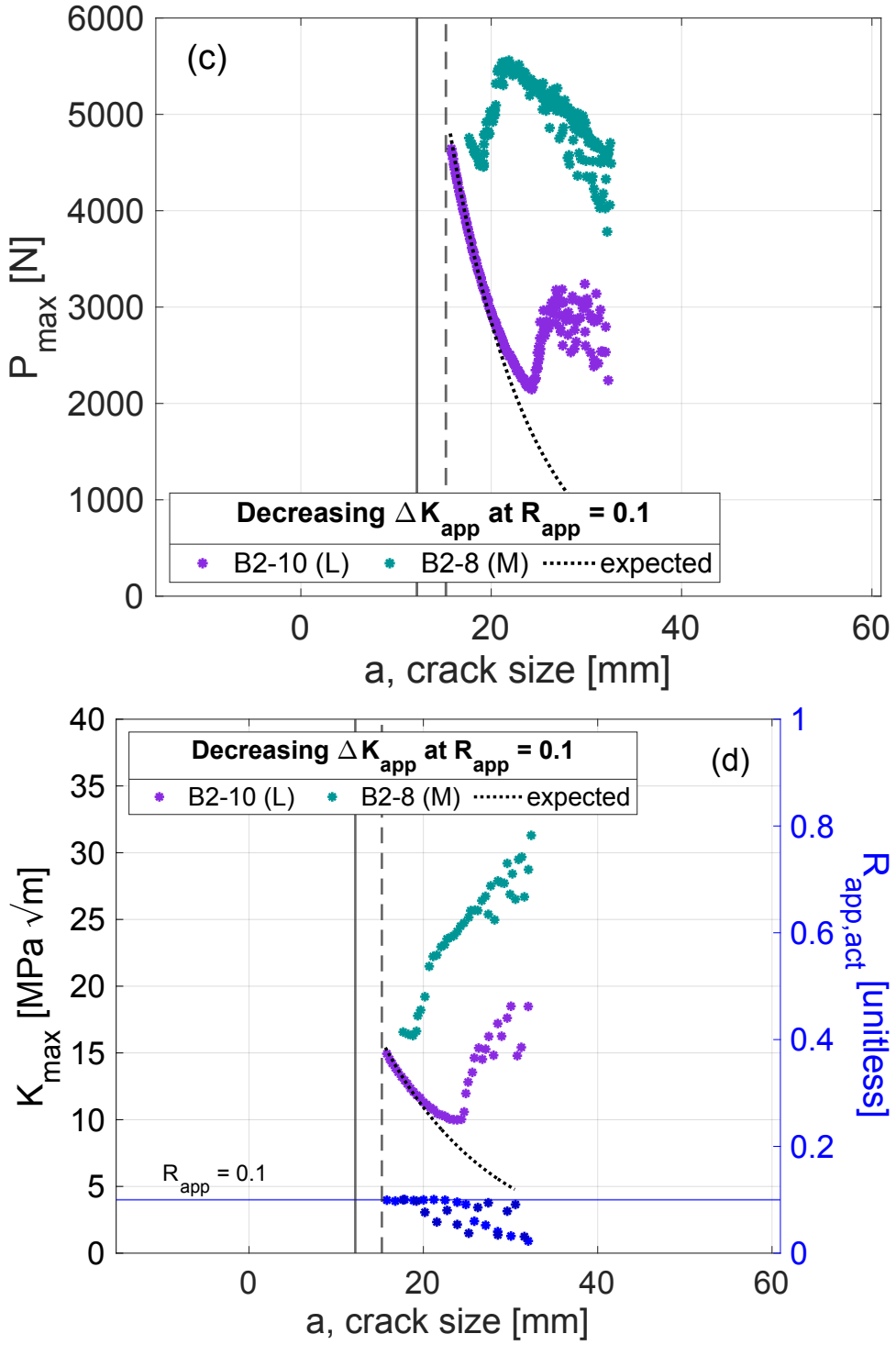

***Figure 3.11**: P_{max} as a function of crack size (a) and K_{max} (left exis) with $R_{app,act}$ (blue markers, right axis) as a function of crack size (b) for constant ΔK_{app} fatigue tests. P_{max} as a function of crack size (c) and K_{max} (left axis) with $R_{app,act}$ (blue markers, right axis) as a function of crack size (d) for decreasing ΔK_{app} fatigue tests showing deviation from expected control in test method.*

As revealed in **Figure 3.11**(a), tests of the middle and high stress state specimens under constant ΔK_{app} did not follow the expected loads at small crack sizes, but as K_{res} decreased in magnitude (and consequently, P_{open} also decreased) the applied loads approached the expected values based on the control parameters. The low stress state specimen followed the expected applied loads throughout the entire FCGR test. Despite deviations in applied load, an evaluation of the actual stress ratio ($R_{app,act}$) revealed the constant ΔK_{app} tests were loaded at the intended R_{app} of 0.1 (**Figure 3.11**(b)). **Figure 3.11**(c) shows that during the decreasing ΔK_{app} tests, the middle stress state specimen never experienced the expected applied loads, and the low stress state specimen had the intended loads up to a crack size of 24 mm. In the case of the decreasing ΔK_{app} tests, the erroneous estimates of crack size during the test led to the application of values of K_{max} and $R_{app,act}$ that were different from those that were intended (**Figure 3.11**(d)).

Despite the unexpected loading, a reasonable estimation of K_{res} is still found in these specimens using the OLCC Z(a) method (**Figure 3.10**(a) and **Figure 3.10**(b)). This outcome can be attributed to the post-test analysis of compliance data in which a linear regression above P_{open} rather than above the fixed 40% of P_{max} is used to determine ε_{res} and an accurate calculation of crack size. Rather than suggesting limitations in the OLCC method, the results of **Figure 3.11** show limitations in the FCGR test procedure and control software. Specifically, to conduct FCGR tests in the presence of a significant compressive residual stress intensity factor, the operator must monitor and adjust, or the software must automatically adjust, the lower limit of the compliance fit region to exclude the influence of crack closure. Preferably, more advanced test control software that could intelligently select and adjust the least squares fit range for linear compliance calculations of crack size would rectify the situation. Subsequent FCGR tests in constant and increasing ΔK_{app} control were conducted for specimens from positions 2 and 9 where crack size

was found from compliance data at high levels of applied load (65% to 95% P_{max}). **Figure 3.12**(a) shows that with this approach the applied P_{max} matched the values expected for the entire FCGR test (**Figure 3.12**(b) shows that K_{max} and $R_{app,act}$ were also as expected).

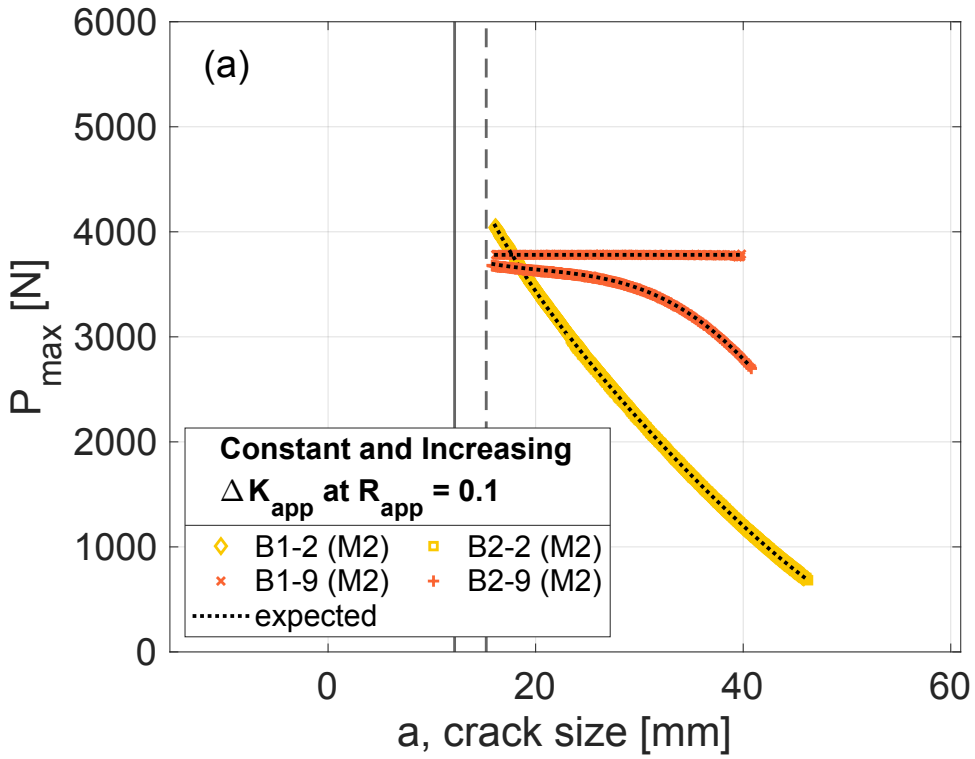

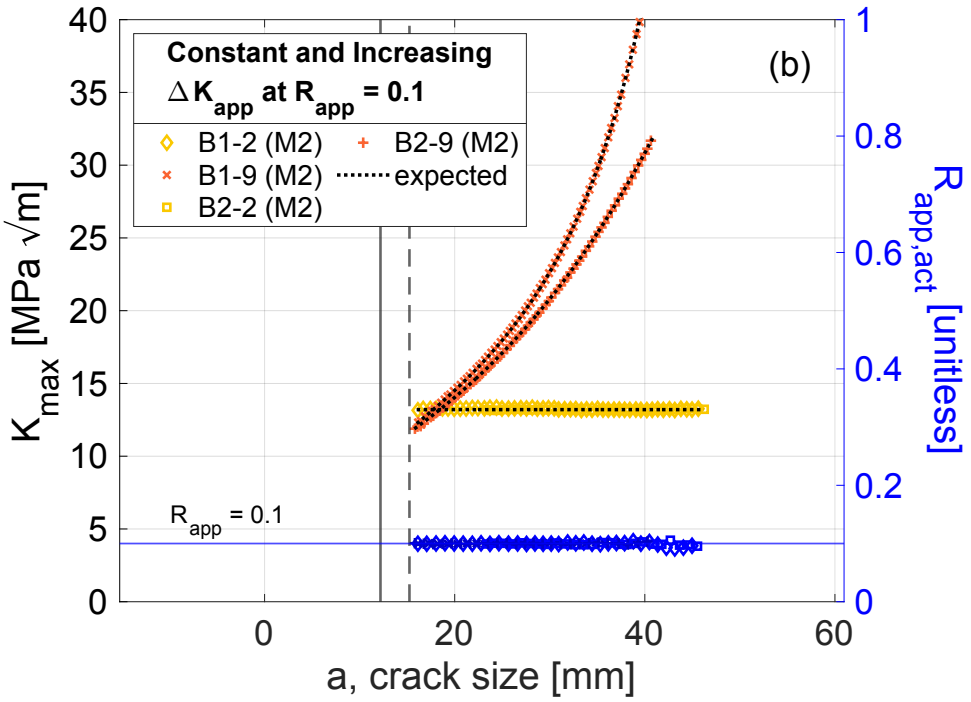

***Figure 3.12**: P_{max} as a function of crack size (a) and K_{max} (left axis) with $R_{app,act}$ (blue markers, right axis) as a function of crack size (b) for constant ΔK_{app} fatigue tests and increasing ΔK_{app} fatigue tests for (M2) stress state demonstrating P_{max} control for the entire crack size.*

Plasticity Effects in OLCC

The K_{res} results from the increasing FCGR tests of positions 2 and 9 are shown in **Figure 3.13**. The specimens of position 2 were tested at a constant ΔK_{app} and the specimens of position 9 at ΔK_{app} increasing conditions. Additionally, a slitting measurement of K_{res} was performed while machining the notch of B1-2 (M2) and B1-9 (M2) to determine K_{res} in the notch plane (left of the solid vertical line indicating the notch tip). In this manner, full K_{res} profiles for B1-2 (M2) and B1-9 (M2) across nearly the entire specimen width were found. The small differences in the notch slitting of B1-2 (M2) and B1-9 (M2) (**Figure 3.13**) supports the earlier result (**Figure 3.10**(a)) of a slight difference in K_{res} of specimens removed at positions far from the block mid-line, but on opposite sides (i.e., specimens 1 and 10, or specimens 2 and 9), where higher numbered positions exhibit lower magnitude K_{res}. The OLCC K_{res} results are consistent with the notch slitting, also reflecting a small difference with specimen extraction location. Data from both the constant ΔK_{app}

specimens of position 2 demonstrate a smooth K_{res} profile for the entirety of the FCGR test and are used as a reference for the data from position 9 specimens. In the case of the increasing ΔK_{app} tests of position 9, the trend in OLCC K_{res} agrees with the expected (position 2) trend, but deviates at large crack sizes.

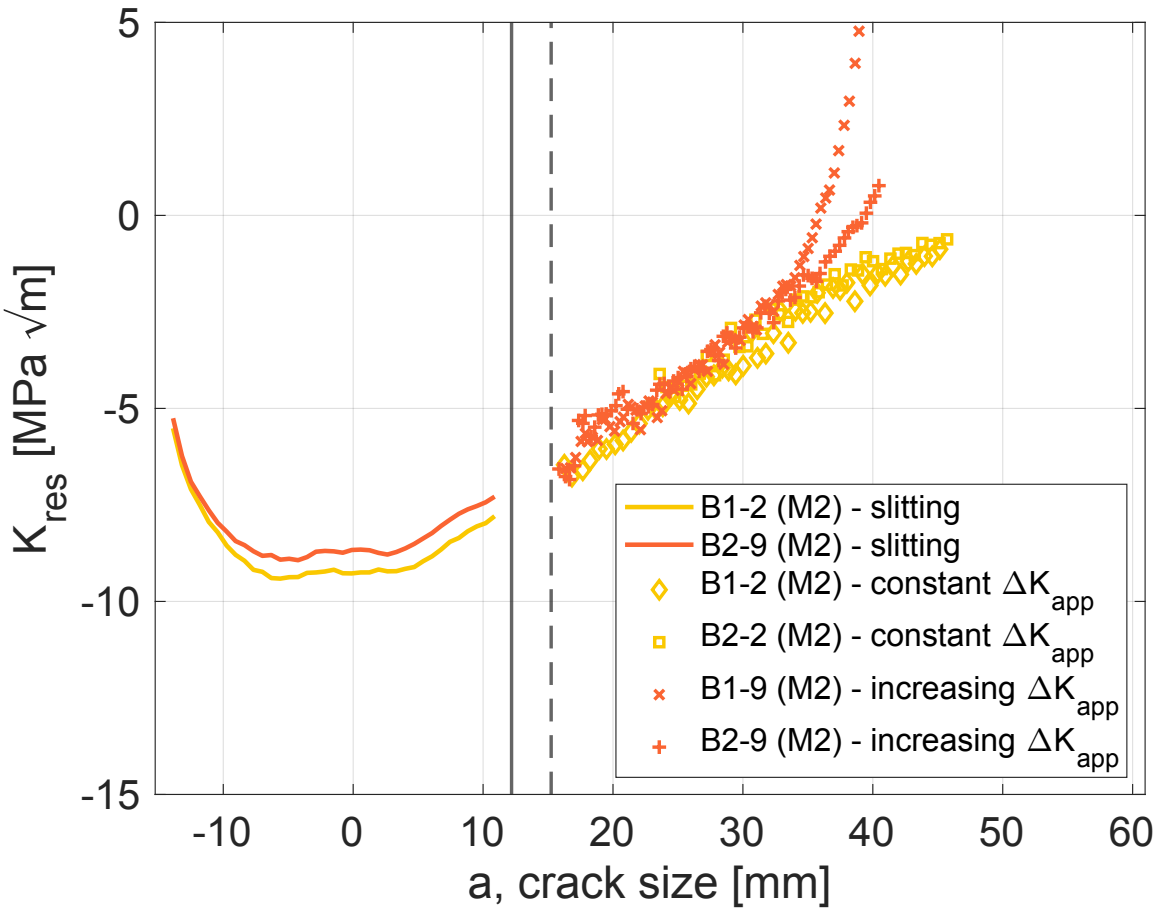

***Figure 3.13**: OLCC K_{res} profiles for constant ΔK_{app} fatigue tests and increasing ΔK_{app} fatigue tests of M2 stress state.*

Previous work has suggested limitations with the OLCC method due to plasticity in the remaining ligament (having size of W-a) [9], and proposed an analysis of the plastic zone size as a function of crack size to assess this effect. The plastic zone size is a function of specimen yield strength and K_{max} (and therefore, crack size and applied load) [32]. **Figure 3.14** illustrates the plastic zone size for plane stress, calculated from the equation inset in **Figure 3.14**, divided by the

size of the remaining ligament ($r_p/(W - a)$) as a function of crack size in the four tests of **Figure 3.13**. The K_{max} at each crack size and the material yield strength of 414 MPa were used for plastic zone size calculations. A reasonable limit for remaining ligament effects is identified when r_p approaches 5% of the remaining ligament (black horizontal line) [33].

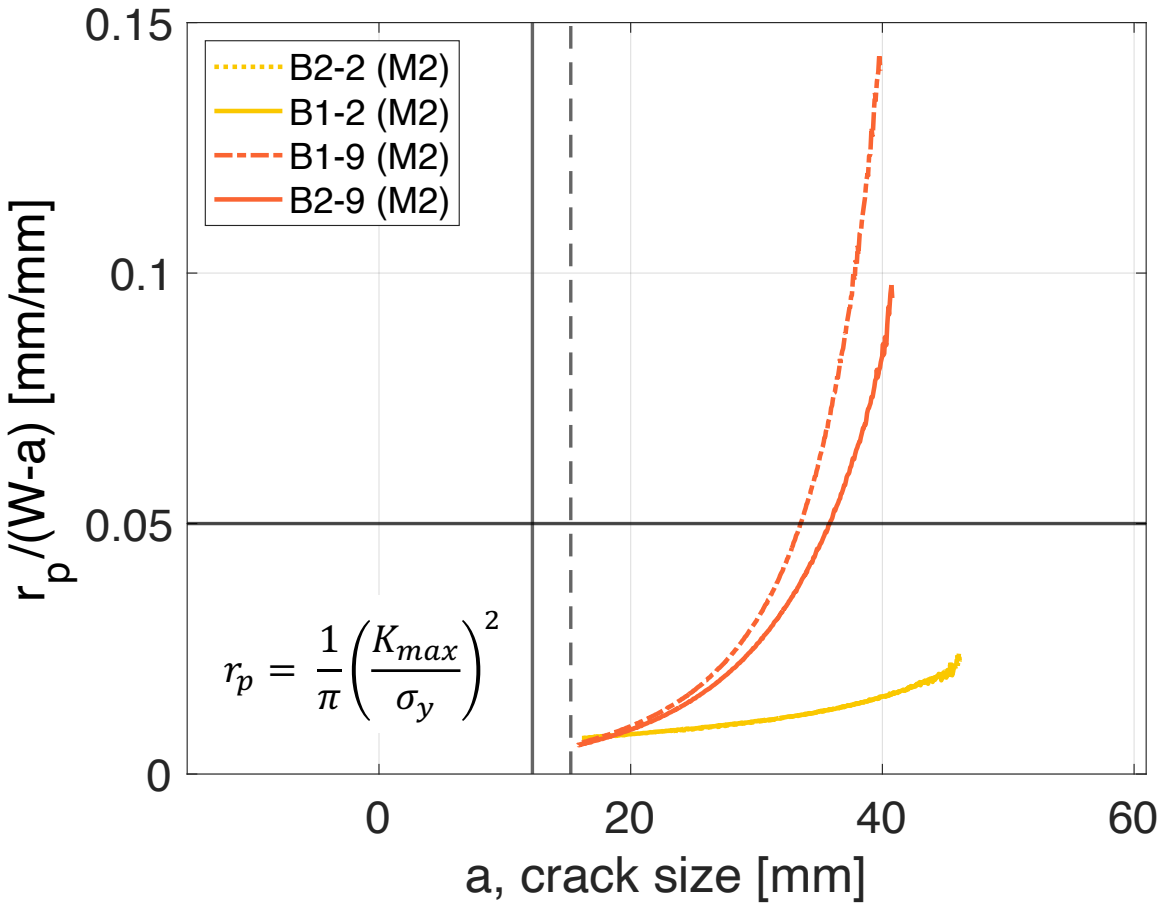

***Figure 3.14**: Ratio of plastic zone size to remaining ligament size for M2 stress state specimens.*

The increasing ΔK_{app} tests (specimens B1-9 and B2-9) have plastic zone sizes that increase rapidly as crack size increases, approaching and surpassing 5% of the remaining ligament. When r_p becomes too large in relation to the remaining ligament, LEFM concepts break down and no longer permit accurate determinations of ε_{res} (which then contains a plastic deformation component) used for K_{res} calculations. If OLCC K_{res} data are excluded when $r_p \geq 0.05(W - a)$, there is agreement among OLCC K_{res} found under constant and increasing ΔK_{app} tests for samples with

the same level of residual stress; here, the exclusion applies for crack sizes larger than 34 and 37 mm for specimens B1-9 (M2) and B2-9 (M2), respectively, as shown in **Figure 3.15**.

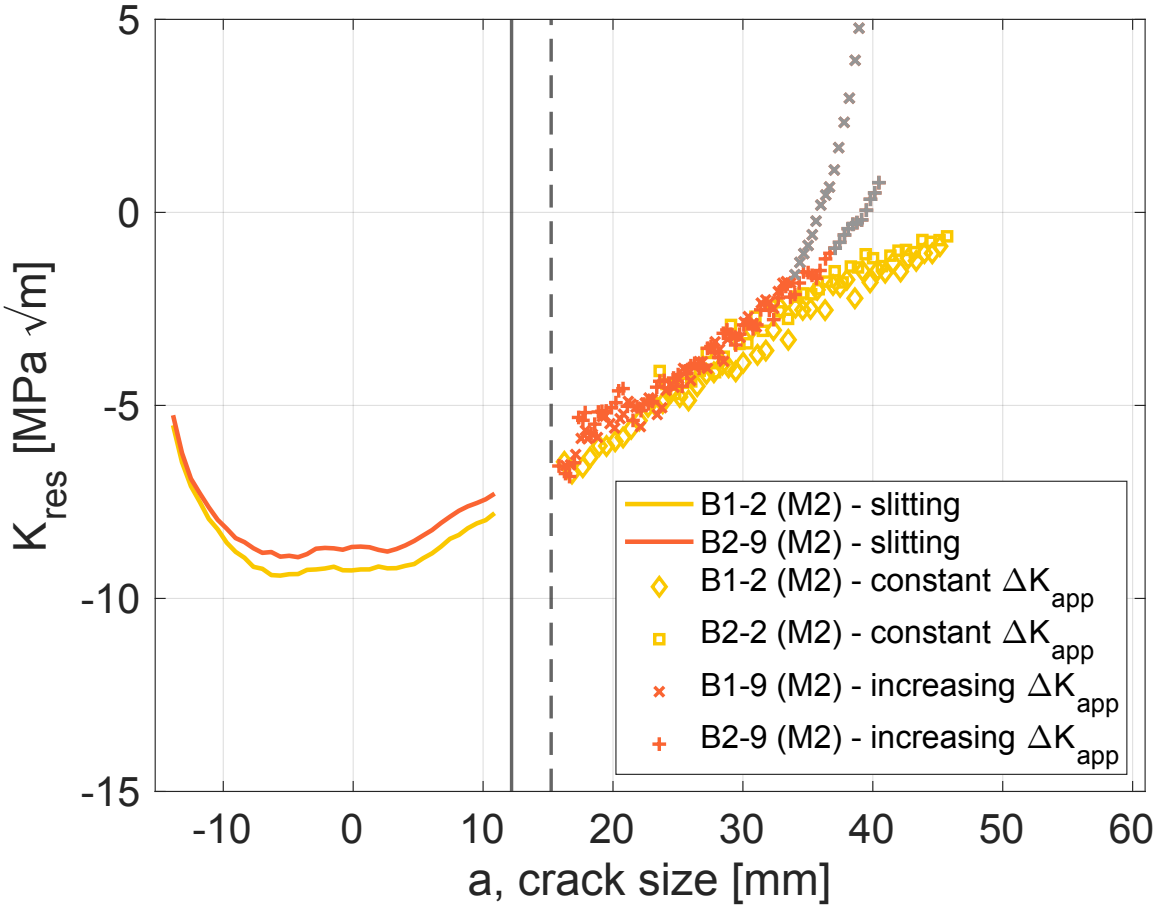

***Figure 3.15**: OLCC K_{res} profiles for constant ΔK_{app} fatigue tests and increasing ΔK_{app} fatigue tests of M2 stress state with points having plastic zone size greater than 5% of the remaining ligament grayed out.*

3.3.3. Fatigue Crack Growth Rates

Fatigue crack growth rate data from the constant ΔK_{app} tests from the low residual stress specimens (positions 1 and 10) and the second medium residual stress specimens (positions 2 and 9) are shown in **Figure 3.16**(a). Data from specimens at positions 3 and 8 are excluded because applied loads deviated from those intended, as described above (**Figure 3.11**(a)). Data for the high residual stress specimen (B1-6 (H)) are excluded because of applied load deviation (**Figure 3.11**(a)) and because excessive deviation of the crack path from the crack plane make the FCGR

data invalid according to ASTM E647 [24]. The data from the present AA7050-T74 specimens with compressive K_{res} are compared to those reported by Newman et al. for AA7050-T7451 [34] at an applied stress ratio of 0.1 (black line), which are presumed to be unaffected by bulk residual stress. Differences decrease as crack size and/or ΔK_{app} increase (**Figure 3.16**(a)). Under constant ΔK_{app}, medium stress state specimens (B1-2 (M2) and B2-2 (M2)) demonstrate the lowest crack growth rates with both specimens showing excellent agreement in FCGR behavior. The low stress state specimens (B2-1 (L) and B1-10 (L)) demonstrate fatigue crack growth rates that are closer to the value reported by Newman et al. with B2-1 (L) having lower FCGRs than B1-10 (L). This difference in FCGRs in the low stress state is consistent with the differences in K_{res} in **Figure 3.10**(a) (relative to position 1, position 10 has smaller magnitude K_{res} and higher FCGR).

The FCGRs from the increasing ΔK_{app} tests of position 9 and the decreasing ΔK_{app} test of position 10 are presented in **Figure 3.16**(b). The increasing ΔK_{app} tests are truncated at the crack size where r_p reaches 5% of the remaining ligament. The decreasing ΔK_{app} test data are limited to smaller crack sizes where the applied P_{max} corresponded to the intended loads ($a \leq 22$ mm). The FCGRs of 16(b) are also compared to those reported by Newman et al. [34] at an applied stress ratio of 0.1 (black line). **Figure 3.16**(b) shows that FCGRs over a range of ΔK_{app} values, for the medium (B1-9 (M2) and B2-9 (M2)) and low stress state (B2-10 (L)) specimens, are lower than those in material free of residual stress, which is consistent with negative K_{res} profiles found in slitting (**Figure 3.5**(b)) and by OLCC (**Figure 3.10**(a) and **Figure 3.13**).

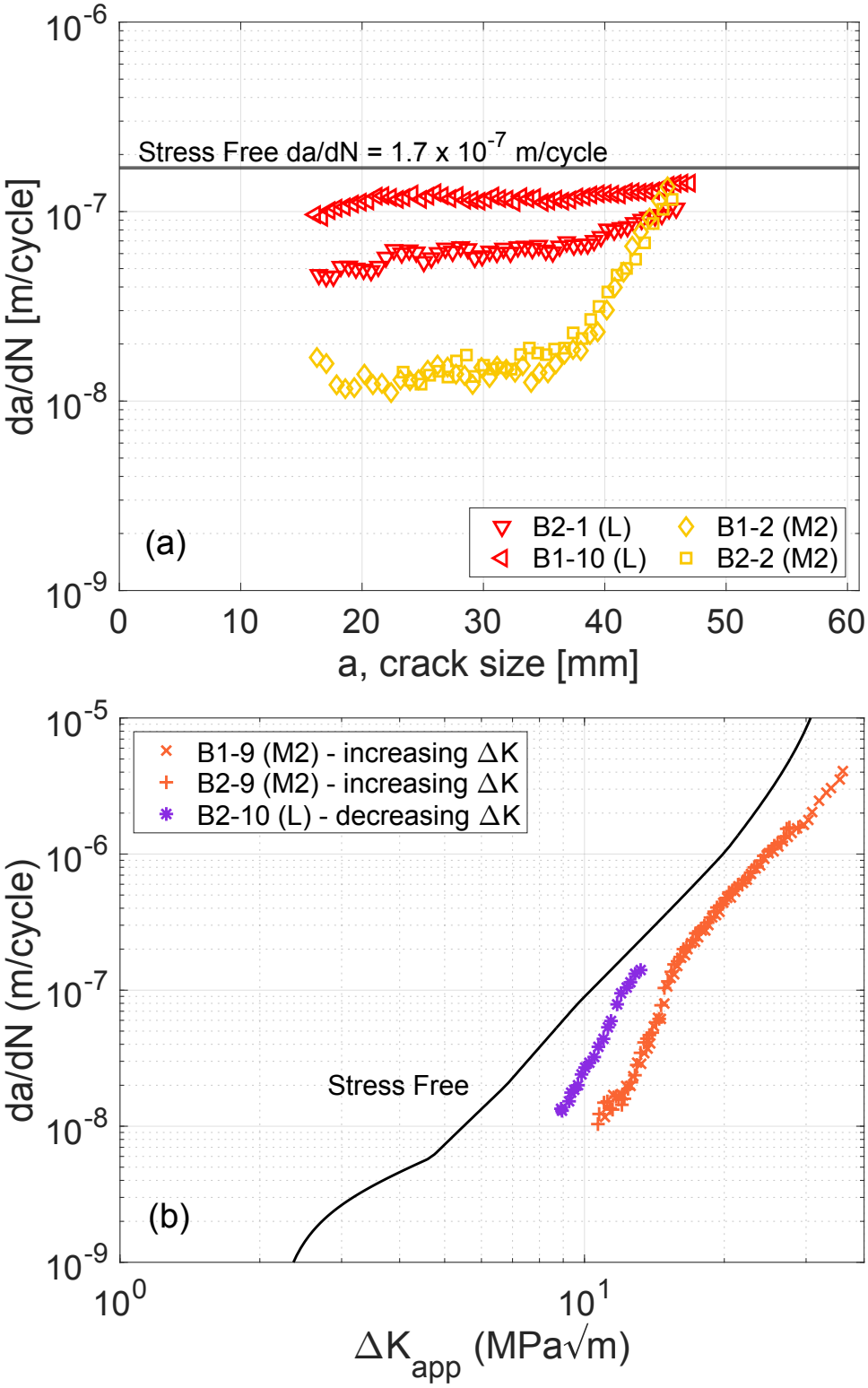

***Figure 3.16**: Measured FCGR data under (a) constant ΔK_{app} = 12 MPa·m$^{0.5}$ test conditions and (b) increasing and decreasing ΔK_{app} test conditions with expected FCGR for AA7050-T7451 at R = 0.1 [34].*

3.4. Conclusions

The residual stress intensity factor (K_{res}) characterizes the effect of residual stress on the response of a cracked body, which is known to affect measured fatigue crack growth rate (FCGR) data. Prior work has shown K_{res} can be determined through a destructive testing method, notably slitting of a secondary specimen. However, recent developments have led to the establishment of the on-line crack compliance method (OLCC) that can be used to determine K_{res} during an FCGR test, eliminating the need for secondary specimens [14, 15]. To support the broader implementation of the OLCC method, this work has presented details of OLCC data analysis methods, applied these methods in the context of FCGR tests under a range of loading conditions, and compared OLCC K_{res} data to data obtained by the slitting method. Tests were performed in compact (C(T)) specimens removed from blocks of AA7050-T74 material with residual stress from the quench and age heat treatment. All specimens exhibited negative values of K_{res} with specific specimens having larger or smaller levels of K_{res} depending on the position from which they had been removed from the blocks. The work of this study revealed:

1. The back-face strain approach works well for measuring deformation for the OLCC method. This work complements prior publications that described the OLCC method using crack mouth opening displacement.

2. The three data analysis methods explored in this study – OLCC Z(a) (Schindler's influence function), OLCC central difference ratio, and OLCC derivative ratio – are valid approaches for analyzing residual strain data to determine K_{res} via post-test data analysis. A comparison to slitting results from a secondary specimen validated OLCC as useful and accurate.

3. The OLCC central difference ratio method eliminated an erroneous systematic shift in the values of K_{res} that was present in the OLCC backward difference ratio method. However, since the OLCC central difference ratio method estimates a change in deformation over a finite interval of crack size by a difference, the overall noise in the K_{res} values was higher as compared to the other data reduction methods that use more robust derivative estimates.

4. Both OLCC Z(a) and OLCC derivative ratio methods utilize incremental polynomial derivative estimation and provided nominally identical results. The OLCC Z(a) method depends on the existence of a reliable influence function for the fatigue specimen geometry of interest. For the compact (C(T)) geometry with back-face strain measurement, an influence function has been developed and published in the literature [23]. As such, the OLCC Z(a) method was chosen as a best practice for the implementation of OLCC in this study.

5. In the case of constant ΔK_{app} control tests and constant applied load amplitude tests, the OLCC method provided accurate measurements of K_{res} relative to measurements from slitting.

6. In the case of decreasing ΔK_{app} control tests, crack face contact influenced the estimation of crack size leading to inaccurate test control at the low applied loads associated with small values of ΔK_{app}. While these issues did not affect the determination of K_{res}, carefully choosing test control and post-test data analysis parameters is recommended to obtain accurate and useful FCGR results when specimens have significant levels of compressive residual stress.

7. In the case of increasing ΔK_{app} tests, limitations are present due to plasticity effects in the remaining ligament for long cracks. When the plastic zone size reached 5% of the remaining ligament size, the OLCC method provided inaccurate results, similar to what has been observed in prior work.

Acknowledgements

This work was supported by a NASA Space Technology Research Fellowship (CMS - 80NSSC19K1132). The authors recognize valuable discussions regarding OLCC with Dr. Mark James of Howmet Aerospace. Additional partial funding for this research was provided by the University of California, Davis and by donations to the Department of Materials Science and Engineering.

References

1. Ball, D.L., et al., *A Detailed Evaluation of the Effects of Bulk Residual Stress on Fatigue in Aluminum.* Advanced Materials Research, 2014. **891-892**: 1205-1211.

2. Garcia, C., et al., *Fatigue crack growth in residual stress fields.* International Journal of Fatigue, 2016. **87**: 326-338.

3. LaRue, J.E. and S.R. Daniewicz, *Predicting the effect of residual stress on fatigue crack growth.* International Journal of Fatigue, 2007. **29**(3): 508-515.

4. Bucci, R., *Effect of Residual Stress on Fatigue Crack Growth Rate Measurement*, in *Fracture Mechanics: Thirteenth Conference, ASTM STP 743*R. Roberts, Editor. 1981, American Society for Testing and Materials: West Conshohocken, PA. 28-47.

5. Beghini, M. and L. Bertini, *Fatigue Crack-Propagation through Residual-Stress Fields with Closure Phenomena.* Engineering Fracture Mechanics, 1990. **36**(3): 379-387.

6. Beghini, M., L. Bertini, and E. Vitale, *Fatigue-Crack Growth in Residual-Stress Fields - Experimental Results and Modeling.* Fatigue & Fracture of Engineering Materials & Structures, 1994. **17**(12): 1433-1444.

7. McClung, R.C., *A literature survey on the stability and significance of residual stresses during fatigue.* Fatigue & Fracture of Engineering Materials and Structures, 2007. **30**(3): 173-205.

8. Vosikovsky, O., L.P. Trudeau, and A. Rivard, *Effect of Residual-Stresses on Fatigue Crack-Growth Threshold.* International Journal of Fracture, 1980. **16**(4): R187-R190.

9. James, M., et al., *A Methodology for Partitioning Residual Stress Effects From Fatigue Crack Growth Rate Test Data.* Materials Performance and Characterization, 2016. **5**(3): 194-214.

10. Hill, M.R. and J. Kim, *Fatigue Crack Closure in Residual Stress Bearing Materials.* Journal of ASTM International, 2011. **Vol 9**(No 1): 104071.

11. Parker, A.P., *Stress Intensity Factors, Crack Profiles, and Fatigue Crack Growth Rates in Residual Stress Fields*, in *Residual Stress Effects in Fatigue, ASTM STP 776*. 1982, American Society for Testing and Materials: West Conshohocken, PA. 13-31.

12. Schindler, H.J., W. Cheng, and I. Finnie, *Experimental determination of stress intensity factors due to residual stresses.* Experimental Mechanics, 1997. **37**(3): 272-277.

13. Hill, M.R. and J.E. VanDalen, *Evaluation of Residual Stress Corrections to Fracture Toughness Values.* Journal of ASTM International, 2008. **5**(8): 101713.

14. Donald, J.K. and D.A. Lados, *An integrated methodology for separating closure and residual stress effects from fatigue crack growth rate data.* Fatigue & Fracture of Engineering Materials & Structures, 2006. **30**(3): 223-230.

15. Lados, D.A., D. Apelian, and J.K. Donald, *Fracture mechanics analysis for residual stress and crack closure corrections.* International Journal of Fatigue, 2007. **29**(4): 687-694.

16. Lados, D.A. and D. Apelian, *The Effect of Residual Stress on the Fatigue Crack Growth Behavior of Al-Si-Mg Cast Alloys - Mechanisms and Corrective Mathematical Models.* Metallurgical and Materials Transactions A-Physical Metallurgy and Materials Science, 2006. **37A**: 133-145.

17. Newman, J.A., et al., *Characterization of Residual Stress Effects on Fatigue Crack Growth of a Friction Stir Welded Aluminum Alloy*. 2015. NASA Langley Research Center, Hampton, VA. Report No. NASA/TM–2015-218685.

18. Hill, M.R., *Chapter 4: The Slitting Method*, in *Practical Residual Stress Measurement Methods*G.S. Schajer, Editor. 2013, Wiley. 89-108.

19. Schajer, G.S. and M.B. Prime, *Use of inverse solutions for residual stress measurements.* Journal of Engineering Materials and Technology-Transactions of the ASME 2006. **128**(3): 375-382.

20. Prime, M.B., *Residual Stress Measurement by Successive Extension of a Slot: The Crack Compliance Method.* Applied Mechanics Reviews, 1999. **52**: 75-96.

21. Cheng, W. and I. Finnie, *Residual Stress Measurement and the Slitting Method*. Mechanical Engineering Series, ed. F.F. Ling. 2007, New York, NY: Springer.

22. Schindler, H.J., *Determination of Residual Stress Distributions from Measured Stress Intensity Factors.* International Journal of Fracture, 1995. **74**: R23-R30.

23. Olson, M.D. and M.R. Hill, *Determination of residual stress intensity factor in the compact tension coupon.* Engineering Fracture Mechanics, 2012. **88**: 28-34.

24. E647-15, *Standard Test Method for Measurement of Fatigue Crack Growth Rates*. 2015. ASTM International: West Conshohocken, PA.

25. E837-20, *Standard Test Method for Determining Residual Stresses by the Hole-Drilling Strain-Gage Method*. 2020. ASTM International: West Conshohocken, PA.

26. *MATLAB. (2021). version 9.10.0 (R2021a).* Natick, Massachusetts; The MathWorks Inc.

27. Hill, M.R. and M.D. Olson, *Repeatability of the Contour Method for Residual Stress Measurement.* Experimental Mechanics, 2014. **54**(7): 1269-1277.

28. Olson, M.D., et al., *Characterisation of residual stresses in heat treated, high strength aluminium alloy extrusions.* Materials Science and Technology, 2016. **32**(14): 1427-1438.

29. Ribeiro, R.L. and M.R. Hill, *Measurement-driven, model-based estimation of residual stress and its effect on fatigue crack growth. Part 2: fatigue crack growth testing and modeling.* International Journal of Fatigue, 2022: 107044.

30. *7050: High-Strength Structural Alloy*, in *Properties and Selection of Aluminum Alloys*, Vol 2B, ASM Handbook. K. Anderson, J. Weritz, and J.G. Kaufman, Editors. 2019, ASM International. 423–427.

31. E1823-21, *Standard Terminology Relating to Fatigue and Fracture Testing*. 2021. ASTM International: West Conshohocken, PA.

32. Meyers, M.A. and K.K. Chawla, *Mechanical Behavior of Materials, 2nd Edition.* Mechanical Behavior of Materials, 2nd Edition, 2009: 1-856.

33. James, M.A., *Private Communication*. 2022.

34. Newman Jr., J.C., Yamada, Y., and Newman, J. A. , *Crack-Closure Behavior of 7050 Aluminum Alloy near Threshold Conditions for Wide Range in Load Ratios and Constant Kmax Tests.* Journal of ASTM International, 2010. **7**: 102490.

Chapter 4:
Effects of Residual Stress on Orientation Dependent Fatigue Crack Growth Rates in Additively Manufactured Stainless Steel [3]

Abstract

Localized heating and resulting temperature gradients during additive manufacturing (AM) creates significant residual stress that influences mechanical behavior, such as fatigue performance. To quantify residual stress effects on fatigue crack growth in AM materials, crack growth rates parallel and perpendicular to the build direction in directed energy deposition (DED) Type 304L austenitic stainless steel were measured. The on-line crack compliance method was used to determine the residual stress intensity factor, K_{res}, while simultaneously collecting fatigue crack growth rate (FCGR) data. Constant applied alternating stress intensity factor (constant ΔK_{app}) tests revealed the primary influence on measured FCGR is the orientation dependent K_{res}. Critical analysis of the compliance data from decreasing ΔK_{app} tests was used to quantify K_{res}, which was then used to correct FCGR data in the near-threshold regime. Results demonstrated that the fatigue response of DED Type 304L is inherently similar to that of annealed wrought Type 304/304L.

Keywords: additive manufacturing, fatigue crack growth, residual stress intensity factor, on-line crack compliance, directed energy deposition

[3] Submitted: Smudde, C.M., et al., *Effects of Residual Stress on Orientation Dependent Fatigue Crack Growth Rates in Additively Manufactured Stainless Steel.* International Journal of Fatigue, 2022.

4.1. Introduction

Directed energy deposition (DED), a common additive manufacturing (AM) method, enables fabrication of fully dense metal components layer-by-layer directly from computer aided design models. Residual stress is an important side effect of the processing due to the inherently complex thermal history imposed during deposition of the material. Specifically in DED, significant temperature gradients lead to the formation of high residual stress in the build direction [1-3]. The deposited material experiences continuous remelting and repeated solidification as subsequent layers are added, resulting in a residual stress profile in the build direction that is tensile at the edges (surface zone) and compressive in the center of wall builds [3]. Whereas residual stress can be minimized by tailoring the processing parameters, complete stress relief is difficult without post-processing [1]. Due to the same rapid solidification that results in residual stress, nonequilibrium microstructures are formed in DED materials, which consist of grains with non-uniform size and shape. For example, the solidification and growth of grains follow the heat-flow direction, resulting in a variety of elongated shapes [2]. Both residual stress and microstructure morphology may influence the mechanical performance of DED materials, specifically under the low applied cyclic loading of near-threshold fatigue crack growth ($da/dN < 10^{-8}$ m/cycle [4]).

Residual stress and microstructure must be assessed to achieve accurate characterization of mechanical properties and fatigue crack growth rates (FCGRs) in DED materials. A thorough investigation of and correction for the influence of residual stress on orientation dependent fatigue crack growth rates in the near-threshold regime of DED Type 304L stainless steel have not been reported. Moreover, the orientation dependence of residual stress has not been considered in this context. Smith, et al. explored the specimen orientation dependence of high cycle fatigue life of a DED Type 304L austenitic stainless steel, but they did not consider the orientation dependence of

residual stress [5]. Other studies have identified anisotropic fatigue crack growth behavior in structural alloys produced by AM and found that the orientation dependence decreased after heat treatments [6-9]. Since the heat treatments were at sufficiently high temperatures to relax the residual stress and recrystallize the material, the anisotropy of residual stress and microstructure likely contributed to the observed orientation dependence of the fatigue crack growth response in as-built AM materials of those studies.

In fatigue, crack growth is typically characterized as a function of the applied alternating stress intensity factor range (ΔK_{app}). Residual stress contributes to the total stress intensity factor acting at the crack tip and is quantified by the residual stress intensity factor (K_{res}), which combines with both the maximum and the minimum applied stress intensity factors ($K_{max,app}$ and $K_{min,app}$). Since K_{res} is essentially a mean stress effect, a positive value will increase the total stress intensity factor ratio (R_{tot}), whereas a negative value will reduce R_{tot}. A larger mean stress, represented by a larger R_{tot}, results in higher fatigue crack growth rates, indicating that the measured fatigue threshold can be markedly reduced and observed fatigue crack growth rates can be increased in the case of positive K_{res} [10] – and the opposite is true in the case of negative K_{res}.

An accurate method of quantifying K_{res} is necessary to account for the influence of residual stress on fatigue behavior. The on-line crack compliance (OLCC) method allows for the determination of K_{res} through the analysis of compliance data as a function of crack size [11-15]. Using a correction method based on the linear elastic fracture mechanics concepts of superposition [11, 13, 14], the influence of residual stress on individual test specimens can be determined and fatigue crack growth data can be corrected to quantitatively account for the impact of process-induced residual stress. To date, this method to assess and correct fatigue crack growth rates has not been applied to AM materials.

Accordingly, the goal of this study is to demonstrate the influence of residual stress on fatigue crack growth rates in DED Type 304L stainless steel material and to evaluate the orientation dependence of the intrinsic fatigue response after correcting for residual stress. Fatigue crack growth rate experiments are performed on compact (C(T)) specimens with crack growth oriented both parallel and perpendicular to the build direction under conditions of both constant ΔK_{app} and decreasing ΔK_{app}. Load versus deformation (back-face strain, BFS) data are analyzed via the OLCC method to determine the residual stress intensity factor as a function of crack size ($K_{res}(a)$). In this study, $K_{res}(a)$ determined by the OLCC method is compared to values determined from a destructive measurement (slitting experiment) of a secondary specimen [16]. The measured FCGR data of DED material are then corrected for residual stress using $K_{res}(a)$ from OLCC. An investigation of the microstructural contributions to crack growth is used to enhance understanding of the intrinsic material behavior.

4.2. Material and Methods

4.2.1. Material and Specimens

Type 304L stainless steel powder was built via DED in a Laser Engineered Net Shaping (LENS®) 750 workstation at Sandia National Laboratories in California. The resulting composition of the deposited material is nominally the same as that of the starting powder. Four replicate vertical wall builds with nominal dimensions of 107 mm (Z-direction or build direction) x 55.9 mm (Y-direction) x 7.62 mm (X-direction) were each deposited on individual stainless steel baseplates with identical processing parameters and are denoted as DED1, DED2, DED3, and DED4. Processing was optimized to achieve greater than 99% density as described in an earlier study of the same material [16]. Tensile properties of similarly processed DED Type 304L are superior to solution annealed (conventionally manufactured) Type 304/304L stainless steel wrought material [17].

The DED vertical walls were removed from their baseplates via wire electrical discharge machining (EDM). A segment was removed for material characterization before three compact (C(T)) fatigue specimens with a thickness (B) of 6.35 mm and width (W) of 26.4 mm were extracted at different distances above the baseplate (bottom (B), middle (M), and top (T) in **Figure 4.1**). The C(T) specimens were not centered in the Y-direction as result of the removal of the segments for material characterization (highlighted in light blue in **Figure 4.1**). Specimens oriented with loading both parallel and perpendicular to the build direction were utilized to evaluate crack growth in the horizontal (H in **Figure 4.1**(a)) and vertical (V in **Figure 4.1**(b)) directions.

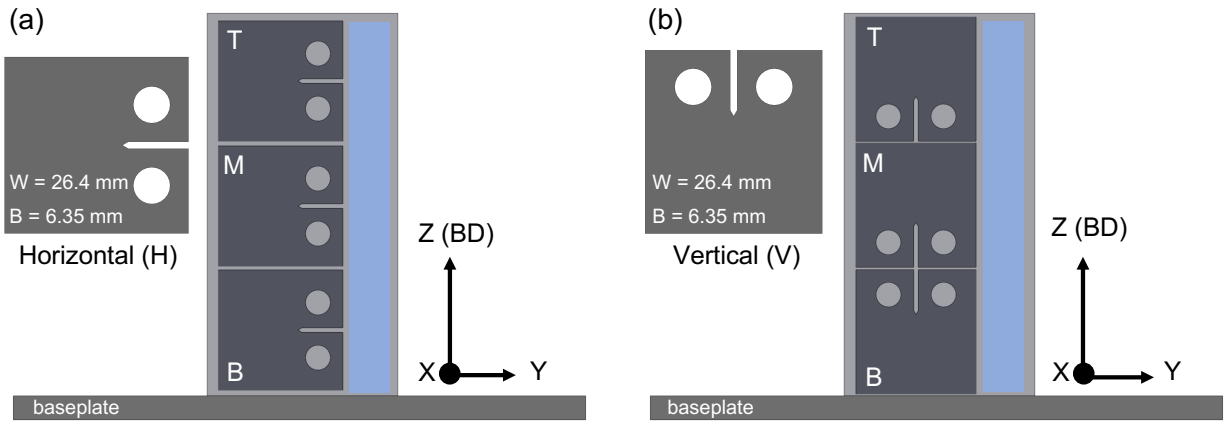

***Figure 4.1**: Schematic of DED Type 304L builds of each orientation showing extraction location for top, middle, and bottom compact (C(T)) specimens. The segments shown in light blue on the right side of the builds were removed for material characterization.*

Eight specimens were used in this study to evaluate residual stress intensity factors (K_{res}) and fatigue crack growth rate behavior. An equal number were tested with crack growth oriented horizontal (H) and vertical (V). Specimens were differentiated by their build number (DED1, DED2, DED3, or DED4) and by their extraction location (B, M, or T), as identified in previous work [16]. Four specimens in each orientation from multiple builds were tested to verify

reproducibility. K_{res} results from destructive slitting from Ref. [16] are also included for comparison to the OLCC method.

For reference, the test method designations for the specimens extracted from the DED Type 304L stainless steel are presented in **Table 4.1**. Additionally, three wrought specimens extracted from a dual certified Type 304/304L solution annealed stainless steel plate were tested for comparison and are also listed in the table.

Table 4.1: Specimen designation for K_{res} and FCGR evaluation.

Specimen	FCGR test	Specimen	FCGR test	Specimen	FCGR test
DED1-B (H)	decreasing ΔK_{app}	**DED3-B (V)**	decreasing ΔK_{app}	**DED1-M (H)**	slitting [16]
DED2-M (H)	constant ΔK_{app}	**DED3-M (V)**	constant ΔK_{app}	**Wrought1**	constant ΔK_{app}
DED1-T (H)	decreasing ΔK_{app}	**DED3-T (V)**	decreasing ΔK_{app}	**Wrought2**	decreasing ΔK_{app}
DED2-T (H)	decreasing ΔK_{app}	**DED4-T (V)**	decreasing ΔK_{app}	**Wrought3**	decreasing ΔK_{app}

4.2.2. Fatigue Crack Growth Rate Tests

Prior to fatigue crack growth rate testing, a notch was introduced to all specimens by wire EDM to a nominal crack size, a_n, of 5.1 mm ($a_n/W \approx 0.19$) in accordance with ASTM E647 [4]. Fatigue precracking and testing were performed on an Instron 1331 servohydraulic load frame controlled by MTS 790.40 TestStar software under K-control conditions at an applied stress intensity factor ratio of $R_{app} = 0.1$ and frequency of 10 Hz. Crack size was monitored by the compliance method in which the modulus was assumed to be that of a fully dense austenitic stainless steel, 200 GPa. The MTS 790.40 fatigue crack growth software was modified to accept a back-face strain (BFS) input for the compliance method; additional detail can be found in the literature [16].

All specimens were precracked to an initial crack size, a_o, of 6.6 mm ($a_o/W = 0.25$) using a load shedding methodology in accordance with ASTM E647 [4]. Constant applied alternating stress intensity factor tests with ΔK_{app} = 6.6 MPa·m$^{0.5}$ were used to evaluate the influence of process-induced residual stress on fatigue crack growth rates. Decreasing ΔK_{app} tests with a starting $K_{max,app}$ = 11.6 MPa·m$^{0.5}$ and a load shedding parameter of C = -0.08 mm^{-1} were performed to further probe near-threshold FCGR behavior.

Compliance data (load and BFS) with 500 data points from three consecutive cycles represent an average compliance at each crack size and were recorded at crack size increments of 0.051 mm ($\Delta a/W \approx 0.002$). Following completion of each test, these data were evaluated to verify crack size at each recorded increment and to determine K_{res} as a function of crack size via the OLCC Z(a) method described below. While the fatigue crack growth rate tests were performed at a fixed applied stress intensity factor ratio (constant R_{app}), residual stress acts at the crack tip and the total stress intensity factor ratio (R_{tot}) must include the effects of K_{res}:

$$R_{tot}(a) = \frac{K_{min,app}(a)+K_{res}(a)}{K_{max,app}(a)+K_{res}(a)} \tag{4.1}$$

where $K_{min,app}(a)$ and $K_{max,app}(a)$ are determined from the applied cyclic loads and $K_{res}(a)$ is calculated at each increment of crack size.

4.2.3. On-line Crack Compliance Method

The on-line crack compliance (OLCC) method was recently developed to calculate the residual stress intensity factor, K_{res}, as a function of crack size from data collected during a traditional fatigue crack growth rate test [11-15]. Derived from a fracture mechanics description of the residual stress intensity factor (K_{res}), the OLCC method enables the simultaneous determination of traditional FCGR data and quantification of $K_{res}(a)$ to correct the data for the

influence of residual stress using a single specimen. Residual stress in a material shifts the load-deformation (BFS in this study) data, such that the compliance plot does not extrapolate to zero deformation at zero load as expected in a stress-free material. Moreover, the residual stress relaxes and redistributes as the crack grows, resulting in a continuous shift in the deformation at zero load that can be quantified. A recent study [18] has explored an improved methodology for data reduction using BFS data and Schindler's geometry dependent influence function (Z(a)) [19, 20]. This OLCC Z(a) method for data reduction only requires the determination of the residual strain $\varepsilon_{res}(a)$, which represents the shift in deformation data at zero load, and a geometry dependent influence function [18]. The calculation for the OLCC Z(a) method is described in Equation (4.2):

$$K_{res}(a) = \frac{E'}{Z(a)} \frac{d\varepsilon_{res}(a)}{da} \tag{4.2}$$

where E′ is the elastic modulus for a fully dense material (in this case of plane stress for fatigue tests, 200 GPa). An influence function developed by Olson and Hill for the C(T) specimen geometry [21] was used in this study.

To depict the OLCC Z(a) method for data reduction, an example set of compliance data from a constant ΔK_{app} test with AM induced residual stress (specimen DED2-M (H)) is illustrated in **Figure 4.2**. Compliance plots for two crack sizes are shown in this figure: one for a crack size of interest (a_i) and a second for a crack size preceding a_i by *m* increments (a_{i-m}), where *m* is taken to be large for illustration. To determine $K_{res}(a)$ via the OLCC method, a singular value of residual strain, $\varepsilon_{res}(a_i)$, is measured at each crack size, a_i, by extrapolating the linear region of compliance data to zero load as represented by the dashed lines in **Figure 4.2**. In this manner, the $\varepsilon_{res}(a_i)$ can be determined for all crack size increments. In the edge crack fatigue specimens of this study, the contribution of AM induced residual stress is tensile and maintains an open crack wake throughout

the tests. Since crack closure is absent when the crack wake remains open, the compliance data are entirely linear.

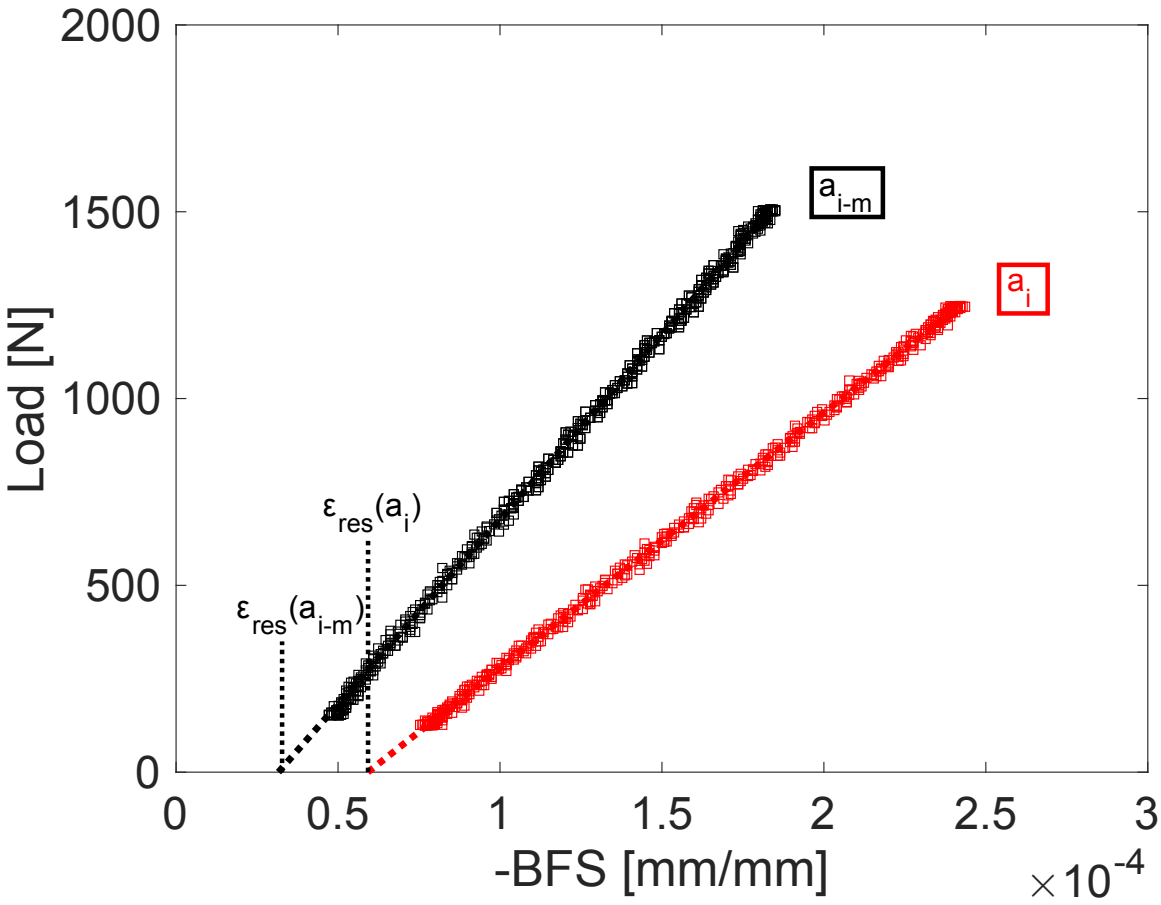

***Figure 4.2**: Schematic of determination of residual strain, $\varepsilon_{res}(a_i)$, for the OLCC Z(a) method from a compliance plot of load and -BFS.*

The derivative of the residual strain as a function of crack size in Equation (4.2) was determined numerically by using a quadratic polynomial regression fit similar to that described for crack growth rate calculations in ASTM E647 with 2N+1 consecutive data points centered around each value of crack size [4]; this method truncates N points at the beginning and end of the data set. Therefore, it is important to minimize the chosen value of N to avoid loss of data at either end of the data set, especially in fatigue specimens with small values of W (26.4 mm in this study). However, at small values of N, high levels of noise can arise in the K_{res} profile. To determine an

appropriate N for this study, K_{res} was calculated by the OLCC method and compared for three values (N = 5, 10, and 12) for a specimen tested under constant ΔK_{app} conditions (DED2-M (H)). A value of N = 10 was used in previous work for specimens with larger W [18].

4.2.4. Characterization of Crack Profiles

Crack path micrographs were collected after fatigue testing. Samples including the crack tip were cut via wire EDM from specimens that had been tested at constant ΔK_{app} (DED2-M (H), DED3-M (V) and Wrought1). Samples were then mounted in epoxy and ground to 1200 grit with SiC paper prior to polishing with an alumina suspension of 3 μm, 1 μm, and 0.3 μm. Samples were then vibropolished for 9 hours with 0.05 μm colloidal silica. The microstructure of the DED Type 304L material was explored by backscatter electron (BSE) imaging, including grain morphologies surrounding the crack path. A Thermo Fisher Quattro ESEM operating at 5 kV and 0.46 nA revealed the differences in grain sizes and shapes in the DED material as compared to annealed wrought material.

4.3. Results and Discussion

4.3.1. K_{res} from On-line Crack Compliance

The residual stress intensity factor (K_{res}) as a function of crack size was determined using residual strain (ε_{res}) and the Schindler influence function as described by the OLCC method of Equation (4.2). In **Figure 4.3**, ε_{res} for two constant ΔK_{app} tests (DED2-M (H) and DED3-M (V)) is compared to the strain measurements from slitting of a horizontal specimen from Ref. [16]. The location of the notch tip (solid vertical line) and the end of the precrack zone (dotted vertical line) are indicated in the figure. The slitting measurement was made prior to the introduction of a fatigue starter notch and therefore strain is measured at values of negative crack size (crack size is measured with respect to the load line, not the front face of the specimen).

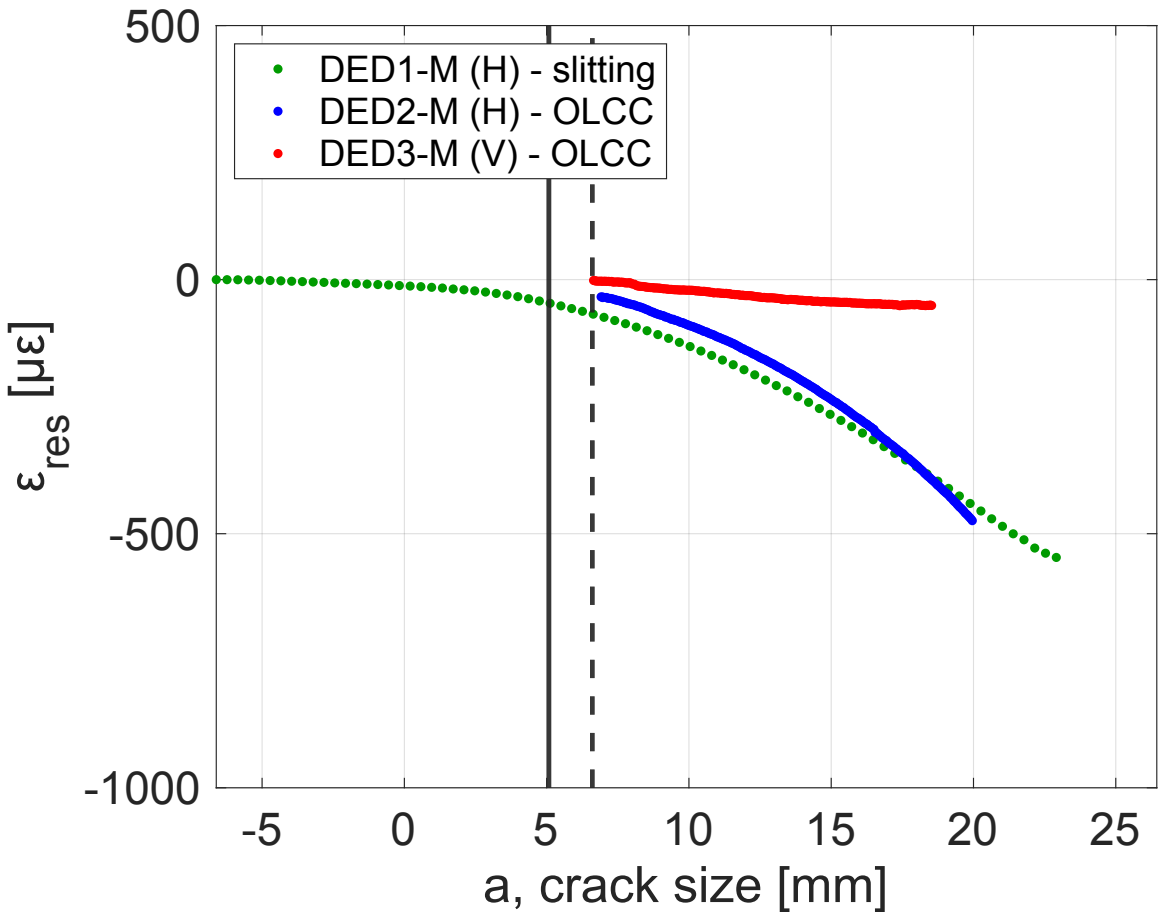

***Figure 4.3**: Residual strain (ε_{res}) from OLCC of DED2-M (H) and DED3-M (V) tested under constant ΔK_{app} condition and slitting of DED1-M (H).*

Residual strain ($\varepsilon_{res}(a)$) measurements from slitting and from the OLCC method exhibit similar trends in **Figure 4.3** for horizontally oriented specimens (DED1-M (H) and DED2-M (H), respectively), suggesting the derivative (hence $K_{res}(a)$) will have similar values. The residual strain data from the vertically oriented specimen (DED3-M (V)) have a more gradual slope and exhibit a small change as crack size increases throughout the fatigue crack growth rate test. Thus, the vertically oriented specimen is expected to exhibit small (and relatively constant) values of $K_{res}(a)$ and small effects of residual stress on the fatigue crack growth rates.

Figure 4.4(a-c) shows the K_{res} results for horizontal specimen DED2-M (H) for three different values of N: 5, 10, and 12 corresponding to Δa of 0.56 mm, 1.07 mm, and 1.27 mm. The

smaller loads and smaller strains measured in the material of this study (as compared to [18]) require smoothing over larger crack increments to achieve a reasonable K_{res} profile. Since macroscale residual stress does not vary on the length scale of millimeters, using a higher N (compared to those [18]) is a valid approach to data reduction and N = 12 (**Figure 4.4**(c)) was used to analyze data in this study. However, to minimize the truncation of data (since W is small), N = 5 (**Figure 4.4**(a)) was used for 7 increments of crack size at the beginning (i = 6 to 13) of the OLCC data analysis prior to the use of N = 12. A similar strategy was implemented at the end of the data set to reduce the amount of truncated data.

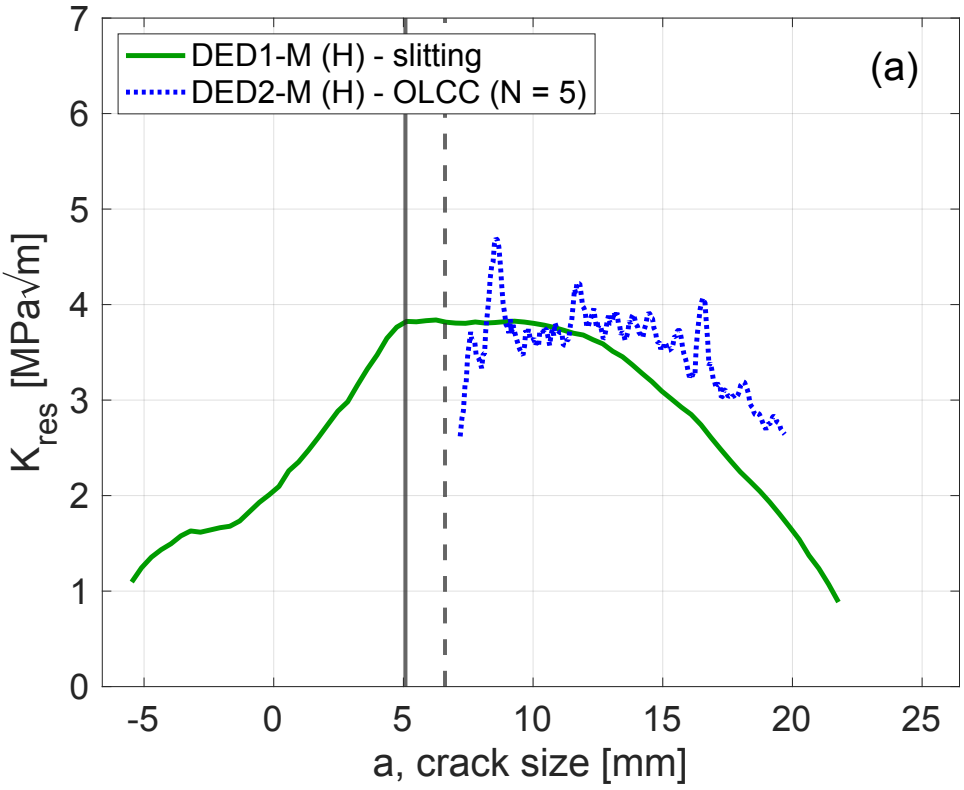

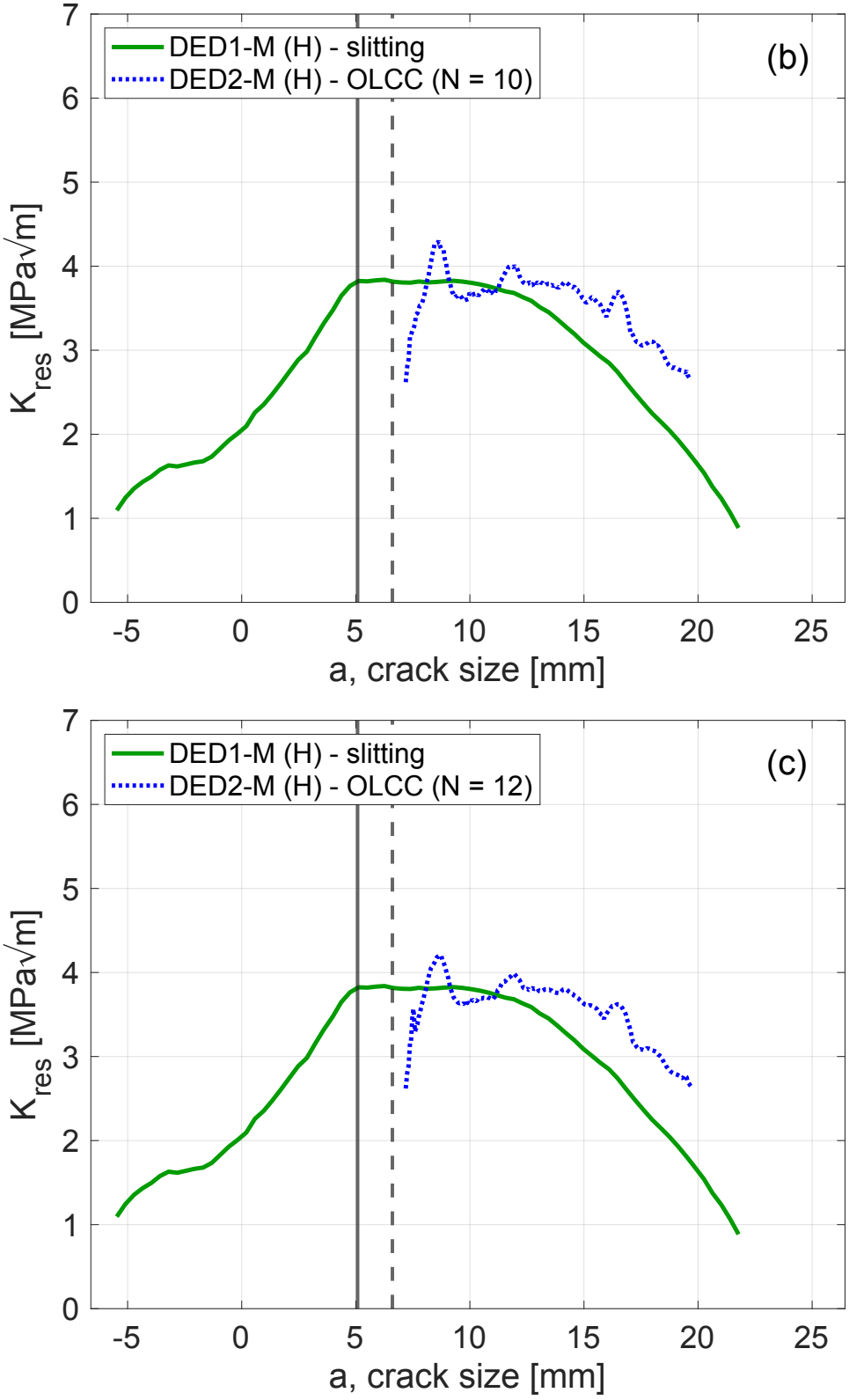

***Figure 4.4**: Comparison of choice of N values (values of N: 5, 10, and 12 corresponding to Δa of 0.56 mm, 1.07 mm, and 1.27 mm) for OLCC data analysis of specimen DED2-M (H) with slitting of DED1-M (H) [16] for reference.*

In **Figure 4.5**, the $K_{res}(a)$ results from the constant ΔK_{app} fatigue crack growth tests of the horizontal and vertical orientations are compared to values from specimen slitting of Ref. [16]. Despite small scale oscillations in K_{res} from OLCC attributed to experimental noise and instrumentation limitations, the horizontal test specimen (DED2-M (H)) agrees well with the slitting data from DED1-M (H) [16], both of which have K_{res} values of around 4 MPa·m$^{0.5}$ at the beginning of crack growth, and which decreases continuously as the crack extends. K_{res} of this magnitude can significantly impact the total stress intensity factor ratio (Equation (4.1)) in the near-threshold regime. For example, a ΔK_{app} of 6.6 MPa·m$^{0.5}$ with $R_{app} = 0.1$ corresponds to $K_{min,app}$ and $K_{max,app}$ of 0.7 MPa·m$^{0.5}$ and 7.3 MPa·m$^{0.5}$, respectively. With the addition of K_{res} of 4 MPa·m$^{0.5}$, R_{tot} is 0.42. While the overall magnitude of $K_{res}(a)$ from OLCC matches the slitting measurement, it deviates at longer crack sizes. In contrast, the vertical specimen (DED3-M (V)) is shown to have negligible residual stress effects on fatigue crack growth, evident by very low K_{res} values (0 – 1 MPa·m$^{0.5}$) that trend towards zero as the crack grows. This level of K_{res} is consistent with that present in the annealed (nominally stress-free) wrought material (**Figure 4.5**).

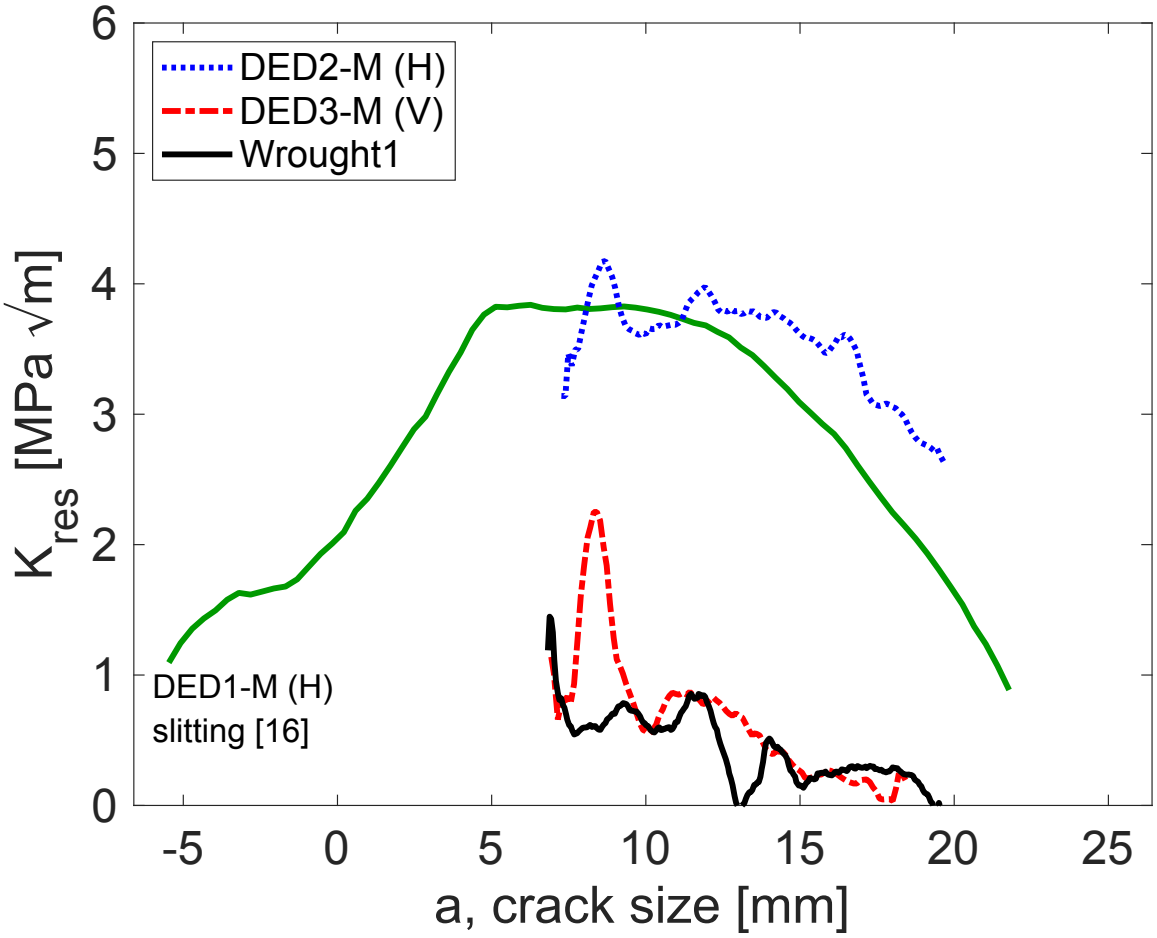

***Figure 4.5**: $K_{res}(a)$ for specimens DED2-M (H), DED3-M (V), and Wrought1 tested under constant ΔK_{app} condition compared to slitting measurement of DED material (DED1-M (H))* [16].

The large spike in the K_{res} at a crack size of 8 mm for DED3-M (V) (**Figure 4.5**) can be attributed to a transient in the $\varepsilon_{res}(a)$ slope at this crack size as shown in **Figure 4.6**. Prior to a crack size of 8 mm, the decrease in the strain versus crack size data is gradual. At a crack size of 8 mm there is a transient change in slope, which rapidly recovers to a slope consistent with that prior to the transient. This dependence of residual strain on crack size is amplified during the derivative determination of the data reduction and results in the spike in the $K_{res}(a)$ profile.

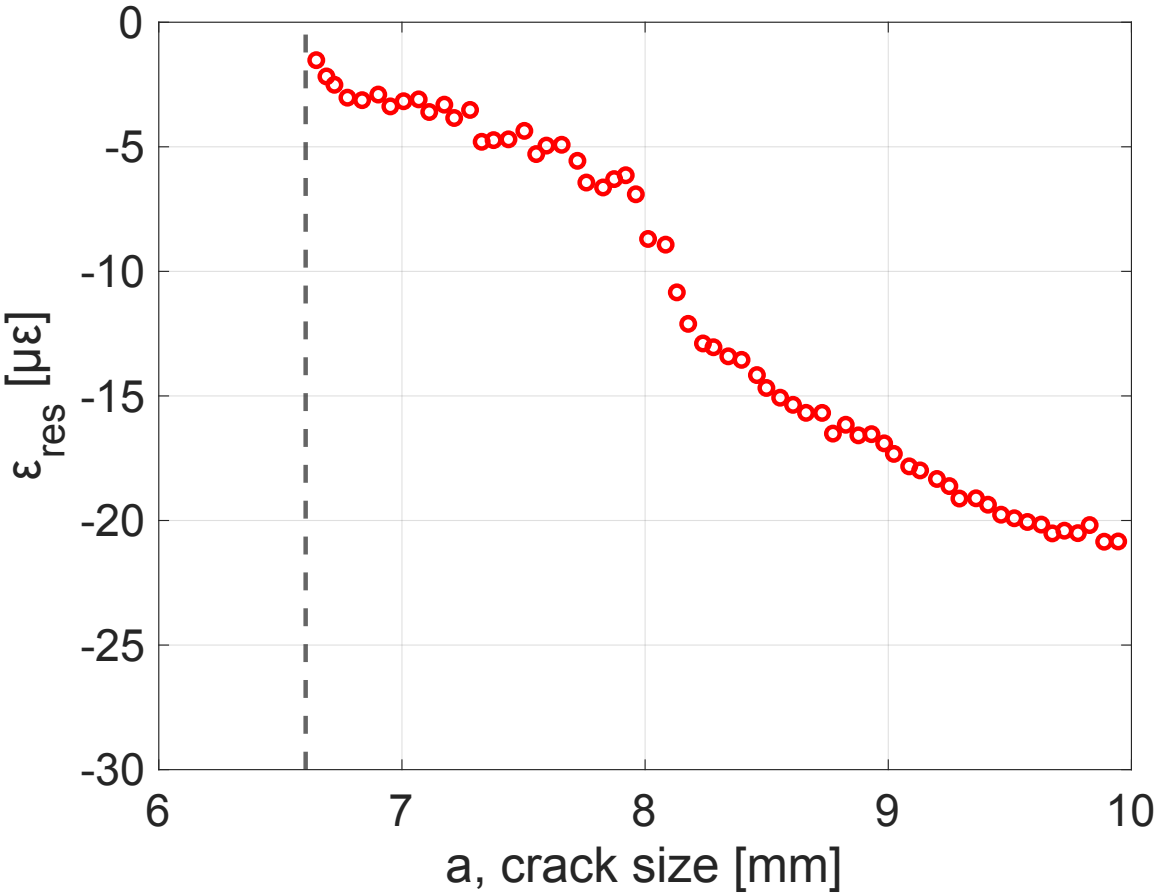

***Figure 4.6**: Detailed view of transient in residual strain ($\varepsilon_{res}(a)$) for DED3-M (V) tested under constant ΔK_{app} condition near 8 mm crack size.*

Figure 4.7 presents the K_{res} results from the constant and decreasing ΔK_{app} fatigue crack growth tests for all specimens. The $K_{res}(a)$ profiles reveal a clear difference between H and V orientations. The crack growth specimens tested under decreasing ΔK_{app} conditions were found to have similar $K_{res}(a)$ profiles as DED2-M (H) and DED3-M (V) tested under constant ΔK_{app} conditions. Comparison of the two testing configurations (constant ΔK_{app} and decreasing ΔK_{app}) across several builds shows consistent K_{res} profiles demonstrating the repeatability of the DED method and the consistency of process-induced residual stress. All horizontal orientation specimens, regardless of extraction location with respect to build height, had similar $K_{res}(a)$ values (3.5 - 4.5 MPa·m$^{0.5}$ for a < 17 mm). For example, all DED1 specimens (B, M, and T) show similar values of K_{res} around 4 MPa·m$^{0.5}$ at the notch tip, which decreases as crack size increases. The

K_{res}(a) values of DED2-T (H) agree with those of DED2-M (H) and start at around 3.5 MPa·m$^{0.5}$ at the notch tip. Variability in K_{res}(a) between specimens of the same orientation is more apparent in the vertical specimens with the OLCC results from the decreasing ΔK_{app} tests (DED3-B (V), DED3-T (V), and DED4-T (V)) having slightly higher values of K_{res}(a) of around 1.5 MPa·m$^{0.5}$ as compared to the constant ΔK_{app} test (DED3-M (V)) with values around 0.5 MPa·m$^{0.5}$. All wrought specimens have K_{res} values that are small and agree well, independent of test condition.

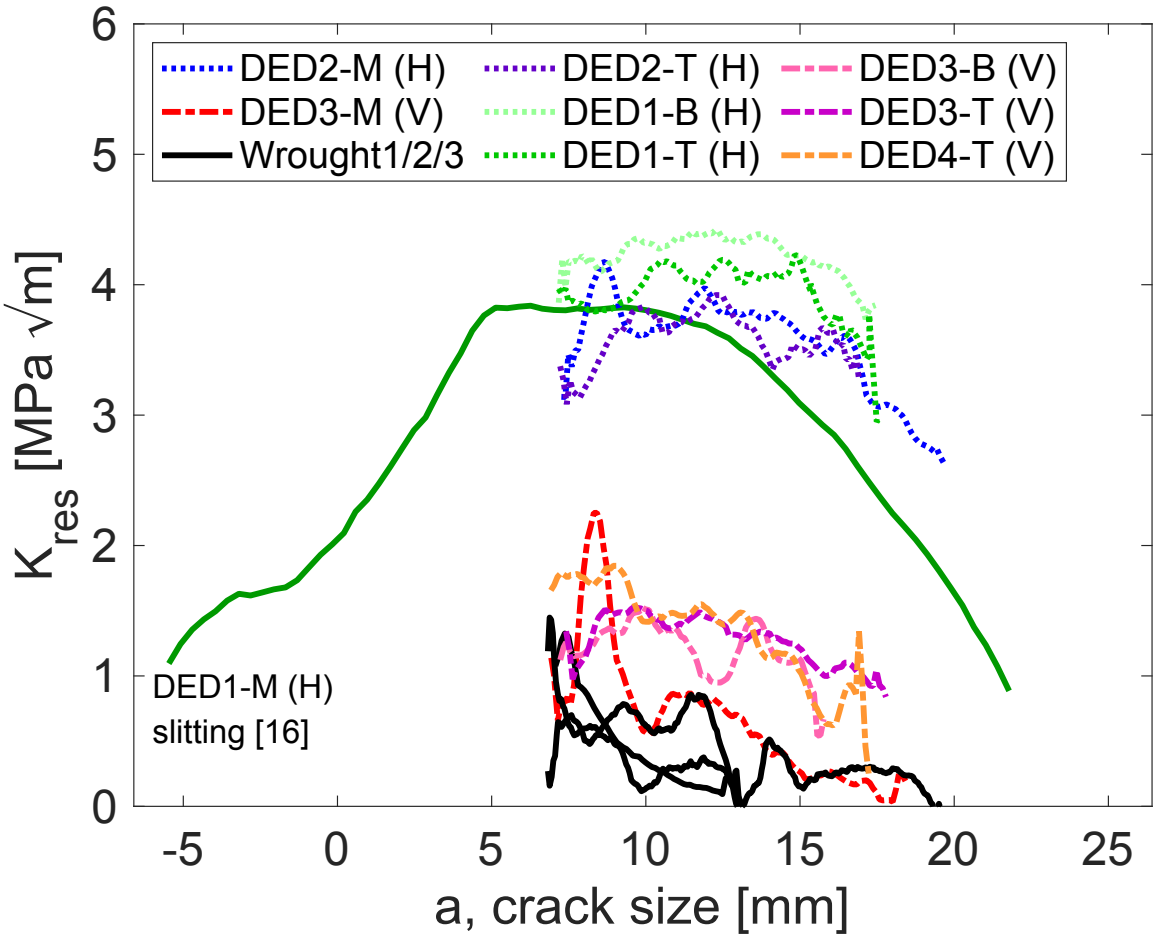

***Figure 4.7**: K_{res} data as a function of crack size for all specimens.*

4.3.2. Fatigue Crack Growth Rates

Figure 4.8(a) illustrates the fatigue crack growth rates as a function of crack size for DED Type 304L stainless steel in both the horizontal and vertical orientations and for wrought Type 304/304L material at constant ΔK_{app} and R_{app} of 6.6 MPa·m$^{0.5}$ and 0.1, respectively. The highest

crack growth rates were observed in the horizontal specimen at the beginning of the fatigue test, and they decreased gradually as the crack extended. The vertical specimen displayed similar fatigue crack growth rates to the wrought material, although the rates diverged for crack sizes greater than about 15 mm. Color is added in **Figure 4.8**(b) to show the changes in R_{tot} with crack extension as determined from the OLCC method (Equation (4.1)). For the horizontal specimen, R_{tot} varied from about 0.45 at the beginning of the fatigue test to about 0.35 at the conclusion of the test, compared to the R_{app} of 0.1. The crack growth rates of the vertical specimen were noticeably slower and R_{tot} was significantly lower than for the horizontal specimen (although the change of R_{tot} was about the same, evolving from 0.2 to about 0.1). The difference of R_{tot} between the vertical and horizontal specimens can be attributed to differences in the values of $K_{res}(a)$, whereas the similar change of R_{tot} over the course of the test is reflected in the similar trends in the $K_{res}(a)$ profiles for the two orientations. While the spike in $K_{res}(a)$ is not seen in the FCGR data of the vertical specimen, it is reflected in the R_{tot}, since R_{tot} is directly related to $K_{res}(a)$ through Equation (4.1). At the location of the $K_{res}(a)$ spike in **Figure 4.5** (i.e., about 8 mm), R_{tot} for the vertical specimen is 0.35, compared to values between 0.2 and 0.1 for most of the test. For the wrought material, R_{tot} remains close to R_{app} of 0.1 throughout the entire fatigue test due to small values of $K_{res}(a)$ illustrated in **Figure 4.7**.

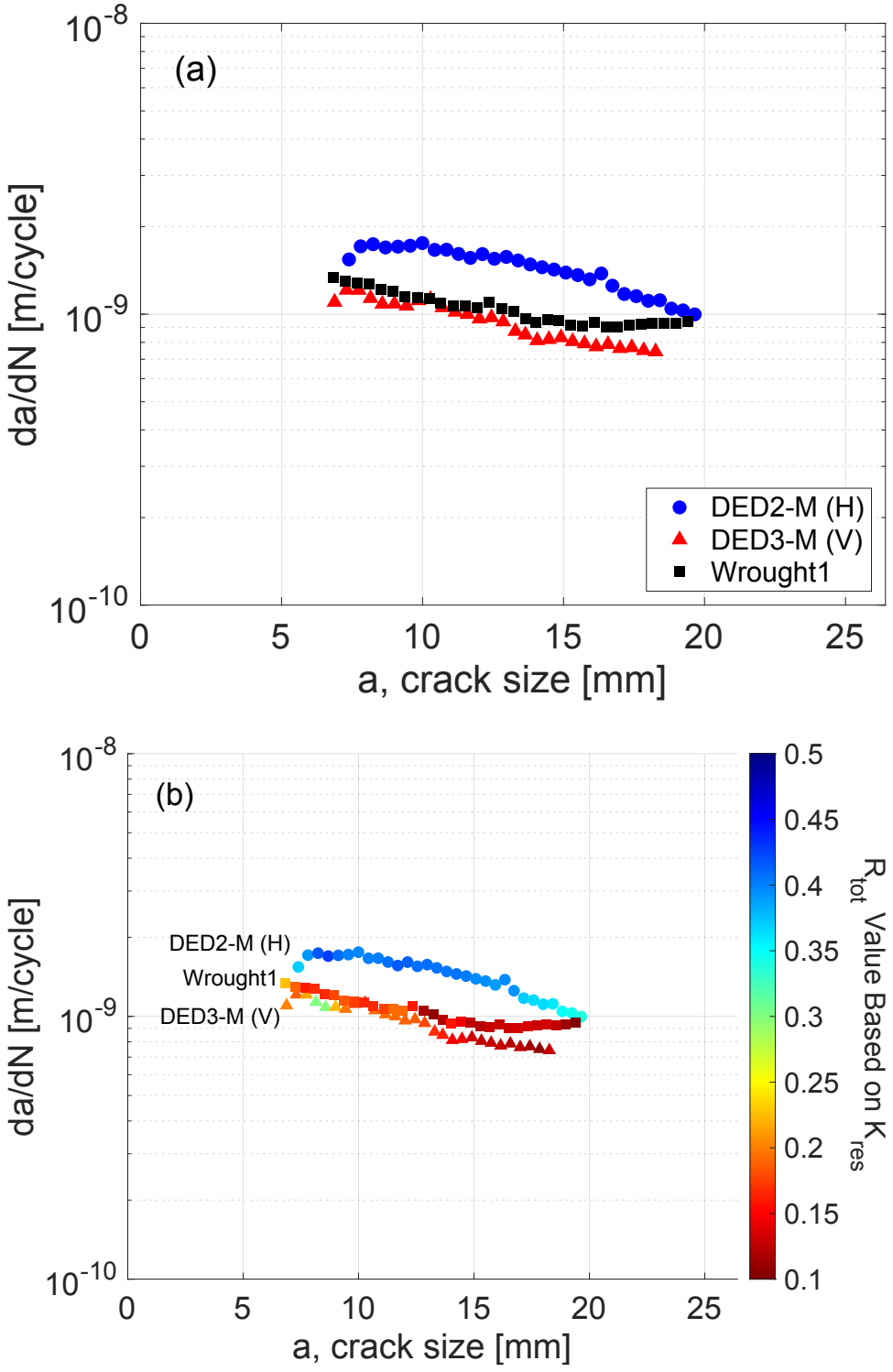

***Figure 4.8**: Fatigue crack growth rates (da/dN) plotted versus crack size for specimens DED2-M (H), DED3-M (V), and Wrought1 tested under constant ΔK_{app} condition (a) without and (b) with R_{tot}.*

The constant ΔK_{app} tests did not result in constant FCGRs in DED material as would be expected in the absence of crack closure or residual stress. In the case of the horizontal specimens, tensile residual stress significantly increased the total stress intensity factor, increasing the mean stress intensity factor and the measured FCGRs as compared to the vertical specimens and wrought material. Since R_{tot} is similar to R_{app} for both the vertical specimens and the wrought specimens, the small differences in measured fatigue crack growth rates between the two conditions are attributed to differences in crack path interactions with the surrounding microstructure.

Fatigue crack growth rates from the decreasing ΔK_{app} tests are shown in **Figure 4.9**. The horizontal specimens exhibit some specimen-to-specimen variability in the measurements, whereas the FCGRs of the vertical specimens agree closely. The crack growth rates in the horizontal specimens are all higher than those in the vertical specimens, consistent with the orientation dependent fatigue behavior described above for these DED materials. The measured fatigue crack growth rates in the near-threshold regime ($da/dN < 10^{-8}$ m/cycle) are higher for both orientations of DED material compared to the annealed wrought condition. Despite similar $K_{res}(a)$ to the vertical DED specimens, the wrought material showed a higher apparent fatigue threshold and lower fatigue crack growth rates for all values of ΔK_{app}. This trend is attributed to crack closure observed in the compliance plots of [16], which decreases the measured FCGRs.

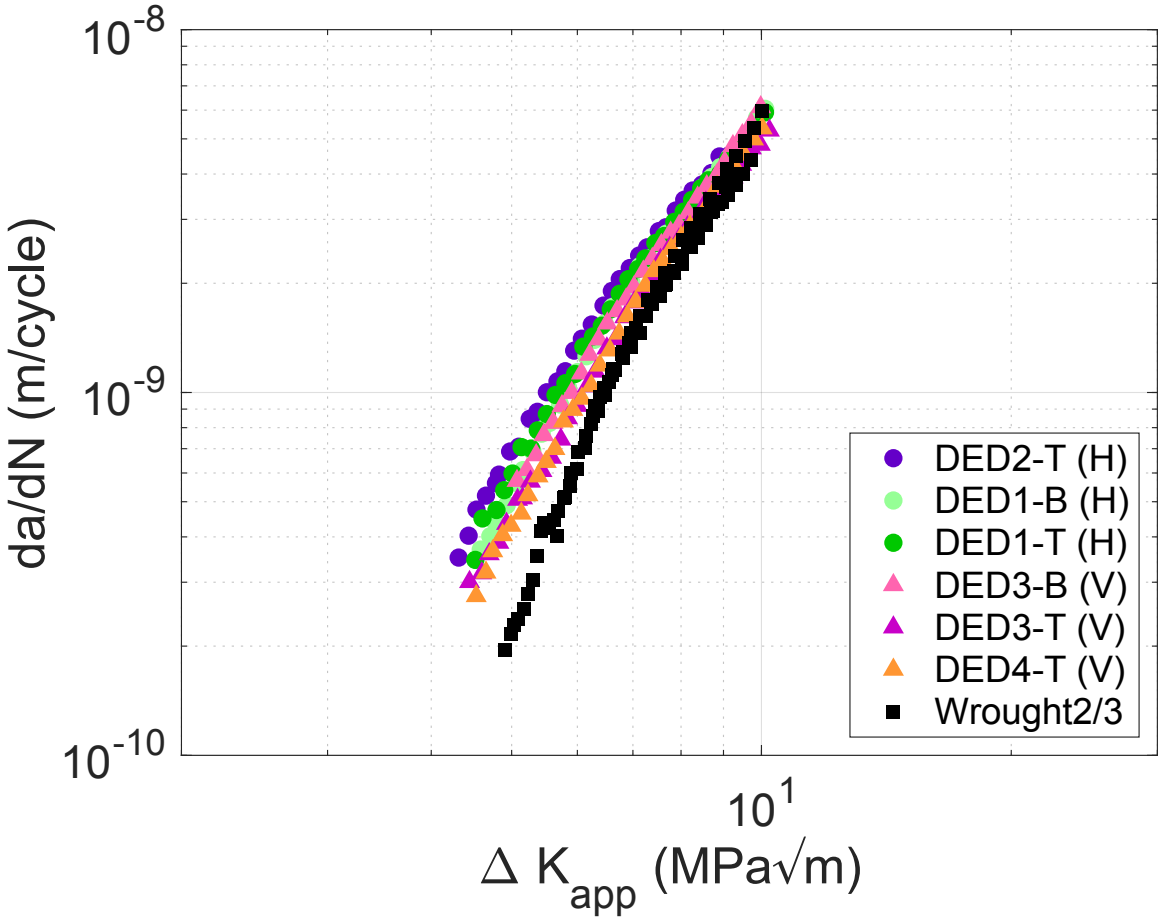

***Figure 4.9**: Fatigue crack growth rates (da/dN) plotted against ΔK_{app} for decreasing ΔK_{app} test conditions.*

4.3.3. Corrected Fatigue Crack Growth Rates

The fatigue crack growth rate test data can be corrected to account for the effects of residual stress by normalizing the rates to a common mean stress or R value. This adjustment can be accomplished with the Walker relationship [22], as expressed in [11, 14]:

$$\Delta K_{corr}(a) = \Delta K_{eff}(a)^{1-n}\left(K_{max,app}(a) + K_{res}(a)\right)^{n}\left(1 - R_{app}\right)^{n} \qquad (4.3)$$

where ΔK_{corr} represents the corrected alternating stress intensity factor. The normalization parameter, n, in Equation (4.3) was found to be 0.25 in a previous study [16], consistent with literature values for structural metals [14, 16, 23]. The adjusted compliance ratio (ACR) method

outlined in the appendix of ASTM E647 was adopted for both materials to account for crack closure and determine ΔK_{eff} [4, 24]. For the DED material in this study, the effects of crack closure are minimal because of the tensile residual stress (H) and crack tip processes that maintained an open crack wake (V). Thus, Equation (4.3) primarily accounts for the contributions of $K_{res}(a)$ to the applied stress intensity factors in the DED material. In contrast, the wrought material exhibits small values of $K_{res}(a)$, but large amounts of crack closure, therefore ΔK_{eff} differs significantly from ΔK_{app} in the correction (Equation (4.3)).

Figure 4.10(a) illustrates the corrected fatigue crack growth rate data for the horizontal and vertical specimens using $K_{res}(a)$ from the OLCC method and ΔK_{ACR}. All data nominally collapse onto a single curve that is shifted to slightly higher ΔK compared to **Figure 4.9**. The FCGRs for the wrought material were similarly analyzed using both ΔK_{ACR} and $K_{res}(a)$ to determine ΔK_{corr} values and are included in **Figure 4.10**(b) for comparison to the DED material. Due to closure (meaning $\Delta K_{ACR} < \Delta K_{app}$) and a nominally zero $K_{res}(a)$, the FCGRs for the wrought material are shifted to slightly lower ΔK. Corrected fatigue crack growth rate data for the DED Type 304L austenitic stainless steel are similar for both orientations (vertical and horizontal) and agree with the FCGRs of the corrected wrought material, demonstrating similar intrinsic material performance between DED and wrought material.

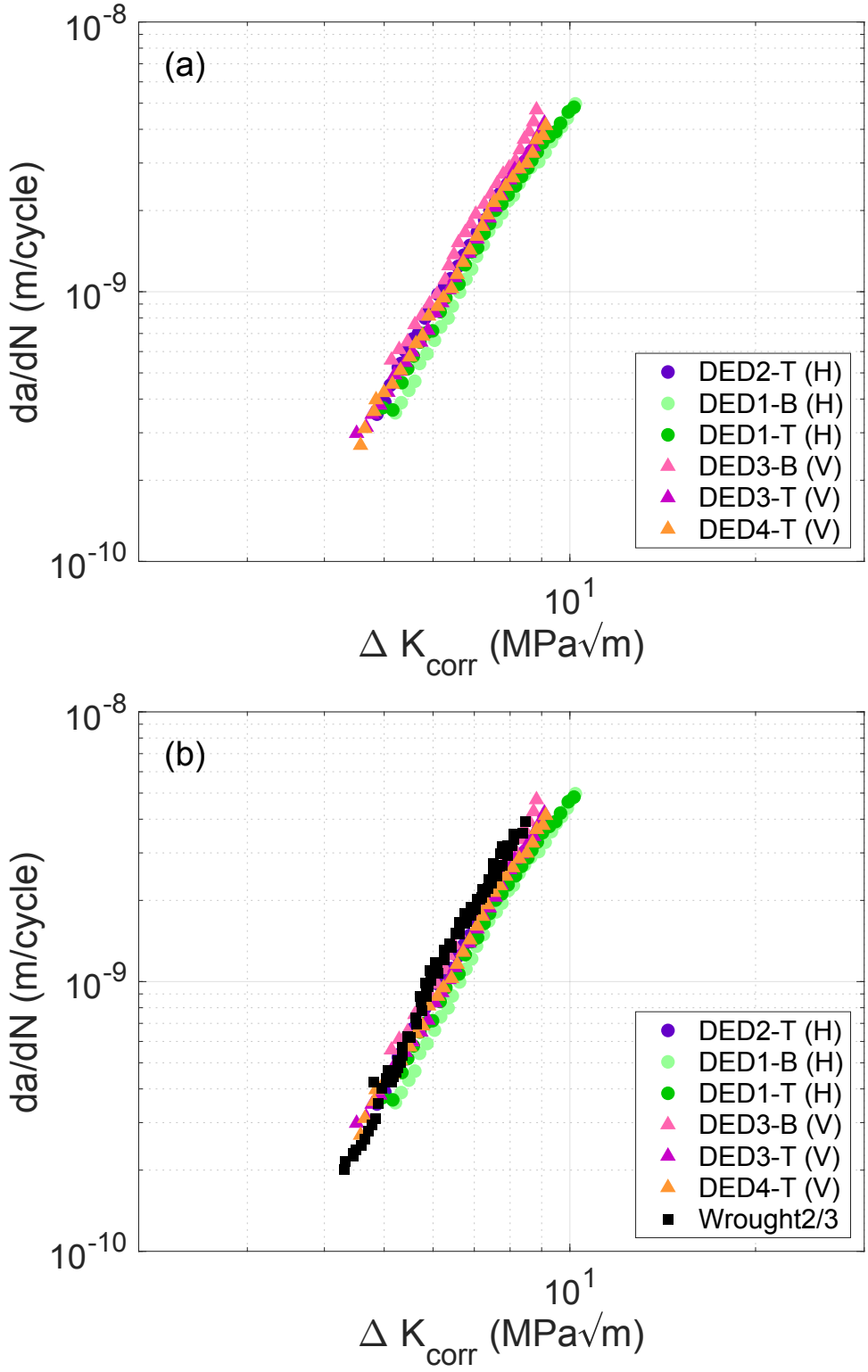

***Figure 4.10**: Fatigue crack growth rates (da/dN) plotted versus ΔK_{corr} for horizontal and vertical crack growth (a) alone and (b) with wrought material included for comparison.*

4.3.4. Characterization of Crack Profiles

Figure 4.11 shows BSE images of grain size and morphology in the Y-Z plane surrounding the crack path of the DED material in the horizontal and vertical crack growth orientations (**Figure 4.11**(a) and **Figure 4.11**(b), respectively). Both images reveal an elongation of grains in the build direction (Z) from the temperature gradient induced during the deposition of the DED material. Furthermore, the influence of the hatch scan pattern is visible in the alternating fine equiaxed grains and larger columnar grains in **Figure 4.11**(a) and **Figure 4.11**(b) at the same scale as the 640 μm hatch spacing [16]. A BSE image of grain size and morphology of the wrought material is shown in **Figure 4.12**. The DED microstructure has a grain size ranging from 1-50 μm, whereas the wrought material has an average grain size of 40 μm with an equiaxed morphology expected from the annealed condition.

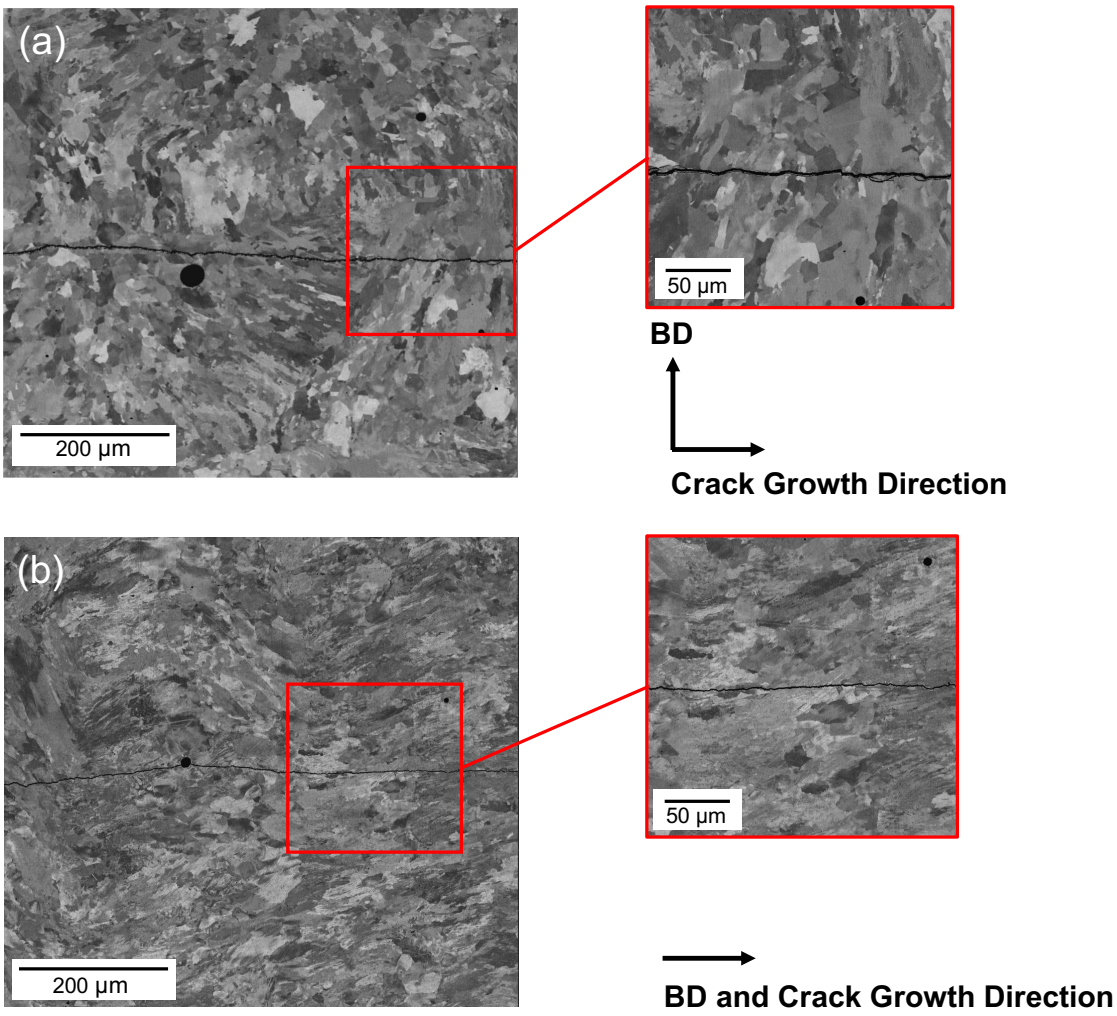

***Figure 4.11**: BSE of crack path of DED material from (a) horizontal crack growth and (b) vertical crack growth with the direction of crack growth indicated by a black arrow.*

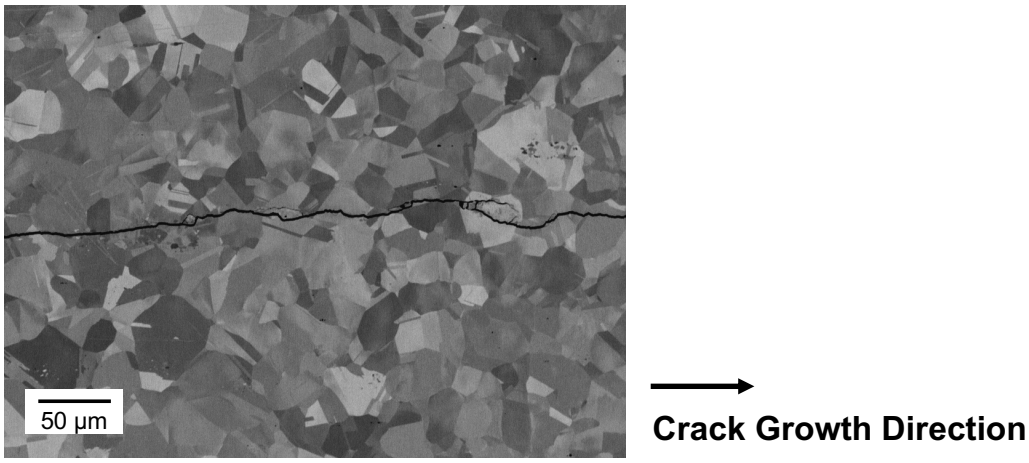

***Figure 4.12**: BSE of crack path of wrought material with the direction of crack growth indicated by a black arrow.*

The DED material exhibits transgranular crack growth with some branching (especially in the horizontal growth direction), but with an overall straight crack path (**Figure 4.11**). Crack paths do not appear to be significantly influenced by the elongated grain shape in the build direction in the DED material; overall crack paths are straight for both orientations. While the magnitudes of $K_{res}(a)$ differ significantly between horizontal and vertical crack growth orientations, the positive residual stress intensity factor from tensile residual stress is sufficient to maintain an open crack wake (no crack closure) and promote a straight crack path. In contrast, the wrought material exhibits greater crack branching and a more tortuous transgranular crack path as compared to the DED material.

4.4. Conclusions

Fatigue crack growth rates of DED Type 304L austenitic stainless steel were measured under constant and decreasing ΔK_{app} conditions. Crack growth was oriented perpendicular (H – horizontal) and parallel (V – vertical) to the build direction to explore the influence of process-induced residual stress on crack growth rates. The on-line crack compliance (OLCC) method with the Schindler influence function (Z(a)) data reduction technique was applied to the test data and showed distinctive residual stress intensity factor (K_{res}) profiles for each orientation. Backscatter electron (BSE) large area images provided insight into the crack path profiles of the DED material. These experiments reveal the following trends:

1. The application of the OLCC method provided values of $K_{res}(a)$ for individual fatigue specimens that showed overall agreement for those of the same orientation. $K_{res}(a)$ was higher in specimens oriented for horizontal crack growth (3.5 – 4.5 $MPa \cdot m^{0.5}$) than those oriented for vertical growth (0.5 – 1.5 $MPa \cdot m^{0.5}$). The small $K_{res}(a)$ values in the

vertical specimens were on the same order as of those in solution annealed (stress-free) wrought material (0 – 1.0 MPa·$m^{0.5}$).

2. The DED material exhibited higher FCGRs as a function of ΔK_{app} when compared to wrought specimens of the same geometry and test conditions. This observation is consistent with the $K_{res}(a)$ values determined from the OLCC method and is attributed to greater residual stress in the build direction. $K_{res}(a)$ combines with the maximum and minimum applied stress intensity factors ($K_{max,app}$ and $K_{min,app}$), resulting in a total stress intensity factor ratio (R_{tot}) that varies as K_{res} varies with crack extension.

3. Using consistent methods, correcting the DED FCGR data for the primary influence of $K_{res}(a)$ shifts the data to higher values of ΔK, reduces the spread in FCGRs due to orientation, and brings agreement with the FCGRs of annealed wrought material corrected primarily for the influence of crack closure, demonstrating similar intrinsic behavior between DED and wrought materials.

4. Both orientations of crack growth in DED material revealed similar crack path behavior and an open crack wake (consistent with tensile residual stress). Differences in crack path due to microstructure in the AM material appear relatively small, especially compared to the influence of residual stress on fatigue crack growth rates.

Acknowledgements

This work was supported by a NASA Space Technology Research Fellowship (CMS – Grant Number 80NSSC19K1132) and material was provided by Sandia National Laboratories. Sandia National Laboratories is a multi-mission laboratory managed and operated by National Technology & Engineering Solutions of Sandia, LLC, a wholly owned subsidiary of Honeywell International Inc., for the U.S. Department of Energy's National Nuclear Security Administration under contract DE-NA0003525. This paper describes objective technical results and analysis. Any subjective views or opinions that might be expressed in the paper do not necessarily represent the views of the U.S. Department of Energy or the United States Government. The material characterization described in this study was carried out at the Advanced Materials Characterization and Testing facility in the Department of Materials Science and Engineering at UC Davis. The SEM was acquired using a Thermo Fisher Quattro S ESEM funded through the NSF-MRI program DMR-1725618.

References

1. Rangaswamy, P., et al., *Residual stresses in LENS (R) components using neutron diffraction and contour method.* Materials Science and Engineering A-Structural Materials Properties Microstructure and Processing, 2005. **399**(1-2): 72-83.

2. Hofmeister, W., et al., *Solidification in direct metal deposition by LENS processing.* JOM-Journal of the Minerals Metals & Materials Society, 2001. **53**(9): 30-34.

3. Li, C.L., Z.Y.; Fang, X.Y.; Guo,Y.B.;, *Residual Stress in Metal Additive Manufacturing.* 4th CIRP Conference on Surface Integrity (CSI 2018), 2018. **Procedia CIRP 71 (2018)**: 348–353.

4. E647-15, *Standard Test Method for Measurement of Fatigue Crack Growth Rates*. 2015. ASTM International: West Conshohocken, PA.

5. Smith, T.R., et al. *Orientation Effects on Fatigue Behavior of Additively Manufactured Stainless Steel*. in *Proceedings of the ASME 2017 Pressure Vessels & Piping Conference*. 2017. Waikoloa, Hawaii, USA.

6. Yadollahi, A., et al., *Effects of crack orientation and heat treatment on fatigue-crack-growth behavior of AM 17-4 PH stainless steel.* Engineering Fracture Mechanics, 2020. **226**: 106874.

7. Yadollahi, A., et al., *Effects of building orientation and heat treatment on fatigue behavior of selective laser melted 17-4 PH stainless steel.* International Journal of Fatigue, 2017. **94**: 218-235.

8. Syed, A.K., et al., *An experimental study of residual stress and direction-dependence of fatigue crack growth behaviour in as-built and stress-relieved selective-laser-melted Ti6Al4V.* Materials Science and Engineering a-Structural Materials Properties Microstructure and Processing, 2019. **755**: 246-257.

9. Riemer, A., et al., *On the fatigue crack growth behavior in 316L stainless steel manufactured by selective laser melting.* Engineering Fracture Mechanics, 2014. **120**: 15-25.

10. Ritchie, R.O., *Near-threshold fatigue-crack propagation in steels.* International Metals Reviews, 1979. **24**(1): 205-230.

11. Donald, J.K. and D.A. Lados, *An integrated methodology for separating closure and residual stress effects from fatigue crack growth rate data.* Fatigue & Fracture of Engineering Materials & Structures, 2006. **30**(3): 223-230.

12. Lados, D.A., D. Apelian, and J.K. Donald, *Fracture mechanics analysis for residual stress and crack closure corrections.* International Journal of Fatigue, 2007. **29**(4): 687-694.

13. Lados, D.A. and D. Apelian, *The Effect of Residual Stress on the Fatigue Crack Growth Behavior of Al-Si-Mg Cast Alloys - Mechanisms and Corrective Mathematical Models.* Metallurgical and Materials Transactions A-Physical Metallurgy and Materials Science, 2006. **37A**: 133-145.

14. James, M., et al., *A Methodology for Partitioning Residual Stress Effects From Fatigue Crack Growth Rate Test Data.* Materials Performance and Characterization, 2016. **5**(3): 194-214.

15. Newman, J.A., et al., *Characterization of Residual Stress Effects on Fatigue Crack Growth of a Friction Stir Welded Aluminum Alloy*. 2015. NASA Langley Research Center, Hampton, VA. Report No. NASA/TM–2015-218685.

16. Smudde, C.M., et al., *The influence of residual stress on fatigue crack growth rates of additively manufactured Type 304L stainless steel.* International Journal of Fatigue, 2022. **162**: 106954.

17. Smith, T.R., et al. *Effects of Extreme Hydrogen Environments on the Fracture and Fatigue Behavior of Additively Manufactured Stainless Steels*. in *Proceedings of the ASME 2019 Pressure Vessels & Piping Conference*. 2019. San Antonio, TX, USA.

18. Smudde, C.M., J.C. Gibeling, and M.R. Hill, *Validation of On-line Crack Compliance Data Analysis Methods for the Residual Stress Intensity Factor.* Submitted to Engineering Fracture Mechanics, 2022.

19. Schindler, H.J., W. Cheng, and I. Finnie, *Experimental determination of stress intensity factors due to residual stresses.* Experimental Mechanics, 1997. **37**(3): 272-277.

20. Schindler, H.J., *Determination of Residual Stress Distributions from Measured Stress Intensity Factors.* International Journal of Fracture, 1995. **74**: R23-R30.

21. Olson, M.D. and M.R. Hill, *Determination of residual stress intensity factor in the compact tension coupon.* Engineering Fracture Mechanics, 2012. **88**: 28-34.

22. Dowling, N.E., *Mechanical behavior of materials : engineering methods for deformation, fracture, and fatigue*. 4th ed. 2013, Boston: Pearson. Chapter 9: 416-490.

23. Ronevich, J.A., C.R. D'Elia, and M.R. Hill, *Fatigue crack growth rates of X100 steel welds in high pressure hydrogen gas considering residual stress effects.* Engineering Fracture Mechanics, 2018. **194**: 42-51.

24. Donald, J.K., G.H. Bray, and R.W. Bush, *An evaluation of the adjusted compliance ratio technique for determining the effective stress intensity factor.* Fatigue and Fracture Mechanics: Twenty-Ninth Volume, ASTM STP 1332, American Society for Testing and Materials, West Conshohocken, PA, 1999: 674-695.

Chapter 5:
Evaluation of Residual Stress Reproducibility and Orientation Dependent Fatigue Crack Growth in PBF Stainless Steel [4]

Abstract

The complex thermal gradients of additive manufacturing (AM) result in residual stress and distinctive grain morphologies that influence mechanical performance and contribute to concern regarding the fatigue properties of AM parts. In this study, residual stress, microstructure, and fatigue crack growth rates were compared in AM Type 304L stainless steel produced by laser powder bed fusion (PBF) on different systems using similar process parameters. Residual stress was remarkably consistent in the PBF builds. Backscatter electron large area grain maps revealed similar grain morphologies in the different builds, all of which exhibited elongated grains in the build direction and inhomogeneous grain size and shape. Fatigue crack growth investigated both parallel and perpendicular to the build direction revealed higher measured fatigue crack growth rates in the near-threshold regime in both orientations of the PBF material compared to wrought material. The difference in near-threshold fatigue crack growth is attributed to the influence of processing-induced residual stress, which was quantified by the residual stress intensity factor determined using the on-line crack compliance method. These values were then used to account for residual stress effects to reveal a convergence of the corrected FCGR data of PBF and wrought specimens.

Keywords: Additive manufacturing, laser powder bed fusion, residual stress, residual stress intensity factor, fatigue crack growth

[4] Submitted: Smudde, C.M., et al., *Evaluation of Residual Stress Reproducibility and Orientation Dependent Fatigue Crack Growth in PBF Stainless Steel.* Additive Manufacturing, 2022.

5.1. Introduction

Laser powder bed fusion (PBF) is one of the most common additive manufacturing (AM) processes and offers freedom in the design and optimization of engineering components. However, the current incomplete understanding of processing-structure-property relationships and the consequent structural reliability of as-built components are limiting factors in the widespread adoption of AM technology. Specifically, in the cyclic loading conditions of fatigue, accurate prediction of damage evolution is still a major challenge in engineering design [1, 2]. The layer-by-layer build process of PBF material leads to high temperature gradients, fast cooling rates, and remelting of material as subsequent layers are added. This complex thermal history results in high tensile residual stress near (at and just below) surfaces and compressive residual stress in the center of resultant vertical wall builds [3, 4]. In addition, PBF materials typically have fine nonequilibrium and inhomogeneous microstructures, the development of which is controlled by the thermal history of the deposition process [5-7]. Both residual stress and microstructure morphology formed in PBF influence fatigue performance, yet the optimum methodology to either mitigate or account for their effects has not been established [3, 8, 9]. In addition, the reproducibility of residual stress has not been explored previously [10]. Engineering estimates of fatigue life and structural reliability depend on knowledge and repeatability of measured fatigue crack growth rates. Therefore, to accurately predict fatigue performance and promote PBF technology, it is necessary to understand the effects of material characteristics, such as residual stress and microstructure, on fatigue crack growth rates (FCGRs) in as-built material, as well as to explore build-to-build variability.

Residual stress influences fatigue behavior, specifically FCGRs, by contributing to stress at the crack tip. The resulting residual stress intensity factor, $K_{res,}$ is a function of crack size,

orientation, and location in the AM build. Under cyclic loading, K_{res} adds both to the maximum and minimum applied stress intensity factors ($K_{app,max}$ and $K_{app,min}$). Because K_{res} is known to vary considerably with crack size, FCGRs measured in residual stress-bearing materials are generated under a non-constant total stress intensity factor ratio ($R_{tot} = (K_{min,app}+K_{res})/(K_{max,app}+K_{res})$), which differs from the applied ratio ($R_{app} = K_{min,app}/K_{max,app}$). Evolving K_{res} and R_{tot} significantly influence FCGRs in PBF material [11, 12], primarily in the near-threshold regime ($da/dN < 10^{-8}$ m/cycle [13]) where applied loads are low and K_{res} can approach $K_{app,min}$ and/or $K_{app,max}$. Previous investigations of near-threshold FCGRs reported anisotropic behavior that was attributed to the unique columnar grain microstructures typical of PBF material [11, 14, 15]. In these studies, the machine, build size, and specimen geometry all differed, and the relationships between fatigue, orientation, and microstructure were not consistent. This lack of consistency of processing conditions and results in previous studies demonstrates that the repeatability and reproducibility remain challenging in PBF technology [10].

Quantifying residual stress and orientation dependence of FCGRs in PBF material is an important step to understanding the reproducibility of the process and fatigue performance of the as-built materials. Numerical models are typically used to account for the effects of residual stress on FCGRs and predict the mechanical performance of PBF structures [16]. However, an experimental approach of measuring K_{res} by the on-line crack compliance (OLCC) method can be used to account for the influence of residual stress in traditional fatigue crack growth rate data [17-23]. This approach enables the determination of K_{res} as a function of crack size and has successfully been used to account for K_{res} in AM materials produced via directed energy deposition (DED) [17].

The main objective of this study is to evaluate and compare residual stress in PBF components in four similarly processed Type 304L stainless steel AM builds produced via PBF on three different AM platforms. Additionally, the dependence of FCGRs on orientation of crack growth is explored. Slitting measurements are used to evaluate the reproducibility of residual stress in these PBF materials. Microstructure is explored through backscatter electron (BSE) large area grain maps of grain morphologies in the different builds. Fatigue crack growth rates are evaluated in compact (C(T)) fatigue specimens from each build and crack growth in the near-threshold regime is assessed in two orientations: parallel (vertical) and perpendicular (horizontal) to the build direction. The influence of residual stress on FCGRs is quantified by K_{res} as determined by the OLCC method for each individual fatigue specimen [17-23]. These values of K_{res} are then used to correct measured fatigue crack growth rates [17, 18, 20, 21, 24, 25] to compare the intrinsic fatigue performance of PBF with that of annealed wrought material.

5.2. Material and methods

5.2.1. Material

Four nominally identical vertical D-ring wall structures (**Figure 5.1**) were built by laser powder bed fusion on three different commercial machines (EOS, Renishaw and 3D Systems) at three independent laboratories (L, N, and S, respectively). Two equivalent builds were produced on the 'L' platform approximately one year apart (designated as L1 and L2). All builds utilized the same heat of Type 304L stainless steel powder with the nominal composition shown in **Table 5.1**. Each laboratory independently developed proprietary processing parameters to optimize deposited material density and tensile ductility. In general, the laser power was 220-240W with a scan speed of ~1 m/s, resulting in similar energy densities of ~60 J/mm^3 in each build. All three laboratories utilized a hatch spacing of 0.1 mm. Measured tensile properties for the PBF material

under evaluation revealed yield strengths in the range of 416-440 MPa, demonstrating similar strength among the builds [26].

Table 5.1: Type 304L stainless steel powder composition (wt%)

Fe	Cr	Ni	Mn	Si	C	N	P	S
Bal	18.4	9.8	1.4	0.6	0.018	0.06	0.012	0.005

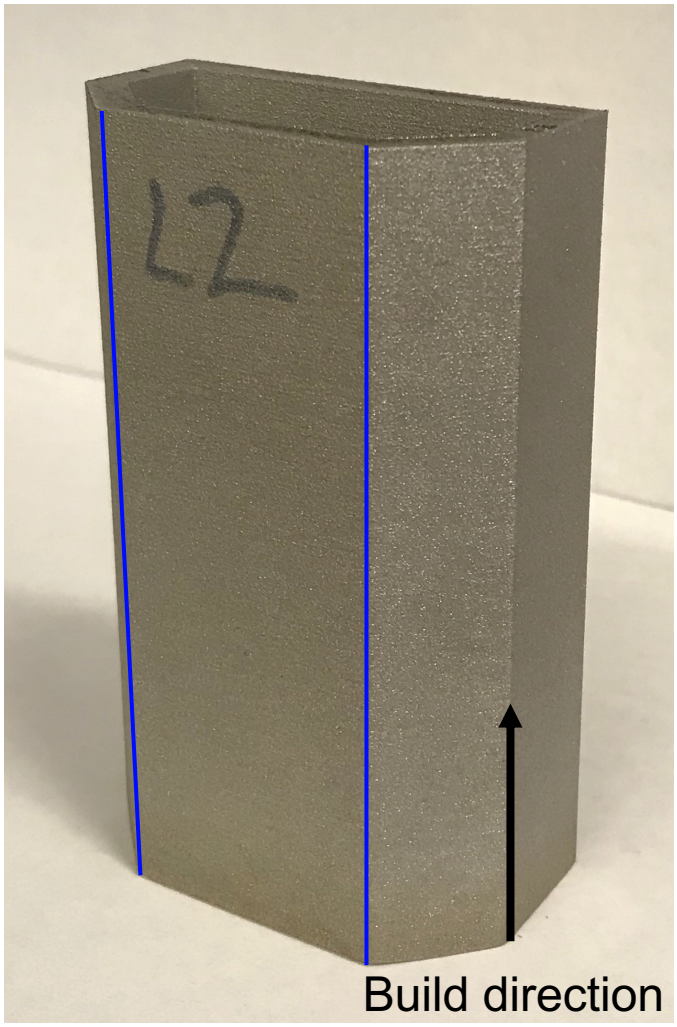

Figure 5.1*: PBF-L2 with material (plate) isolation indicated by thin vertical blue lines and the build direction by the arrow.*

Material for fatigue testing was isolated from the PBF builds via wire electrical discharge machining (EDM). The plate of material from which fatigue specimens were extracted is within the thin vertical blue lines shown in **Figure 5.1**. Two builds (PBF-L1 and PBF-S) were designated for the evaluation of FCGR behavior perpendicular to the build direction, meaning the crack growth direction was horizontal (H) and loading was applied along the build direction. PBF-L2 and PBF-N were designated for the evaluation of FCGR behavior parallel to the build direction where the crack growth direction was vertical (V), and loading was applied normal to the build direction (**Figure 5.2**). From each PBF build, three C(T) fatigue test specimens (bottom (B), middle (M), and top (T)) were extracted from the removed plates for testing under constant and decreasing applied alternating stress intensity factor ($\Delta K_{app} = K_{app,max} - K_{app,min}$) conditions as designated in **Table 5.2**. Each specimen is designated by build laboratory, extraction position in relation to the build plate, and crack growth orientation. For example, PBF-L1-M (H) is the middle specimen from laboratory L PBF build evaluating horizontal crack growth.

Table 5.2: Specimen designation for K_{res} and FCGR evaluation in this study

Build	Fatigue Crack Growth Orientation	Specimen Position and Test Condition	Specimen Position and Test Condition
PBF-L1	H - horizontal	B, T – decreasing ΔK_{app}	M – constant ΔK_{app}
PBF-L2	V - vertical	B, T – decreasing ΔK_{app}	M – constant ΔK_{app}
PBF-S	H - horizontal	B, T– decreasing ΔK_{app}	M – constant ΔK_{app}
PBF-N	V - vertical	B, T– decreasing ΔK_{app}	M – constant ΔK_{app}

In addition to the PBF material, solution annealed dual certified wrought Type 304/304L stainless steel of a composition previously reported [24] was investigated for comparison. Four C(T) specimens with the same width and thickness as the PBF specimens were tested under constant (Wrought 1 and Wrought 2) and decreasing (Wrought 3 and Wrought 4) ΔK_{app} loading conditions.

5.2.2. Material Characterization

Large area backscatter electron (BSE) grain morphology mapping was performed on each build to evaluate the microstructures of PBF materials processed on different AM platforms. Crack tip regions were extracted via wire EDM from specimens that had been tested at constant ΔK_{app} (PBF-L1-M (H), PBF-L2-M (V), PBF-S-M (H), PBF-N-M (V), and Wrought 1). These crack-tip sections were then mounted in epoxy and progressively ground with SiC paper down to 1200 grit. Polishing with alumina suspensions of 3 μm, 1 μm, and 0.3 μm then preceded automatic vibropolishing for 9 hours with 0.05 μm colloidal silica. A Thermo Fisher Quattro ESEM operating at 5 kV and a current of 0.46 nA was used to examine grains in the PBF and wrought materials.

5.2.3. Slitting Measurements and K_{res} Quantification

Prior to machining C(T) specimens for fatigue testing, process-induced residual stress in the PBF material was evaluated. Measurements were made on the plates removed from the builds as shown in **Figure 5.1**. Build direction residual stress as a function of position across the plate was determined by the slitting method [27] on the planes between specimen positions indicated by horizontal black lines in **Figure 5.2**. Micro-Measurements CEA-09-062UWA-350 strain gages were applied on the EDM surface (indicated by yellow rectangles in **Figure 5.2**) at two equally spaced locations (1 and 2). Incremental cutting along the planes of interest at fixed increments of 0.84 mm resulted in a redistribution of residual stress and a corresponding change in strain at the

back face (back-face strain, BFS) measured as a function of cut depth. Detailed descriptions of the slitting method are found in the literature [25, 27, 28]. Similar slitting measurements were performed on C(T) specimens during the introduction of the notch as indicated by the red lines in **Figure 5.2**.

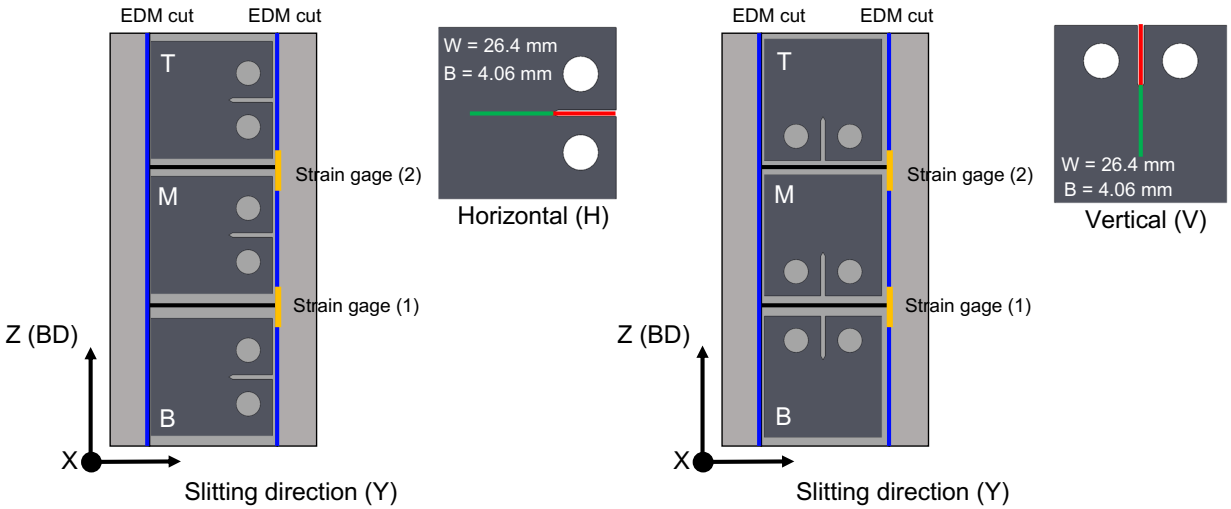

***Figure 5.2**: Schematic of slitting measurements and C(T) specimen extraction in the PBF material. Blue lines correspond to blue lines of Figure 1.*

Values of Mode I K_{res} (driven by residual stress acting normal to the cut plane) in the notch were determined from the residual BFS data, ε_{res}, as a function of crack size (cut depth) collected during the slitting measurements. The strain values and a geometry dependent influence function (Z(a)) as described by Schindler [29, 30] were used in Equation (5.1) to determine K_{res}:

$$K_{res}(a) = \frac{E'}{Z(a)} \frac{d\varepsilon_{res}(a)}{da} \tag{5.1}$$

where E′ is the elastic modulus (plane stress) and the derivative of the strain with respect to cut depth is approximated using a quadratic polynomial regression of 2N + 1 data points centered around each value of cut depth [13, 17, 23], with N = 2 for the slitting measurements. The Schindler

influence function (Z(a)) for the C(T) geometry was available from the earlier work of Olson and Hill [31].

The on-line crack compliance method was used to determine the residual stress intensity factor, K_{res}, in the crack plane (green lines of **Figure 5.2**) from compliance data generated during fatigue tests [18-23]. Similar to relaxation during the slitting measurement, residual stress normal to the crack plane relaxes and redistributes as the crack extends, resulting in an offset of the compliance data (load versus deformation), which can be quantified as residual strain (ε_{res}). For finite intervals of crack growth, an approximation of the derivative of residual strain with respect to crack size (a) can be used to determine K_{res} using Equation (5.1). The OLCC method enables measurement of K_{res} while simultaneously collecting fatigue crack growth rate data. When calculating the derivative in Equation (5.1) for OLCC, N = 12 was used because ε_{res} data from the fatigue tests had more noise than those in a slitting experiment. Furthermore, a lower value of N was used for small crack sizes to minimize data truncation as described in previous work [17].

5.2.4. K control fatigue crack growth rate tests

Compact specimens of width (W) 26.4 mm and thickness (B) 4.06 mm were used to evaluate fatigue crack growth rate behavior. Fatigue testing was performed on an Instron 1331 servohydraulic load frame controlled by MTS 790.40 TestStar software under K-control conditions in lab air at an applied stress intensity factor ratio of $R_{app} = 0.1$ and frequency of 10 Hz. The software was modified to accept a BFS input for the compliance method of monitoring crack size [13] in which the modulus was assumed to be that of a fully dense austenitic stainless steel, 200 GPa [17, 24]. For all fatigue tests, a Micro-Measurements CEA-13-032UWA-350 strain gage was centered on the crack plane on the back face of each C(T) specimen with an additional gage

on a secondary specimen for temperature compensation. Strains were monitored using a Vishay Instruments P3500 strain indicator with a calibrated output to the MTS TestStar controller.

Constant ΔK_{app} fatigue tests were performed at K_{max} of 7.3 MPa·m$^{0.5}$. Decreasing ΔK_{app} tests began at an initial K_{max} of 11.6 MPa·m$^{0.5}$ and employed a load shedding parameter of C = -0.08 mm^{-1} [13]. Prior to fatigue crack growth rate testing, all specimens were precracked under decreasing ΔK_{app} conditions using the crack growth routine (rather than the precracking routine) in the TestStar software to a crack size of 6.6 mm (a/W = 0.25) in accordance with ASTM E647 [13]. In this manner, compliance data at the crack size of the notch were saved for each specimen, allowing complete post-test analysis of data from notch size to final crack size. Compliance data with 500 data points from three consecutive cycles were recorded to represent an average fatigue cycle for each crack size and were saved at crack size increments of 0.051 mm. After testing, all compliance data were then analyzed in MATLAB [32] to determine crack size, FCGRs, ΔK_{app}, and K_{res} via the OLCC method. Post-test analysis of the data verified crack size as calculated by the TestStar software and facilitated the determination of corrected alternating stress intensity factors (ΔK_{corr}) that account for the effects of varying R_{tot} due to K_{res} contributions [18-20].

5.3. Results and discussion

5.3.1. Materials Characterization

Backscatter electron images of grain size and morphology of the PBF and wrought materials are shown in **Figure 5.3** and **Figure 5.4**, respectively. Despite different machines and manufacturing details, all four PBF builds have similar grain morphologies (size and shape), showing an elongation of grains in the build direction (Z) from the directional solidification of the material. Qualitatively, PBF-S has slightly smaller average grain size as compared to the others, PBF-L1 has slightly larger grain size, and PBF-L2 and PBF-N are indistinguishable from each

other. The similarities in microstructure are expected due to the similar energy densities used in the processing of the Type 304L stainless steel powders. The energy density, which is a function of laser power and scan speed, controls the thermal history and therefore the cooling rates [5-7]. The cooling rates and the cyclic reheating of subsequent layers dictate microstructure development. The similar size and shape of grains in these four PBF materials is nominally consistent with the similar processing conditions and suggests mechanical properties may also be comparable. In comparison, the wrought material (**Figure 5.4**) features an equiaxed and uniformly-sized grain structure with grain sizes similar to the long axis of the elongated grains seen in the PBF materials. As such, it can be inferred from these evident differences in grain morphology that FCGRs in the near-threshold regime may differ between annealed wrought and AM materials.

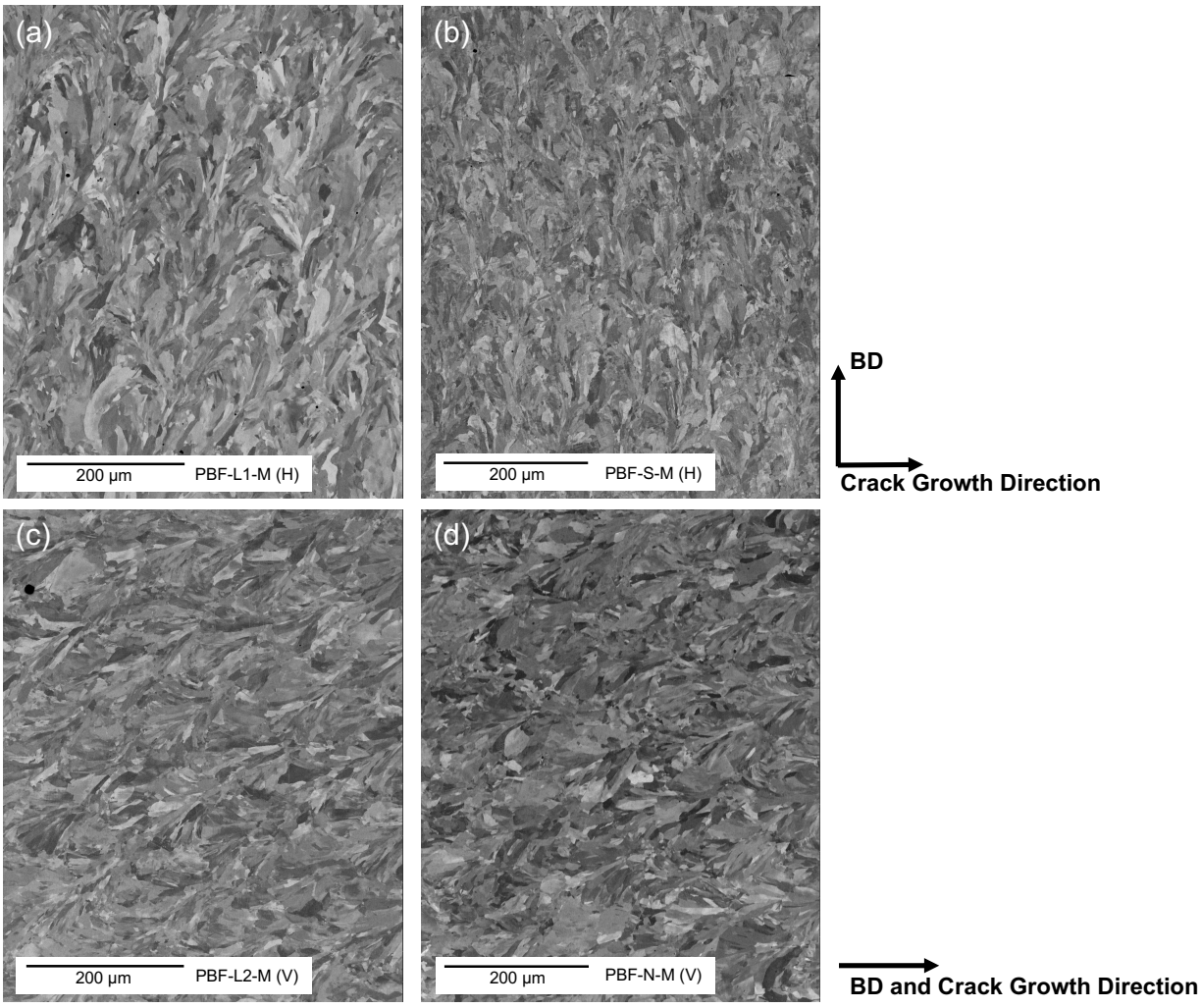

***Figure 5.3**: BSE large area grain maps of PBF material (a) PBF-L1-M (H), (b) PBF-S-M (H), (c) PBF-L2-M (V), and (d) PBF-N-M (V) from the middle (M) C(T) specimens.*

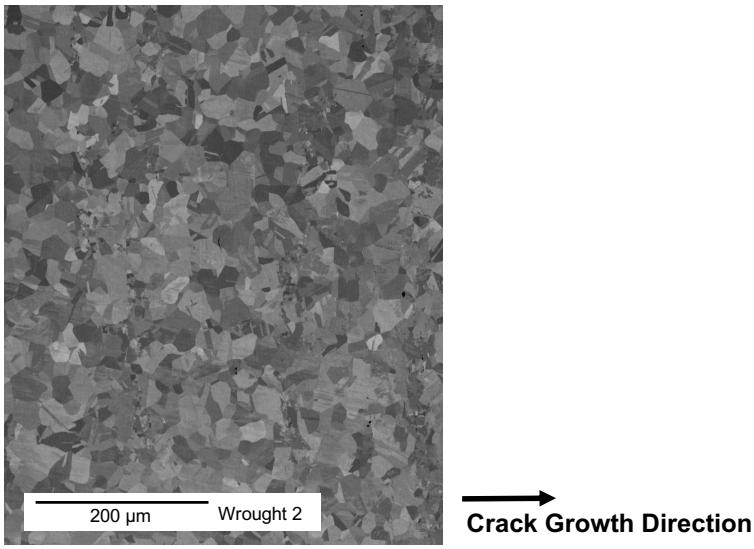

Figure 5.4*: BSE large area grain maps displaying equiaxed grain structure of wrought material.*

5.3.2. Slitting Measurements

For plates from all PBF builds, tensile residual stress of approximately 200 MPa is present at the edges along with compressive residual stress of about -100 MPa near the center as shown in **Figure 5.5**. For each build, there is not a significant difference in residual stress at the different heights above the build plate (1 and 2 in **Figure 5.2**). Since each PBF build has a large number of layers and rapid cooling rates from the deposition process, large residual stress was expected [11]. The maximum values determined during slitting are approximately 50% of the measured yield strengths of the materials. All four PBF builds exhibit consistent residual stress within ±10 MPa over most of the profiles. These results demonstrate reproducibility of residual stress in PBF builds of the same geometry produced at different laboratories, on different machines, and using similar energy densities. After the plate slitting measurements, C(T) specimens were extracted from the PBF material for fatigue testing (**Figure 5.2**). The tensile residual stress at the edges of the PBF material is expected to result in positive (tensile) K_{res} in the edge crack C(T) specimens.

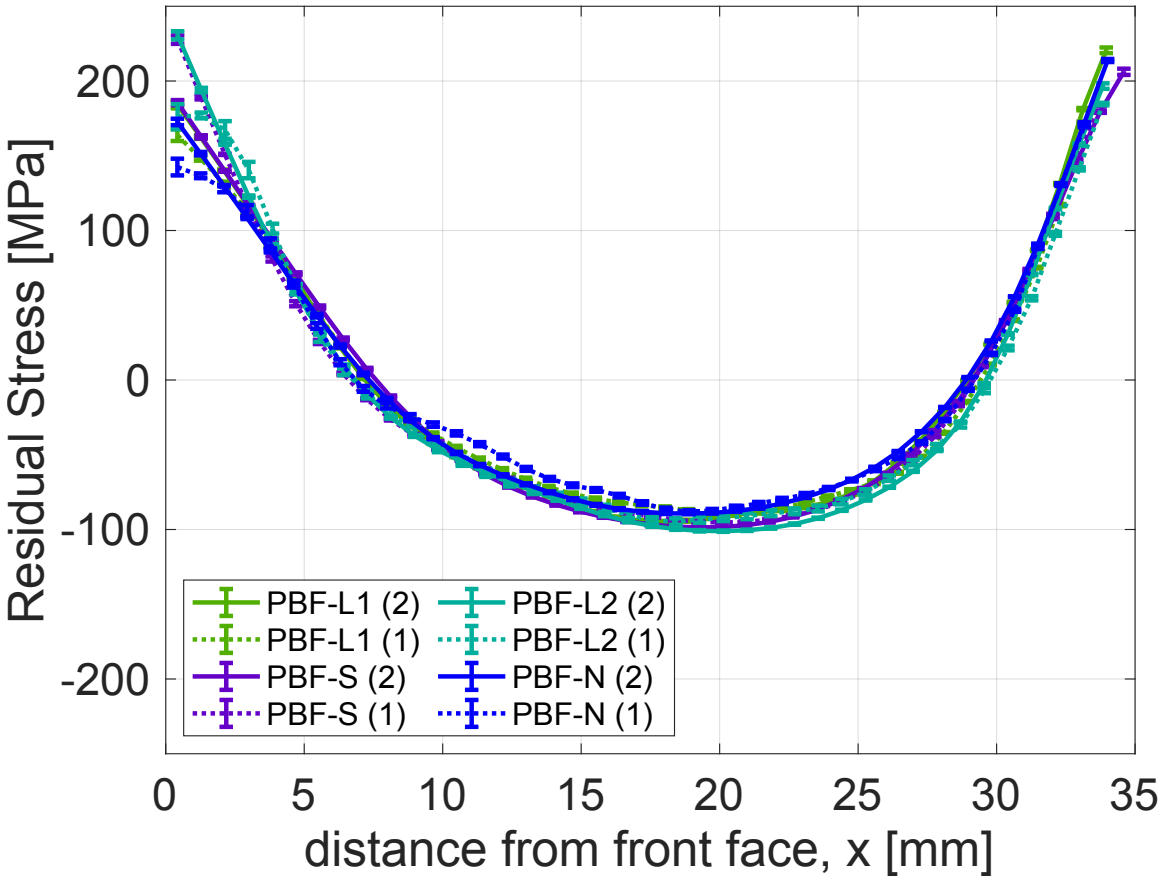

***Figure 5.5**: Residual stress profiles obtained from slitting of PBF wall builds at locations 1 and 2 as shown in **Figure 5.2**.*

5.3.3. K_{res} in C(T) Specimens

The residual stress intensity factors (K_{res}) as a function of crack size for each specimen are shown in **Figure 5.6**. The locations of the notch tip (solid vertical line) and the end of the precrack zone (dotted vertical line) are indicated. Prior to precracking, a slitting measurement was performed to find K_{res} in the notch plane (left of the solid line). Subsequently, the OLCC method was used to determine K_{res} in the crack plane (right of the dashed line). As such, a profile of K_{res} for the majority of the C(T) width could be determined. In each figure (**Figure 5.6**(a)-(d)), K_{res} from notch slitting and OLCC of two wrought specimens is included for comparison.

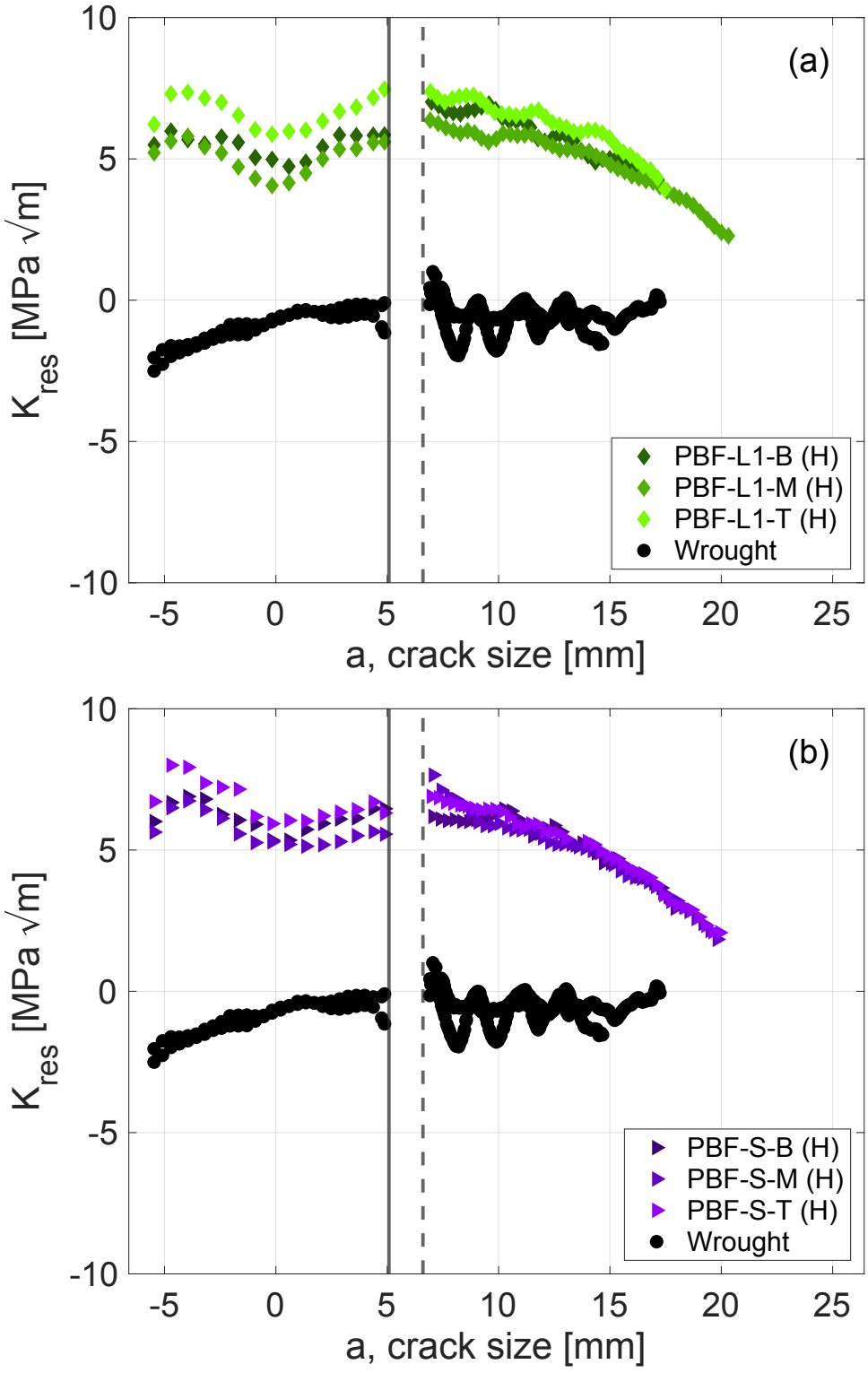
(a)
PBF-L1-B (H)
PBF-L1-M (H)
PBF-L1-T (H)
Wrought
K_{res} [MPa $\sqrt{m}$]
a, crack size [mm]
(b)
PBF-S-B (H)
PBF-S-M (H)
PBF-S-T (H)
Wrought
K_{res} [MPa $\sqrt{m}$]
a, crack size [mm]

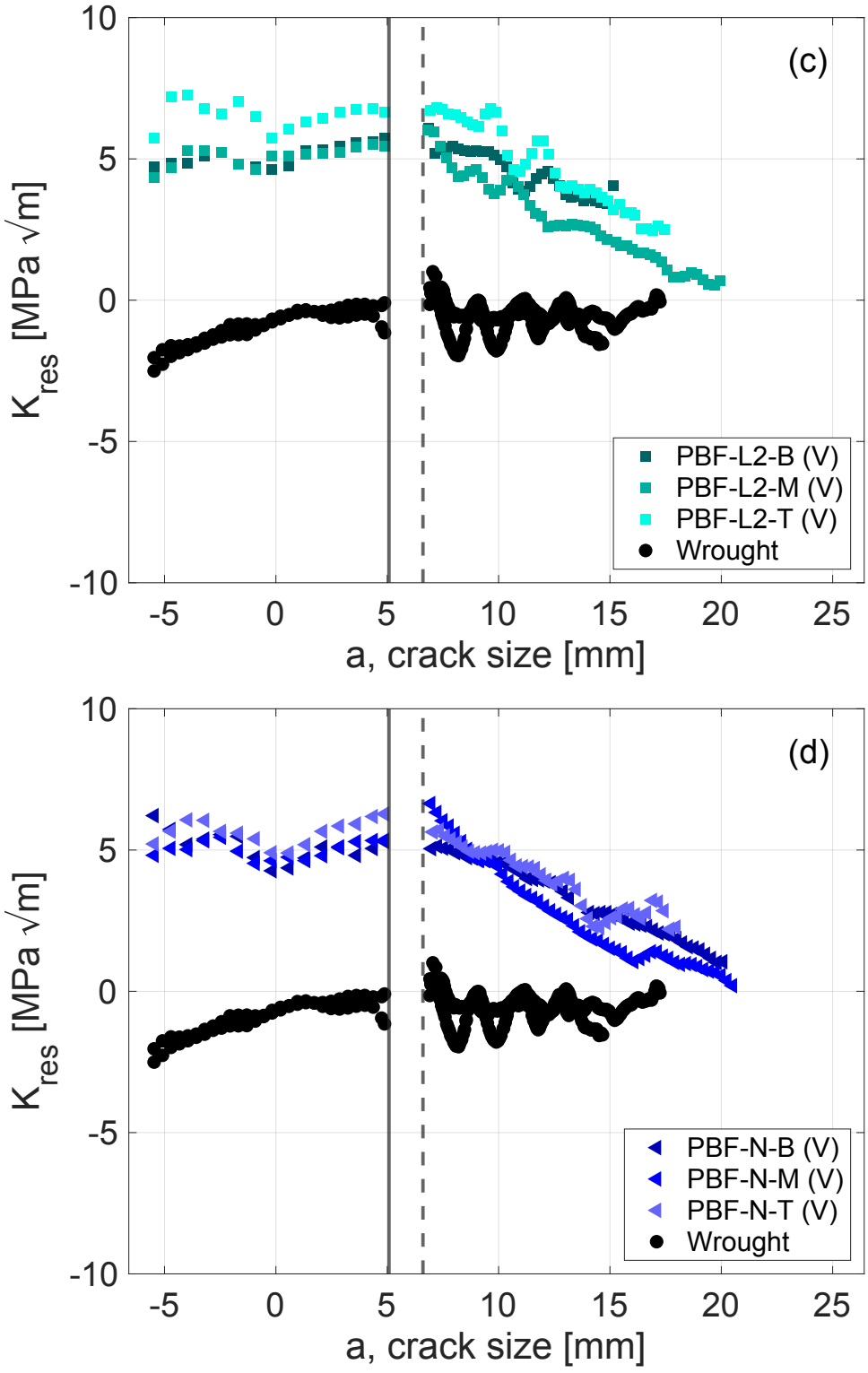

***Figure 5.6**: Full K_{res} profile for PBF C(T) fatigue specimens with notch slitting to the left of the solid line and OLCC to the right of the dashed line (end of precrack) compared to selected wrought data.*

Overall, K_{res} is consistent for all specimens. This is the case whether tests were performed using constant ΔK_{app} (M) or decreasing ΔK_{app} tests (B and T), and is independent of specimen position (B, M, and T), demonstrating there is minimal variation of residual stress in the build direction. The horizontal crack growth specimens (PBF-L1 (H) and PBF-S (H)) were all found to have similar K_{res} values (6.5 - 7.5 MPa·$m^{0.5}$) at the notch size. The K_{res} values decreased gradually throughout crack growth, but fatigue tests were terminated prior to K_{res} reaching zero. Evaluation of the vertical crack growth specimens (PBF-L2 (V) and PBF-N (V)) revealed a K_{res} profile of slightly smaller magnitude than those from the horizontal test specimens (5.0 - 6.5 MPa·$m^{0.5}$) at the notch size, but K_{res} for the V orientation approached zero more rapidly as the cracks extended than in the H orientation. There is some difference in K_{res} between specimens at different build heights in the vertical specimens (PBF-L2 (V) and PBF-N (V)), suggesting the residual stress component in the Y-direction is not as uniform as the component in the Z-direction. All wrought specimens have K_{res} values that agree well and are approximately zero. While the two wrought specimens display some fluctuations in OLCC K_{res} data, the slitting K_{res} are in excellent agreement. One possible contributor to the larger fluctuations in OLCC K_{res} for wrought specimens could be crack closure that was observed as deviations from linearity in the compliance data of all wrought specimens. Crack closure may interfere with residual strain measurement. In comparison, the positive K_{res} in PBF specimens eliminated closure, as evident in their fully linear compliance data.

5.3.4. Fatigue Crack Growth Rate Behavior

Figure 5.7 illustrates the fatigue crack growth rates at constant ΔK_{app} = 6.6 MPa·$m^{0.5}$ for horizontal and vertical PBF specimens compared to values in wrought specimens. In all PBF specimens, FCGRs decrease monotonically with crack size, consistent with the general shape of the K_{res} profiles. The FCGRs for the horizontal specimens, both PBF-S (H) (right triangles) and

PBF-L1 (H) (diamonds), agree very well. The FCGRs of PBF-N (V) (left triangles) are initially similar to the two horizontal specimens (2.5 x 10^{-9} m/cycle near a = 7 mm) but deviate at longer crack sizes corresponding to the steeper decline in K_{res} profile for this orientation. The FCGRs of PBF-L2 (V) (squares) are approximately parallel to PBF-N (V) but shifted to slightly lower rates (2 x 10^{-9} m/cycle near a = 7 mm). Both wrought specimens (circles) display similar FCGRs, which are demonstrably lower than all PBF rates.

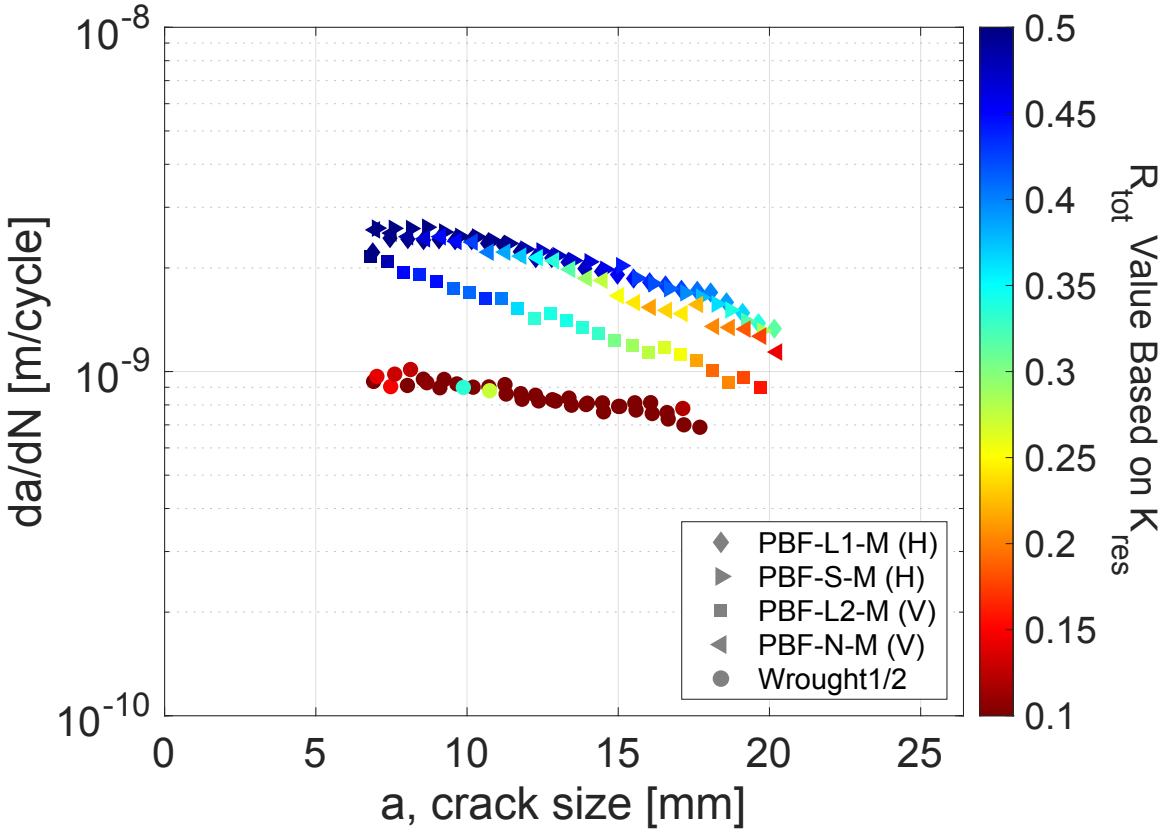

***Figure 5.7**: FCGRs (left axis) from constant ΔK_{app} = 6.6 MPa·$m^{0.5}$ tests of PBF and wrought materials. R_{tot} from K_{res} determined via OLCC method is shown in color (right axis).*

Cracks growing in both orientations in PBF specimens experience significant contributions of positive K_{res} to the total stress intensity factors, which lead to higher R_{tot} in PBF compared to wrought and is consistent with higher measured FCGRs. Since the K_{res} in the (H) specimens decreases more gradually towards zero as compared to the (V) specimens (**Figure 5.6**), the FCGRs

also decrease more gradually. In the case of the wrought material, the effects of crack closure increase as the crack extends, resulting in a decrease in FCGRs with crack size. PBF-L2-M (V), despite having similar values of K_{res}, exhibits lower FCGRs compared to the other specimens for all values of crack size. Post-test examination of the fracture surface of PBF-L2-M (V) revealed a twisted crack path (**Figure 5.8**); partial shear loading on the twisted crack could have led to lower fatigue crack growth rates in this specimen.

Figure 5.8*: Photograph of twisted crack path of PBF-L2 -M (V). Location in the specimen indicated by the red box.*

For all specimens, the constant ΔK_{app} tests do not result in a constant fatigue crack growth rate. To understand this effect, the K_{res} profiles of **Figure 5.6** were used to calculate for each specimen the total stress intensity factor ratio, R_{tot}, as a function of crack size. The color scale of **Figure 5.7** shows that R_{tot} differs from R_{app} and how it evolves with crack extension due to the presence of residual stress. In the horizontal specimens (PBF-L1 (H) and PBF-S (H)), R_{tot} decreases from about 0.5 to 0.3, which is smaller than the change of about 0.45 to 0.15 observed in the vertical specimens (PBF-L2 (V) and PBF-N (V)). Since they are nominally free of residual stress (annealed), R_{tot} in the wrought specimens remains close to 0.1 throughout the entire fatigue test. **Figure 5.7** demonstrates the influence of tensile residual stress and corresponding positive

K_{res} on both measured FCGRs and total stress intensity factor ratio compared to the stress-free state.

Fatigue crack growth rates from the decreasing ΔK_{app} tests are shown in **Figure 5.9**. The measured FCGRs of specimens with horizontal and vertical crack growth demonstrate excellent agreement; regardless of the machine on which the PBF material was processed, the FCGRs are the same in these builds processed with similar energy density. The slight differences in K_{res} in the two orientations shown in **Figure 5.6** do not significantly influence the measured FCGRs. When compared to results from wrought material, the PBF data in the near-threshold regime exhibit significantly higher fatigue crack growth rates; for example, at ΔK_{app} of 6 MPa·m$^{0.5}$, the wrought material exhibits a FCGR of 4 x 10^{-10} m/cycle compared to 1.3 x 10^{-9} m/cycle of the PBF material.

Values of the threshold for fatigue crack growth, ΔK_{th}, were estimated by performing a linear regression of log da/dN versus log ΔK using 30 data points between FCGRs of 10^{-9} and 10^{-10} m/cycle and calculating the operational ΔK_{th} by extrapolating to a crack growth rate of 10^{-10} m/cycle [13]. The corresponding fatigue crack growth thresholds are 5.10 MPa·m$^{0.5}$ (2 tests) and 3.47 MPa·m$^{0.5}$ (6 tests with standard deviation ± 0.15 MPa·m$^{0.5}$) for wrought and PBF materials, respectively. However, it is important to recognize that this value of ΔK_{th} is not an intrinsic material property for the PBF material because it is influenced by residual stress, which is dependent on processing parameters, build geometry, and the test specimen details including geometry and extraction location.

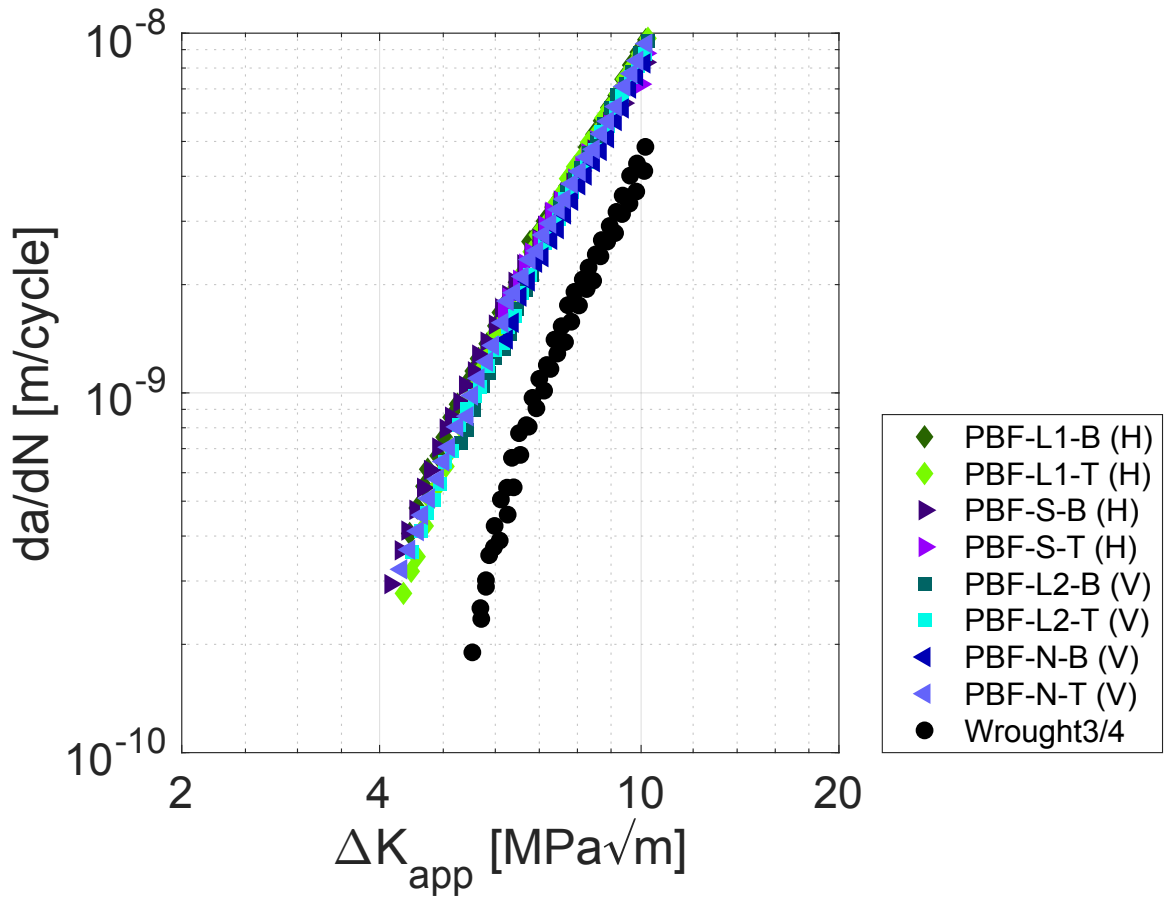

***Figure 5.9**: Measured FCGRs for PBF decreasing tests with wrought data for comparison.*

5.3.5. Crack Path Characterization

The fracture surfaces of specimens Wrought 4 and PBF-S-B (H) are presented in **Figure 5.10**. Final crack size was measured with ImageJ [33] using an average of nine equally spaced positions through the specimen thickness. Measured crack sizes agreed with the values for crack size calculated by the test control software within 5% [13]. Additionally, the fracture surfaces reveal relatively straight fatigue crack paths and show extensive deformation in the uncracked ligament from monotonically breaking the specimens. The fatigue surface of the wrought material appears comparatively matte (**Figure 5.10**(a)), in contrast to the PBF fatigue surface (**Figure 5.10**(b)), reflecting greater surface roughness. This roughness indicates greater tortuosity in the crack wake of the wrought material, consistent with the observed crack closure and reduced crack growth rate as the crack extended in the constant ΔK_{app} tests.

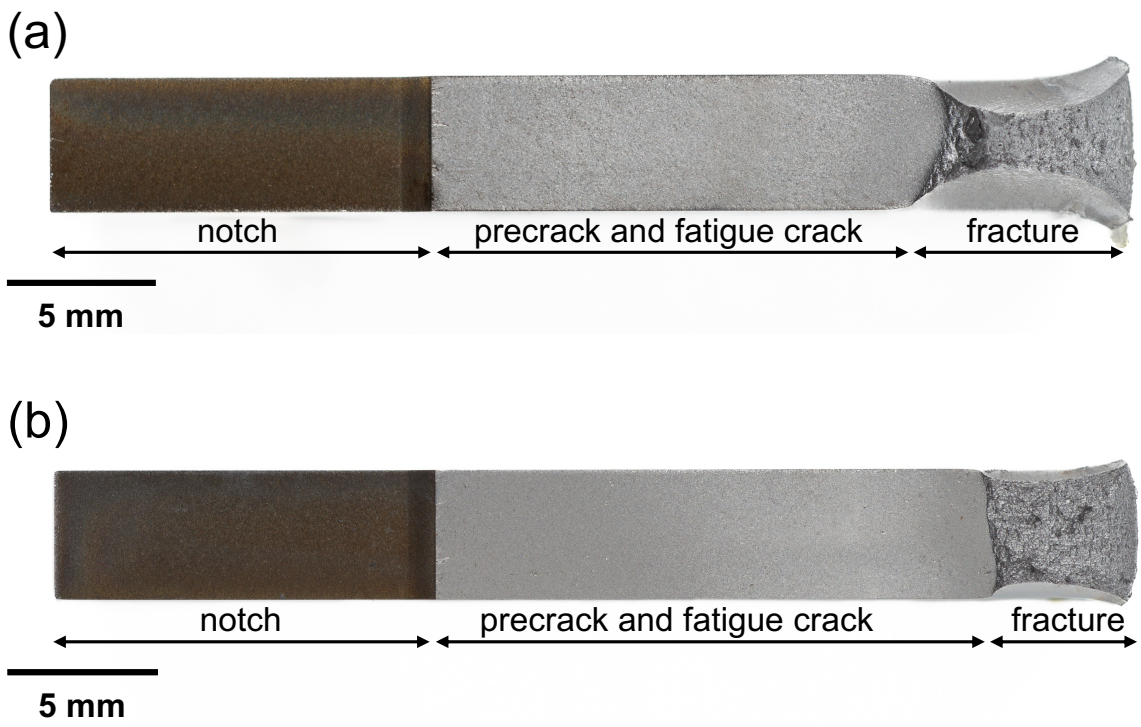

***Figure 5.10**: Surfaces of (a) Wrought 4 and (b) PBF-S-B (H) specimens including EDM notch, fatigue crack (and precrack), and fracture.*

BSE images of the crack path of the constant ΔKapp tests of PBF and wrought specimens are shown in **Figure 5.11** and **Figure 5.12**, respectively. Cracks propagated in a transgranular manner in both PBF and wrought materials. Furthermore, in the PBF material, crack growth in both the horizontal and vertical directions does not appear to be significantly influenced by the elongated grain shape and displays limited evidence of crack branching. The positive Kres throughout crack growth leads to faster FCGRs and an open crack wake in the PBF specimens as compared to wrought material. Unlike the differences in apparent surface roughness shown in **Figure 5.10**, the tortuosity and minimal crack branching in the wrought material (**Figure 5.12**) appear only slightly greater than in the PBF material. These observations highlight the fact that the inhomogeneous microstructure has a much less significant effect on fatigue crack growth behavior in the PBF specimens than does the tensile residual stress.

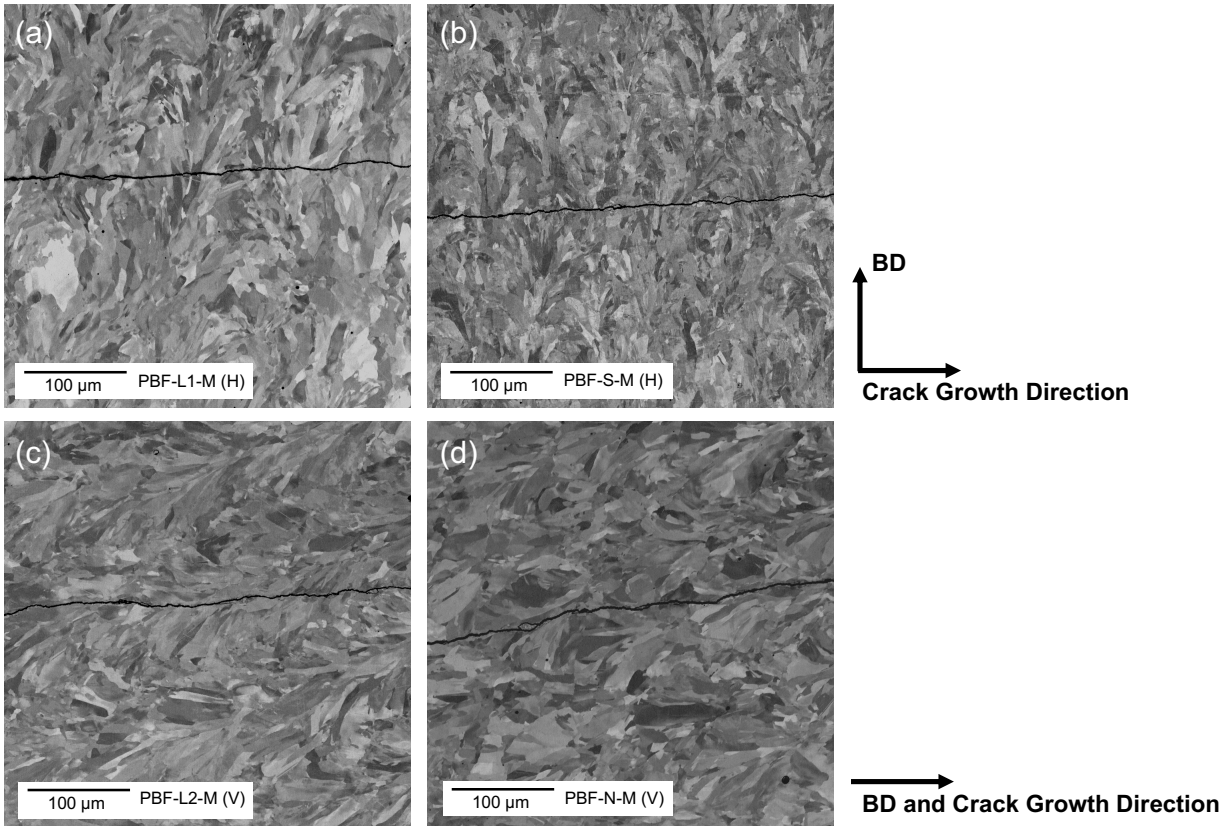

Figure 5.11*: Crack path BSE images of all PBF material (a) PBF-L1-M (H), (b) PBF-S-M (H), (c) PBF-L2-M (V), and (d) PBF-N-M (V).*

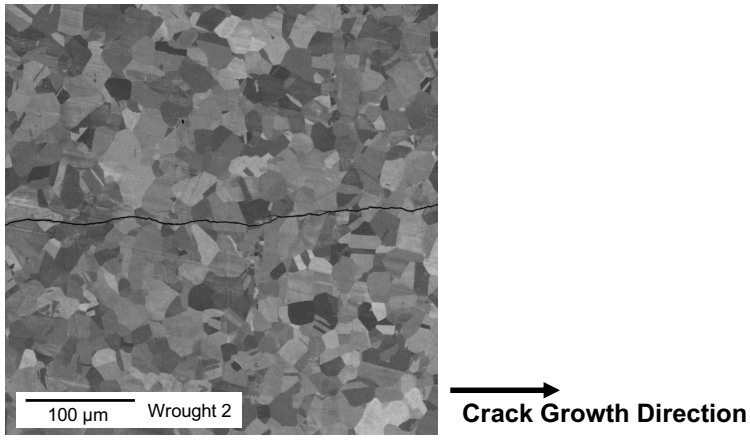

Figure 5.12*: Crack path BSE image of wrought material.*

5.3.6. Corrected Fatigue Crack Growth Rates

All FCGR data were corrected to account for the extrinsic effects of crack closure and residual stress by normalizing the rates to a common R value. This adjustment was accomplished

by the Walker relationship [34], in conjunction with K_{res} from the OLCC (**Figure 5.6**) to correct the FCGR data to R_{app} of 0.1 as expressed in [18-21]:

$$\Delta K_{corr}(a) = \Delta K_{eff}(a)^{1-n}\left(K_{max,app}(a) + K_{res}(a)\right)^{n}\left(1 - R_{app}\right)^{n} \quad (5.2)$$

where ΔK_{corr} represents the corrected alternating stress intensity factor. The normalization parameter, *n*, was previously found to be 0.25 for AM Type 304L stainless steel [24]. The adjusted compliance ratio (ACR) method outlined in the appendix of ASTM E647 was used to account for crack closure and determine ΔK_{eff} [13, 35].

Figure 5.13 illustrates the corrected fatigue crack growth rates for all wrought and PBF specimens in this study. Negligible crack closure ($\Delta K_{eff} = \Delta K_{app}$) in the PBF material is consistent with fatigue crack growth through a tensile residual stress field that leads to contributions of K_{res} that increase R_{tot} compared to R_{app} [36]. In contrast, the wrought material exhibits small values of K_{res} but significant crack closure, resulting in $\Delta K_{eff} \neq \Delta K_{app}$. However, to maintain a consistent approach, the same analysis procedure was applied to all specimen data, both PBF and wrought.

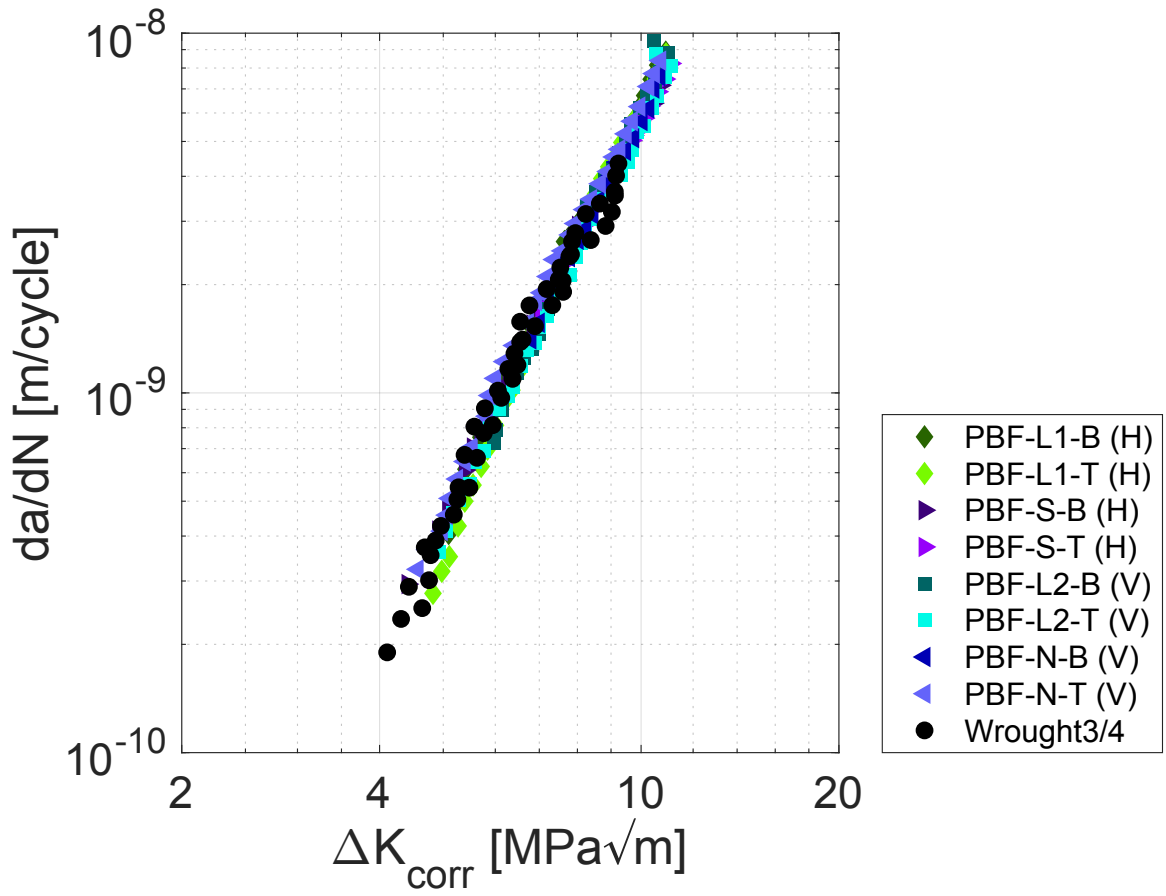

***Figure 5.13**: Corrected FCGRs for PBF decreasing tests with a comparison to data for conventional wrought material.*

The corrected FCGR data for the PBF material shift ΔK_{app} to higher values of ΔK_{corr} as compared to the uncorrected test data shown in **Figure 5.9**. In contrast, for the wrought material, ΔK_{app} are shifted to lower values of ΔK_{corr} after data corrections. These shifts bring the data for the two materials into agreement. When the corrected data of **Figure 5.13** are analyzed and compared, the estimated PBF and wrought fatigue thresholds are 3.73 ± 0.29 MPa·m$^{0.5}$ and 3.70 ± 0.42 MPa·m$^{0.5}$, respectively. These two values are not significantly different, indicating similar intrinsic fatigue resistance. The larger standard deviations in corrected threshold values compared to uncorrected values can be attributed to variations in the K_{res} data. In addition, FCGRs of the two materials overlap at high crack growth rates approaching the Paris regime, where the effects of microstructure on crack tip processes are normally less important.

The results of **Figure 5.13** compared to those of **Figure 5.9** demonstrate the importance of incorporating residual stress into the analysis of fatigue crack growth rate data from AM specimens. To further emphasize the need to quantify the influence of K_{res} on the measured crack growth rates, two additional decreasing ΔK_{app} fatigue crack growth tests were conducted (one in the horizontal growth orientation and one in the vertical orientation). Decreasing ΔK_{app} tests of PBF-S-T (H) and PBF-N-B (V) were stopped at a crack size approximately a/W = 0.5 and restarted at the same initial K_{max} as the first portion of the decreasing test (11.6 MPa·$m^{0.5}$). The data in terms of ΔK_{app} in **Figure 5.14**(a) show an offset between the measured crack growth rates of the first portion (d1) and the second portion (d2) of both tests. Using the methodology described above, all data were corrected for K_{res} using ΔK_{corr}, which also includes ΔK_{ACR} corrections. The resulting FCGR data collapse onto a single curve (**Figure 5.14**(b)). In other words, the offset in the uncorrected data demonstrates the influence of the local K_{res} and the sensitivity of the measured FCGRs to crack tip location in the specimen because the residual stress contribution (K_{res}) changes as the crack extends. Furthermore, the methodology described herein corrects for changes in R_{tot}, thus enabling determination of the intrinsic fatigue response of the material unbiased by residual stress and/or crack closure.

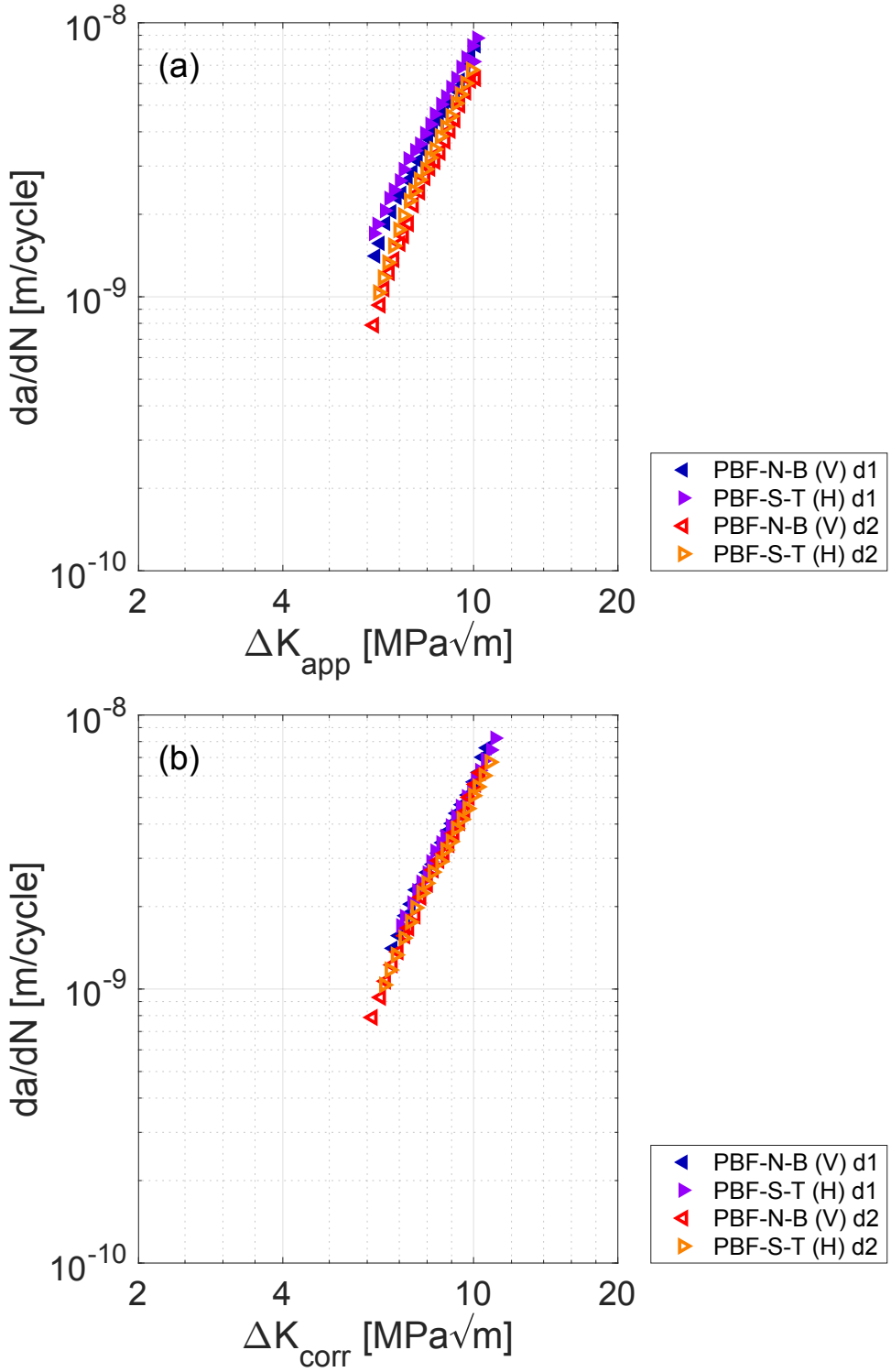

***Figure 5.14**: Applied and corrected FCGR test data for decreasing tests restarted midway through the test.*

5.4. Conclusions

Constant and decreasing ΔK_{app} fatigue crack growth rate (FCGR) tests of specimens with crack growth oriented perpendicular (horizontal - H) and parallel (vertical - V) to the build direction were used to explore the reproducibility of process-induced residual stress effects on crack growth rates in laser powder bed fusion (PBF) Type 304L stainless steel. Slitting measurements provided residual stress profiles for the four builds in this study. The application of the on-line crack compliance (OLCC) method with the Schindler influence function (Z(a)) data analysis method provided residual stress intensity factor (K_{res}) profiles along with FCGR data for PBF material produced on three different machines, which are located at different laboratories. In addition, backscatter electron (BSE) large area grain images showed nominal variation of the microstructure in the four different builds. The results of these experiments reveal the following specific points:

1. Residual stress measurements in plates cut from PBF builds from three different machines demonstrated consistent values of tensile (near the edges) and compressive (at the center) residual stress in builds with similar dimensions. These results demonstrate that remarkably consistent residual stress (± 10 MPa) can be obtained in PBF builds manufactured at different laboratories by different users on different machines.

2. A comparison of fatigue crack growth rates of specimens oriented for crack growth horizontal and vertical revealed small differences in FCGRs under constant ΔK_{app} conditions. The only difference was due to a twisted crack path observed in one specimen (PBF-L2-M (V)) that led to anomalously low crack growth rate. Excellent agreement of FCGRs was obtained under decreasing ΔK_{app} conditions.

3. The residual stress intensity factor, K_{res}, determined by the on-line crack compliance method in individual fatigue specimens indicated that high levels of tensile residual stress influence FCGRs in specimens of both orientations. Only a slight orientation dependence of residual stress was indicated. The horizontal specimens (H) had peak K_{res} values from 6.5 to 7.5 $MPa \cdot m^{0.5}$, while the vertical specimens (V) had 5 to 6.5 $MPa \cdot m^{0.5}$. Additionally, K_{res} in vertical specimens decreased more quickly towards zero as crack size increased compared to horizontal specimens.

4. Measured FCGRs of all PBF specimens demonstrated higher fatigue crack growth rates for all values of ΔK_{app} in the near-threshold regime when compared to annealed wrought material. Additionally, the PBF material had an estimated fatigue crack growth threshold that was 30% lower than that calculated for the wrought material.

5. When corrected for the influence of K_{res}, the intrinsic fatigue performance of the PBF materials was nearly identical to that of annealed wrought material corrected for crack closure. The similar corrected fatigue crack growth threshold values for PBF and wrought materials indicated that residual stress accounts for the primary difference in the observed fatigue crack growth rates.

6. Transgranular crack growth was observed in the PBF materials and in the wrought material. The elongated grains of the PBF materials compared to the equiaxed grains in the wrought material had a negligible influence on the intrinsic fatigue performance in the near-threshold regime.

Acknowledgements

This work was supported by a NASA Space Technology Research Fellowship (CMS – Grant 80NSSC19K1132) and material was provided by Sandia National Laboratories. Sandia National Laboratories is a multi-mission laboratory managed and operated by National Technology & Engineering Solutions of Sandia, LLC, a wholly owned subsidiary of Honeywell International Inc., for the U.S. Department of Energy's National Nuclear Security Administration under contract DE-NA0003525. This paper describes objective technical results and analysis. Any subjective views or opinions that might be expressed in the paper do not necessarily represent the views of the U.S. Department of Energy or the United States Government. The material characterization described in this study was carried out at the Advanced Materials Characterization and Testing facility in the Department of Materials Science and Engineering at UC Davis. The SEM images were acquired using a Thermo Fisher Quattro S ESEM funded through the NSF-MRI program DMR-1725618.

References

1. Yadollahi, A. and N. Shamsaei, *Additive manufacturing of fatigue resistant materials: Challenges and opportunities.* International Journal of Fatigue, 2017. **98**: 14-31.
2. Afroz, L., et al., *Fatigue behaviour of laser powder bed fusion (L-PBF) Ti-6Al-4V, Al-Si-Mg and stainless steels: a brief overview.* International Journal of Fracture, 2022. **235**(1): 3-46.
3. Mercelis, P. and J.P. Kruth, *Residual stresses in selective laser sintering and selective laser melting.* Rapid Prototyping Journal, 2006. **12**(5): 254-265.
4. Fatemi, A., et al., *Fatigue behaviour of additive manufactured materials: An overview of some recent experimental studies on Ti-6Al-4V considering various processing and loading direction effects.* Fatigue & Fracture of Engineering Materials & Structures, 2019. **42**(5): 991-1009.
5. Narasimharaju, S.R., et al., *A comprehensive review on laser powder bed fusion of steels: Processing, microstructure, defects and control methods, mechanical properties, current challenges and future trends.* Journal of Manufacturing Processes, 2022. **75**: 375-414.
6. Qiu, C., et al., *A comprehensive study on microstructure and tensile behaviour of a selectively laser melted stainless steel.* Scientific Reports, 2018. **8**(1): 7785.
7. Tan, C., et al., *Microstructural characterization and properties of selective laser melted maraging steel with different build directions.* Science and Technology of Advanced Materials, 2018. **19**(1): 746-758.
8. DebRoy, T., et al., *Additive manufacturing of metallic components – Process, structure and properties.* Progress in Materials Science, 2018. **92**: 112-224.
9. Mukherjee, T., W. Zhang, and T. DebRoy, *An improved prediction of residual stresses and distortion in additive manufacturing.* Computational Materials Science, 2017. **126**: 360-372.
10. Dowling, L., et al., *A review of critical repeatability and reproducibility issues in powder bed fusion.* Materials & Design, 2020. **186**: 108346.
11. Syed, A.K., et al., *An experimental study of residual stress and direction-dependence of fatigue crack growth behaviour in as-built and stress-relieved selective-laser-melted Ti6Al4V.* Materials Science and Engineering a-Structural Materials Properties Microstructure and Processing, 2019. **755**: 246-257.
12. Vrancken, B., et al., *Residual stress via the contour method in compact tension specimens produced via selective laser melting.* Scripta Materialia, 2014. **87**: 29-32.
13. E647-15, *Standard Test Method for Measurement of Fatigue Crack Growth Rates*. 2015. ASTM International: West Conshohocken, PA.
14. Wu, L.L., Z.H. Jiao, and H.C. Yu, *Study on fatigue crack growth behavior of selective laser-melted Ti6Al4V under different build directions, stress ratios, and temperatures.* Fatigue & Fracture of Engineering Materials & Structures, 2022. **45**(5): 1421-1434.

15. Riemer, A., et al., *On the fatigue crack growth behavior in 316L stainless steel manufactured by selective laser melting.* Engineering Fracture Mechanics, 2014. **120**: 15-25.

16. Karpenko, O., S. Oterkus, and E. Oterkus, *Investigating the influence of residual stresses on fatigue crack growth for additively manufactured titanium alloy Ti6Al4V by using peridynamics.* International Journal of Fatigue, 2022. **155**: 106624.

17. Smudde, C.M., et al., *Effects of Residual Stress on Orientation Dependent Fatigue Crack Growth Rates in Additively Manufactured Stainless Steel.* Submitted to International Journal of Fatigue, 2022.

18. Donald, J.K. and D.A. Lados, *An integrated methodology for separating closure and residual stress effects from fatigue crack growth rate data.* Fatigue & Fracture of Engineering Materials & Structures, 2006. **30**(3): 223-230.

19. Lados, D.A., D. Apelian, and J.K. Donald, *Fracture mechanics analysis for residual stress and crack closure corrections.* International Journal of Fatigue, 2007. **29**(4): 687-694.

20. Lados, D.A. and D. Apelian, *The Effect of Residual Stress on the Fatigue Crack Growth Behavior of Al-Si-Mg Cast Alloys - Mechanisms and Corrective Mathematical Models.* Metallurgical and Materials Transactions A-Physical Metallurgy and Materials Science, 2006. **37A**: 133-145.

21. James, M., et al., *A Methodology for Partitioning Residual Stress Effects From Fatigue Crack Growth Rate Test Data.* Materials Performance and Characterization, 2016. **5**(3): 194-214.

22. Newman, J.A., et al., *Characterization of Residual Stress Effects on Fatigue Crack Growth of a Friction Stir Welded Aluminum Alloy*. 2015. NASA Langley Research Center, Hampton, VA. Report No. NASA/TM–2015-218685.

23. Smudde, C.M., J.C. Gibeling, and M.R. Hill, *Validation of On-line Crack Compliance Data Analysis Methods for the Residual Stress Intensity Factor.* Submitted to Engineering Fracture Mechanics, 2022.

24. Smudde, C.M., et al., *The influence of residual stress on fatigue crack growth rates of additively manufactured Type 304L stainless steel.* International Journal of Fatigue, 2022. **162**: 106954.

25. Ronevich, J.A., C.R. D'Elia, and M.R. Hill, *Fatigue crack growth rates of X100 steel welds in high pressure hydrogen gas considering residual stress effects.* Engineering Fracture Mechanics, 2018. **194**: 42-51.

26. San Marchi, C.W., et al., *Fatigue and Fracture Behavior of Additively Manufactured Austenitic Stainless Steel*, in *ASTM STP 1620: Structural Integrity of Additive Manufactured Parts.* N. Shamsaei, et al., Editors. 2020, ASTM International: West Conshohocken, PA. 381-398.

27. Hill, M.R., *Chapter 4: The Slitting Method*, in *Practical Residual Stress Measurement Methods* G.S. Schajer, Editor. 2013, Wiley. 89-108.

28. Cheng, W. and I. Finnie, *Residual Stress Measurement and the Slitting Method*. Mechanical Engineering Series, ed. F.F. Ling. 2007, New York, NY: Springer.

29. Schindler, H.J., W. Cheng, and I. Finnie, *Experimental determination of stress intensity factors due to residual stresses.* Experimental Mechanics, 1997. **37**(3): 272-277.

30. Schindler, H.J., *Determination of Residual Stress Distributions from Measured Stress Intensity Factors.* International Journal of Fracture, 1995. **74**: R23-R30.

31. Olson, M.D. and M.R. Hill, *Determination of residual stress intensity factor in the compact tension coupon.* Engineering Fracture Mechanics, 2012. **88**: 28-34.

32. *MATLAB. (2021). version 9.10.0 (R2021a).* Natick, Massachusetts; The MathWorks Inc.

33. Rasband, W.S., *ImageJ.* U. S. National Institutes of Health.

34. Dowling, N.E., *Mechanical behavior of materials : engineering methods for deformation, fracture, and fatigue*. 4th ed. 2013, Boston: Pearson. Chapter 9: 416-490.

35. Donald, J.K., G.H. Bray, and R.W. Bush, *An evaluation of the adjusted compliance ratio technique for determining the effective stress intensity factor.* Fatigue and Fracture Mechanics: Twenty-Ninth Volume, ASTM STP 1332, American Society for Testing and Materials, West Conshohocken, PA, 1999: 674-695.

36. Antunes, F., et al., *Fatigue Crack Growth in Maraging Steel Obtained by Selective Laser Melting.* Applied Sciences, 2019. **9**(20): 4412.

Chapter 6:
Comparison of Fatigue Crack Growth in Additively Manufactured Stainless Steel Processed by Different Methods [5]

Abstract

Highly localized heating and steep temperature gradients of additive manufacturing (AM) processes lead to the formation of significant residual stress and distinctive grain morphologies dependent on the deposition process. Both of these characteristics may contribute to the mechanical behavior of AM materials. In this study, fatigue crack growth resistance of AM Type 304L stainless steel produced by both directed energy deposition and powder bed fusion was evaluated and compared for crack growth parallel and perpendicular to the build direction. Decreasing and constant alternating stress intensity factor tests were used to assess fatigue crack growth behavior in the near-threshold regime and to reveal the importance of residual stress to the observed fatigue crack growth rates. Data for annealed wrought material were included for comparison. The residual stress intensity factor, K_{res}, was then used to correct for the influence of residual stress on measured fatigue crack growth rates. These corrections brought all results into agreement with the intrinsic behavior of wrought material, indicating that differences in processing method and specimen orientation are accounted for through differences in residual stress. Furthermore, the role of grain morphology was insignificant in this austenitic stainless steel material and crack growth was transgranular for all tested specimens.

Keywords: Additive manufacturing, directed energy deposition, laser powder bed fusion, residual stress, fatigue crack growth

[5] To be adapted for journal submission: Smudde, C.M., et al., *Comparison of Fatigue Crack Growth in Additively Manufactured Stainless Steel Processed by Different Methods.*.

6.1. Introduction

The two major metal additive manufacturing (AM) processes, laser directed energy deposition (DED) and laser powder bed fusion (PBF), are layer-by-layer manufacturing techniques that involve melting and subsequent solidification of feedstock powders. Each method has its own distinct process parameters such as laser power (P) and scan velocity (V) that control unique thermal cycles with steep temperature gradients, high cooling rates, and cyclic reheating/remelting of previously deposited layers [1, 2]. In both AM processes, the complex thermal history results in significant residual stress and nonequilibrium microstructures that evolve during the cyclic reheating of subsequent layers [3], and which are known to influence mechanical performance. Mechanical behavior, specifically fatigue performance, of AM components is not well understood, which prevents the technology from realizing its full potential in cyclic load bearing applications [4]. There is a direct relationship between thermal history and build characteristics such as microstructure and residual stress. Yet, a direct comparison of the microstructure, residual stress, and fatigue performance of different AM manufacturing methods has not been performed. A deeper understanding of the factors that affect the reliability of AM fatigue performance such as microstructural heterogeneity and residual stress is critical for the widespread adoption of the technology.

The objective of this study is to compare fatigue crack growth rates of additively manufactured material produced via directed energy deposition and powder bed fusion. Fatigue crack growth rates in the near-threshold regime were measured in two orientations, both perpendicular and parallel to the build direction. The process-induced residual stress of the as-built materials was characterized through slitting measurements and was used to determine the consistency of residual stress development in identical (DED) and similar (PBF) builds. The

influence of process-induced residual stress on fatigue crack growth behavior was quantified by the stress intensity factor, K_{res}, determined via the on-line crack compliance method [5-9]. These values were then used to correct the measured fatigue crack growth data for the influence of residual stress [5, 8]. Furthermore, microstructural contributions to crack path behavior were evaluated and compared for the different AM materials.

6.2. Materials and Methods

Additively manufactured Type 304L stainless steel material built via directed energy deposition (DED) and powder bed fusion (PBF) was evaluated in this study. The materials produced by both methods have been previously investigated individually [10, 11, 12], but their properties and performance have not been directly compared. The chemical composition of gas atomized feedstock powders conformed to ASTM requirements for austenitic Type 304L stainless steel material [13] and has been reported elsewhere for PBF and DED in Refs. [10] and [12], respectively. Since the small differences in chemical composition were not expected to significantly influence fatigue performance, the processing method was considered the primary difference in the Type 304L materials under consideration.

Two replicate DED builds were fabricated as vertical walls with nominal dimensions of 110 mm (Z-direction, build direction) x 56 mm (Y-direction, long transverse or width) x 7.6 mm (X-direction, thickness). All DED builds were made on the same machine with the same processing parameters over the course of several weeks, which were optimized for 99.9% density and are described in earlier studies of the same material [11, 12]. Additionally, two nominally identical PBF builds were fabricated one year apart on the same machine at different times with comparable strength and ductility. The PBF builds were deposited as vertical D-shaped cylinders with processing parameters described in previous work [10]. Nominal dimensions of the wall of

interest were 110 mm (Z-direction) x 36 mm (Y-direction) x 5.1 mm (X-direction). One build from each processing method was used to evaluate fatigue crack growth rates parallel to the build direction (vertical) and one build from each method was used to assess crack growth perpendicular to the build direction (horizontal). Three compact (C(T)) specimens were extracted from each build for fatigue testing.

Microstructural heterogeneity was evaluated through electron backscatter diffraction (EBSD) imaging of the DED and PBF materials. Samples for material characterization were extracted via wire electrical discharge machining (EDM), mounted in epoxy and ground to 1200 grit prior to polishing with an alumina suspension of 3 μm, 1 μm, and 0.3 μm. Samples were then vibropolished for 8-9 hours with 0.05 μm colloidal silica prior to examination in the SEM. A Scios Dual-Beam FIB/SEM operating at 15 kV with 3 μm step size was used to examine differences in grain sizes and shapes in the DED and PBF materials in X-Y and X-Z planes. In addition, crack tip sections were extracted by wire EDM from tested specimens and electron backscatter (BSE) imaging on a ThermoFisher Quattro ESEM operating at 5 kV and 0.46 nA was used to reveal fatigue crack growth profiles in the DED and PBF materials. Secondary electron (SE) imaging on the same instrument operating at 5 kV and 0.11 nA was used to examine fatigue surfaces.

Process-induced residual stress in both materials was evaluated prior to fatigue crack growth rate testing to evaluate the consistency and reproducibility of the residual stress in the DED and PBF builds. Plates from each build with similar dimensions in Y and Z were removed via wire EDM as shown by the thin vertical blue lines in **Figure 6.1**. Vishay CEA-06-062UW-350 strain gages were applied on the EDM surface at two equally spaced locations (1 and 2). Build direction residual stress as a function of cut depth was then determined by the slitting method on the two planes of interest (horizontal black lines) [14]. The slitting method is a one-dimensional

mechanical relaxation technique that uses strain measured at fixed cut increments to determine an average of the through thickness (X-direction) residual stress acting in the build direction (Z-direction) as a function of position across the plate (Y-direction). Detailed descriptions of this method are presented elsewhere [14, 15, 16]. Additional slitting measurements were performed during the machining of the specimen notches as indicated by the red lines in **Figure 6.1**(c).

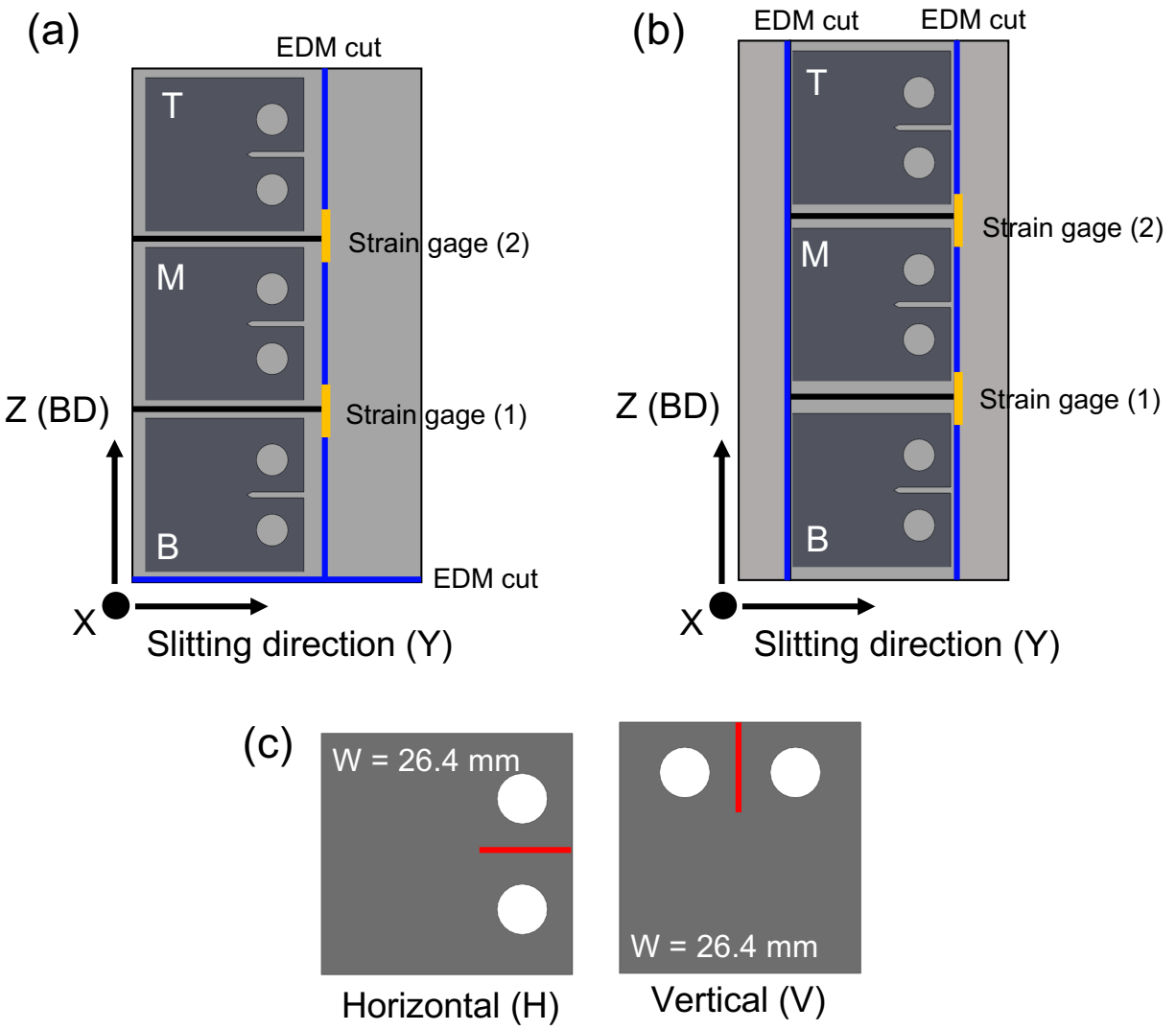

***Figure 6.1**: Schematic of slitting measurements and specimen extraction of (a) DED and (b) PBF material with (c) C(T) specimen geometry and orientation.*

To evaluate the contribution of residual stress to the stress intensity factor, values of K_{res} acting normal to the cut plane were determined from the strain data collected during the slitting

measurements. The derivative of the strain with respect to cut depth (or crack size), dε/da, was found using a polynomial regression outlined and described in previous work [10, 11, 17, 18]. The strain derivative and a geometry dependent influence function (Z(a)) as described by Schindler [19] were then used to determine K_{res} as a function of crack size:

$$K_{res}(a) = \frac{E'}{Z(a)} \frac{d\varepsilon(a)}{da} \tag{6.1}$$

where E′ is the elastic modulus (plane stress in this work).

The residual stress intensity factor was also determined in the crack plane of fatigue specimens using the on-line crack compliance (OLCC) method during the FCGR tests [5, 8, 9]. In this method, the residual strain (ε_{res}) is quantified by extrapolating the linear region of the load versus deformation data (i.e., compliance data) to zero load. The value of ε_{res} is nominally equivalent to the strain determined by a slitting measurement and can be used to determine K_{res} in the same way (Equation (6.1)). A detailed methodology for determining K_{res} from the compliance data of a fatigue crack growth rate test using Schindler's influence function has been recently developed [18].

The DED and PBF materials were machined into compact (C(T)) specimens in accordance with ASTM E647 [17] for the evaluation of FCGR behavior with a specimen width (W) of 26.4 mm and thickness of 6.35 mm (DED) or 4.06 mm (PBF). Specimens from the top and bottom (T and B) were used to evaluate near-threshold crack growth rates in K-control tests with decreasing applied alternating stress intensity factor (decreasing ΔK_{app}), while specimens from the middle (M) were tested under conditions of constant ΔK_{app}. Consistent with specimen designations of previous work [10, 11, 12], FCGRs perpendicular to the build direction (horizontal (H) crack growth) were determined from specimens extracted from builds denoted DED2 and PBF-L1, whereas FCGRs

parallel to the build direction (vertical (V) crack growth) were determined from specimens extracted from builds DED3 and PBF-L2. For reference, the specimen designations and the associated FCGR test condition are presented in **Table 6.1**. FCGR data of AM material were compared to a reference material of dual certified annealed wrought Type 304/304L austenitic stainless steel tested under decreasing ΔK_{app} conditions. Two wrought specimens of each thickness, 6.35 mm and 4.06 mm, were tested to provide a direct comparison for the DED and PBF specimens, respectively.

Table 6.1: Specimen designation for K_{res} and FCGR measurements

Specimen	Specimen	Specimen	Specimen	FCGR test condition
DED2_B (H)	DED3_B (V)	PBF-L1_B (H)	PBF-L2_B (V)	decreasing ΔK_{app}
DED2_M (H)	DED3_M (V)	PBF-L1_M (H)	PBF-L2_M (V)	constant ΔK_{app}
DED2_T (H)	DED3_T (V)	PBF-L1_T (H)	PBF-L2_T (V)	decreasing ΔK_{app}

An Instron 1331 servohydraulic load frame was utilized for fatigue testing in lab air at an applied stress ratio of R_{app} = 0.1 and frequency of 10 Hz. All specimens were notched via wire EDM and fatigue precracked under decreasing ΔK_{app} conditions to a crack size (a) of 6.6 mm (a/W = 0.25) in accordance with ASTM E647 [17]. Gages at the back face of each fatigue specimen were used to monitor back-face strain (BFS) [10, 11]. The MTS 790.40 fatigue crack growth software running on a MTS TestStar control system was modified to accept this BFS input to determine compliance and crack size [13]. Constant ΔK_{app} fatigue tests were performed at ΔK_{app} of 6.6 MPa·m$^{0.5}$ and decreasing ΔK_{app} fatigue tests had an initial K_{max} of 11.6 MPa·m$^{0.5}$ and a load shedding parameter of C = -0.08 mm^{-1} [17]. During the fatigue crack growth tests, load and BFS

data (i.e., compliance data) with 500 data points were recorded at crack size increments of 0.051 mm. Compliance data were then used for post-test data analysis to K_{res} via the on-line crack compliance (OLCC) method.

6.3. Results and Discussion

EBSD images of two unique microstructural planes (X-Y and Y-Z) are shown in **Figure 6.2**(a) and **Figure 6.2**(b) for the DED and PBF materials, respectively. Both exhibit a distinct elongation of grains in the build direction with no evidence of texture. Since preferential grain orientations can lead to accelerated crack growth specific directions, the random texture in the DED and PBF material suggests anisotropic fatigue crack growth behavior can be attributed to the unique grain morphology and/or process-induced residual stress.

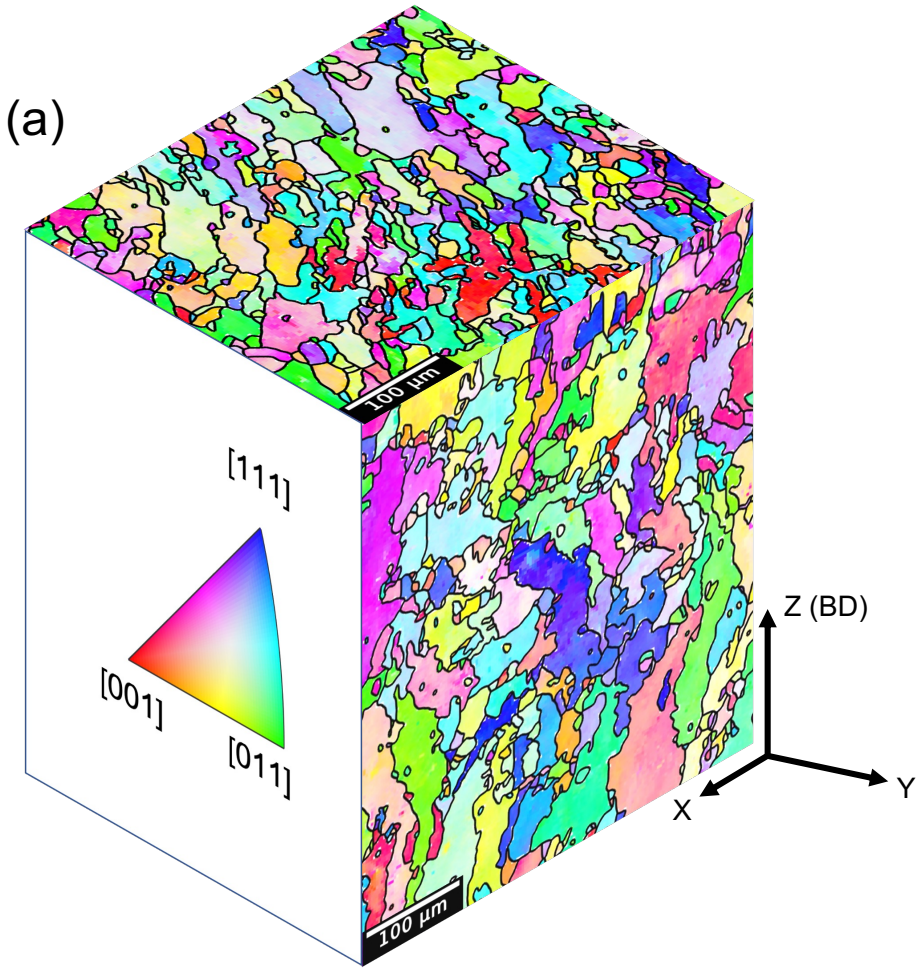

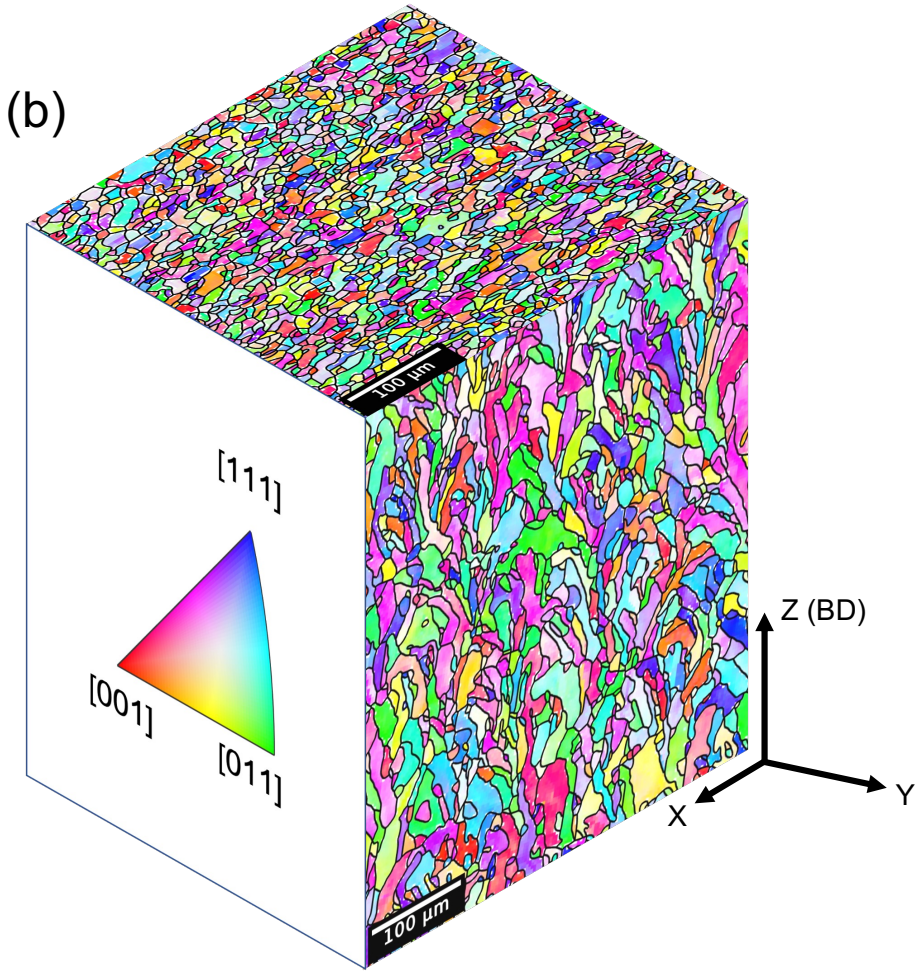

***Figure 6.2**: EBSD orientation images for (a) DED material and (b) PBF material.*

The grain morphology of the DED material represents a large distribution of shapes and sizes, but with an average grain size that is larger than that of the PBF material. The DED process generally results in thicker layers with average cooling rates ranging from 100 - 10000 K/s [20-23]. In contrast, the PBF process typically has a smaller layer thickness with significantly higher cooling rates of 10^6 - 40 x 10^6 K/s [24]. As such, smaller solidification layers and faster cooling rates in the PBF process limit grain growth as compared to DED. The resulting finer microstructure of the PBF material would commonly be thought to benefit fatigue initiation resistance [25]. In contrast, the coarser grains observed in DED material are expected to benefit fatigue crack growth.

Results from the initial slitting measurements made prior to FCGR specimen extraction are shown in **Figure 6.3**. The overall residual stress profiles of both AM materials show a steep gradient of stress between the center, which is in compression, and the edges of the plates, which are in tension. The tensile residual stress at the edges contributes to positive K_{res} throughout the entire cut depth. Residual stress and K_{res} results from the four slitting measurements of the DED plates demonstrate excellent agreement. Since the DED builds were made with identical processing parameters, the agreement of the slitting results indicates repeatability in the measurement. The four results of the PBF plates also agree well, indicating that the build direction residual stress is reproducible in the two PBF builds even though they were made at different times. The extracted DED plates were not centered in the Y-direction of the wall builds (vertical blue lines in **Figure 6.1**). As such, there is asymmetry in the residual stress profiles of the DED material that is not seen in those of the PBF. The greater residual stress in PBF material, both tensile at the edges and compressive at the center, is attributed to the steeper temperature gradients, which are characteristic of the PBF process.

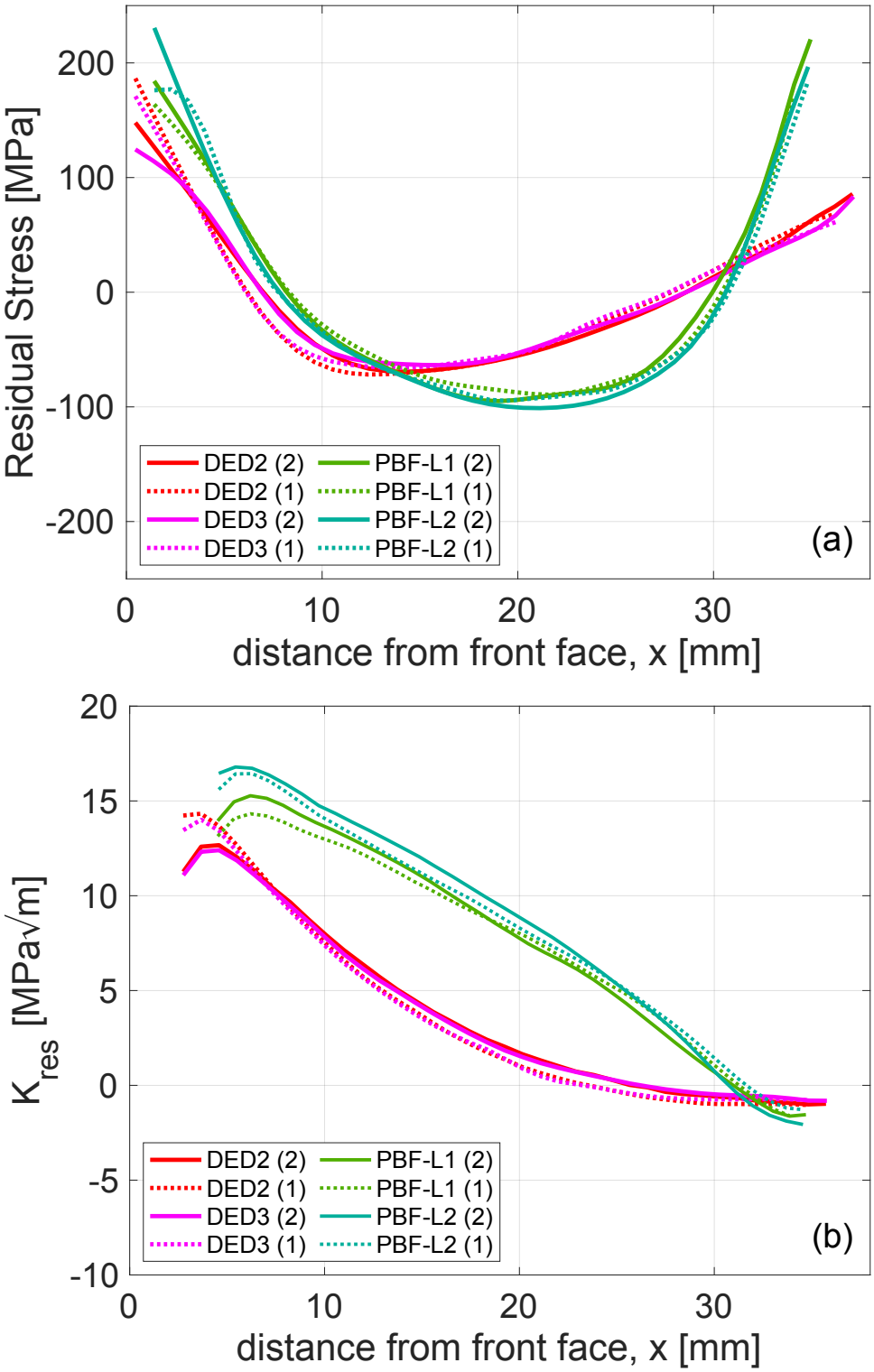

***Figure 6.3**: (a) Residual Stress (RS) and (b) K_{res} profiles from slitting of DED and PBF plates.*

Figure 6.4(a) and **Figure 6.4**(b) present the K_{res} results from notch slitting and OLCC for the DED and PBF C(T) specimens, respectively. The DED specimens have significant positive

K_{res} (4 to 3.5 MPa·$m^{0.5}$ at the notch) in the horizontal orientation (H) but have negligible K_{res} (~1 MPa·$m^{0.5}$ at the notch) in the vertical (V). The difference in K_{res} between orientations reflects significant residual stress in the build (Z) direction and very little residual stress in the lateral (Y) direction. In addition, **Figure 6.4**(a) shows good agreement among all specimens of DED2, suggesting build direction residual stress does not vary throughout the build height. The PBF specimens of **Figure 6.4**(b) have larger values of K_{res} at the notch tip (near the dashed line) as compared to DED for both orientations (H and V). Furthermore, K_{res} decreases more quickly as crack size increases in the PBF specimens. K_{res} in the horizontal specimens (H) varies from 6.5 at the notch to 3 MPa·$m^{0.5}$ at the longest crack size. In the vertical specimens (V), K_{res} varies from 5 to 1 MPa·$m^{0.5}$. While there are differences in K_{res} between the two orientations in the PBF specimens, neither orientation has negligible K_{res} as in DED (V).

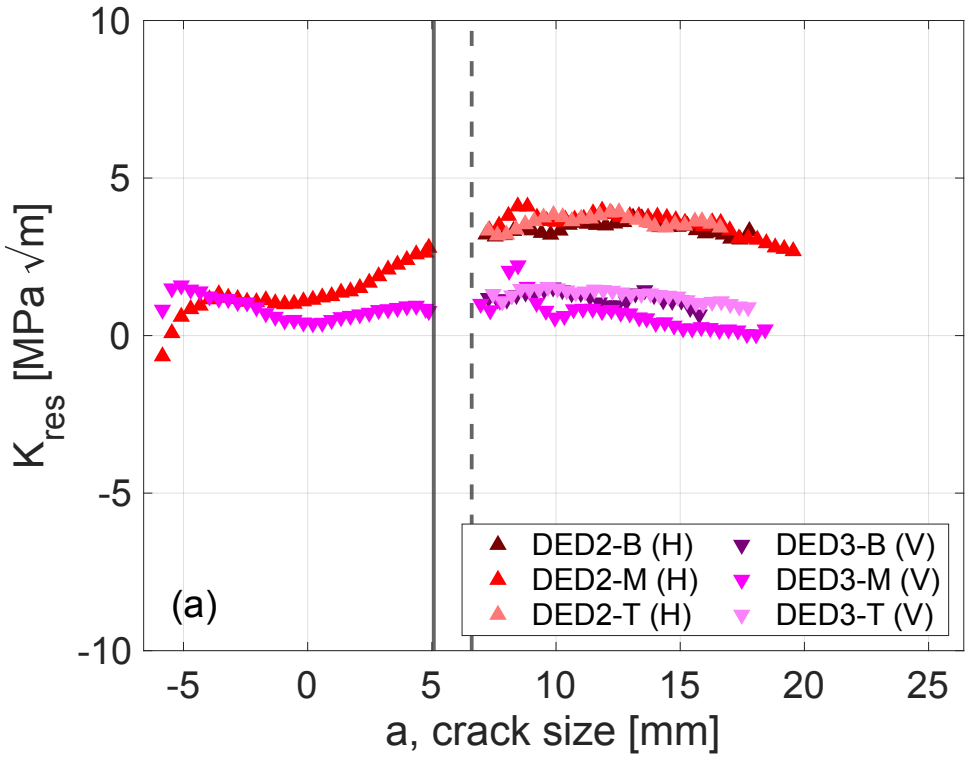

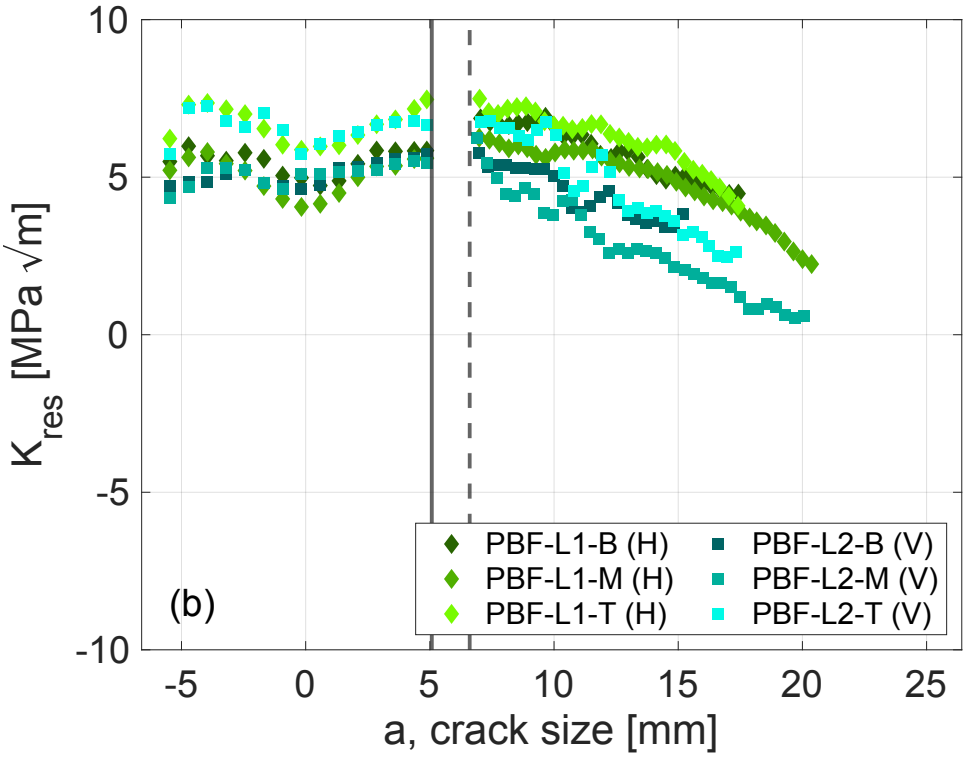

***Figure 6.4**: Full K_{res} profile for (a) DED and (b) PBF C(T) fatigue specimens with notch slitting to the left of the solid line and OLCC to the right of the dashed line (end of precrack).*

Fatigue crack growth rates from the constant ΔK_{app} fatigue tests are shown in **Figure 6.5**. The trends in FCGRs of the DED and PBF specimens follow the those in the K_{res} results shown in **Figure 6.4**(a) and **Figure 6.4**(b), respectively. All FCGRs in these AM materials decrease as crack size increases. As the crack grows and the residual stress redistributes, the influence of tensile RS at the crack tip decreases and K_{res} decreases towards zero. K_{res} is superimposed on both the minimum ($K_{min,app}$) and maximum ($K_{max,app}$) values of K_{app}, thus a positive K_{res} has the effect of increasing the mean value of K and the FCGRs. The PBF (H) specimen has the highest positive K_{res} for all crack sizes, which contributes to this material and orientation displaying the highest FCGRs. PBF (V) and DED (H) have similar values of K_{res}, and the FCGRs agree. DED (V) displayed negligible $K_{res,}$ and it follows that it has the slowest FCGRs. Unlike the other specimens, tensile residual stress does not enhance the driving force for crack growth to the same extent in DED (V).

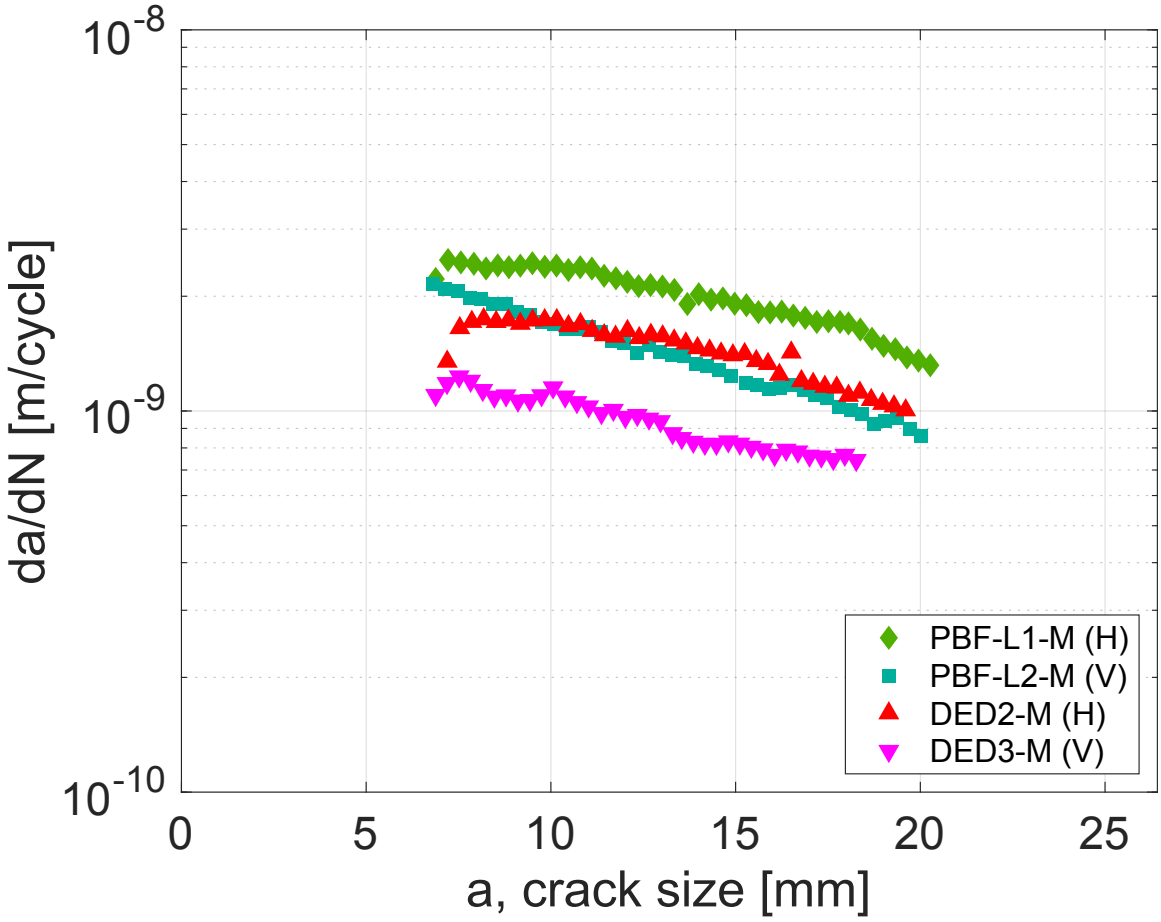

***Figure 6.5**: Measured FCGRs for DED and PBF in constant ΔK_{app} tests.*

Both DED and PBF specimens demonstrated transgranular fatigue crack growth. Despite differences in grain size shown in **Figure 6.2**(a) and **Figure 6.2**(b), the polished sections extracted from specimens tested at constant ΔK_{app} revealed similar crack profiles (**Figure 6.6**). The differences in grain morphologies did not significantly influence the crack path interactions with the microstructures. This similarity of crack profiles supports the significance of the influence of residual stress on FCGRs in AM materials.

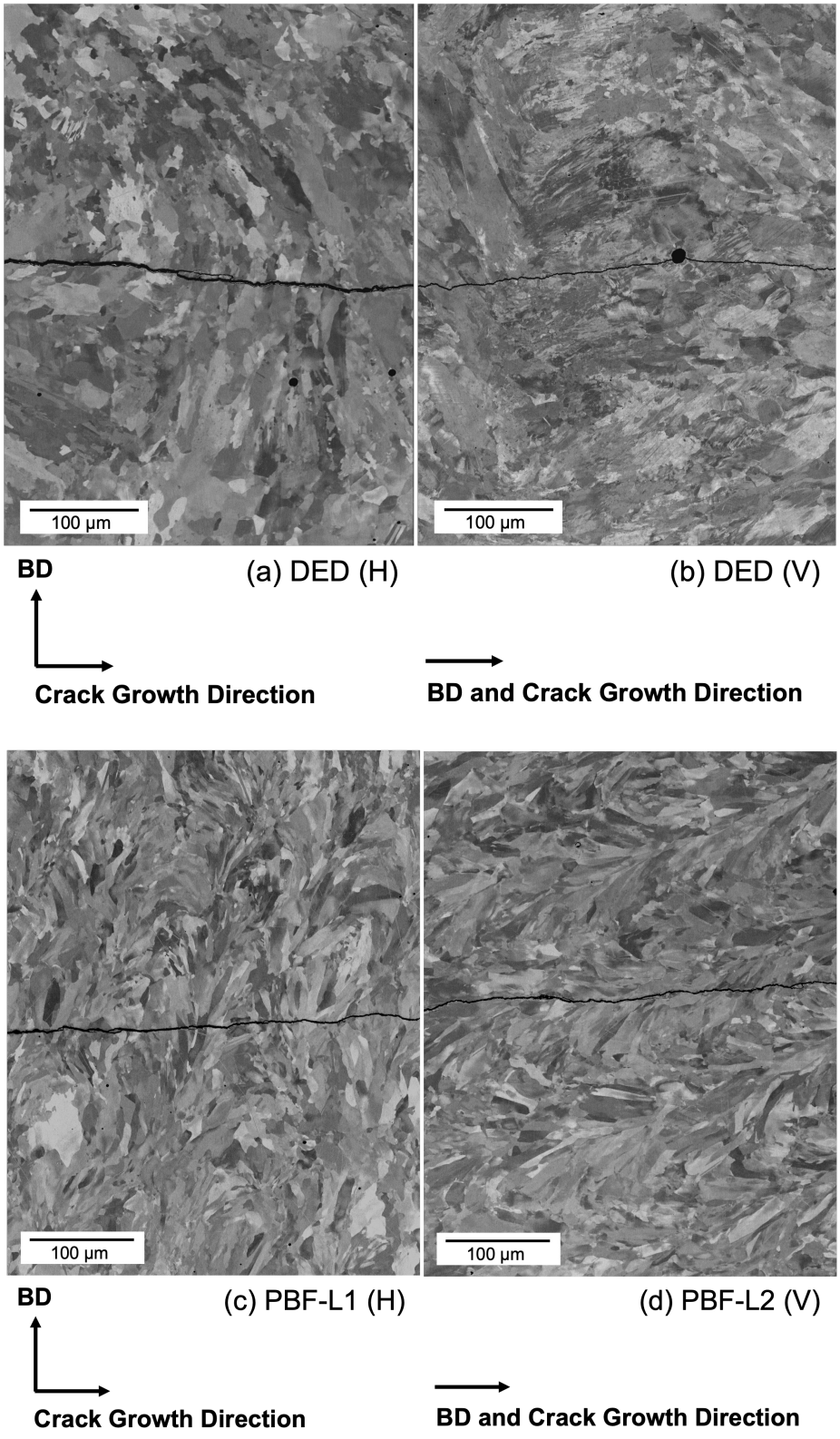

***Figure 6.6**: Crack path profiles of (a) DED2-M (H) (b) DED3-M (V) (c) PBF-L1-M (H) and (d) PBF-L2-M (V).*

The measured FCGRs for the decreasing ΔK_{app} tests are presented in **Figure 6.7**(a). To connect the influence of process on FCGR behavior, data were compared to annealed wrought Type 304/304L material. Following the trends in **Figure 6.4**(a) and **Figure 6.4**(b) where K_{res} of both DED and PBF converge to similar values in each orientation at crack sizes greater than 16 mm (~2.5 MPa·m$^{0.5}$ in (H) and ~0.5 MPa·m$^{0.5}$ in (V)), the FCGRs of the two AM materials converge to a nominally common value of ΔK_{app} between 4 and 5 MPa·m$^{0.5}$ at the lowest measured crack growth rates. At high values of ΔK_{app} from the beginning of the fatigue tests, the PBF specimens have higher FCGRs as compared to the DED consistent with the higher tensile values of K_{res} in the former. Additionally, since the DED has greater differences in K_{res} based on orientation, there is a larger spread in the measured FCGRs for DED specimens in the near-threshold regime as compared to the PBF specimens. When the measured FCGRs of AM specimens are compared to those of annealed wrought specimens, both DED and PBF specimens have higher FCGRs at all values of ΔK_{app}. The difference in the measured wrought data is attributed to the increase in crack closure effects in the thinner specimens (B = 4.06 mm). Since ΔK_{app} is nominally a function of load, crack size and specimen geometry, a thinner specimen requires a smaller load to impose the same value of ΔK_{app} at any given crack size.

The influence of crack closure on ΔK_{app} was accounted for using the adjusted compliance ratio (ACR) method outlined in the appendix of ASTM E647 [17, 26]. Subsequently, the influence of residual stress was corrected for using a method based on the Walker relationship [27] in conjunction with K_{res} determined from the OLCC method [5-7]. To maintain a consistent approach, the same analysis procedure was applied to all specimen data. **Figure 6.7**(b) shows the corrected FCGR data for the AM materials compared to those of wrought material. When decreasing ΔK_{app} test data from AM specimens are corrected – primarily for the contributions of K_{res} [5, 6, 8, 10, 11,

12, 15] - all data collapse into a single curve independent of processing method and orientation. Furthermore, the corrected AM FCGR behavior agrees with the intrinsic material performance of annealed wrought material that has been corrected primarily for the influence of crack closure. The agreement of the corrected data of the DED and PBF fatigue specimens with those of annealed wrought highlights the significant influence of AM process-induced residual stress on fatigue crack growth behavior.

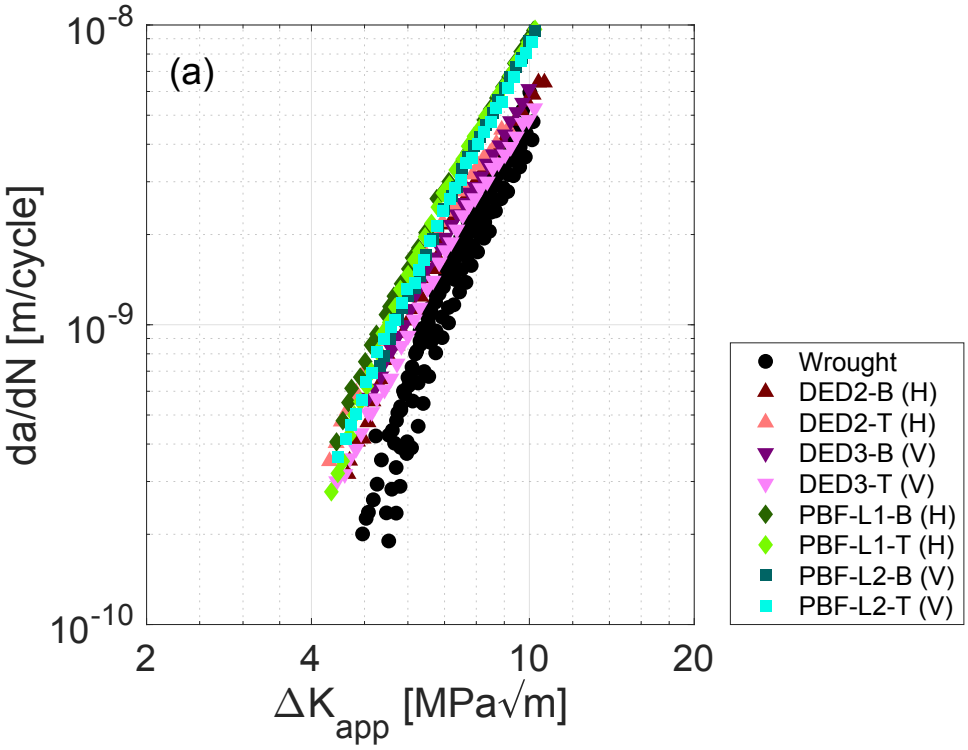

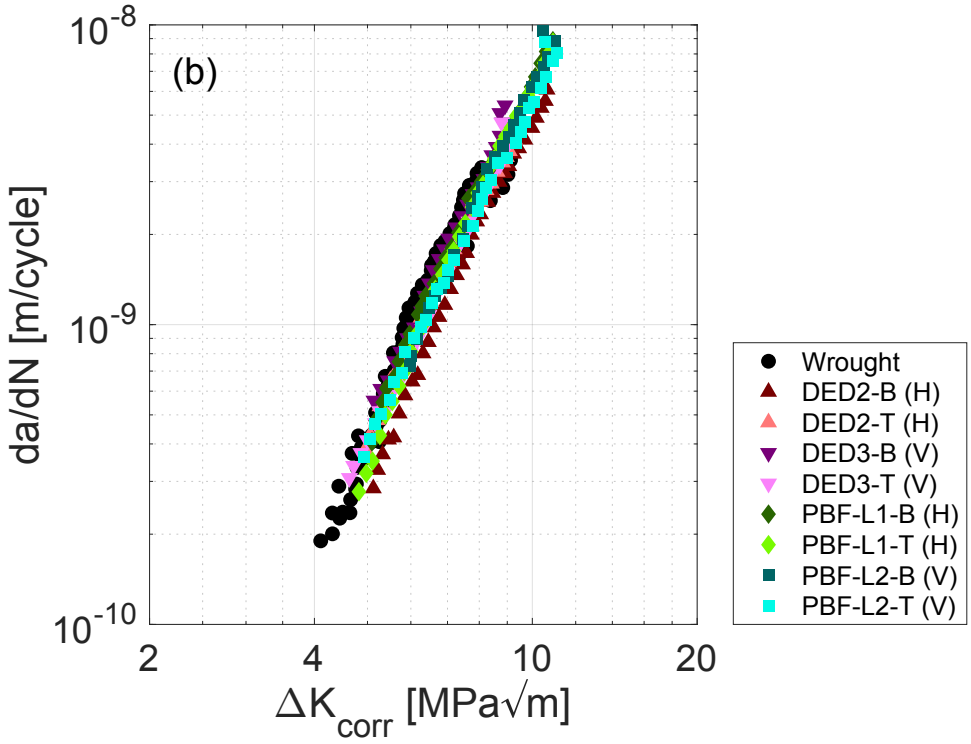

***Figure 6.7**: (a) Measured FCGRs for DED and PBF compared to wrought and (b) corrected.*

After fatigue testing, specimens from decreasing ΔK_{app} tests were fractured open by rapid loading for evaluation and comparison of the fatigue surfaces. The fatigue crack surfaces illustrated in **Figure 6.8**(a)-(d) reveal relatively smooth crack paths with similar levels of roughness in the near-threshold regime for select specimens in this study (DED2-T (H), PBF-L1-T (H), Wrought (B = 6.35 mm), and Wrought (B = 4.06 mm)). Striations are visible in a few locations, a few pores are apparent in the DED specimen, and a small number of secondary cracks can be observed in all specimens. Overall, these images from the interior of the specimens are consistent with the crack profiles shown in **Figure 6.6** and reflect relatively flat, transgranular crack paths observed in these materials. They also confirm that the grain morphologies of the AM materials have little impact on the fatigue crack growth process in this single-phase Type 304L stainless steel.

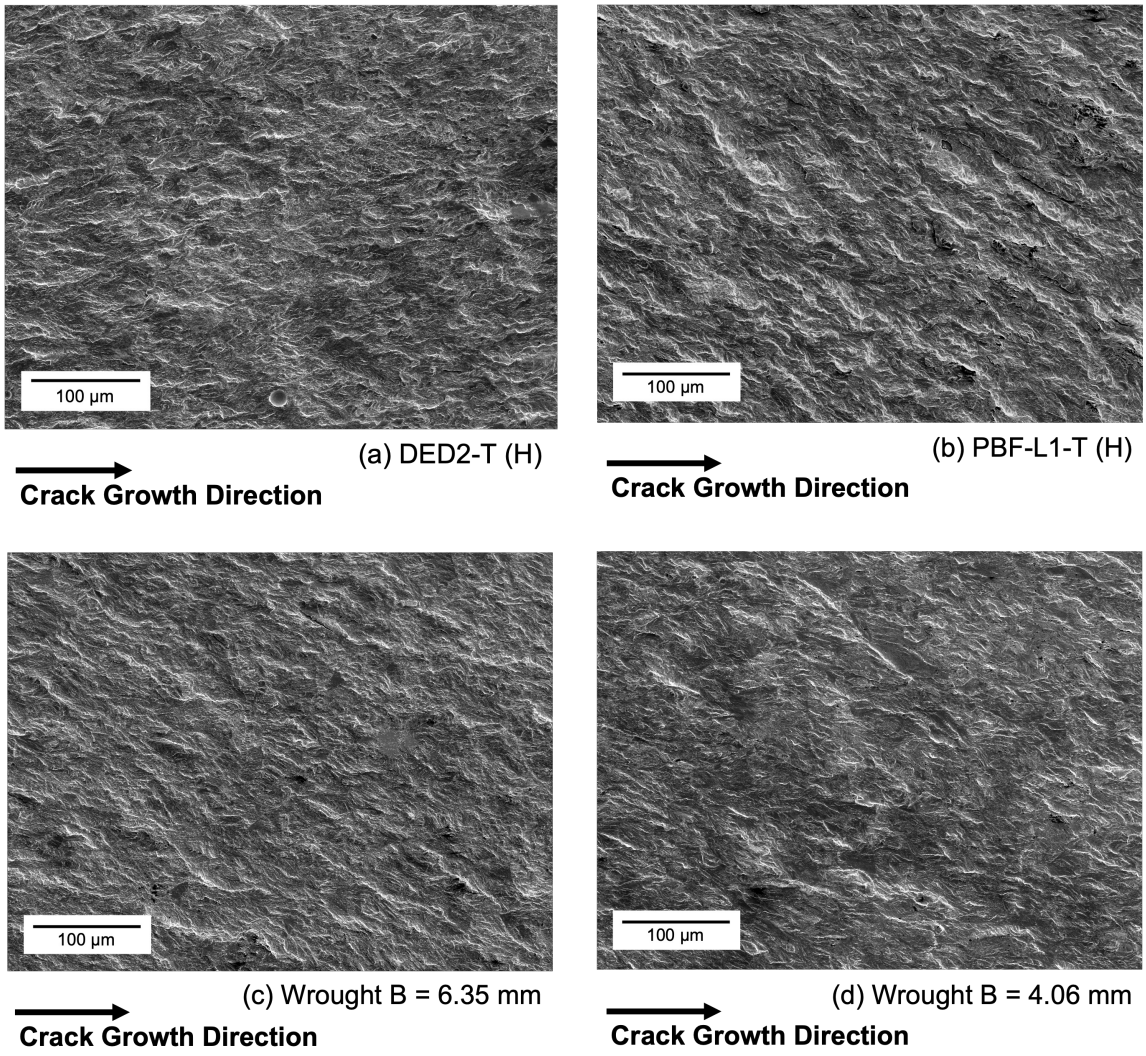

***Figure 6.8**: Fatigue crack surface images of (a) DED2-T (H) (b) PBF-L1-T (H) (c) Wrought (B = 6.35 mm) and (d) Wrought (B = 4.06 mm). Build direction is normal to the crack surface for the AM specimens.*

6.4. Conclusions

In conclusion, a comparison of residual stress and fatigue crack growth rates of additively manufactured Type 304L stainless steel produced by DED and PBF illustrates some significant findings. Slitting measurements verified consistency and reproducibility in the residual stress in the two AM processing methods. Greater residual stress in PBF builds compared to DED builds is attributed to higher cooling rates, which is a consequence of the fundamental differences in the t processes. Measurements of FCGRs in DED and PBF materials both parallel and perpendicular to

the build directions reveal differences that can be attributed to residual stress. Specifically, the PBF material featured comparatively larger tensile residual stress in both orientations resulting in higher fatigue crack growth rates than observed in the DED material. Electron backscatter diffraction (EBSD) images revealed similar grain shapes for both processing methods, although the grain sizes in the PBF material were smaller than in the DED. The results of this study demonstrate that residual stress differences from the two AM processes have a significant impact on measured FCGRs. Correcting the data for the influence of the residual stress intensity factor brings the data for both processing methods and both test orientations into agreement for this austenitic single-phase Type 304L stainless steel. Furthermore, the corrected results agree with those for an annealed wrought reference material similarly corrected for the influence of fatigue crack closure. Finally, transgranular crack propagation was observed in all cases, indicating that grain size and morphology have a relatively insignificant effect on fatigue crack growth compared to the more significant effect of residual stress.

Acknowledgements

This work was supported by a NASA Space Technology Research Fellowship (CMS) and material was provided by Sandia National Laboratories. Sandia National Laboratories is a multi-mission laboratory managed and operated by National Technology & Engineering Solutions of Sandia, LLC, a wholly owned subsidiary of Honeywell International Inc., for the U.S. Department of Energy's National Nuclear Security Administration under contract DE-NA0003525. This paper describes objective technical results and analysis. Any subjective views or opinions that might be expressed in the paper do not necessarily represent the views of the U.S. Department of Energy or the United States Government. Parts of this study were carried out at the UC Davis Center for Nano and Micro Manufacturing (CNM2). Additional material characterization in this study was carried out at the Advanced Materials Characterization and Testing facility in the Department of Materials Science and Engineering at UC Davis. The SEM images were acquired using a Thermo Fisher Quattro S ESEM funded through the NSF-MRI program DMR-1725618.

References

1. Li, C.L., Z.Y.; Fang, X.Y.; Guo,Y.B.;, *Residual Stress in Metal Additive Manufacturing.* 4th CIRP Conference on Surface Integrity (CSI 2018), 2018. **Procedia CIRP 71 (2018)**: p. 348–353.

2. Lewandowski, J.J. and M. Seifi, *Metal Additive Manufacturing: A Review of Mechanical Properties.* Annual Review of Materials Research, Vol 46, 2016. **46**: p. 151-186.

3. DebRoy, T., et al., *Additive manufacturing of metallic components – Process, structure and properties.* Progress in Materials Science, 2018. **92**: p. 112-224.

4. Shamsaei, N. and J. Simsiriwong, *Fatigue behaviour of additively-manufactured metallic parts.* Procedia Structural Integrity: 3rd International Symposium on Fatigue Design and Material Defects (FDMD 2017), 2017. **7**: p. 3-10.

5. Donald, J.K. and D.A. Lados, *An integrated methodology for separating closure and residual stress effects from fatigue crack growth rate data.* Fatigue & Fracture of Engineering Materials & Structures, 2006. **30**(3): p. 223-230.

6. Lados, D.A. and D. Apelian, *The Effect of Residual Stress on the Fatigue Crack Growth Behavior of Al-Si-Mg Cast Alloys - Mechanisms and Corrective Mathematical Models.* Metallurgical and Materials Transactions A-Physical Metallurgy and Materials Science, 2006. **37A**: p. 133-145.

7. Lados, D.A., D. Apelian, and J.K. Donald, *Fracture mechanics analysis for residual stress and crack closure corrections.* International Journal of Fatigue, 2007. **29**(4): p. 687-694.

8. James, M., et al., *A Methodology for Partitioning Residual Stress Effects From Fatigue Crack Growth Rate Test Data.* Materials Performance and Characterization, 2016. **5**(3): p. 194-214.

9. Newman, J.A., et al., *Characterization of Residual Stress Effects on Fatigue Crack Growth of a Friction Stir Welded Aluminum Alloy*. 2015. NASA Langley Research Center, Hampton, VA. Report No. NASA/TM–2015-218685.

10. Smudde, C.M., et al., *Evaluation of Residual Stress Reproducibility and Orientation Dependent Fatigue Crack Growth in PBF Stainless Steel* To be submitted: Additive Manufacturing, 2023.

11. Smudde, C.M., et al., *Effects of Residual Stress on Orientation Dependent Fatigue Crack Growth Rates in Additively Manufactured Stainless Steel.* Submitted to International Journal of Fatigue, 2022.

12. Smudde, C.M., et al., *The influence of residual stress on fatigue crack growth rates of additively manufactured Type 304L stainless steel.* International Journal of Fatigue, 2022. **162**: p. 106954.

13. A240/A240M-19 *Standard Specification for Chromium and Chromium-Nickel Stainless Steel Plate, Sheet, and Strip for Pressure Vessels and for General Applications*. 2019. ASTM International: West Conshohocken, PA.

14. Hill, M.R., *Chapter 4: The Slitting Method*, in *Practical Residual Stress Measurement Methods*, G.S. Schajer, Editor. 2013, Wiley. p. 89-108.

15. Ronevich, J.A., C.R. D'Elia, and M.R. Hill, *Fatigue crack growth rates of X100 steel welds in high pressure hydrogen gas considering residual stress effects.* Engineering Fracture Mechanics, 2018. **194**: p. 42-51.

16. Cheng, W. and I. Finnie, *Residual Stress Measurement and the Slitting Method*. Mechanical Engineering Series, ed. F.F. Ling. 2007, New York, NY: Springer.

17. E647-15, *Standard Test Method for Measurement of Fatigue Crack Growth Rates*. 2015. ASTM International: West Conshohocken, PA.

18. Smudde, C.M., J.C. Gibeling, and M.R. Hill, *Validation of On-line Crack Compliance Data Analysis Methods for the Residual Stress Intensity Factor.* Submitted to Engineering Fracture Mechanics, 2022.

19. Schindler, H.J., W. Cheng, and I. Finnie, *Experimental determination of stress intensity factors due to residual stresses.* Experimental Mechanics, 1997. **37**(3): p. 272-277.

20. Griffith, M.L., et al., *Understanding the microstructure and properties of components fabricated by Laser Engineered Net Shaping (LENS).* Solid Freeform and Additive Fabrication-2000, 2000. **625**: p. 9-20.

21. Hofmeister, W., et al., *Solidification in direct metal deposition by LENS processing.* JOM-Journal of the Minerals Metals & Materials Society, 2001. **53**(9): p. 30-34.

22. Zheng, B., et al., *Thermal Behavior and Microstructural Evolution during Laser Deposition with Laser-Engineered Net Shaping: Part I. Numerical Calculations.* Metallurgical and Materials Transactions A, 2008. **39**(9): p. 2228-2236.

23. Zheng, B., et al., *On the evolution of microstructure and defect control in 316L SS components fabricated via directed energy deposition.* Materials Science and Engineering a-Structural Materials Properties Microstructure and Processing, 2019. **764**: p. 138243.

24. Hooper, P.A., *Melt pool temperature and cooling rates in laser powder bed fusion.* Additive Manufacturing, 2018. **22**: p. 548-559.

25. Suresh, S., *Fatigue of materials*. 2nd ed. 1998, Cambridge and New York: Cambridge University Press. 679 pp.

26. Donald, J.K., G.H. Bray, and R.W. Bush, *An evaluation of the adjusted compliance ratio technique for determining the effective stress intensity factor.* Fatigue and Fracture Mechanics: Twenty-Ninth Volume, ASTM STP 1332, American Society for Testing and Materials, West Conshohocken, PA, 1999: p. 674-695.

27. Dowling, N.E., *Mechanical behavior of materials : engineering methods for deformation, fracture, and fatigue*. 4th ed. 2013, Boston: Pearson. Chapter 9: 416-490.

Chapter 7:
Summary and Future Work

7.1. Summary

This work has advanced the understanding of the influence of processing methods on mechanical properties of additively manufactured (AM) materials, further developed the methods of characterizing residual stress effects on fatigue crack growth performance by quantifying the residual stress intensity factor (K_{res}), and applied those methods to interpret the results of fatigue crack growth rate (FCGR) experiments in AM materials.

The primary findings can be summarized as follows:

1. In Chapter 2, near-threshold fatigue crack growth rate (FCGR) data of edge cracks growing perpendicular to the build direction (horizontal) in directed energy deposited (DED) Type 304L austenitic stainless steel were determined to be influenced significantly by the presence of tensile residual stress. A comparison to annealed wrought material revealed faster measured fatigue crack growth rates in the DED material in the as-built condition. A slitting experiment of a sacrificial specimen demonstrated the significant contributions of residual stress to the driving force of crack growth: the measured K_{res} values in the DED specimen were large in comparison to the $K_{min,app}$ and $K_{max,app}$ values of the near-threshold FCGR experiment. Using the values of K_{res} from slitting to correct the test data provided an estimate of the intrinsic material crack growth performance that accounted for the effects of residual stress. This performance was similar to the FCGR data of annealed wrought material that had been corrected for crack closure effects.
2. In Chapter 3, the on-line crack compliance (OLCC) method was used to provide accurate predictions of K_{res} without the need for a secondary specimen in AA7050-T74

edge crack specimens with compressive residual stress. New data analysis techniques were developed and validated so that a clear and concise OLCC methodology would be available for standardization. K_{res} values in this work agreed well with the results of slitting measurements in replicate specimens. As such, it was concluded that the OLCC method was an accurate means of quantifying K_{res} without the need to sacrifice material, allowing FCGR data and K_{res} values to be collected in the same test.

3. In Chapters 4 and 5, near-threshold fatigue crack growth rates of edge cracks in DED and powder bed fused (PBF) Type 304L austenitic stainless steel were evaluated in two different orientations with respect to the build direction. Measured fatigue crack growth rates reflected the differences in process-induced residual stress in the two materials. Orientation dependent residual stress resulted in different fatigue crack growth behavior in the DED specimens. The horizontal specimens exhibited higher FCGRs as compared to the vertical (specimens oriented with cracks growth parallel to the build direction). Higher average K_{res} measured by the OLCC method in the DED specimens oriented for crack growth perpendicular to the build direction led to higher measured FCGRs as compared to those oriented parallel that had lower values of K_{res}. In comparison, implementing the OLCC method to determine K_{res} revealed small variations in K_{res} among PBF specimens and both orientations of specimens had similar measured FCGRs.
4. Finally, DED and PBF materials are compared in Chapter 6. High tensile residual stress acting at the crack tip enhanced crack growth and led to faster fatigue crack growth rates in the threshold regime of PBF 304L than the DED 304L. Differences in K_{res} between the two orientations in both DED and PBF were consistent with differences in

measured FCGRs. However, when FCGR data were corrected for K_{res} from OLCC, the intrinsic material behavior was similar for all specimens, highlighting the importance of accounting for residual stress effects on fatigue of AM materials. Furthermore, the corrected FCGR data for the DED and PBF specimens agreed with those of an annealed wrought material corrected primarily for crack closure. In addition, electron backscatter diffraction (EBSD) imaging revealed elongated grains in the build direction in both materials. While the average grain size in PBF was smaller than that in DED, neither material microstructure demonstrated obvious texture in grain orientation. Since both materials have anisotropic microstructures, it was concluded that the residual stress has a large impact on fatigue crack growth rates and the unique AM microstructure does not have a significant influence.

7.2. Future Work

The present work demonstrated the significant influence process-induced residual stress has on measured fatigue crack growth rates of AM material. As such, a thorough understanding of the effects of residual stress is critical for accurate predictions of fatigue life and reliable engineering design. Some opportunities for future work on residual stress in AM materials include:

1. **Performing stress relief heat treatments on DED and PBF Type 304L stainless steel and comparing the measured FCGRs and K_{res} values to those presented in this work**. Heat treatments that result in stress relief may also result in microstructure evolution, which can detrimentally affect the material strength. Therefore, it would be important to also compare the strength and grain morphology of the AM material before and after stress relief in addition to using the methods further developed in this work to compare FCGR behavior and K_{res} values. Finally, the corrected FCGR data of as-built

material and stress relieved material can be compared to each other and to data for annealed wrought to reveal the overall influence of processing methods and post processing strategies on mechanical performance of AM material.

2. **Assessing the accuracy of process model predictions of residual stress effects on FCGRs in AM material**. Engineering design requires accurate model predictions of service life for fatigue critical applications, therefore validating model predictions of FCGRs is critical to the integration of AM technology. By using AM material with reliable processing parameters and well characterized residual stress profiles, K_{res} can be measured via destructive slitting method in secondary specimens and compared to model predictions of the same material. Then, measured K_{res} and predicted K_{res} can be used to estimate FCGRs based on R_{tot} and K_{tot} and well known FCGR data curve for comparable stress-free material. Primary specimens can be tested, and the experimental results compared to the predictions.
3. **Mitigating residual stress through process parameter manipulation and exploring the effects on resulting fatigue crack growth rate behavior.** A long-term goal of AM technologies is to be able to use as-built components that require limited post-processing to achieve improved structural reliability, relative to the current work. So, determining whether the manipulation of process parameters can improve crack growth rate performance by minimizing residual stress magnitudes or manipulating the distribution of tensile and compressive residual stress in different parts of the build would be beneficial for the advancement of AM.
4. **Measuring residual stress fields at a smaller length scale for applications in fatigue crack initiation testing and modeling**. Residual stress can be classified by the

different length scales under consideration. In this work, macroscale residual stress across the part scale (mm) was considered. However, knowledge of residual stress between and among grains (μm) can aid in the predictions of fatigue crack initiation by enhancing the accuracy of current models. Therefore, determining a method for quantifying K_{res} at these length scales is of interest. A possible approach comparable to the slitting method introduces a cut using a focused ion beam (FIB) on a scanning electron microscope (SEM) and the deformation is measured using digital image correlation (DIC) after each increment. This method, known as microscale slotting, has not been validated for use with AM material, yet could provide estimates of K_{res} at the microscale for model predictions of fatigue crack initiation.

Thank you